PROPAGATION OF LIGHT IN DISORDERED MEDIA:

A SEARCH FOR ANDERSON LOCALIZATION

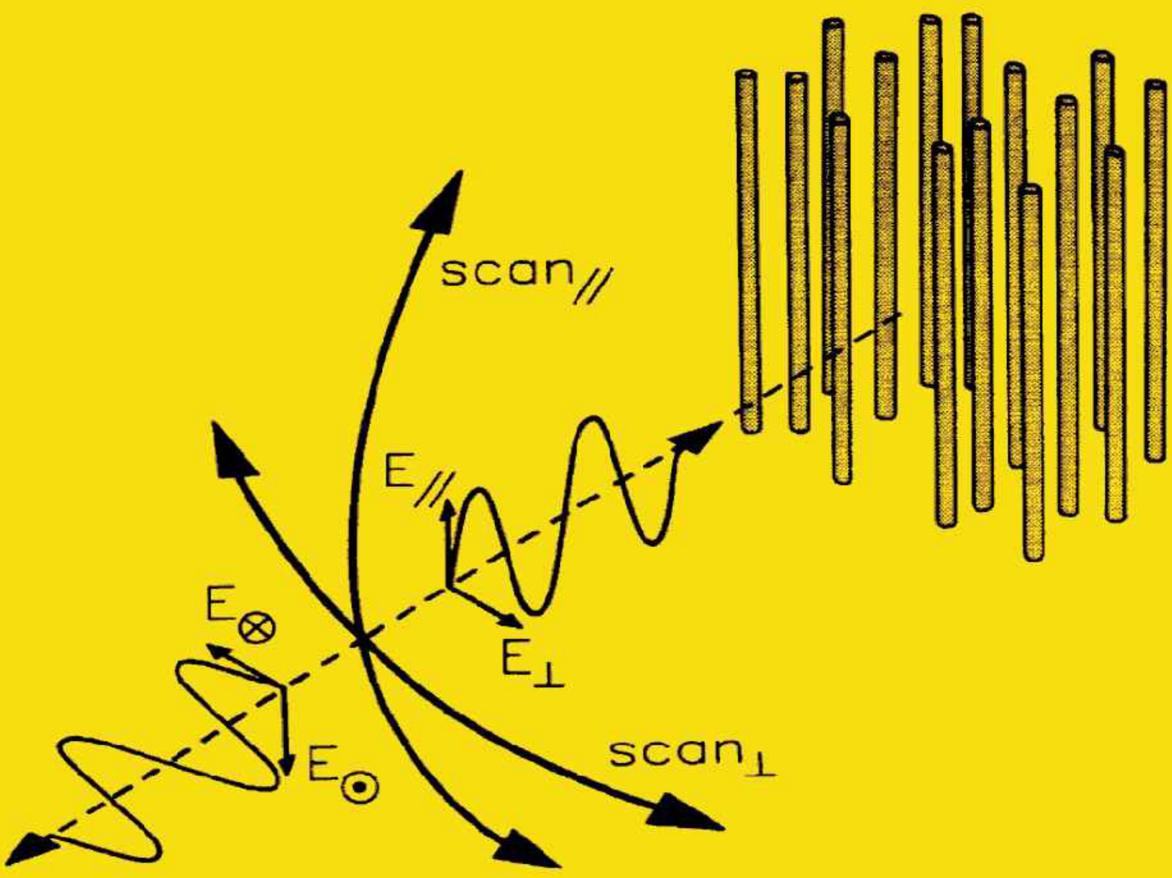

M.B. van der Mark

PROPAGATION OF LIGHT IN DISORDERED MEDIA:

A SEARCH FOR ANDERSON LOCALIZATION

M.B. van der Mark

PROPAGATION OF LIGHT IN DISORDERED MEDIA:

A SEARCH FOR ANDERSON LOCALIZATION

ACADEMISCH PROEFSCHRIFT

ter verkrijging van de graad van doctor
aan de Universiteit van Amsterdam
op gezag van de Rector Magnificus
Prof. Dr. S. K. Thoden van Velzen
in het openbaar te verdedigen in de Aula der Universiteit
(Oude Lutherse Kerk, ingang Singel 411, hoek Spui),
op donderdag 14 juni 1990 te 13.30 uur

door

Martinus Bernardus van der Mark

geboren te Beemster

Promotor: Prof. Dr. A. Lagendijk

Faculteit der Natuur- en Sterrenkunde

The work described in this thesis was part of the research program
of the "Stichting voor Fundamenteel Onderzoek der Materie (FOM)"
and was carried out at the

Natuurkundig Laboratorium der
Universiteit van Amsterdam
Valckenierstraat 65
1018 XE Amsterdam
The Netherlands

where a limited number of copies of this thesis are available

aan de lezer

Contents

Chapter 1

Introduction

1.1 Anderson localization

Localization as introduced by P.W. Anderson[1] refers to a dramatic change in the propagation of an electron when it is subject to a spatially random potential.[2] Normally, the electron is scattered diffusively, resulting in a finite conductivity. In this multiple scattering process, interference can be neglected. At localization the interference of (multiple) scattered waves cannot be neglected any more, but indeed its influence becomes essential.

Several approaches can be used to describe the phenomenon of localization in a disordered medium. One of these methods is to look at the transport properties of the electron in a conductor containing random scattering centers. In this picture localization is concerned with the vanishing of the conductivity or diffusion coefficient. This view of localization was given a thorough foundation by Götze,[3] and later workers,[4] who used transport equations of the mode-coupling type.

The dimension d of the disordered medium (see also Sect. 2.1.1) is a crucial parameter. I n dimension $d = 1$ and $d = 2$ any degree of disorder will lead to a finite localization length while in $d = 3$ a certain critical degree of disorder is needed before localization will set in. The measure of disorder in the medium is the mean free path λ_{mf} of the electron. So in case of a three-dimensional system there is a critical mean free path λ_{cr} corresponding to a mobility edge, and the heuristic Ioffe-Regel criterion $\lambda_{mf} \lesssim \lambda$ for localization, modified by Mott[5] to

$$\lambda_{mf} \lesssim \frac{\lambda}{2\pi} , \tag{1.1}$$

applies. Here λ is the wavelength of the electron. If this condition is met, the wave character of the wave(function) is completely lost and localization is established. In other words, there is a phase transition in the propagation of the wave through the disordered system as a function of randomness. At the mobility edge, $\lambda_{mf} = \lambda_{cr}$, the localization length λ_{loc} is still infinitely long, but becomes measurable if λ_{mf} is sufficiently smaller than

λ_{cr} so that $\lambda_{loc} < L$, with L the size of the sample (see also Chapter 7). The occurence of localization also depends on the type of randomness in the medium. I will assume the randomness in the system is statistically homogeneous, thereby excluding localization in disordered systems with underlying order.

Although the majority of theories of localization has been developed for the Schrödinger wave equation, it is quite clear that the concept is much broader. This was a.o.[6] first recognized by Lagendijk in early 1985. In principle, for almost any wave equation localized solutions can be obtained when solved for a random medium. This becomes clear when one realizes that the Ioffe-Regel criterion can be applied to all wave phenomena. Several experiments have been suggested in which localization of waves could be observed.[7–9] Localization of electromagnetic waves is of particular interest because one deals with classical (non quantum-mechanical) waves with a vector nature, described by a well-established and well-studied set of equations basically different from the Schrödinger wave equation. This makes localization of light a fascinating field in which modern developments of condensed matter physics can be applied to linear optics.

Despite all effort that has been made, clear evidence for the existence of a mobility edge in $d = 2$ or $d = 3$ has not been observed for electromagnetic waves yet, and, for as far as we know, neither for electrons or any other wave. However, precursors were observed in the form of some significant interference effects, and a lot of multiple-scattering theory which describes those interference effects has been developed the past few years.

1.2 Anderson localization: Why should it happen?

When considering propagation of a wave through a disordered system, one might at first glance expect that, since all phase information is scrambled, interference will not play a part. As I will explain now, it can easily be seen that this is not true.

Suppose we consider the propagation of a wave in a random medium from point A to B (See Fig. 1.1). One should consider all possible paths from A to B. In the left-hand diagram of Fig. 1.1 two of them, I and II, are depicted. If the complex amplitudes along these paths are a_I and a_{II} respectively, the probability for arriving at B is $(a_I + a_{II})^2 = a_I^2 + a_{II}^2 + 2a_I a_{II}$, in which the incoherent contribution embraces the sum of the squares, whereas the cross product refers to the coherent or interference contribution. When one considers all possible paths, all interference terms will have different signs and magnitudes, and very likely cancel, so the average probability for arriving at B is $a_I^2 + a_{II}^2$. This random phase approximation appears to be very wrong for a medium close to the localization transition, but one can already point out much weaker conditions under which it breaks down.

Consider the transport of a wave in a random medium from point A onto itself as shown in the right-hand diagram in Fig. 1.1. Let us focus on arbitrary path I, and path II, which is the same as path I but traversed in opposite sense. The contributions of path I and II always add up coherently, because the waves traveled the same distance and consequently have the same phase. If one would add them up incoherently one would underestimate the returning probability by a factor of two.

Imagine a random distribution of very small strong scatterers, each having a size comparable or smaller than a wavelength, and a cross section σ. For a low density of scatterers, that is for σ small compared to the free area among scatterers, the probability for a wave to return to the original point will be small (this is why a self-avoiding random walk approximation can often be justified), though still twice the value for ballistics. Now, if we increase the density (decreasing mean free path), the probability for a sequence of scattering events to come back on the original scatterer will grow. When the free area among scatterers becomes less than their cross sections, the probability to return can be substantial, and, remember, is twice as high as "classically" expected, and therefore might dominate. In this regime, it is thinkable that a (self-consistent) random cavity mode, consisting of all kinds of loop and backscattering processes, develops, thereby reducing the diffusion constant D of the wave in the medium. For Anderson localization the diffusion constant approaches zero.

1.3 About scattering of electrons and light

In the first Section, it was explained why Anderson localization of light is such an interesting field, and already some differences and analogies between scattering of electrons and light were mentioned. Here, I will elucidate them in more detail. An overview of analogies

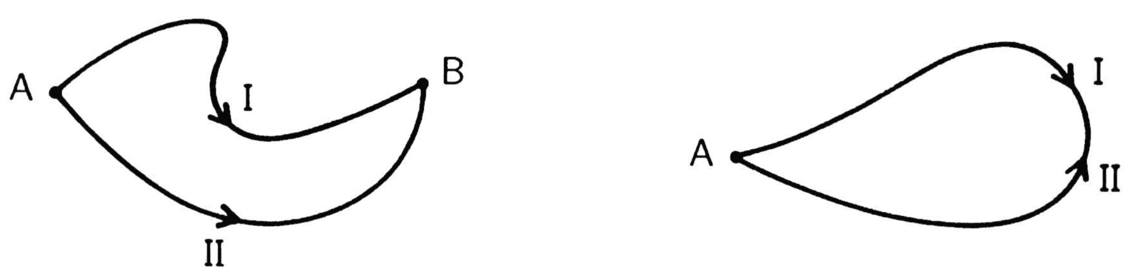

Figure 1.1: *Left: two possible paths (I and II) for wave propagation from A to B in a random medium. Right: a possible path (I) and its time-reversed counterpart (II) contributing to the returning probability for wave propagation from A.*

in optics and electronics is given in Ref. 10.

Elastic scattering is at the basis of localization. Inelastic scattering causes loss of coherence so that interference and hence localization effects are affected. In the case of electrons, inelastic scattering amounts to changing the energy of the electrons, while their number is conserved. The most important inelastic process in light propagation however is absorption, and amounts to removing intensity from the wave.

Electrons are described by a scalar wave function or, if spin-dependent interactions are involved, by a two-component spinor. For the scalar case, the long-wavelength limit for scattering is s-wave scattering which is isotropic and wavelength independent. Light is described by a three-dimensional vector field, and the long-wavelength (Rayleigh) limit is p-wave scattering (induced-dipole radiation) which, although there is symmetry with respect to forward and backward scattering, is not isotropic. Moreover, the cross section for Rayleigh-scattering varies with the inverse-fourth power of the wavelength. The very important long-wavelength limit in localization is therefore totally different for electrons and light, and from a certain point of view probably in favor for electrons.

Experimentally, electron localization is studied through the electrical conductance of a sample, usually some mesoscopic structure.[11,12] An important aspect is the possibility to influence the interference by applying a magnetic field (Aharonov-Bohm effect). In light scattering the net flux is not easily determined and, under accessable experimental conditions, the interference can not be influenced. On the other hand, it is possible to perform angular-resolved and time-resolved scattering experiments with light.

Finally, in the electronic case, an important complication is that electrons have a mutual interaction. In classical linear optics, light-light interaction is absent and a single-wave theory is exact.

Chapter 2

How to observe localization

In observing Anderson localization of light, two important questions regarding the medium and the detection technique arise: "What should the medium look like, and whereof should it consist?" and: "How can we get information from the light scattered from the medium, and what kind of source should we use?". An overview of experiments in the field of localization of light is given in Ref. 13.

2.1 The medium

A possible candidate for a medium to obtain localization in, will appear to be white: it should consist of very strongly-scattering, non-absorbing particles. Those particles should therefore consist of a very transparant material having a high refractive index and a size comparable to the wavelength of the incoming wave. Further, the contrast in refractive index of the scatterers with the material in which they are embedded should be as high as possible to obtain the highest scattering efficiency.

What we apparently need is a material with a very high real part of the refractive index, combined with a very low value for the imaginary part. Surveying the electromagnetic spectrum on the refractive index of materials, one comes to the conclusion that probably the best materials can be found in the optical regime. At very long wavelengths however, a medium build up from metal spheres would also be interesting, but there we have to realize that a medium should preferably extend over many wavelenghts in order to give multiple scattering and interference a chance. This will certainly give some problems due to the inevitable large size of the system.

Ideally a medium in which light could be localized probably looks like a perfect (diffusive) reflector for light outside, and acts as a trap of light inside. A system which shows these phenomena acts as a "white hole"; light that comes from the outside will very likely be reflected, where at the same time the light inside cannot get out. Only a top layer of the medium will be penetrable by the incoming wave and will allow the internal waves to leak out.[14]

Considering the shape of the medium, an infinite medium would be preferable from a theoretical point of view. A practical shape however is that of a slab, which still allows you to do theory in simple coordinates and with relatively convenient boundary conditions (see Chapter 4). More practical is that well-defined transmission and reflection experiments are possible, in which the thickness of the slab is an important parameter.

2.1.1 Topology and dimension

Apart from its constitution, the dimensionality, topology and nature of the disorder[15] of the system are very important parameters for localization. In this thesis, I will only consider statistically homogeneous and continuous media in dimension $d = 2$ and $d = 3$.

Nevertheless, it is very interesting to look for localization phenomena in media with an other topology or randomness such as a network made of microwave cavities containing a random scatterer at every crossing,[16] or fractal networks.[17,18] Since those networks, due to their guiding properties, already exclude some degrees of freedom for the propagating waves compared to free space, the localization properties of these systems will be quite different from continuous and homogeneous media.

In Section 1.1, I already mentioned that the existence of the mobility edge is strongly dependent upon dimension. From theoretical study on the propagation of waves in random and incommensurate structures, and scaling theory,[20–23] the situation for infinite and lossless systems seems to be the following: In a medium with dimension $d = 1$, there is always localization. For $d = 2$, the situation is similar, although the localization length generally is much longer, and very sensitive to the kind of disorder. It is the so-called (lower) critical dimension; introduction of a little loss in the system, or making the system finite may already destroy localization. In $d = 3$ there is a mobility edge, this means that at least a certain degree of disorder is needed before localization sets in. In Section 1.1 we have seen that this corresponds to a critical value for the mean free path λ_{cr} with $\lambda_{cr} \lesssim \lambda/2\pi$. Although it seems somewhat academic to mention, in dimension $d = 4$, localization exists only marginally: it is the upper critical dimension,[24] so there is no Anderson localization for $d > 4$.

The apparent relation that a wave in a higher dimension is harder to localize is plausible because for systems with arbitrary dimension d, the returning probability is proportional to r^{1-d}, as it is a measure for the intensity of a scattered (hyper)spherical wave at a distance r. An implication of this is that in a one-dimensional system only the phase of the wave depends on the distance r between scatterers, which makes localization theory for $d = 1$ comparatively trivial.

A classical diffusion problem in a disordered medium can be described by a random walk.[19] The problems of both the unrestricted and self-avoiding random walk can be studied, and generally give different solutions. There are however many problems in physics where those solutions are the same for a high enough dimension, for example $d > 4$. The probability for returning in a point in that d-dimensional space is then of measure zero, and a mean-field approach is justified: the scatterer does not change its own field. Since localization is also concerned with the probability of return (which we may characterize by the term "self-doubling random walk"), this can give a hint about the dependence of localization on the dimensionality of the medium.

It is clear that a system with dimension $d = 3$ is the most natural, and therefore experimentally the easiest to construct. Realization of a medium with dimension $d = 1$ might be done in several ways,[25] depending on the nature of the wave.[26] Optically it can be imagined as a random stack of partially transmitting mirrors.[27] Eventually, diffraction into the other two dimensions is however inevitable. For microwaves, a conducting waveguide containing dielectric scatterers might be used. Here, succesful measurements may be disturbed by impedance mismatch and (cavity) losses. Apart from elecromagnetic waves, one can also think about propagating electrons in very thin conducting wires,[28] or propagation of a transverse wave in a vertically suspended string with some random masses attached to it.[29] Systems with $d = 3$ and $d = 2$ are part of our research and will be discussed in Chapters 5 and 6. Media with $d = 4$ or higher cannot be constructed, but in some cases it appears to be possible to map a higher-dimensional scalar-wave equation on some lower-dimensional vector-wave equation.[30,31] As a matter of fact, this might have important implications on the existence of Anderson localization of light in a three-dimensional medium.

2.2 The detection

To prepare a medium in which the propagation of light might be studied is one thing. The other is, how to find out what is going on in that medium when it is illuminated.

There seem to be several ways to observe Anderson localization of light in a slab, and I will discuss them very briefly. In Chapter 5, some experiments and their results will be discussed in detail.

2.2.1 Transmission through a slab

One way to observe Anderson localization is to look at the transmission of light through a slab which is illuminated from one side with a parallel coherent beam, as a function of the

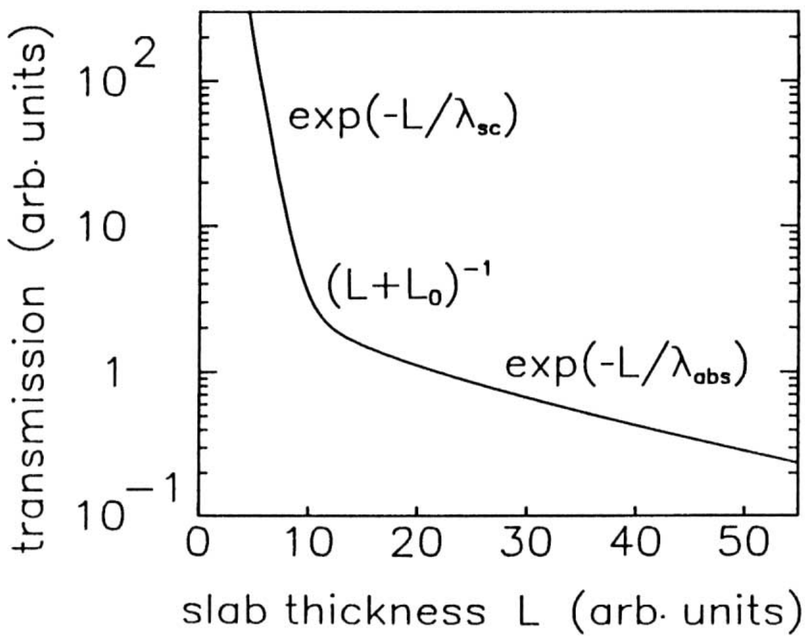

Figure 2.1: *Schematic presentation of the transmission as a function of sample thickness.*

slab thickness L. One should first realize, and study in detail, what a "normal" strongly scattering medium should do. In Fig. 2.1 we have plotted schematically the expected behavior. First, for small L, one expects a strong decrease of the transmission because of the scattering of light out of the coherent beam. This gives rise to an exponential decay for the coherent part of the transmitted radiation with a decay length λ_{sc}, the scattering mean free path. For larger L one arrives at the diffusive regime, and the dependence should be roughly as L^{-1}. The third regime arises because eventually the diffuse light, which traverses very long distances in the sample, gets absorbed. The characteristic length λ_{abs} associated with this absorption is for isotropic scatterers given by $\lambda_{abs} = \lambda_{sc}/\sqrt{3(1-a)}$, in which the scattering mean free path has been used, and where a, the albedo, gives the probability in a single-scattering event of being scattered rather than absorbed. It is clear that albedos very close to one (typical values for $1-a$ are 10^{-5}) can still give rather short characteristic inelastic decay lengths.

If Anderson localization would occur, the diffusive regime should be absent, or at least modified dramatically. Particularly, it would be expected to bend over to an exponential decay with a characteristic length λ_{loc}, the localization length. It is obvious, that because absorption also gives an exponential decay, it will be hard to separate the effects of localization and absorption. Anderson[6] and John[8] have speculated on the behavior of transmission and backscattering as a function of sample size and absorption. They came to very different conclusions. In Chapter 7 I will return to this in some detail.

2.2.2 Angular-resolved backscattering

Another way of monitoring the Anderson localization transition would be the observation of angular-resolved backscattering. If the mean free path is not short enough to make the diffusion constant vanish as a result of Anderson localization, one may still observe interference effects that affect this constant. Let us look at interference effects in multiple scattering. A well known phenomenon in the scattering of coherent light by a rigid random medium is "laser speckle", which results from interference between scattered waves that traveled through the sample along different light paths (by "light path" I mean a sequence of scattering events s_1,s_2,...,s_f). If the scatterers are allowed to move over distances of the order of the wavelength of the light or more at the time scale of the measurement, the spatial distribution of the scattered intensity will be the average of a rapidly changing speckle pattern, and therefore essentially angle independent. Liquid random samples in which the scatterers are subject to Brownian motion,[32,33] or rigid random samples that are spun, yield scattered-intensity patterns that almost look as they would if interference between light paths did not exist. One type of interference however survives: in the direction of pure backscattering, the waves that travel along the same light path in opposite directions (time-reversed paths) will always have the same phase and interfere constructively (actually this holds only for the backscattered light component polarized parallel to the incident beam, but for the moment we neglect polarization effects). Moving away from this direction, a difference in phase $\Delta\phi$ develops, which increases with the angle

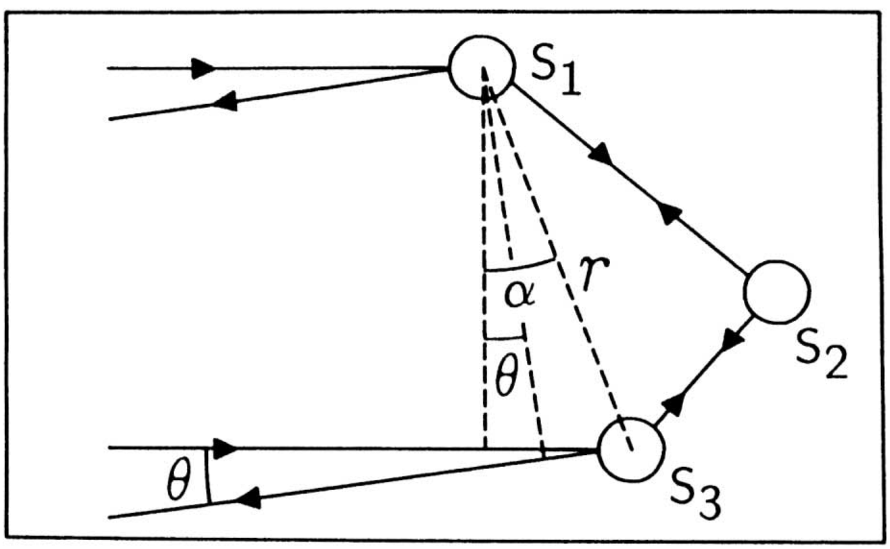

Figure 2.2: *Time-reversed pair of light paths. In case of exact backscattering the paths are equally long. In all other directions there will be a phase difference between the time reversed waves.*

θ between the incoming and outgoing wave vectors and further depends on the relative positions of the first and last scatterer s_1 and s_f, according to

$$\Delta\phi = \frac{r}{\lambda}\{\sin\alpha - \sin(\alpha-\theta)\} = \frac{2r}{\lambda}\cos(\alpha-\theta)\sin(\theta/2) \ , \tag{2.1}$$

where r is the distance between s_1 and s_f (see Fig. 2.2). With increasing θ the interference for an individual light path will oscillate between constructive and destructive interference. At $\theta = 0$ all time-reversed pairs interfere constructively, at small θ only light paths with large values of r will interfere destructively, and at large θ constructive and destructive interference will average out (c.f. Fig. 2.3). Thus, within a certain solid angle around the direction of pure backscattering there will be an enhanced intensity (see Fig. 2.4). In other words, interference increases the returning probability and hence reduces the amount of light transmitted by the sample. This can be interpreted as a reduction of the diffusion coefficient. This phenomenon of coherent backscattering from a random medium was recognized by Barabanenkov,[34] and Kuga and Ishimaru[35] but first linked to localization theory by van Albada and Lagendijk,[36] and Wolf and Maret.[37] It is seen as a precursor to Anderson localization, and is therefore often refered to as weak localization. Since the displacement r scales with the mean free path, the width of the cone of enhanced backscattering is expected to be inversely proportional to the mean free path. With the speed of light in the random medium c_{med}, the Boltzmann diffusion constant is defined as $D_B = c_{med}\lambda_{mf}/3$ which will, like the mean free path, decrease with increasing randomness of the medium.

From the former paragraphs one might conclude that in order to detect weak localization, one should merely look for enhanced backscattering. Enhanced backscattering has been known for long. An early reference to it was made by the 16$^{\text{th}}$ century Italian artist Benvenuto Cellini[38] who interpreted a halo that he observed around just the shadow of his own head among the shadows of a group of people as a sign of genius. There is also more recent experimental work,[39] and a number of possible explanations not involving interference have been very thoroughly discussed.[40] Enhanced backscattering may result for instance from shadow effects (only in the direction of pure backscattering one will not see scatterers that are located in the shadow of other scatterers) lens action, (dew drops may focus sunlight onto a plant leaf and refract much of the scattered light into the backward direction), or retroreflection (e.g. by cubic crystals). We may conclude that once enhanced backscattering is detected, one still needs to prove that it results from interference before it may be attributed to weak localization. The inverse proportionality between the mean free path and the width of the cone of enhanced backscattering seems to be a good criterion.

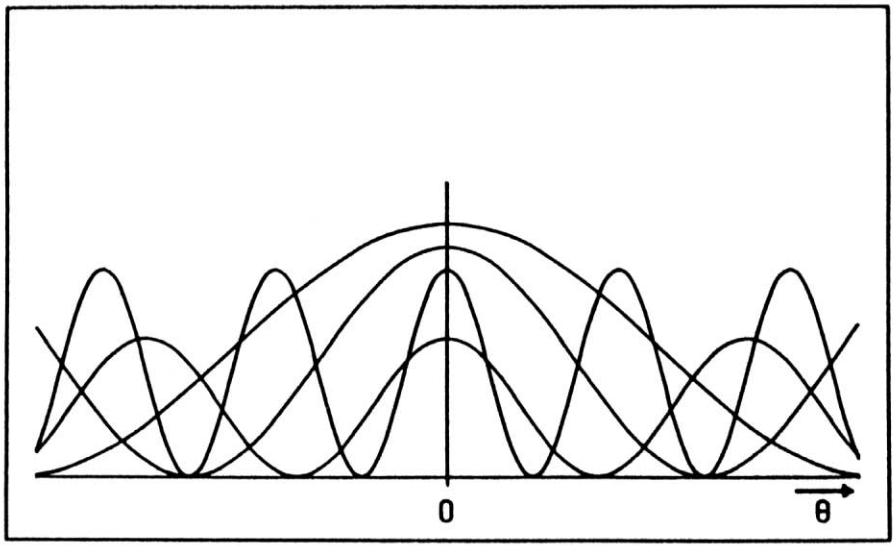

Figure 2.3: *A number of two-point source interference patterns belonging to different time-reversed pairs of waves.*

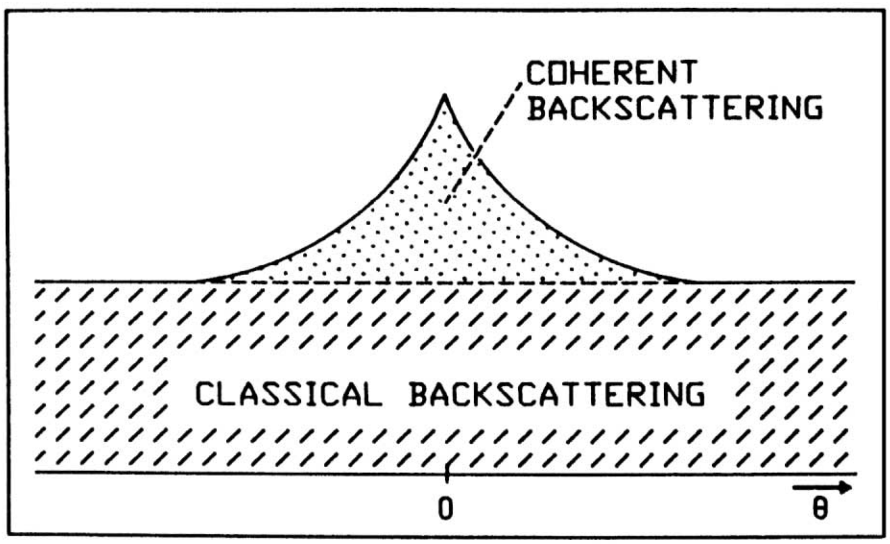

Figure 2.4: *Sum of the two-point-source interference patterns of all contributing time-reversed pairs of light paths.*

2.2.3 Time-resolved experiments

Localization is concerned with the slowing down of diffusion, and so one can think of different types of time-dependent measurements to directly probe the light transport, and hence measure the diffusion constant directly. High resolution in time can be obtained, for example, Vreeker et al.[41,42] studied the width of the coherent backscattering cone as a function of the length of the light paths in a time-resolved experiment on femtosecond scale. Others studied the decay of the transmitted intensity of random samples in the optical[43] and microwave[44] regime respectively. Here, the diffusion constant D can be found from the exponential decay of the diffusively transmitted intensity as a function of time. In Chapter 5 I will report on similar time-resolved experiments that we performed only recently. The interpretation of these very interesting experiments is given a theoretical basis in Chapter 4.

2.2.4 Determination of correlation in speckle

In Section 2.1, we have seen that weak localization of light results from interference between time-reversed pairs of waves, and gives a correction to the "classical" intensity pattern for backscattering. It has become understood that this is not the only type of correlation that affects the scattered-intensity pattern. The characteristic "speckle" pattern in diffusively scattered light from a laser finds its origin in a short-range correlation.[45] Further, the same interference that gives rise to universal conductance fluctuations in metals,[46] occurs in multiple scattering of light as well.[47]

These fluctuations give us another way to determine the diffusion constant. It is possible to measure the rate of change of the speckle pattern observed in the transmission of some medium on changing the wavelength of the light.[48–50] The diffusion constant can be determined from the width at half height $\Delta\nu_{\frac{1}{2}}$ of $\langle I(\nu)I(\nu+\Delta\nu)\rangle - \langle I(\nu)\rangle\langle I(\nu+\Delta\nu)\rangle$, the correlation function, for which theoretical approximations exist. Theory predicts three different correlation terms:[51,52] the short-range correlation,[53] often revered to as "memory effect", the long-range correlation,[54] and the size-independent correlation,[46] which is the source of universal conductance fluctuations (UCF). Also observation of the rate of change on varying the angle at which the medium is observed is a way to determine the diffusion constant, a possibility which is not present in the electronic conduction case where only the total transmission can be measured.[55,56]

Furthermore one might expect that the transition from diffusive propagation to a localized state will be associated with various observable fluctuation phenomena.

Chapter 3

Scattering by a single particle

In Section 3.1 some single-particle properties will be discussed as an introduction to Chapter 4, where multiple scattering is treated extensively. Three kinds of scatterers will be treated, namely point scatterers, spheres, and cylinders. Some very good books on single scattering have been written by Van de Hulst[57] and Bohren and Huffman.[58] The latter contains some very practical computer programs to calculate the scattering properties of spheres (Mie scattering) and cylinders, which formed the basis of my own, more extended, programs.

Strictly speaking the scattering matrix S of the individual particles can only be found when the particle is spherical or cylindrical. For a collection of papers dealing with single-particle scattering of arbitrary shape, see Ref. 59.

3.1 Green's functions in arbitrary dimension

In the one-particle case it is useful to separate the fluctuating part of the dielectric constant from the (empty) medium part as

$$n^2(\vec{r}) = n^2[1 + \mu(\vec{r})] \ , \tag{3.1}$$

in which case the wave equation can be written as

$$\Delta\Psi(\vec{r}) + k_0^2\Psi(\vec{r}) = -\mu(\vec{r})k_0^2\Psi(\vec{r}) \ , \tag{3.2}$$

where k_0 is the magnitude of the wave vector associated with the surrounding empty (that is without scatterers) medium, $k_0 = 2\pi/\lambda = 2\pi n/\lambda_{vac}$. The empty-space Green's function for the amplitude is defined as the solution of

$$\Delta g(\vec{r}_1, \vec{r}_2) + k_0^2 g(\vec{r}_1, \vec{r}_2) = \delta(\vec{r}_1 - \vec{r}_2) \ , \tag{3.3}$$

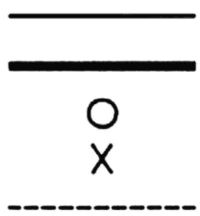

g	empty-space Green's function
G	full Green's function
$-\mu k_0^2$	one-particle Born operator
S	single-particle scattering operator
	connection to identical particle

Figure 3.1: *Drawing convention for elements of diagrams.*

which for dimension $d = 3$, $d = 2$, and $d = 1$ respectively is given by

$$g_3(\vec{r}_1, \vec{r}_2) = -\frac{\exp(ik_0|\vec{r}_1 - \vec{r}_2|)}{4\pi|\vec{r}_1 - \vec{r}_2|} , \tag{3.4}$$

$$g_2(\vec{r}_1, \vec{r}_2) = -\frac{1}{2\pi} K_0(-ik_0|\vec{r}_1 - \vec{r}_2|) , \tag{3.5}$$

$$g_1(r_1, r_2) = \frac{\exp(ik_0|r_1 - r_2|)}{2ik_0} . \tag{3.6}$$

and in k-space

$$g(\vec{k}, \vec{k}\,') = \frac{\delta(\vec{k} - \vec{k}\,')}{k_0^2 - k^2} , \tag{3.7}$$

Defining an incoming wave, $\Psi_{inc}(\vec{r}_1)$, as the solution of the wave equation without the presence of the scatterer, Eq. (3.2) can be transformed into

$$\Psi(\vec{r}_1) = \Psi_{inc}(\vec{r}_1) - \int g(\vec{r}_1, \vec{r}_2)\mu(\vec{r}_2)k_0^2\Psi(\vec{r}_2)d\vec{r}_2 . \tag{3.8}$$

This equation can be solved formally by introducing the scattering operator $S(\vec{r}_1, \vec{r}_2)$:

$$\Psi(\vec{r}_1) = \Psi_{inc}(\vec{r}_1) + \int g(\vec{r}_1, \vec{r}_2)S(\vec{r}_2, \vec{r}_3)\Psi(\vec{r}_3)d\vec{r}_2 d\vec{r}_3 . \tag{3.9}$$

Clearly the first-order solution ($\Psi(\vec{r}_3) = \Psi_{inc}(\vec{r}_3)$) for S is

$$S(\vec{r}_1, \vec{r}_2) = -\mu(\vec{r}_1)k_0^2\delta(\vec{r}_1 - \vec{r}_2) . \tag{3.10}$$

Iteration of Eq. (3.8) results in an explicit sum of scattering events (we will not bother with the convergence of these series here). Each term in the series represents a higher-order scattering contribution (still for one particle). In Fig. 3.2 we have depicted this series for S in diagrams, where the conventions for drawing of diagrams of Fig. 3.1 have been used. To facilitate the treatment of many scatterers the particle has been labeled α. Defining the Fourier transform of $S(\vec{r}_1, \vec{r}_2)$ with respect to wave vectors $\vec{k}_{in}$ and $\vec{k}_{out}$ (incoming and outgoing wave vectors) results in the quantity, $S(\vec{k}_{out}, \vec{k}_{in})$ with $\vec{k}_{in}$ on shell (the far-field limit): $k_{in} = k_0$;

$$S(\vec{k}, \vec{k}\,') = (2\pi)^{-3} \iint S(\vec{r}, \vec{r}\,')e^{-i\vec{k}\cdot\vec{r}}e^{i\vec{k}\,'\cdot\vec{r}\,'}d\vec{r}d\vec{r}\,' , \tag{3.11}$$

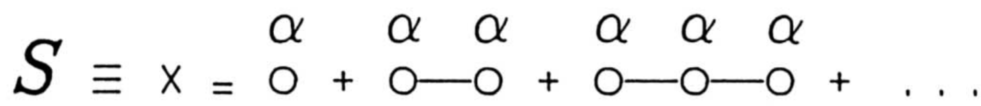

Figure 3.2: *Born series for the scattering operator.*

The complex scattering amplitude of length $f(\vec{k}_{out}, \vec{k}_{in})$ is introduced as

$$f(\vec{k}_{out}, \vec{k}_{in}) = -2\pi^2 S(\vec{k}_{out}, \vec{k}_{in}) \ , \tag{3.12}$$

which by integrating over all scattering angles can be related to the scattering cross section

$$\sigma_{sca,3}(k_{in}) = \int |f(\vec{k}_{out}, \vec{k}_{in})|^2 d\Omega = \int_0^{\pi}\int_0^{2\pi} |f(\vec{k}_{out}, \vec{k}_{in})|^2 \sin\theta d\theta d\phi \ . \tag{3.13}$$

for $d = 3$, while for $d = 2$ the scattering cross section per unit length is given by

$$\sigma_{sca,2}(k_{in}) = \int_0^{2\pi} |f(\vec{k}_{out}, \vec{k}_{in})|^2 d\phi \ . \tag{3.14}$$

The optical theorem connects the total cross section, the so-called extinction cross section, to the imaginary part of the S matrix for forward scattering,[60] which in dimension $d = 3$ and $d = 2$ gives:

$$\sigma_{ext,3}(k_{in}) = \frac{4\pi}{k_0}\mathrm{Im}\{f(\vec{k}_{in}, \vec{k}_{in})\} \ , \tag{3.15}$$

$$\sigma_{ext,2}(k_{in}) = 4\,\mathrm{Im}\{f(\vec{k}_{in}, \vec{k}_{in})\} \ . \tag{3.16}$$

For $d = 1$ the optical theorem may be confusing since an amount of energy of non-zero measure is scattered forward ($\vec{k}_{in} = \vec{k}_{out}$), which makes it impossible to distinct the scattered wave from the unperturbed wave.

3.2 Scattering by a point, sphere, and cylinder

In this section I will give the reader an impression of what the light-scattering properties of small and regularly shaped dielectric particles are.

In the multiple scattering theory of Chapter 4, *isotropic point scatterers* will be used. These however are non-existing for electromagnetic waves. A point scatterer for these waves is what is known as a *Rayleigh scatterer*, and acts as an *induced-dipole radiator*. The radiation pattern is as a consequence of the *vector* nature of light non-isotropic, and the cross section appears to be inversely proportional to the ratio of the wavelength and the size of the particle to the fourth power, and thus goes to zero for a true point.

An important class of scatterers appear to be the dielectric particles which have their size comparable to the wavelength of the scattered wave. Those particles scatter very efficiently but highly anisotropic. A multiple scattering theory with these particles would be enormously difficult, and is from a practical point of view nearly impossible.

However, the single-particle scattering of a plane electromagnetic wave from a dielectric or metallic sphere of arbitrary size is exactly solvable, and is known as Mie theory, first given by G. Mie in 1908. The solution is given in terms of the so-called amplitude functions $S_{\|}(\theta)$ and $S_{\perp}(\theta)$, one for each possible polarization state. The subscripts $\perp$ and $\|$ refer respectively to the light vibrating perpendicularly and parallel to the plane through the directions of propagation of the incident and scattered waves. These amplitude functions are connected to Eq. (3.15) by

$$f(\vec{k}_{out}, \vec{k}_{in}) = \frac{i}{k_0} S(\theta) \; , \tag{3.17}$$

which is very practical to know if we want to compare the multiple-scattering theory from Chapter 4 to an experimental scattering problem.

If we use the conventions of Van de Hulst,[57] the cross sections for scattering, extinction, and backscattering (the latter also known as the radar cross section) are given by

$$\sigma_{sca} = \frac{1}{k_0^2} \int_{4\pi} [|S_{\perp}(\theta)|^2 \sin^2\phi + |S_{\|}(\theta)|^2 \cos^2\phi] d\Omega \; , \tag{3.18}$$

$$\sigma_{ext} = \frac{4\pi}{k_0^2} \mathrm{Re}\{S(\theta = 0)\} \; , \tag{3.19}$$

$$\sigma_{back} = \frac{4\pi}{k_0^2} |S(\theta = \pi)|^2 \; . \tag{3.20}$$

For a plane wave with intensity I_0 scattered from the sphere we find an intensity I for linearly polarized light at distance r (in the far field) from the scatterer:

$$I(r) = \frac{1}{r^2 k_0^2} [|S_{\perp}(\theta)|^2 \sin^2\phi + |S_{\|}(\theta)|^2 \cos^2\phi] I_0 \; , \tag{3.21}$$

Further we can define the absorption cross section σ_{abs}, which is given by $\sigma_{abs} \equiv \sigma_{ext} - \sigma_{sca}$, and the cross section for radiation pressure σ_{pr}, which is given by $\sigma_{pr} = \sigma_{ext} - \langle\cos\theta\rangle\sigma_{sca}$. Here, $\langle\cos\theta\rangle$ is the average cosine of the angle at which the light is scattered. Note that for an isotropic scatterer $\sigma_{pr} = \sigma_{ext}$.

The absorption of a particle can conveniently be characterized by means of the albedo a, which is defined as $a \equiv \sigma_{sca}/\sigma_{ext}$ and is a measure for the non-absorbed fraction of the light that has interacted with it. With the geometric cross section $\sigma_{geo} \equiv \pi r_{sph}^2$, where r_{sph} is the radius of the sphere, we can define the efficiency factors Q_{ext}, etc., by $Q_{ext} \equiv \sigma_{ext}/\sigma_{geo}$. To give the reader some feeling of the scattering efficiency for different

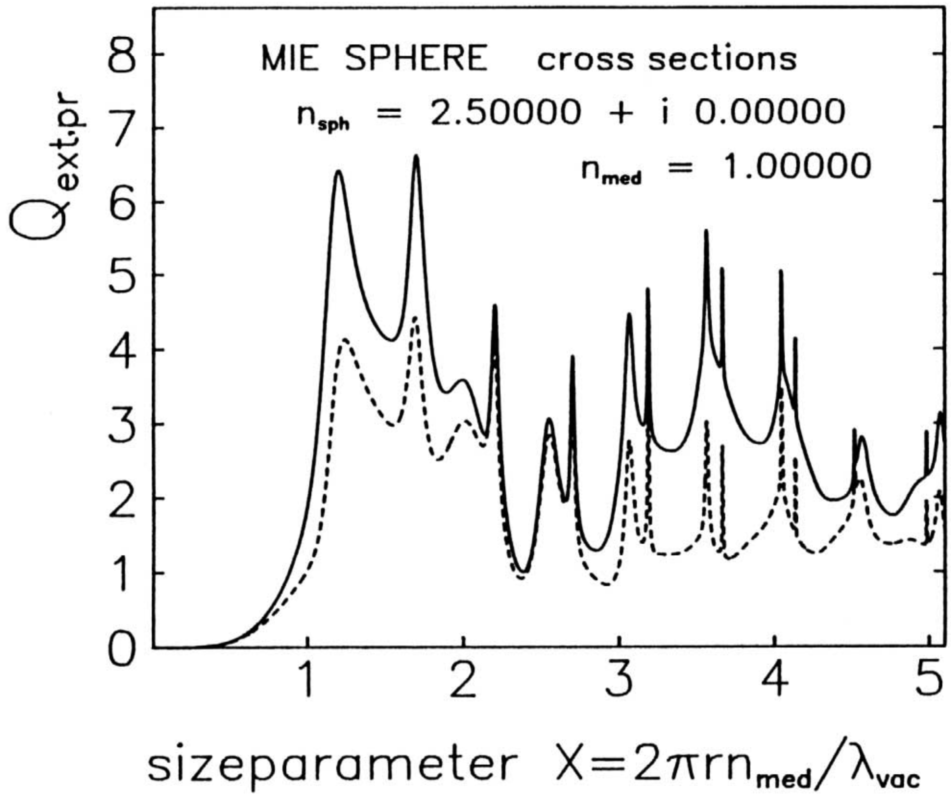

Figure 3.3: *Efficiency factor for extinction, Q_{ext} (solid line), and radiation pressure, Q_{pr} (dashed line), as a function of the size parameter $x = 2\pi r_{sph} n_{med}/\lambda_{vac}$ for a sphere having a refractive index ratio of $m = n_{sph}/n_{med} = 2.5$ and albedo $a = 1$ (non-absorbing dielectric particle). Notice the sharp resonances.*

sizes of spheres, a typical dependence of the efficiency factor Q_{ext} on the size parameter $x = 2\pi r_{sph} n_{med}/\lambda_{vac}$ of the scatterer is shown in Fig. 3.3. The refractive index of the sphere is indicated by n_{sph}, and n_{med} is the refractive index of the surrounding medium. The theory allows n_{sph} to be complex, thus making the description of metallic spheres possible as well.

We can define in exactly the same way also cross sections for *cylinders*, using the amplitude functions $T_\perp(\theta)$ and $T_\parallel(\theta)$. The subscripts $\perp$ and $\parallel$ refer respectively to the light vibrating perpendicularly and parallel to the long axis of the rod. As we will see in Chapter 6, cylinders are of special interest since a bunch of parallel rods, illuminated perpendicularly to their long axis, can act as a multiple scattering medium with an effective dimension $d = 2$. The given cross sections should be interpreted as *cross sections per unit length*, and note that they are, unlike with the spheres, dependent on the polarization of

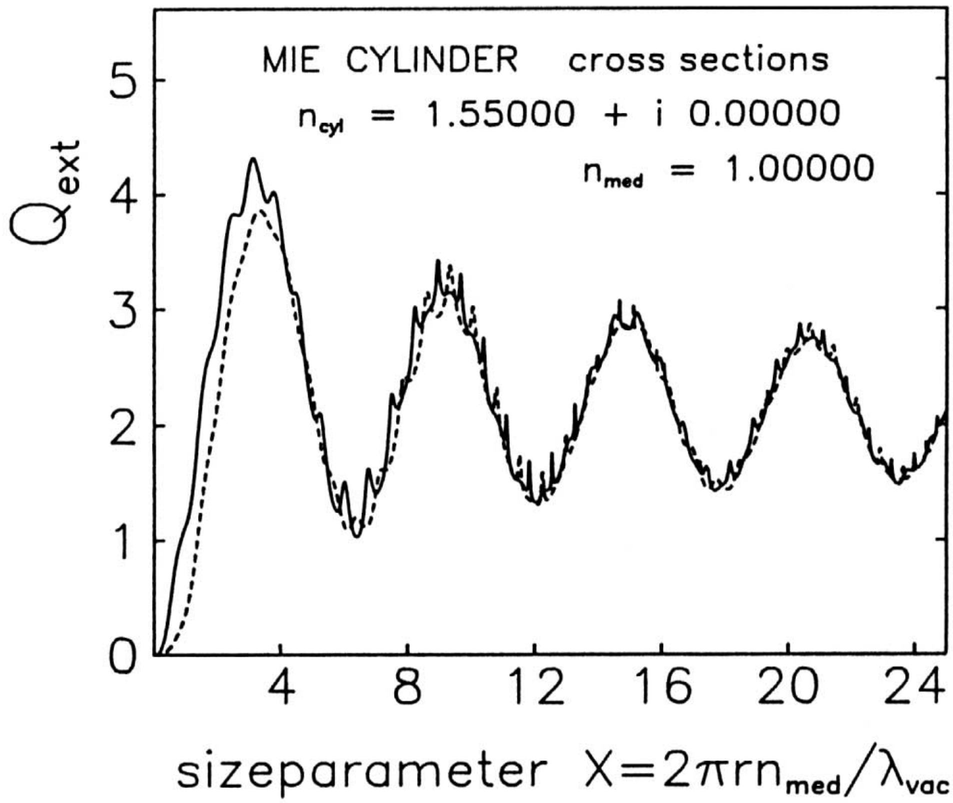

Figure 3.4: *Efficiency factor for extinction Q_{ext} for both the parallel (solid line) and perpendicular (dashed line) polarization as a function of the size parameter $x = 2\pi r_{cyl} n_{med}/\lambda_{vac}$ for a cylinder having a refractive index ratio of $m = n_{cyl}/n_{med} = 1.55$ and albedo $a = 1$.*

the incident wave:

$$\sigma_{sca;\|,\perp} = \frac{2}{\pi k_0} \int_0^{2\pi} |T_{\|,\perp}(\theta)|^2 d\theta \ , \tag{3.22}$$

$$\sigma_{ext;\|,\perp} = \frac{4}{k_0} \mathrm{Re}\{T_{\|,\perp}(\theta = 0)\} \ , \tag{3.23}$$

$$\sigma_{back;\|,\perp} = \frac{8}{\pi k_0} |T_{\|,\perp}(\theta = \pi)|^2 \ , \tag{3.24}$$

and with Eq. (3.16) we have

$$f(\vec{k}_{out}, \vec{k}_{in}) = \frac{i}{k_0} T(\theta) \ , \tag{3.25}$$

For a plane wave with intensity I_0 scattered from the cylinder we find an intensity I for linearly polarized light at distance r (in the far field) from the scatterer:

$$I_{\|,\perp}(r) = \frac{2}{\pi r k_0} |T_{\|,\perp}(\theta)|^2 I_0 \ , \tag{3.26}$$

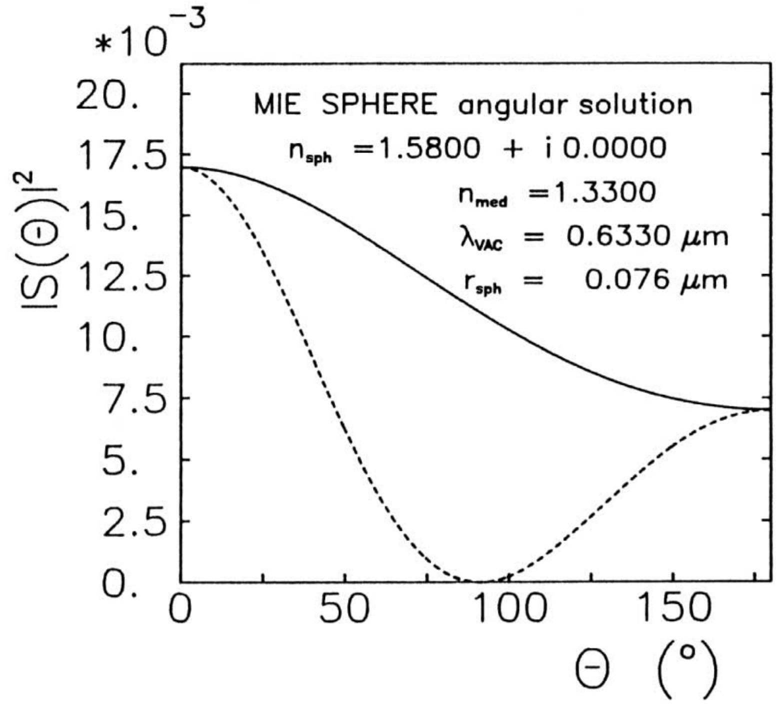

Figure 3.5: *152 nm polystyrene sphere in water:* $n_{sph} = 1.58$, $n_{med} = 1.33$, $\lambda_{vac} = 633\,nm$ *and* $x = 1.00$. *The scattering is more or less isotropic for* $|S_{\|}(\theta)|^2$ *(solid line). Due to the pronounced minimum in* $|S_{\perp}(\theta)|^2$ *(dashed line) the scattered light at these angles is strongly polarized (Rayleigh limit).*

The geometric cross section per unit length is defined as $\sigma_{geo} = 2r_{cyl}$, where r_{cyl} is the radius of the cylinder. In Fig. 3.4 we see the extinction efficiency of a cylinder as a function of the size parameter for both possible polarization states.

The cross section for radiation pressure, σ_{pr}, is defined in the same way as it was for spheres. Unfortunately Q_{pr} for cylinders is not given in terms of a series in neither Ref. 57 or Ref. 58. In the Appendix to this chapter I will therefore derive it myself.

The angular distribution of the radiated intensity from a scatterer is strongly dependent on the actual size and refractive index of the particle, respectively compared to the incident wavelength and refractive index of the surrounding medium. For dielectric particles, roughly three different types can be distinguished: (i) Those that are very small, which are the Rayleigh scatterers (see Fig. 3.5), they have a "donut-shaped" radiation pattern; (ii) Those that are very large compared to the wavelength, their scattering pattern is strongly peaked in forward direction and almost independent of polarization (see Fig. 3.6) (for enormously big particles, which are in the limit of geometrical optics, a calculation of the scattering of the particle in terms of a partial waves expansion may become impossible); (iii) A small collection of "in between" particles, with a size parameter close to about

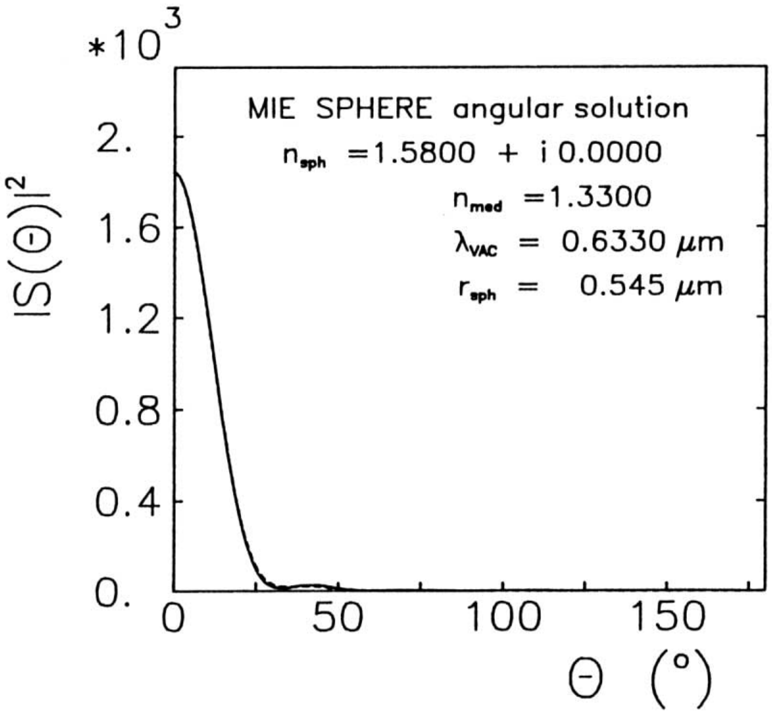

Figure 3.6: 1.091 μm *polystyrene sphere in water:* $n_{sph} = 1.58$, $n_{med} = 1.33$, $\lambda_{vac} = 633$ *nm and* $x = 7.20$. *The scattering is strongly peaked in forward direction and unpolarized* ($|S_{\parallel}(\theta)|^2$ *(solid line) is almost equal to* $|S_{\perp}(\theta)|^2$*) (dashed line).*

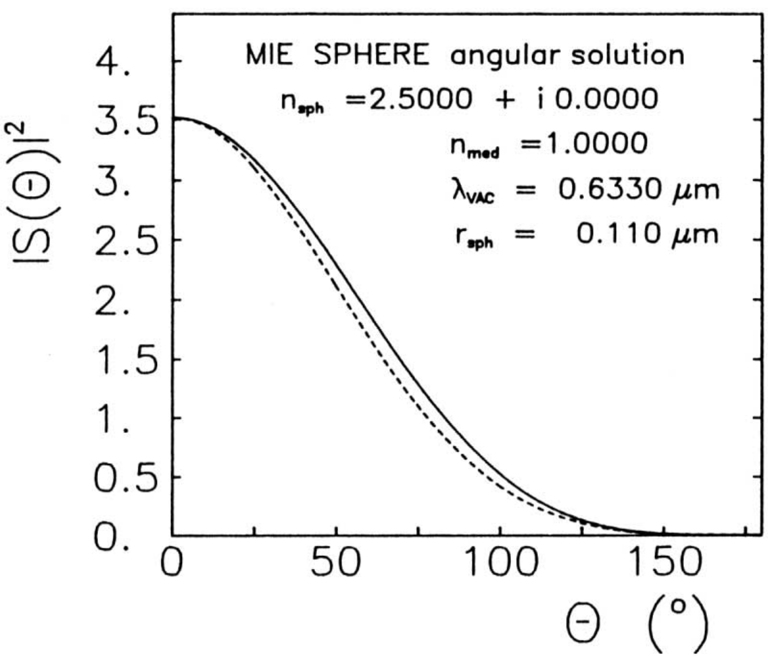

Figure 3.7: 220 *nm anatase sphere* (TiO_2) *in air:* $n_{sph} \simeq 2.50$, $n_{med} = 1.00$, $\lambda_{vac} = 633$ *nm and* $x = 1.09$. *The scattering is mostly in the forward half space, and almost unpolarized (solid line:* $|S_{\parallel}(\theta)|^2$, *dashed line:* $|S_{\perp}(\theta)|^2$*).*

1.0 or 2.0 dependent on the refractive index contrast between sphere and medium, which scatter essentially only in the forward half space (see Fig. 3.7). All chosen values in these figures are realistic. In Sect. 5.2.2 some important implications of the vector character of light in multiple scattering will be discussed. It will appear, that these implications are strongly dependent on the size of the scatterers involved. For conducting particles a similar categorization can be made, however, I will not go into detail because they are no part of this work.

3.2.1 A measurement on a single scatterer

One might ask how well the Mie theory applies on scatterers in practical circumstances, and do some measurement. In this way one will also get an impression of the performance of the measuring devices involved. In order to test the experimental set-up for the measurement of the backscattering of light from a random medium, which will be described in more detail in Chapter 6, I positioned a fused silica fiber perpendicular to the approximately 2 cm wide laserbeam, wich can be regarded as the incoming plane wave. The fiber (type NRC FSV-10 single mode) was stripped from its jacket and had a diameter of approximately 125 μm. The refractive index was unknown but was expected to be close to but a somewhat higher than 1.457, where the slightly higher refractive index of the 4 μm core should play a negligible part. If the fiber's shape would not be cylindrical, but for instance elliptical, the theory would not apply, and rotation of the fiber along its axis would show a change in the scattering pattern.

The backscattered intensity pattern for both polarizations was recorded as a function of angle, and is shown as a solid line in Fig. 3.8, The dotted line represents the same measurement, but is plotted in opposite direction. Because the scattering pattern from a cylindrical scatterer should be symmetrical, an impression of the experimental error is given by comparing these curves.

A theoretical pattern was fitted to the measurement by changing both diameter and refractive index and is shown in Fig. 3.9. It appears that *no other combination* of diameter and refractive index will give a good fit, and that the actual values can be determined to more than five (and potentially six or more) significant figures! In the present set-up, systematic errors may occur due to changes in the refractive indices of the silica and air with temperature and moisture.

We can conclude that apparently this glass fiber is very cylindrical, and one can find from one, non-destructive experiment both its refractive index and diameter. More important is, that with the combination of Mie theory, a single fiber and a simple power meter, a very complicated set-up can be calibrated *absolutely* in both angular linearity and recorded intensity!

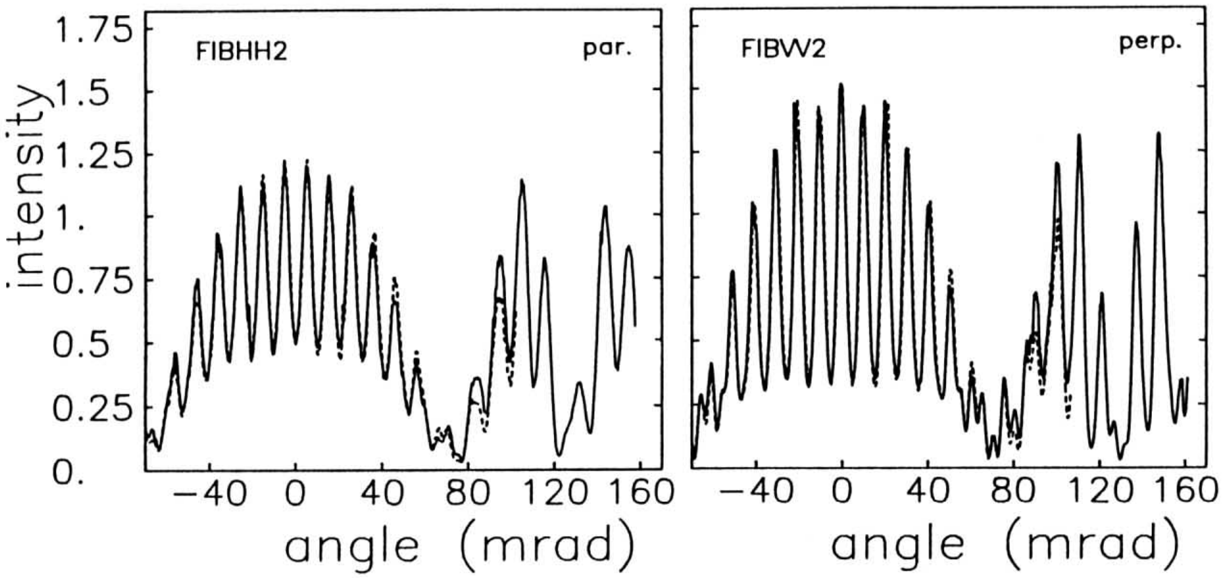

Figure 3.8: *Backscattered intensity for a (round) fused silica fiber with a diameter of 125 μm at a wavelength of 633 nm. The light was linearly polarized, respectively parallel (par.) and perpendicularly (perp.) to the fiber's axis.*

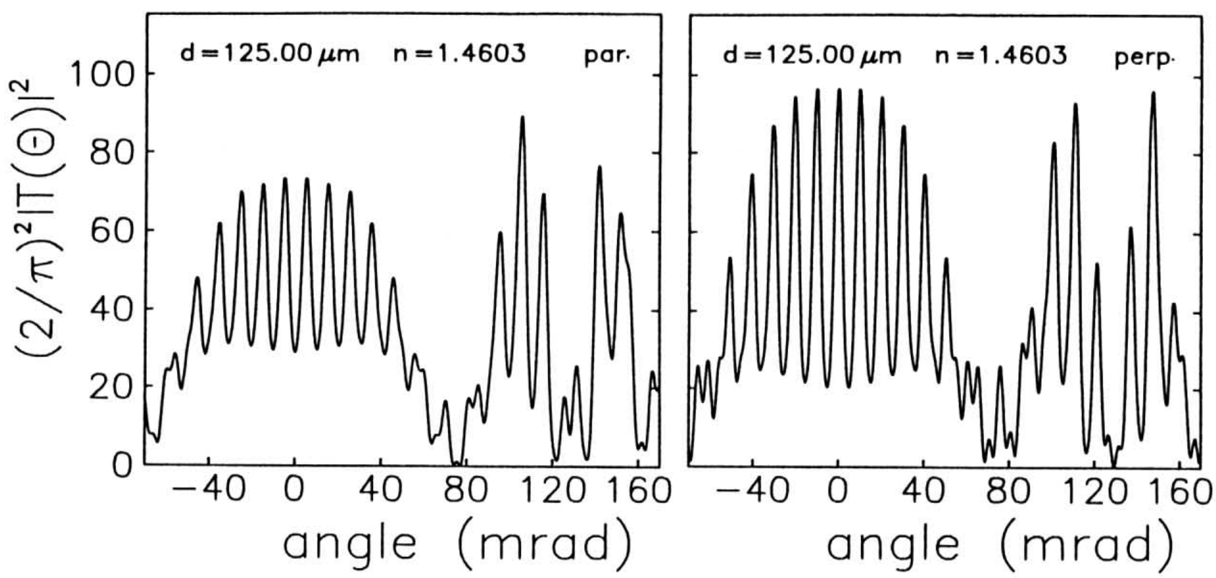

Figure 3.9: *Theoretical backscattered intensity of a cylinder with a diameter of 125.00 μm, and a refractive index of $n_{cyl} = 1.4603$ at a vacuum wavelength of $\lambda_{vac} = 632.995$ nm. The refractive index of air was chosen to be $n_{med} = 1.00029$. Both of the linear polarizations $|T_{\perp}(\theta)|^2$ (perp.) and $|T_{\parallel}(\theta)|^2$ (par.) are shown.*

3.3 Appendix

3.3.1 Cross section of a cylinder

Here I will give formula for calculating the cross sections of a cylinder at normal incidence. To actually calculate the amplitude functions $T_{\|}(\theta)$ and $T_{\perp}(\theta)$, it is convenient to have an expression in terms of a summable series, rather than to solve an integral numerically. But what is more important, particularly for calculating Q_{sca} and Q_{pr} is, that in these series the angular part is integrable analytically, which will save a lot of numerical work.

First, take a look at Q_{sca}, which can be represented in the forms:

$$Q_{sca} = \frac{1}{\pi x}\int_0^{2\pi} |T(\theta)|^2 d\theta = \frac{2}{x}\left[|c_0|^2 + \sum_{n=1}^{\infty} |c_n|^2\right] \ , \tag{3.27}$$

where the coefficient c_n can be calculated, and moreover, is important in calculating all other properties as well. In the book of Van de Hulst,[57] the coefficient c_n is called a_n or b_n for the calculation of $T_{\|}$ and $T_{\perp}$ respectively, with

$$T(\theta) = c_0 + 2\sum_{n=1}^{\infty} c_n \cos(n\theta) \ . \tag{3.28}$$

To calculate Q_{pr}, we first have to find $\langle\cos\theta\rangle$. As folows directly from its definition, that it is the average cosine of the angle at which the light (intensity) is scattered, we can write:

$$\begin{aligned}
\langle\cos\theta\rangle Q_{sca} &= \frac{1}{\pi x}\int_0^{2\pi} |T(\theta)|^2 \cos\theta d\theta = \frac{1}{\pi x}\int_0^{2\pi} c_0 c_0^* \cos\theta d\theta \\
&+ \frac{1}{\pi x}\int_0^{2\pi} \sum_{n=1}^{\infty} (c_0 c_n^* - c_n c_0^*)\{\cos[(n+1)\theta] + \cos[(n-1)\theta]\} d\theta \\
&+ \frac{2}{\pi x}\int_0^{2\pi} \sum_{k=1}^{\infty}\sum_{n=1}^{k} c_n c_{k-n}^* \{\cos(k\theta) + \cos[(2n-k)\theta]\}\cos\theta d\theta \\
&= \frac{4}{x}\sum_{n=0}^{\infty} \mathrm{Re}\{c_n c_{n+1}^*\} \ .
\end{aligned} \tag{3.29}$$

Now we can employ

$$Q_{pr} = Q_{ext} - \langle\cos\theta\rangle Q_{sca} \ , \tag{3.30}$$

with

$$Q_{ext} = \frac{2}{x}\mathrm{Re}\{c_0\} + \frac{4}{x}\sum_{n=1}^{\infty} \mathrm{Re}\{c_n\} \ . \tag{3.31}$$

From this point the remaining problem is to find the coefficients c_n, which involves spherical Bessel functions with complex argument. A very good algorithm to calculate these is used in the programs of Ref. 58.

Chapter 4

Multiple-scattering theory for a slab

In this chapter a rigorous scalar wave theory will be discussed as a model to represent the coherent backscattering (weak localization), but also the transmission of light for finite slabs. In addition a general theory based on a diffusion approximation will be discussed, and the resulting angular-dependent enhanced-backscattering intensity will be presented in closed form for finite slabs and for general albedo. Transmission and reflection experiments for strongly scattering media are presented in Chapter 5 and 6, where a comparison to the theory will be made. We published most of these results in Ref. 61.

A time-dependent version of the diffusion theory will be presented in Sect. 4.4, as time-resolved measurements of the propagation of ultra-short pulses through disordered media are an important tool to determine the diffusion constant. As I have pointed out, the dimensionality of the observed system is extremely important. Therefore, a two-dimensional theory is presented in the Sect. 4.5. In the last section some non-self-avoiding scattering processes will be introduced. These processes are the same as those responsible for the weak localization of electrons, and will surely be the most important in strong localization of light.

After Van Albada and Lagendijk had discovered weak localization of light,[36] a descriptive theory containing all important features of the experiment became indispensable. We soon realized that much insight in the field of multiple light scattering had already been gathered, but that most results had been communicated in either astrophysical literature or in more technical journals, and did not involve interference. An exception was the work of Kuga and Ishimaru,[35] which we were drawn attention to by Prof. J.P. Woerdman.

Characteristics of multiple light scattering like attenuation, depolarization, anisotropy, etc., are of essential importance in understanding the radiation field in an atmosphere.[62] Even effects as enhanced backscattering have been known in the astrophysical community ("Gegenschein or opposition effect"),[39,40] although different explanations, not involving interference, have been put forward. Excellent books on (multiple) light scattering have been published.[63–65]

From the theoretical side a theory is needed which describes the occurrence of weak localization of light in a finite slab. Two basic simplifications are usually made: (i) supposition of isotropic scalar scattering and (ii) assumption that the scattering can be described with a diffusion equation. We relaxed one of these approximations by not resorting to the diffusion approximation. The theory we developed is essentially a rigorous simplification of the mathematics in the work of Tsang and Ishimaru.[66] Through this simplification we can handle slab widths up to thirty-two mean free paths with albedo equal to one without numerical problems. Our theory is an isotropic-scalar-scattering theory, which means that it can be used only for the experimental results in which incident and detected polarization are parallel. Stephen and Cwillich have treated the phenomenon of weak localization of *vector* waves in the Rayleigh limit (which is not very important for strong localization, because Rayleigh particles inherently scatter only weakly), where they relied on the diffusion approximation.[67] Akkermans et al. have introduced a diffusion approximation for a semi-infinite slab and conservative scattering (albedo equal to 1).[69] We will present an extension of the diffusion approach here to include finite slabs and non-conservative scattering in closed form. This theory will be compared with the rigorous theory. This is important in view of the fact that the observation of the break-down of diffusion theory for thick slabs (Anderson localization) will very likely involve the study of finite size effects of the sample.

4.1 Mapping of scalar and vector waves

In this chapter a scalar theory is developed to describe the multiple scattering of a wave from a homogeneous slab containing *isotropic* point scatterers. This yields an important but quite necessary simplification if we are interested in the scattering of electro-magnetic waves from a slab containing (realistic) anisotropic scatterers.

The dielectric media that scatter light most strongly are those containing scatterers whose size is comparable to the wavelength. In these conditions, scattering is highly anisotropic, and forward scattering predominates. As a result, it takes several scattering events to attain a complete loss of memory of original direction. The crucial parameter here no longer is the scattering mean free path λ_{sc} (wich is related to the scattering cross section by $\lambda_{sc} = (n_0\sigma_{sc})^{-1}$, where n_0 is the number density of scatterers), but the transport mean free path λ_{tr} which may be thought of as the distance to be traveled to attain this loss of memory. They are related by $\lambda_{tr} = \lambda_{sc}/(1-\langle\cos\theta\rangle)$, where $\langle\cos\theta\rangle$ is the average cosine of the angle of scattering. In fact, the transport mean free path is directly related to the cross section for radiation pressure of the scatterers: $\lambda_{tr} = (n_0\sigma_{pr})^{-1}$. So the attenuation of a coherent beam is associated to the scattering mean free path, while the average step size in a diffusion process is described by the transport mean free path.

Another crucial property of *real* scatterers is that, how small ever, they will always absorb a little part of the scattered wave. In the study of Anderson localization, understanding the effect of absorption in multiple scattering is of, sometimes underestimated, importance. Consider a multiple scattering event s_1, s_2, ..., s_n of a wave over n absorbing particles. The absorption of a single particle is given in terms of the albedo a, which is the ratio of the cross sections for scattering σ_{sc} and extinction σ_{ext} respectively. In fact, σ_{ext} is the total cross section, and is given by $\sigma_{ext} = \sigma_{sc} + \sigma_{abs}$, whith σ_{abs} the absorption cross section. So in n scattering events the unabsorbed fraction of the wave will be a^n, and the average length of the trajectory will be $n\lambda_{sc}$. Let n_{in} be the required number of scattering events to obtain a decay in intensity to $1/e$ of the original value, then we have $e^{-1} = a^{n_{in}}$ and $\lambda_{in} = n_{in}\lambda_{sc}$, with λ_{in} the (mean) inelastic length. For albedo a close to 1, $a \simeq 1$, $a^{n_{in}} = a^{1/(1-a)} \simeq e^{-1}$, which gives $n_{in} = 1/(1-a)$ and so, since typical $a = 0.99999$, we find to very good approximation $\lambda_{in} \simeq \lambda_{sc}/(1-a)$. Note that this also holds for *anisotropic* scatterers.

If we now want to know what the average distance is between two points in which the light has decayed to $1/e$ only as a result of absorption, we find the absorbtion length for a d-dimensional random walk: $\lambda_{abs} = \sqrt{\lambda_{mf}\lambda_{in}/d}$, with $\lambda_{mf} \equiv \lambda_{tr}$. So for a 3-dimensional system we find:

$$\lambda_{abs} = \frac{\lambda_{tr}}{\sqrt{3(1-a)\lambda_{tr}/\lambda_{sc}}} \; . \tag{4.1}$$

The implications of this all for the mapping of a vector experiment on a scalar theory are, that the mean free path λ_{mf} has to be interpreted as λ_{sc} only when single scattering is concerned and as λ_{tr} when ever multiple scattering is involved. The absorbtion, which is in the scalar theory by means of the albedo a, has to be corrected by:

$$a' = 1 + \frac{\lambda_{tr}}{\lambda_{sc}}(a-1) \; . \tag{4.2}$$

4.2 Rigorous scalar theory for d=3

Systematic perturbation theory in terms of diagrammatic expansions is a fruitful way of describing wave propagation in random media. A very useful review has been published by Frisch.[60] One immediately distinguishes two cases as far as the character of the inhomogeneities is concerned. In continuous media it is not possible to pick out separate scattering particles whereas in media consisting of discrete scatterers individual scattering centers can be distinguished. The first case is more difficult as one needs all higher (static) spatial correlation functions to characterize the medium. In the continuous medium one usually relies on some simplifying assumption as (Gaussian) decoupling of higher-order

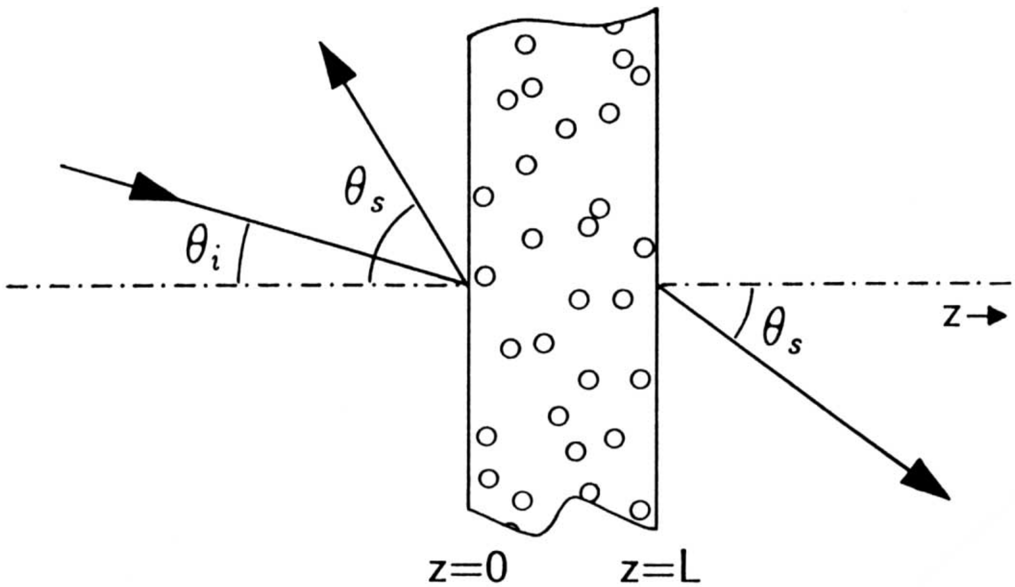

Figure 4.1: *Backscattering and transmission of waves by a slab.*

processes. Here we will assume a statistically homogeneous medium containing point scatterers, so in our theory no particle-particle correlations are involved, and there is no excluded volume as would be the case for a slab containing (real) discrete scatterers.

The system we will study is a collection of identical random scatterers in a slab, see Fig. 4.1. The direction perpendicular to the slab is the z direction and the slab is confined within $[z = 0, z = L]$, so L is the thickness of the slab. A plane wave is coming into the medium from the $-z$ side at angle θ_i. The scattered wave, either in transmission or reflection, is detected in the far field at an angle θ_s. We will assume the scatterers to scatter isotropically.

4.2.1 Amplitude Green's functions

To discuss the many-particle problem we have to modify Eq. (3.1) into

$$n^2(\vec{r}) = n^2[1 + \sum_\alpha \mu(\vec{r} - \vec{r}_\alpha)] \ , \tag{4.3}$$

where the summation is over the scattering centers. The full Green's function for the amplitude is defined as the solution of

$$\Delta G(\vec{r}_1, \vec{r}_2) + k_0^2 \frac{n^2(\vec{r}_1)}{n^2} G(\vec{r}_1, \vec{r}_2) = \delta(\vec{r}_1 - \vec{r}_2) \ . \tag{4.4}$$

In many cases of Green's-function theory of random media statistical homogeneity is obtained by averaging over all the possible positions of the particles with, if necessary, taking into account particle-particle correlations. This gives rise to averaged Green's functions, which are defined by

$$\langle G(\vec{k}_1, \vec{k}_2) \rangle \equiv G(k_1)\delta(\vec{k}_1 - \vec{k}_2) \ , \tag{4.5}$$

or in real space

$$\langle G(\vec{r}_1, \vec{r}_2) \rangle \equiv G(\vec{r}_1 - \vec{r}_2) \ . \tag{4.6}$$

As averaged amplitude Green's functions depend only on one wave vector (or on one space coordinate) no confusion should arise with non-averaged Green's functions. The difference between an empty-space Green's function and an averaged Green's function is that the former relates to the homogeneous medium without the presence of scattering units whereas in the latter a situation is described in which a configurational average has been performed with respect to the positions of all scattering particles.

A useful equation can be obtained from Eq. (4.4) by introduction of the mass operator $\Sigma(\vec{r})$, defined by

$$G(\vec{r}_1) = g(\vec{r}_1) + \int g(\vec{r}_1 - \vec{r}_2)\Sigma(\vec{r}_2 - \vec{r}_3)G(\vec{r}_3)d\vec{r}_2 d\vec{r}_3 \ . \tag{4.7}$$

In order to allow for some formal manipulations and to get a more concise notation Eq. (4.7) can be put in matrix notation,

$$G = g + g\Sigma G \ , \tag{4.8}$$

which can be formally solved as

$$G = [g^{-1} - \Sigma]^{-1} \ . \tag{4.9}$$

In wave-vector space this inversion can be carried out immediately as

$$G(k) = g(k) + g(k)\Sigma(k)G(k) \ , \tag{4.10}$$

which results in

$$G(k) = [g(k)^{-1} - \Sigma(k)]^{-1} = [k_0^2 - k^2 - \Sigma(k)]^{-1} \ . \tag{4.11}$$

From Eq. (4.11) it is clear that the average Green's function deviates from the empty-space Green's function by an effective wave vector $\vec{K} \equiv \vec{K}' + i\vec{K}''$, the magnitude of which is given by $K^2 = k_0^2 - \Sigma(k)$. The real part of K (K') describes a renormalized index of refraction and the imaginary part of K (K'') is connected with the (scattering) mean free path (inverse of the turbidity).

In Fig. 4.2 a diagrammatic expansion is given for the mass operator in case of absence of particle correlations. Successive scattering events cannot relate to the same particle,

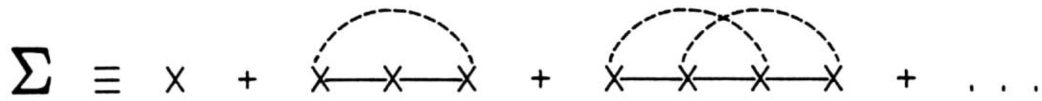

Figure 4.2: *Lowest-order contributions to the self energy.*

since they are already contained in the scattering operator $S(\vec{k}_1, \vec{k}_2)$. In the low-density approximation one finds (retaining only the first term of the expansion presented in Fig. 4.2)

$$\Sigma(k) = (2\pi)^3 n_0 S(\vec{k}, \vec{k}) \ , \quad k = k_0 \ , \tag{4.12}$$

in which n_0 is the density of scatterers. There are two reasons why this approximation will severely break down at high densities: (i) correlations of the scattering events (dependent scattering), and (ii) correlations of the scattering particles. The second effect is well-known and corrections can be found for it (for instance by using approaches originating from gas-kinetic theory like the Percus-Yevick approach).[70,71] The complication of dependent scattering is very important with respect to the localization issue. Some attention has been paid to scattering effects of correlated particles.[70–72]

4.2.2 Intensity Green's functions

We now have to deal with Green's functions related to the intensity rather than to the amplitude. These functions are defined as the following tensor product

$$H \equiv G \times G^* \ , \tag{4.13}$$

i.e. the tensor product of the amplitude Green's function and its complex conjugate, in components:

$$H(\vec{r}_1, \vec{r}_2; \vec{r}_3, \vec{r}_4) \equiv G(\vec{r}_1, \vec{r}_2) G^*(\vec{r}_3, \vec{r}_4) \ . \tag{4.14}$$

Diagrammatic perturbation theory can easily be set up for this intensity Green's function as well.[60] We just double the diagrams and connect identical scattering centers by dashed lines (See Fig. 3.1). We will define the complete (reducible) vertex R as equal to the sum of all connected intensity diagrams H without the incoming and outgoing Green's function. The following matrix equation for $\langle H \rangle$ holds

$$\langle H \rangle = \langle G \rangle \times \langle G^* \rangle + (\langle G \rangle \times \langle G^* \rangle) \langle R \rangle (\langle G \rangle \times \langle G^* \rangle) \ . \tag{4.15}$$

with, for example, for the ensemble average $\langle R \rangle$ of R

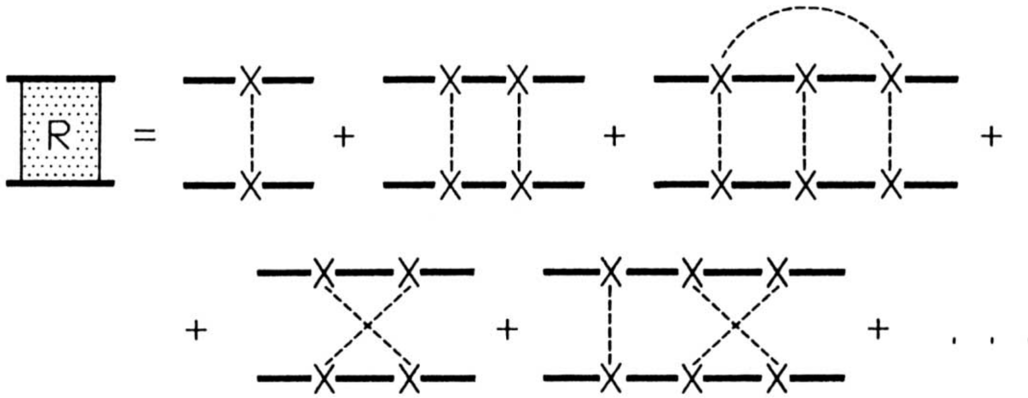

Figure 4.3: *Some lower-order contributions to the total vertex R.*

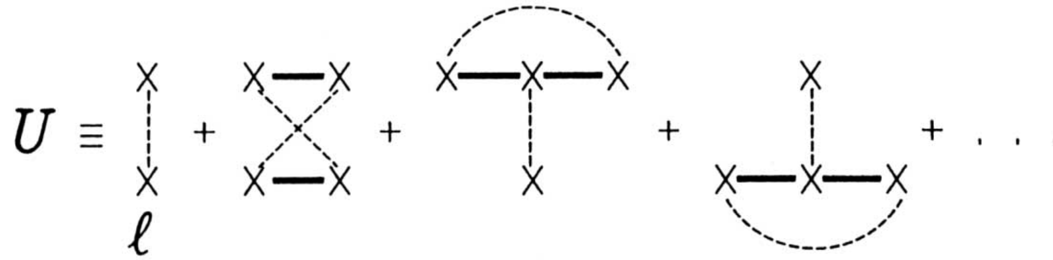

Figure 4.4: *Lowest-order contributions to the irreducible vertex U.*

$$\langle R \rangle \equiv V^{-N} \prod_{\alpha}^{N} \int R \, d\vec{r}_{\alpha} \ , \tag{4.16}$$

with N the number of scatterers in the volume V. In Fig. 4.3 we have depicted some lower-order contributions to $\langle R \rangle$. The equivalent of the mass operator for this type of (intensity) Green's function is the irreducible vertex $\langle U \rangle$ defined for the averaged functions by

$$\langle H \rangle = \langle G \rangle \times \langle G^{*} \rangle + (\langle G \rangle \times \langle G^{*} \rangle)\langle U \rangle \langle H \rangle \ , \tag{4.17}$$

and $\langle U \rangle$ is generated by all double-connected diagrams. The relation between $\langle R \rangle$ and $\langle U \rangle$ is given by

$$\langle R \rangle = \langle U \rangle + (\langle G \rangle \times \langle G^{*} \rangle)\langle U \rangle \langle R \rangle \ . \tag{4.18}$$

In Fig. 4.4 some lower-order contributions to $\langle U \rangle$ are displayed. The incoherent contribution to these diagrams is given by retaining for $\langle U \rangle$ only the lowest-order term $\langle \ell \rangle$ (See Fig. 4.4), which results in the summation of all ladder diagrams. This sum of all ladder diagrams (without ingoing and outgoing lines) will be called $\langle L \rangle$ (See Fig. 4.5). It turns out that the most important interference contribution arises from time-reversed paths (most-crossed diagrams). The sum of all most-crossed diagrams (without ingoing and outgoing lines) will be called $\langle C \rangle$ (See Fig. 4.6). For strong localization theory these most crossed diagrams have to be summed in the irreducible vertex $\langle U \rangle$, $\langle U \rangle = \langle \ell \rangle + \langle C \rangle$ (See Fig. 4.4).[4]

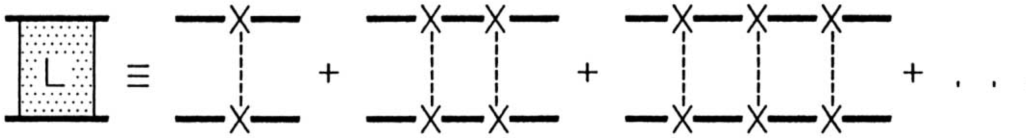

Figure 4.5: *Summation of ladder terms.*

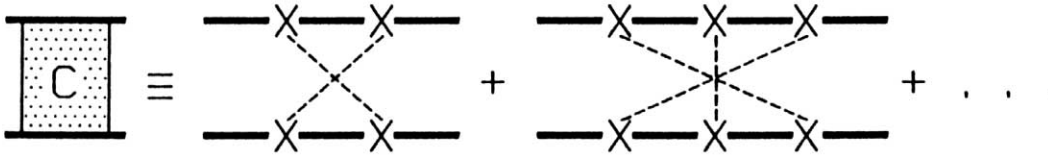

Figure 4.6: *Summation of most-crossed diagrams.*

However, in the weak regime, which is under study here, the most crossed diagrams can be summed in the Green's function itself, $\langle R\rangle = \langle L\rangle + \langle C\rangle$.[73,74] Localization as found in the diagrammatic theory comes about by finding a self-consistent equation which yields a vanishing of the diffusion coefficient in the strongly scattering regime.[4,9,75–77] Basically all these theories are based on ideas developed by Götze to describe localization of electrons.[3] Since in these theories one is only interested in transport coefficients statistical homogeneity can be assumed. This amounts to a considerable simplification as use can be made of (statistical) translational symmetry. Let us first discuss the incoherent contribution to the intensity Green's functions. To that end we have to sum the ladder contribution. The integral equation for $\langle L\rangle$ is

$$\langle L\rangle = \langle \ell\rangle + \langle \ell\rangle(\langle G\rangle \times \langle G^*\rangle)\langle L\rangle \ . \tag{4.19}$$

Next we introduce the assumption of isotropic point scatterers. That is to say

$$S_\alpha(\vec{r}_1,\vec{r}_2) = -4\pi f \delta(\vec{r}_1-\vec{r}_\alpha)\delta(\vec{r}_2-\vec{r}_\alpha) \ , \tag{4.20}$$

where α is a particle index. If we substitute assumption (4.20) into the series expansion for $\langle L\rangle$ (See Fig. 4.5) we see that in each term the incoming space coordinates as well as the outgoing space coordinates have to be equal. So we will try the Ansatz of Tsang and Ishimaru[66]

$$\begin{aligned}\langle L(\vec{r}_1,\vec{r}_2;\vec{r}_3,\vec{r}_4)\rangle &= n_0(4\pi)^2|f|^2\delta(\vec{r}_1-\vec{r}_2)\delta(\vec{r}_1-\vec{r}_3)\delta(\vec{r}_1-\vec{r}_4) \\ &+ F(\vec{r}_1,\vec{r}_2)\delta(\vec{r}_1-\vec{r}_3)\delta(\vec{r}_2-\vec{r}_4) \ ,\end{aligned} \tag{4.21}$$

where the first-order term has explicitly been separated out. Insertion of this Ansatz in into Eq. (4.19) yields an integral equation for $F \equiv F(\vec{r}_1,\vec{r}_2)$ which in matrix form is given by

$$F = n_0^2(4\pi|f|)^4\langle G\rangle\langle G^*\rangle + n_0(4\pi|f|)^2\langle G\rangle\langle G^*\rangle F \ . \tag{4.22}$$

This equation allows for an interpretation of F. Apparently F is the Green's function for the incoherent intensity or incoherent energy density. $F(\vec{r}_1, \vec{r}_2)$ describes the energy density at $\vec{r}_1$ due to a point source at $\vec{r}_2$. If a different source is used (like a damped plane wave) the incoherent energy density can be obtained by integrating the Green's function F over this new source.

In the same way as we did for the ladder diagrams one can solve the summation of most crossed diagrams.[73] The best way is to disentangle the crossed diagrams. To this end we have put arrows on the diagrams for $\langle C \rangle$ to indicate the sense. Let us now look at a typical diagram and rotate the lower part 180°. It now looks very much like a ladder diagram. So if we would include the (non-degenerate) first-order scattering, the summation of crossed diagrams is exactly equal to the ladder sum (for point scatterers) if we permute the appropriate coordinates. So the sum of all most-crossed diagrams is also determined by F:

$$\langle C(\vec{r}_1, \vec{r}_2; \vec{r}_3, \vec{r}_4) \rangle = F(\vec{r}_1, \vec{r}_2) \delta(\vec{r}_1 - \vec{r}_4) \delta(\vec{r}_2 - \vec{r}_3) \ . \tag{4.23}$$

Apparently this tremendous simplification was missed in Ref. 66 (see also Ref. 78). A major part of our task has been fulfilled now. We have found an integral equation, the solution of which can be used to obtain the incoherent and time-reversed interference contributions, described by the ladder- and most-crossed diagrams, for the intensity.

Now we can solve the F propagator from Eq. (4.22), which in components is given by

$$F(\vec{r}_1, \vec{r}_2) = n_0^2 (4\pi)^2 |f|^4 A(\vec{r}_1 - \vec{r}_2) + n_0 |f|^2 \int A(\vec{r}_1 - \vec{r}\,') F(\vec{r}\,', \vec{r}_2) d\vec{r}\,' \ , \tag{4.24}$$

with

$$A(\vec{r}_1, \vec{r}_2) = A(\vec{r}_1 - \vec{r}_2) \equiv (4\pi)^2 \langle G \rangle \langle G^* \rangle = \frac{\exp(-\kappa |\vec{r}_1 - \vec{r}_2|)}{|\vec{r}_1 - \vec{r}_2|^2} \ , \tag{4.25}$$

where $\kappa = 2K'' = \lambda_{mf}^{-1} = n_0 \sigma_{ext}$ is the extinction rate or turbidity, with λ_{mf} the mean free path. Notice that all the spatial integrations for F and related functions are integrations within the slab and not over full space. Using the translational invariance in the (x, y) plane we define the two-dimensional Fourier transform to be

$$F(\vec{r}_1, \vec{r}_2) \equiv F(\vec{r}_\perp, z_1, z_2) = (2\pi)^{-2} \int F(\vec{q}_\perp, z_1, z_2) \exp(i \vec{r}_\perp \cdot \vec{q}_\perp) d\vec{q}_\perp \ , \tag{4.26}$$

where $\vec{r}_\perp = (x_1 - x_2, y_1 - y_2)$. Consequently we have, with the albedo a close to 1: $a \equiv 4\pi n_0 |f|^2 / \kappa$, and with L the thickness of the slab

$$\begin{aligned} F(\vec{r}_\perp, z_1, z_2) &= (\kappa a)^2 A(|\vec{r}_\perp|, |z_1 - z_2|) \\ &+ \frac{\kappa a}{4\pi} \int_0^L \int A(|\vec{r}_\perp - \vec{r}\,'_\perp|, |z_1 - z'|) F(\vec{r}\,'_\perp, z', z_2) d\vec{r}\,'_\perp dz' \ , \end{aligned} \tag{4.27}$$

which gives after Fourier transformation

$$F(\vec{q}_\perp, z_1, z_2) = (\kappa a)^2 A(\vec{q}_\perp, |z_1 - z_2|) + \frac{\kappa a}{4\pi} \int_0^L A(\vec{q}_\perp, |z_1 - z'|) F(\vec{q}\,'_\perp, z', z_2) dz' \ , \tag{4.28}$$

and

$$\begin{aligned}
A(\vec{q}_\perp, z) &= \int A(\vec{r}_\perp, z) \exp(-i\vec{r}_\perp \cdot \vec{q}_\perp) d\vec{r}_\perp \\
&= \int\int \frac{\exp\left(-\kappa\sqrt{r_\perp^2 + z^2}\right)}{r_\perp^2 + z^2} \exp(-ir_\perp q_\perp \cos\phi) r_\perp dr_\perp d\phi \\
&= 2\pi \int r_\perp J_0(r_\perp q_\perp) \frac{\exp\left(-\kappa\sqrt{r_\perp^2 + z^2}\right)}{r_\perp^2 + z^2} dr_\perp \\
&= 2\pi \int_1^\infty \frac{\exp\left(-\kappa z\sqrt{t^2 + \alpha^2}\right)}{\sqrt{t^2 + \alpha^2}} dt \equiv 2\pi W(\tau, \alpha) \ ,
\end{aligned} \tag{4.29}$$

where $J_0(x)$ is the Bessel function of zeroth order and argument x (see Ref. 79), and in which $\tau \equiv \kappa z$, and

$$\alpha \equiv \frac{q_\perp}{\kappa} = \frac{k_0}{\kappa}\sqrt{(\sin\theta_i \cos\phi_i + \sin\theta_s \cos\phi_s)^2 + (\sin\theta_i \sin\phi_i + \sin\theta_s \sin\phi_s)^2} \ , \tag{4.30}$$

where the polar angles refer to the incoming $\hat{K}_i$ and to the scattered direction $\hat{K}_s$. Notice that $W(\tau, \alpha = 0) = E_1(\tau)$, the exponential integral. For reasons of convention we define

$$\Gamma(\tau_1, \tau_2; \alpha) \equiv \frac{1}{4\pi\kappa^2} F(\vec{q}_\perp, z_1, z_2) \ , \tag{4.31}$$

and the (dimensionless) optical thickness $b \equiv \kappa L$ so

$$\Gamma(\tau_1, \tau_2; \alpha) = \frac{a^2}{2} W(|\tau_1 - \tau_2|; \alpha) + \frac{a}{2}\int_0^b W(|\tau_1 - \tau'|; \alpha)\Gamma(\tau', \tau_2; \alpha) d\tau' \ . \tag{4.32}$$

Eq. (4.32) has the form of the Milne equation. It is a Fredholm integral equation of the second kind with singular kernel.[80] Notice the extremely useful property that $\Gamma(\tau_1, \tau_2; \alpha)$ is only coupled to elements of Γ with the same value of τ_2. So apart from the connection through the initial source term, the τ_1 dependence of Γ is decoupled from the τ_2 dependence.

To allow for easy formal manipulations it is very useful to introduce the following matrix multiplication. For matrices $\mathcal{F}$ and $\mathcal{G}$ it is defined as

$$\mathcal{F}\mathcal{G} \equiv \int_0^b \mathcal{F}(\tau)\mathcal{G}(\tau) d\tau \ . \tag{4.33}$$

Notice that if the matrices depend on two τ coordinates the multiplication only involves the first coordinate. With

$$M(\tau_1, \tau_2; \alpha) \equiv \frac{1}{2} W(|\tau_1 - \tau_2|; \alpha) \ , \tag{4.34}$$

Eq. (4.32) can be written in matrix form

$$\Gamma = S + aM\Gamma \ , \tag{4.35}$$

where the initial source, $S = a^2M$, represents two-particle scattering. Taking as initial source $S = a\delta(\tau_1 - \tau_2)$ would include single scattering in Γ. Notice that both of these terms are unbound for $\tau_1 \to \tau_2$. The formal solution of Eq. (4.35) is

$$\Gamma = (1 - aM)^{-1}S \ , \tag{4.36}$$

so the solution of the total scattering problem can be obtained by inverting the matrix $(1 - aM)$. It may also be developed into a power series, in which case the solution takes the form

$$\Gamma = S + aMS + a^2M^2S + a^3M^3S + \cdots \ , \tag{4.37}$$

in which each term is found by multiplying the preceding one with the matrix aM. The physical significance of the power series is that each term corresponds to a separate order of scattering.

Eq. (4.32) is in such a form that direct numerical determination of Γ becomes feasible. The numerical procedure will be dealt with in Sect. 4.2.4 and in Appendices A-C, at the end of this chapter.

4.2.3 Scattering intensity

We have to emphasize that to describe a *real* scattering experiment one can not assume that the system exhibits statistical translational symmetry in all directions. The practical solution to this complication is to perform the calculation in the real-space domain and limit the integration over space in such a way that only the integration over the finite sample is performed. Properly speaking this is only feasible when one assumes a S matrix which is so extremely simple that the integrations in real space can actually be performed, viz., point scatterers.

To describe a scattering experiment we have to consider an inhomogeneous medium since in such an experiment separation of source, target and detector are required. To arrive at the result for the scattered intensity we consider the Green's function for the intensity $\langle \Psi \times \Psi^* \rangle$, which using the wave function equivalent of Eq. (4.7), like Eq. (3.9), is given by

$$\langle \Psi \times \Psi^* \rangle = \langle \Psi_{inc} \rangle \times \langle \Psi^*_{inc} \rangle + (\langle G \rangle \times \langle G^* \rangle)\langle R \rangle(\langle \Psi_{inc} \rangle \times \langle \Psi^*_{inc} \rangle) \ , \tag{4.38}$$

where the cross products of $\langle \Psi \rangle \times \langle \Psi^* \rangle$ average out to give zero.

For the intensity we need $I(\vec{r}) \equiv \Psi(\vec{r})\Psi^*(\vec{r})$ which can be found by writing Eq. (4.38) in its components

$$\begin{aligned} \langle I(\vec{r}) \rangle \equiv \langle \Psi(\vec{r})\Psi^*(\vec{r}) \rangle &= \langle \Psi_{inc}(\vec{r}) \rangle \langle \Psi^*_{inc}(\vec{r}) \rangle \\ &+ \int \langle G(\vec{r}, \vec{r}_1) \rangle \langle G^*(\vec{r}, \vec{r}_3) \rangle \langle R(\vec{r}_1, \vec{r}_2; \vec{r}_3, \vec{r}_4) \rangle \langle \Psi_{inc}(\vec{r}_2) \rangle \langle \Psi^*_{inc}(\vec{r}_4) \rangle d\vec{r}_1 d\vec{r}_2 d\vec{r}_3 d\vec{r}_4 \ . \end{aligned} \tag{4.39}$$

The mean-field amplitude and Green's function depend on the propagation constant in the medium

$$K \equiv K' + iK'' \ , \tag{4.40}$$

which in the weakly scattering limit, $K'' \ll K' \simeq k_0$, can be approximated by

$$K \simeq k_0 + i\frac{\kappa}{2} \simeq k_0 + \frac{2\pi n_0 f}{k_0} \ . \tag{4.41}$$

This is however precisely correct for *resonant* scatterers, for which $i\text{Im}\{S(\vec{k},\vec{k})\} \simeq S(\vec{k},\vec{k})$. The mean-field amplitude function is

$$\langle \Psi_{inc}(\vec{r}_1) \rangle = \exp(i\vec{K}_i \cdot \vec{r}_1) \ , \tag{4.42}$$

where $\vec{K}_i$ is a vector with magnitude K and direction of the incoming wave in the medium. For $K'' \ll K' \simeq k_0$ and almost normal incidence (θ_i small), $\vec{K}_i$ can be approximated by

$$\vec{K}_i = \hat{x}k_0 \sin\theta_i \cos\phi_i + \hat{y}k_0 \sin\theta_i \sin\phi_i + \hat{z}K_{iz} \ , \tag{4.43}$$

$$K_{iz} = \sqrt{K^2 - k_0^2 \sin^2\theta_i} \simeq k_0 \cos\theta_i + \frac{iK''}{\cos\theta_i} \ . \tag{4.44}$$

The mean Green's function is given by

$$\langle G(\vec{r}_1 - \vec{r}_2) \rangle = -\frac{\exp(iK|\vec{r}_1 - \vec{r}_2|)}{4\pi|\vec{r}_1 - \vec{r}_2|} \ , \tag{4.45}$$

when $\vec{r}_1$ and $\vec{r}_2$ are inside the slab, and, for backscattering

$$\langle G_B(\vec{r}_1, \vec{r}_2) \rangle \simeq -\frac{\exp(ik_0 r_1)}{4\pi r_1} \exp(-i\vec{K}_{s,B} \cdot \vec{r}_2) \ , \tag{4.46}$$

when $\vec{r}_2$ is in the slab, and when $\vec{r}_1$ is far outside the slab, and where the outgoing wave vector for backscattering $\vec{K}_{s,B}$ is given approximately by

$$\vec{K}_{s,B} = \hat{x}k_0 \sin\theta_s \cos\phi_s + \hat{y}k_0 \sin\theta_s \sin\phi_s - \hat{z}K_{sz} \ , \tag{4.47}$$

$$K_{sz} \simeq k_0 \cos\theta_s + \frac{iK''}{\cos\theta_s} \ . \tag{4.48}$$

For transmission through the slab we similarly find

$$\langle G_T(\vec{r}_1, \vec{r}_2) \rangle \simeq -\frac{\exp(ik_0 r_1)}{4\pi r_1} \exp(-i\vec{K}_{s,T} \cdot \vec{r}_2) \exp(-K''L/\cos\theta_s) \ . \tag{4.49}$$

The outgoing wave vector for transmission $\vec{K}_{s,T}$ is given approximately by

$$\vec{K}_{s,T} = \hat{x}k_0 \sin\theta_s \cos\phi_s + \hat{y}k_0 \sin\theta_s \sin\phi_s + \hat{z}K_{sz} \ . \tag{4.50}$$

The scattering intensity is best described with the help of γ, the so-called bistatic scattering coefficient,[63] which is independent of distance and the observed area of the medium. The bistatic scattering coefficient can be partitionated into the coefficients for single scattering, ladder and cyclical intensities, and is given by

$$\gamma(\mu_s,\mu_i) \equiv \frac{4\pi r^2}{A\mu_i} I(\vec{r}\,) \equiv \gamma_s(\mu_s,\mu_i) + \gamma_\ell(\mu_s,\mu_i) + \gamma_c(\mu_s,\mu_i) \ , \tag{4.51}$$

where A is the area of the target, and $\mu_{i,s} \equiv \cos\theta_{i,s}$. We can calculate the separate contributions to $\langle R\rangle$, where we separate out the single scattering $\langle \ell \rangle$. $\langle L\rangle$ is given by Eq. (4.21), and $\langle C\rangle$ given by Eq. (4.23). By employing Eqs. (4.42) and (4.46) in Eq. (4.39) gives for the backscattering

$$\begin{aligned} I(r)_{L,C} &= \frac{1}{(4\pi r)^2} \int \exp\{i[\vec{q}_{\perp,i}\cdot(\vec{r}_{2,\perp}-\vec{r}_{4,\perp}) - \vec{q}_{\perp,s}\cdot(\vec{r}_{1,\perp}-\vec{r}_{3,\perp})]\} \\ &\times \ \exp\{ik_0[\mu_i(z_2-z_4)+\mu_s(z_1-z_3)]\} \times \exp\left[-\frac{\kappa}{2}\left(\frac{z_2+z_4}{\mu_i}+\frac{z_1+z_3}{\mu_s}\right)\right] \\ &\times \ F(\vec{r}_1,\vec{r}_2)\delta(\vec{r}_{1,2}-\vec{r}_3)\delta(\vec{r}_{2,1}-\vec{r}_4)d\vec{r}_1 d\vec{r}_2 d\vec{r}_3 d\vec{r}_4 \ , \end{aligned} \tag{4.52}$$

where the labels L, C refer to the indices $1,2$ in the delta functions. We define $\vec{q}_\perp = \vec{q}_{\perp,i} + \vec{q}_{\perp,s}$, $\vec{r}_\perp = \vec{r}_{1,\perp} - \vec{r}_{2,\perp}$, and $\vec{R}_\perp = (\vec{r}_{1,\perp} + \vec{r}_{2,\perp})/2$ and then, with the normalization from the illuminated area of the slab

$$A = \int d\vec{R}_\perp = \text{Volume}/L \ , \tag{4.53}$$

and definition (4.31), we find:

$$\begin{aligned} \gamma_s(\mu_s,\mu_i) &= \frac{a\mu_s}{\mu_i+\mu_s}\left\{1-\exp\left[-b\left(\frac{1}{\mu_i}+\frac{1}{\mu_s}\right)\right]\right\} \ , &(4.54)\\ \gamma_\ell(\mu_s,\mu_i) &= \frac{1}{\mu_i}\int_0^b\int_0^b \Gamma(\tau_1,\tau_2;\alpha=0)\exp\left[-\left(\frac{\tau_1}{\mu_s}+\frac{\tau_2}{\mu_i}\right)\right] d\tau_1 d\tau_2 \ , &(4.55)\\ \gamma_c(\mu_s,\mu_i) &= \frac{1}{\mu_i}\int_0^b\int_0^b \Gamma(\tau_1,\tau_2;\alpha)\cos\left[\frac{k_0}{\kappa}(\mu_i-\mu_s)(\tau_1-\tau_2)\right] \\ &\qquad \times \ \exp\left[-\frac{1}{2}\left(\frac{1}{\mu_i}+\frac{1}{\mu_s}\right)(\tau_1+\tau_2)\right] d\tau_1 d\tau_2 \ , &(4.56) \end{aligned}$$

in agreement with Ref. 66. For the transmission of the slab we find:

$$\begin{aligned} \tilde{\gamma}_R &= \frac{1}{\mu_i A}\int \exp\{i[\vec{q}_{\perp,i}\cdot(\vec{r}_{2,\perp}-\vec{r}_{4,\perp}) - \vec{q}_{\perp,s}\cdot(\vec{r}_{1,\perp}-\vec{r}_{3,\perp})]\} \\ &\times \ \exp\{ik_0[\mu_i(z_2-z_4)-\mu_s(z_1-z_3)]\} \times \exp\left[-\frac{\kappa}{2}\left(\frac{z_2+z_4}{\mu_i}-\frac{z_1+z_3}{\mu_s}\right)\right] \\ &\times \ \exp(-\kappa L/\mu_s)\langle R(\vec{r}_1,\vec{r}_2;\vec{r}_3,\vec{r}_4)\rangle d\vec{r}_1 d\vec{r}_2 d\vec{r}_3 d\vec{r}_4 \ . \end{aligned} \tag{4.57}$$

As we compare Eqs. (4.57) and (4.52), it is immediately clear that there are only some small differences between them, and that some more general formula for Eqs. (4.54)-(4.56) can be given.

We have indicated that the Green's function Γ can be used to calculate the energy density in the slab (see remark following Eq. (4.22)). In the present case the incoming (reduced) intensity I_{ri} is given by

$$I_{ri}(\tau,\hat{k}) = \exp(-\tau/\mu_i)\delta(\hat{k}-\hat{K}_i) \ , \tag{4.58}$$

where $\hat{K}_i$ is the incoming direction. The energy density or the so-called source function $J(\tau)$ which is extensively studied in the literature,[63,64] is given by

$$J(\tau) = \int_0^b \Gamma(\tau,\tau';\alpha=0)\exp(-\tau'/\mu_i)d\tau' \ , \tag{4.59}$$

and using the (complicated) integral equation for Γ as given by Eq. (4.32) one derives a much simpler equation for the incoherent energy density

$$J(\tau) = \frac{a^2}{2}\int_0^b E_1(|\tau-\tau'|)\exp(-\tau'/\mu_i)d\tau' + \frac{a}{2}\int_0^b E_1(|\tau-\tau'|)J(\tau')d\tau' \ , \tag{4.60}$$

which is the Schwarzschild-Milne equation with the source term describing second-order scattering. The incoherent contribution to the bistatic coefficient for backscattering can also be expressed in terms of the energy density,

$$\gamma_\ell(\mu_s,\mu_i) = \frac{1}{\mu_i}\int_0^b J(\tau)\exp(-\tau/\mu_s)d\tau \ . \tag{4.61}$$

So if one is only interested in the ladder contribution to the scattering, the determination of the Green's function $\Gamma(\tau_1,\tau_2)$ is not necessary because the determination of energy density $J(\tau)$ is sufficient. This is a substantial simplification. The (numerical) determination of the solution of the Schwarzschild-Milne equation is straigthforward.[63,64,66,81] The results of γ_ℓ may be compared with the extensive tables in Ref. 64 by multiplying these with a factor $4\mu_s$.

4.2.4 Numerical results for the line shape

The general outline is quite straightforward. We have to solve the integral equation (4.32) numerically and then use the result to calculate the bistatic scattering coefficient $\gamma(\mu_s,\mu_i)$. To do this, we have to calculate the kernel $W(\tau,\alpha)$ first. This problem is discussed in Appendix A. To calculate the scattering problem, it is also important to notice the following symmetry properties of Γ:

$$\Gamma(\tau_1,\tau_2;\alpha) = \Gamma(\tau_2,\tau_1;\alpha) = \Gamma(b-\tau_1,b-\tau_2;\alpha) \ . \tag{4.62}$$

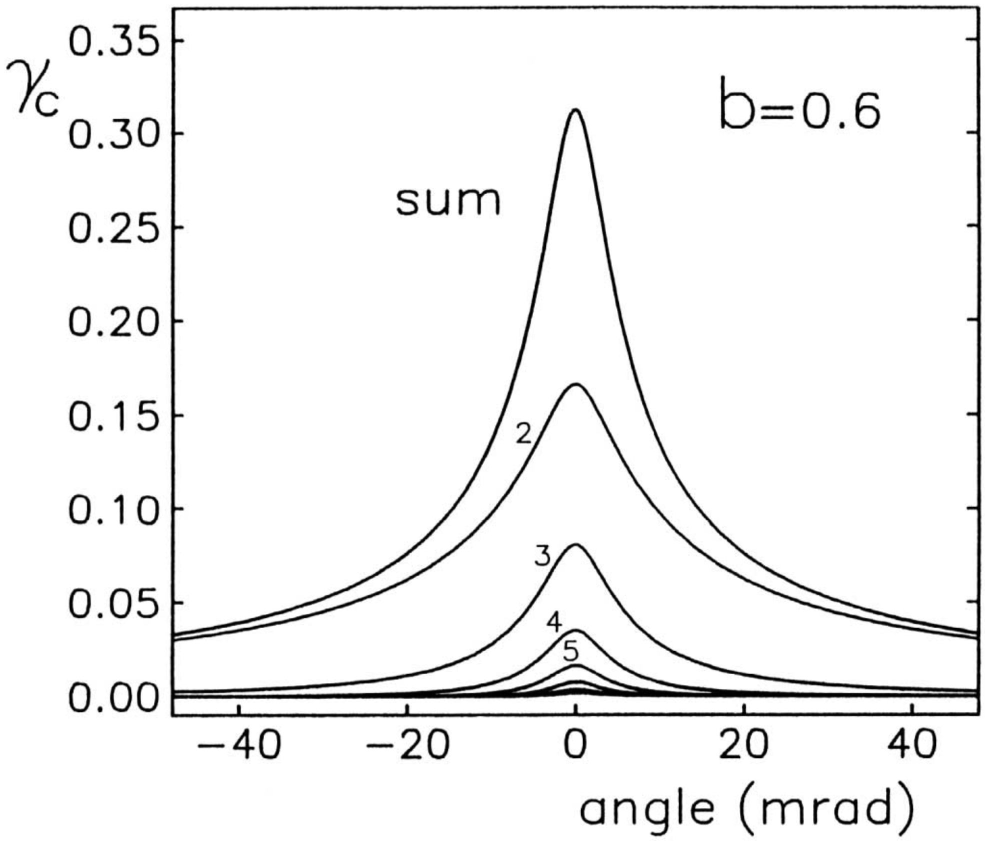

Figure 4.7: *The line-shape of the enhanced backscattering of the second up to the eigtht order of scattering and their sum for slab-thickness $b = 0.6$, $\lambda_{mf}/\lambda = 53.5$, and albedo $a = 1$.*

Γ may be written as a sum of the contributions of the separate orders of scattering. So the total solution is given by

$$\Gamma = \lim_{N\to\infty} \sum_{n=2}^{N} \Gamma_n \ , \tag{4.63}$$

in which $\Gamma_n(\tau_1, \tau_2; \alpha)$ represents the contribution for the n^{th} order of scattering. We can use the iterative formula

$$\Gamma_{n+1}(\tau_1, \tau_2; \alpha) = \frac{a}{2} \int_0^b W(|\tau_1 - \tau'|; \alpha) \Gamma_n(\tau', \tau_2; \alpha) d\tau' \ , \tag{4.64}$$

or

$$\Gamma_{n+1} = aM\Gamma_n \ , \tag{4.65}$$

to calculate the successive orders of scattering, starting with

$$S = a^2 M = \frac{a^2}{2} W(|\tau_1 - \tau_2|; \alpha) \equiv \Gamma_2 \ . \tag{4.66}$$

The details of this calculation are presented in Appendix B.

The convergence of our iterative procedure to the total solution Γ is, except for numerical problems that might occur due to build up of inaccuracy for very high orders of scattering, determined by the albedo a and the optical thickness of the slab b. The thicker the slab and the closer the albedo to 1, the slower the convergence. So albedo close to one is the most difficult and albedo substantially less than one becomes almost trivial. For a semi-infinite slab, the iteration converges as $a^n n^{-3/2}$. In practice this means that it is possible to calculate the whole solution for $b = \infty$ and $a < 0.9$ within 1% accuracy in less than 20 iterations. For the albedo a=1 only slabs with $b < 2$ can be treated with about the same accuracy. In Fig. 4.7 the order by order line shape is given for a typical case.

Of course we are also interested in thick slabs ($b > 2$) with the albedo a close or equal to 1. The solution to this problem is obtained by solving Eq. (4.32) by diagonalization. (See Appendix C). With the diagonalization procedure we can handle slabs up to 32 optical depths with albedo equal to one. In Chapter 5 we will compare the results from the theory with various experiments. If more sophisticated discretization procedures would be invoked we probably could extend this limit substantially. Yet, the backscattering intensity from the $b = 32$ slab is already 95% of the backscattering of the semi-infinite slab. So the only problem left, are very thick slabs ($32 < b < \infty$) in case $a = 1$. However, thick slabs and dominance of high-order scattering processes are precisely the conditions for which a diffusion approximation should hold.

4.3 Diffusion approximation for d=3

First we consider a scattering medium of infinite size and take advantage of the translational invariance in all directions. The three-dimensional Fourier transform is

$$F(\vec{r}_1, \vec{r}_2) \equiv F_0(\vec{r}_1 - \vec{r}_2) \equiv F_0(\vec{r}\,) \equiv (2\pi)^{-3} \int F_0(\vec{q}\,) \exp(i\vec{r} \cdot \vec{q}\,) d\vec{q}\ . \tag{4.67}$$

With Eq. (4.24) we find

$$F_0(\vec{q}\,) = \frac{a\kappa}{4\pi} A(\vec{q}\,) F_0(\vec{q}\,) + a^2\kappa^2 A(\vec{q}\,)\ , \tag{4.68}$$

so that

$$F_0(\vec{r}\,) = a^2\kappa^2 (2\pi)^{-3} \int \frac{A(\vec{q}\,)}{1 - a\kappa A(\vec{q}\,)/(4\pi)} \exp(i\vec{r} \cdot \vec{q}\,) d\vec{q}\ , \tag{4.69}$$

$A(\vec{q}\,)$ can be calculated as

$$\begin{aligned} A(\vec{q}\,) &= \int A(\vec{r}\,) \exp(-i\vec{r} \cdot \vec{q}\,) d\vec{r} \\ &= \int\!\!\int\!\!\int \exp(-\kappa r) \exp(-irq\cos\theta) \sin\theta d\phi d\theta dr \\ &= \frac{4\pi}{q} \int_0^\infty \frac{1}{r} \exp(-\kappa r) \sin(qr) dr \\ &= \frac{4\pi}{q} \arctan(\frac{q}{\kappa})\ , \end{aligned} \tag{4.70}$$

substituting this result in (4.69) and performing the angular integration gives

$$F_0(\vec{r}) = \frac{2a^2\kappa^2}{\pi r} \int_0^\infty \frac{(q/\kappa)\arctan(q/\kappa)}{(q/\kappa) - a\arctan(q/\kappa)} \sin(qr)dq \; . \tag{4.71}$$

The solutions for all definite integrals used in this section can be found in Ref. 79 and Ref. 82.

For the diffusive regime we have $q \ll \kappa$ and we can approximate $\arctan(q/\kappa)$ by (see also p. 222 in Ref. 63)

$$\arctan(x) \simeq \frac{x}{1 + \frac{1}{3}x^2} \; , \quad |x| < 1 \; . \tag{4.72}$$

Notice that this approximation provides a useful cut-off for $q > \kappa$. We introduce $\kappa_a \equiv \lambda_{abs}^{-1}$, with $\kappa_a^2 = 3\kappa^2(1-a)$, and find

$$F_0(\vec{r}) = \frac{2a^2\kappa^3}{\pi r} \int_0^\infty \frac{3q}{q^2 + \kappa_a^2} \sin(qr)dq = \frac{3a^2\kappa^3}{r} \exp(-\kappa_a r) \; , \tag{4.73}$$

which can only be justified for albedo a close to 1. So the solution of Eq. (4.24) in the diffusion approximation for an infinite space is given by

$$F(\vec{r}_1, \vec{r}_2) = F_0(\vec{r}_\perp, z) = \frac{3a^2\kappa^3}{|\vec{r}_1 - \vec{r}_2|} \exp(-\kappa_a|\vec{r}_1 - \vec{r}_2|) \; . \tag{4.74}$$

Define

$$F_0(\vec{q}_\perp, z) \equiv \int F_0(\vec{r}_\perp, z) \exp(-i\vec{r}_\perp \cdot \vec{q}_\perp) d\vec{r}_\perp \; . \tag{4.75}$$

This gives with Eq. (4.74) (compare Eq. (4.29)):

$$\begin{aligned} F_0(\vec{q}_\perp, z) &= 6\pi a^2\kappa^3 \int r_\perp J_0(r_\perp q_\perp) \frac{\exp\left(-\kappa_a\sqrt{r_\perp^2 + z^2}\,\right)}{\sqrt{r_\perp^2 + z^2}} dr_\perp \\ &= \frac{6\pi a^2\kappa^3}{\sqrt{\kappa_a^2 + q_\perp^2}} \exp\left(-z\sqrt{\kappa_a^2 + q_\perp^2}\,\right) \; . \end{aligned} \tag{4.76}$$

Up to now we have considered the statistical homogeneous (infinite) system. One has to include boundary conditions to handle the finite-slab problem. These boundary conditions can be given in the form of trapping planes. If the light passes one of these planes, it can never return, and thus can no longer contribute to the diffusive intensity in the slab. So at the trapping plane the diffuse intensity becomes zero. For light, it is however known that the intensity at the edge of a random medium is finite (this follows for instance from the Milne equation). This can be achieved by putting the trapping planes at a certain distance from the edges of the medium. From the literature[63,64,67,83] we know that the proper boundary conditions are approximately given by putting a trapping plane in $z = -z_0$ and $z = L + z_0$ respectively, which corresponds to values for $F(x, y, z)$

of $F(x_1-x_2, y_1-y_2, -z_0) = 0$ and $F(x_1-x_2, y_1-y_2, L+z_0) = 0$. It appears that $z_0 \simeq 0.7104\lambda_{mf}$ for $a = 1$. Effectively, the diffusive intensity at the edges of the slab, at $z = 0$ and $z = L$ is indeed positive, and not zero as would have been the case for $z_0 = 0$. A diffusion equation with trapping planes can be handled in a straightforward way.[19] The solution of (4.24) for a finite slab in the diffusion approximation is

$$\begin{aligned} F(\vec{r}_1, \vec{r}_2) &= \sum_{n=-\infty}^{\infty} F_0(x_1-x_2, y_1-y_2, z_1-z_2-2n[d+2z_0]) \\ &\quad - F_0(x_1-x_2, y_1-y_2, z_1-z_2+2n[d+2z_0]+2z_0) . \end{aligned} \tag{4.77}$$

The summation in this equation results from the multiple reflection of F in both mirror planes. It is obvious that the thicker the slab, the lower the number of contributing terms. For a semi infinite slab, only the term for $n = 0$ remains.

From definition (4.31) and Eqs. (4.76) and (4.77) it follows

$$\begin{aligned} \Gamma(\tau_1, \tau_2; \alpha) &= \frac{3a^2}{2c} \sum_{n=-\infty}^{\infty} \exp(-c|\tau_1-\tau_2-2nB|) \\ &\quad - \exp(-c|\tau_1+\tau_2+2nB+2\tau_0|) , \end{aligned} \tag{4.78}$$

with

$$c \equiv \sqrt{3(1-a)+\alpha^2} , \tag{4.79}$$

$$\tau_0 \equiv \kappa z_0 , \tag{4.80}$$

$$B \equiv b + 2\tau_0 . \tag{4.81}$$

Let us define

$$\Gamma'(\delta, \sigma; \alpha) \equiv \Gamma(\tau_1, \tau_2; \alpha) , \tag{4.82}$$

$$\delta \equiv \tau_1 - \tau_2 , \tag{4.83}$$

$$\sigma \equiv \tau_1 + \tau_2 . \tag{4.84}$$

After some algebra it turns out that the summation can actually be performed and we get the Green's function Γ in closed form

$$\Gamma'(\delta, \sigma; \alpha) = \frac{3a^2}{2c\,\sinh(cB)} \{\cosh[c\,(B-|\delta|)] - \cosh[c\,(b-\sigma)]\} . \tag{4.85}$$

The special case $c \to 0$, where both $\alpha \to 0$ (the anti-specular or backscattering direction) and $a \to 1$ (no absorbtion), gives

$$\begin{aligned} \Gamma'(\delta, \sigma; \alpha; c=0) &= \frac{3}{4B} \left\{ (B-|\delta|)^2 - (b-\sigma)^2 \right\} \\ &= \frac{3}{2}(\sigma - |\delta| - 2\tau_0) + \frac{1}{2B}[\delta^2 - \sigma^2 + 4\tau_0(1-\sigma)] , \end{aligned} \tag{4.86}$$

which for $b \to \infty$ gives

$$\Gamma(\tau_1, \tau_2; \alpha; c = 0; b = \infty) = 3[\min(\tau_1, \tau_2) - \tau_0] \ . \tag{4.87}$$

Notice that $c = \alpha$ for $a = 1$, and that for the *specular* angle $\alpha = (2k_0/\kappa)\sin\theta$, where $\theta_i = \theta_s = \theta$ (see Eq. (4.30).

The result (4.85) can also be used to calculate the incoherent energy density or source function $J(\tau)$. From Eqs. (4.59), and (4.82)-(4.85) it follows that for a semi-infinite slab ($b = \infty$) the result is given by

$$J_\infty(\tau) = \frac{3a^2\mu_i}{1 - \mu_i^2 c^2}[2Q_+ \exp(-c\tau) - \mu_i \exp(-\tau/\mu_i)] \ , \tag{4.88}$$

with $c = \sqrt{3(1-a)} = \kappa_a/\kappa$ because $\alpha \equiv 0$ for the incoherent part, and

$$Q_\pm \equiv [1 \pm \mu_i c - (1 \mp \mu_i c)\exp(-2c\tau_0)]/4c \ . \tag{4.89}$$

For a finite slab the results are considerably more complicated:

$$J(\tau) = \frac{3a^2\mu_i}{1 - \mu_i^2 c^2}\{P_+ \exp(-c\tau) - P_- \exp[c\,(\tau + 2\tau_0)] - \mu_i \exp(-\tau/\mu_i)\} \ , \tag{4.90}$$

with

$$P_\pm \equiv [Q_+ \exp(\pm cB) + Q_- \exp(-b/\mu_i)]/\sinh(cB) \ . \tag{4.91}$$

Now we are ready to calculate both the reflected and transmitted intensities from the slab as a function of μ_i, μ_s, α, a, b, κ and k_0.

4.3.1 Analytical results for backscattering

The bistatic coefficient arising from the incoherent scattering in the diffusion approximation is calculated to be

$$\begin{aligned} \gamma_\ell(\mu_s, \mu_i) &= \frac{3a^2\mu_s}{1 - \mu_i^2 c^2}\left[\frac{-\mu_i^2}{\mu_i + \mu_s}\left\{1 - \exp\left[-b\left(\frac{1}{\mu_i} + \frac{1}{\mu_s}\right)\right]\right\}\right. \\ &+ \frac{P_+}{1 + \mu_s c}\left\{1 - \exp\left[-b\left(c + \frac{1}{\mu_s}\right)\right]\right\} \\ &- \left.\frac{P_-}{1 - \mu_s c}\exp(2c\tau_0)\left\{1 - \exp\left[b\left(c - \frac{1}{\mu_s}\right)\right]\right\}\right] \ , \end{aligned} \tag{4.92}$$

which for the semi-infinite slab reduces to

$$\gamma_{\ell,\infty}(\mu_s, \mu_i) = \frac{3a^2\mu_s}{1 - \mu_i^2 c^2}\left[\frac{2Q_+}{1 + \mu_s c} - \frac{\mu_i^2}{\mu_i + \mu_s}\right] \ . \tag{4.93}$$

Of course when discussing weak localization of light, one is more interested in the interfer-

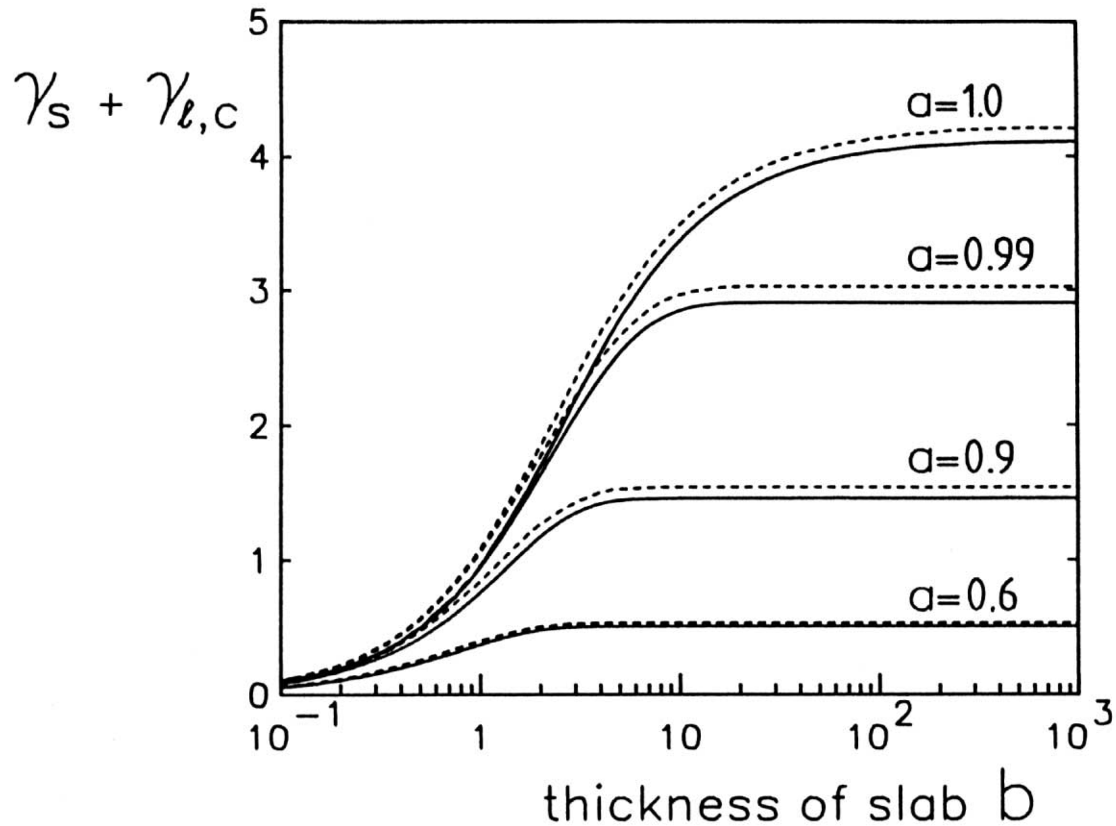

Figure 4.8: *Absolute values of $\gamma_{\ell,c}$ at exactly backscattering ($\gamma_\ell(\mu_s = \mu_i, \mu_i) = \gamma_c(\mu_s = \mu_i, \mu_i)$) with $\mu_i = 1$, as a function of the optical thickness b. Dashed curves represent the result from the exact theory as derived in Sect. 4.2, solid lines give the result from the diffusion approximation. Different curves correspond to different albedos.*

ence contributions than in the incoherent part. However, it is very important to consider the incoherent part as well. The reason is that Eqs. (4.92) and (4.93) are a consequence of the diffusion approximation which can be checked against *rigorous* answers. The Milne equation (4.60) can be solved exactly for all slab thicknesses by numerical methods. The exact results should be compared with the results obtained in Eqs. (4.92) and (4.93). This constitutes a stringent test on the validity of the diffusion theory. It turns out that the results are very good indeed, as will be shown.

There are no reasons to expect the diffusion approximation to be correct for low values of the albedo a. However, if we compare the behavior of this theory with the exact theory (see Fig. 4.8 for comparison of the intensities for precisely backscattering), we conclude that the agreement between the two theories is quite good, even for small albedos.

Let us now consider the interference contribution to the scattering in the diffusion approximation. We define

$$u \equiv \frac{k_0}{\kappa}(\mu_i - \mu_s) \ , \tag{4.94}$$

$$v \equiv \frac{1}{2}\left(\frac{1}{\mu_i} + \frac{1}{\mu_s}\right) \ . \tag{4.95}$$

Using Eq. (4.56), definition (4.82), and the diffusion result Eq. (4.85) the bistatic scattering coefficient for the interference (most-crossed diagrams) terms can easily be shown to be

$$\gamma_c(\mu_s, \mu_i) = \frac{1}{\mu_i}\int_0^b \int_\delta^{2b-\delta} \Gamma'(\delta, \sigma; \alpha)\cos(u\delta)\exp(-v\sigma)d\sigma d\delta \ . \tag{4.96}$$

This integral can be solved exactly. After tedious algebra we find

$$\begin{aligned}
\gamma_c(\mu_s, \mu_i) \;&=\; \frac{3a^2\exp(-vb)}{2\mu_i cv\sinh(cB)}\left[\left\{\frac{u}{(v+c)^2+u^2} - \frac{u}{(v-c)^2+u^2}\right\}\sinh(2c\tau_0)\sin(ub)\right. \\
&+\; \left\{\frac{1}{(v-c)^2+u^2}[v-(v-c)\cosh(2c\tau_0)]\right. \\
&+\; \left.\frac{1}{(v+c)^2+u^2}[v-(v+c)\cosh(2c\tau_0)]\right\}\cos(ub) \\
&+\; \frac{1}{(v-c)^2+u^2}\{(v-c)\cosh[b\,(v-c)-2c\tau_0] - v\cosh[b\,(v-c)]\} \\
&+\; \left.\frac{1}{(v+c)^2+u^2}\{(v+c)\cosh[b\,(v+c)+2c\tau_0] - v\cosh[b\,(v+c)]\}\right] \ .
\end{aligned} \tag{4.97}$$

Note that for pure backscattering, $\mu_i = \mu_s$, $\gamma_\ell = \gamma_c$ in all cases. For $b \to \infty$ expression (4.97) reduces to

$$\gamma_{c,\infty}(\mu_s, \mu_i) = \frac{3a^2\{c + v[1-\exp(-2c\tau_0)]\}}{2\mu_i cv[(v+c)^2+u^2]} \ . \tag{4.98}$$

For an albedo of 1 this agrees with the result of Ref. 69. In Figs. 4.8-4.12 we present the bistatic scattering coefficient γ and the width of the backscattering cone as a function of the optical thickness b and the mean free path λ_{mf}. For a number of cases the results are compared with the exact values calculated with the rigorous theory from Sect. 4.2.

In Fig. 4.9 we compare the lineshapes of the exact theory and the diffusion approximation for two different optical thicknesses, with the albedo $a = 1$. We see, that although their shapes are comparable, the diffusion approximation shows a small underestimation for all angles with respect to the exact theory. Later (Fig. 4.13 and Table I) we will see that this is caused by a small underestimation of the lowest orders of scattering. This also explains why the lineshapes for thin slabs (which consequently contain a lot of low-order scattering) suffer more from this underestimation than those for thick slabs. In Fig. 4.10 we present the (full width at half maximum) linewidth W as a function of the mean free path. From this we conclude that $W\lambda_{mf}/\lambda$ is a constant for a fixed albedo and slab thickness $b = \infty$, at least for $(\lambda_{mf}/\lambda) > 1$. After a detailed study, we have found this

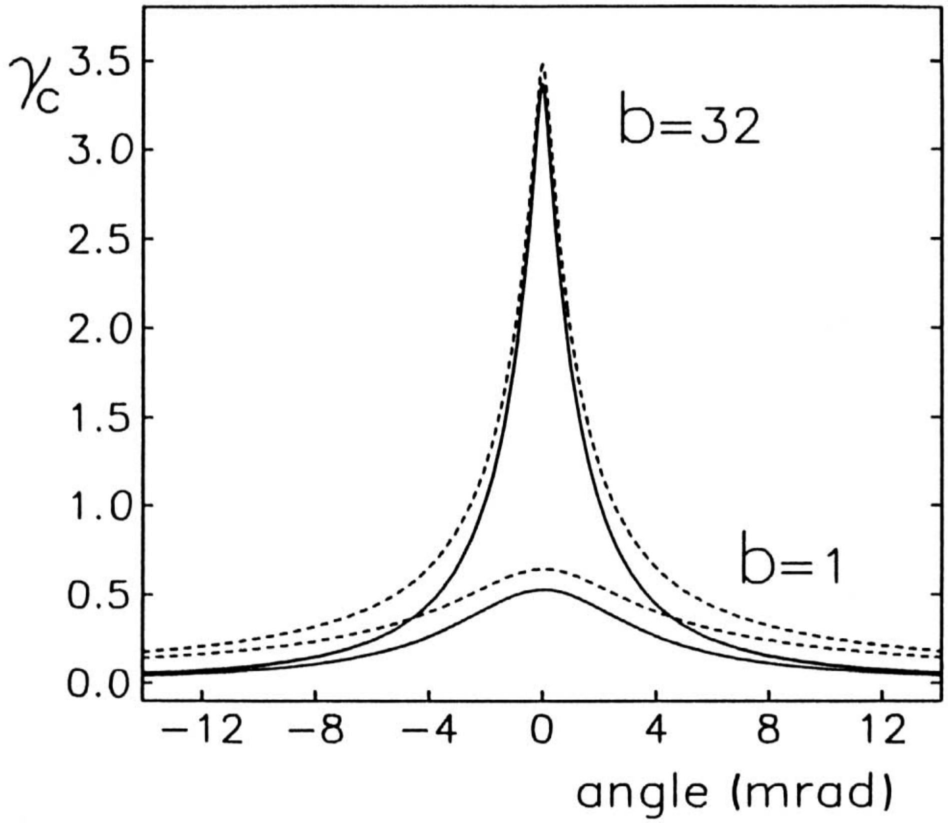

Figure 4.9: *Comparison of the absolute lineshapes, $(\gamma_c(\mu_s, \mu_i)$, as found from the exact theory (dashed lines) and the diffusion approximation (solid lines) for slab-thickness $b = 32$ and $b = 1$, $\lambda_{mf}/\lambda = 53.5$, and albedo $a = 1$.*

to be true for any other value of b as well, as long as the latter condition is fullfilled. This conclusion is used in Fig. 4.11 to plot the value $W\lambda_{mf}/\lambda$ against the optical thickness b. The discrepancy between the exact theory and the diffusion approximation for small b is to be expected.

From the point of view of an experimentalist, it is instructive to calculate so-called "difference slabs" (see Ref. 84). Here, the backscattering intensities from two slabs with optical thicknesses b_1 and b_2 are subtracted. In this way, the scattering contributions coming from the front layer ($\tau < b_1$) can be eliminated, and only the contributions of the light that has been in the back-end of the slab ($b_1 < \tau < b_2$) remain. To be more precise, the backscattering of such a difference slab contains exactly all those light paths that have their *deepest point* at an optical depth τ_d, with $b_1 < \tau_d < b_2$. Since the number of light paths that have their *deepest point* at an optical depth τ_d does not change with the optical thickness b of the sample (at least if $b > \tau_d$), this also holds if that difference slab is situated in the middle of a thicker slab with optical thickness $b > b_2$.

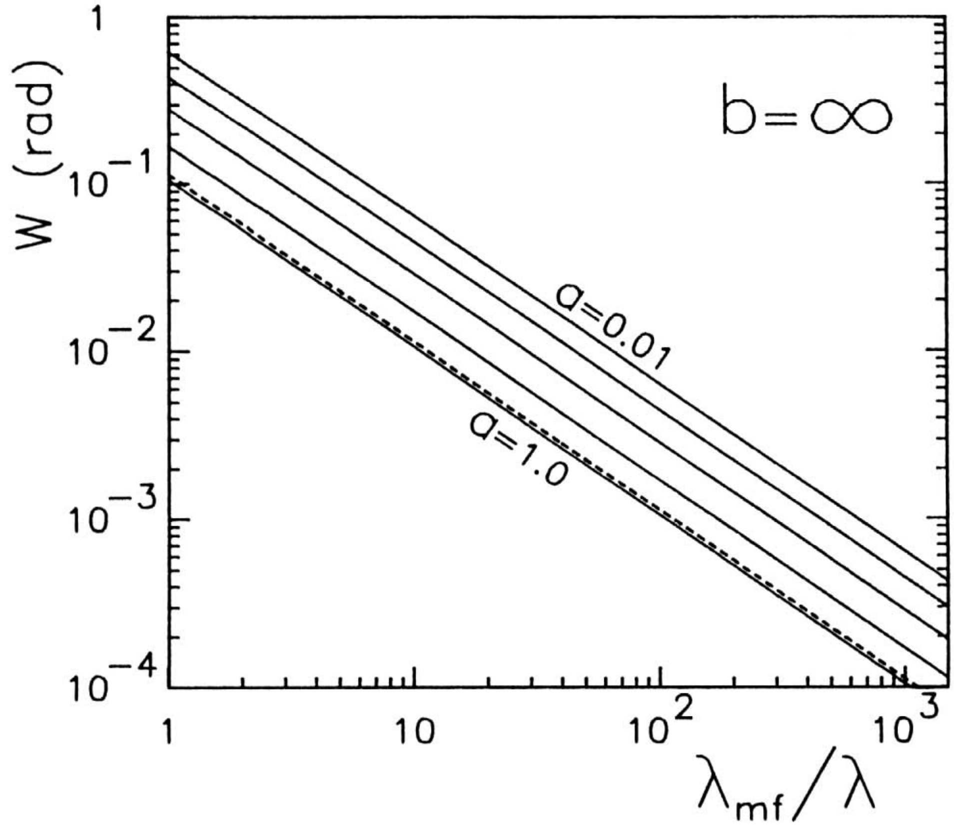

Figure 4.10: *The full width at half maximum W of the backscattering cone, in the diffusion approximation for a semi-infinite slab ($b = \infty$). Curves are given for five different albedos as a function of λ_{mf}/λ. Also for $a = 1$ the exact (extrapolated for $b \to \infty$) result (dashed line) is given.*

The width of the backscattering cone associated with the light paths that have their deepest point in the difference slab b_1 to b_2, or $b_1 < \tau_d < b_2$, is defined as: $W[\gamma_c(b_2) - \gamma_c(b_1)]$, which we can use to define the width, Δ, of the backscatter cone associated with a difference slab of infinitesimal thickness at the optical depth τ_d:

$$\Delta(\tau_d) \equiv \lim_{b_1 \to b_2} W[\gamma_c(b_2) - \gamma_c(b_1)] \ , \quad b_1 < b_2 \ . \tag{4.99}$$

In Fig. 4.12 this is used to plot the value $(\lambda/\lambda_{mf})/\Delta(\tau_d)$ against τ_d for some values of the albedo a. The figure shows that $\Delta(\tau_d)$ is inversely proportional to the optical depth τ_d in case $a = 1$.

It is of interest to analyze the angular dependence of the enhanced backscattering in the neighborhood of the exact backscattering direction. Analysis of $\gamma_{c,\infty}$ near backscattering

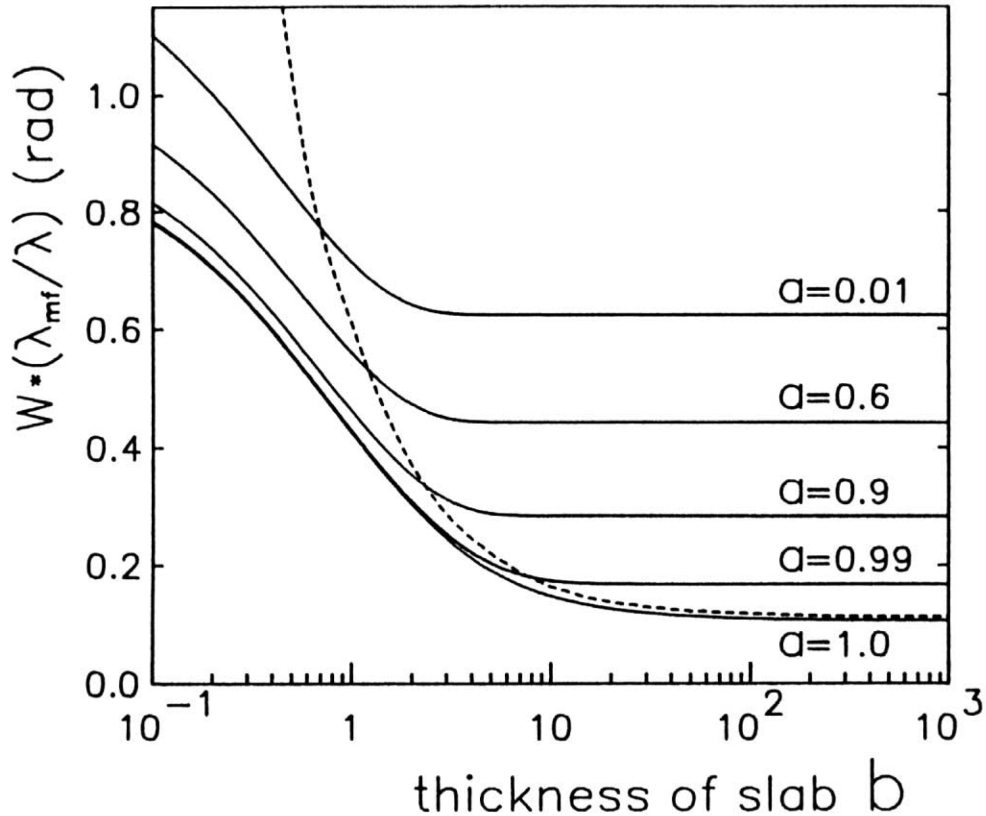

Figure 4.11: *The value $W\lambda_{mf}/\lambda$ is plotted against the optical thickness b. The solid lines give the results from the diffusion approximation for five different values of the albedo. The dashed curve gives the result for the exact theory with $a = 1$.*

angle for the albedo close or equal to 1 (with $\mu_i = 1$) gives

$$\gamma_{c,\infty} = \frac{3a^2}{2}\left[1 + 2\tau_0 - 2(\tau_0+1)^2\sqrt{3(1-a) + \frac{k_0^2}{\kappa^2}\theta_s^2}\right] + O(\theta_s^2) \ , \tag{4.100}$$

which for $a = 1$ gives

$$\gamma_{c,\infty} = \frac{3}{2}\left[1 + 2\tau_0 - 2(\tau_0+1)^2\frac{k_0}{\kappa}|\theta_s|\right] + O(\theta_s^2) \ , \tag{4.101}$$

which clearly shows that the solution is non-analytic for $a = 1$. So we see, that the top of the backscatter cone is a hyperbola for $a < 1$ and a triangle for $a = 1$.

It is extremely useful to decompose the results of the diffusion theory in a summation of terms in which each term describes the next order of scattering. In such a way the theory can even be tested much better against exact theories. To that end we have to express the diffusion result for the bistatic coefficients in a Taylor series of the albedo. Expansion of Eq. (4.98) in the albedo gives the separate contribution γ_n for each order of

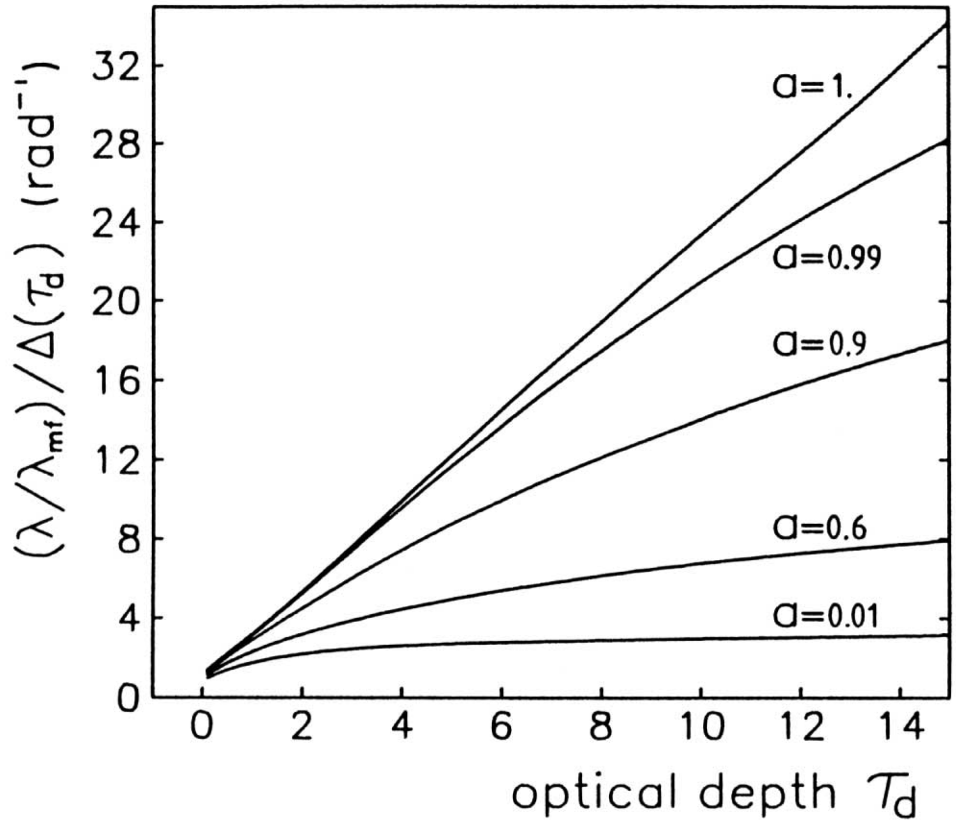

Figure 4.12: *The value $(\lambda/\lambda_{mf})/\Delta(\tau_d)$, associated with a difference slab of infinitesimal thickness at an optical depth τ_d, is plotted against τ_d for five different values of the albedo a. Notice that for $a = 1$ the curve is a straight line which goes through the abscis at $\tau_d \simeq -0.5$. Experimental results are given in Fig. 5.8*

scattering for the case $b = \infty$, and $\mu_i = \mu_s = 1$. This can be done by calculating the n^{th} derivative of $\gamma_{\ell,\infty}$ or $\gamma_{c,\infty}$ and substituting $a = 0$:

$$\gamma_{\ell,c,\infty} = \sum_{n=0}^{\infty} \gamma_n a^n \ , \tag{4.102}$$

$$\gamma_{n=m+2} = \left. \frac{d^m \gamma_{\ell,c,\infty}}{m! da^m} \right|_{a=0} \ , \tag{4.103}$$

The solution is implicitly given by a set of iterative equations

$$\gamma_{n+2} = \frac{d}{2n!} \sum_{m=0}^{n} \frac{\delta_{nm}}{[c(c+1)]^{m+1}} \left[A_m - B_m \frac{\exp(-2c\tau_0)}{c+1} \right] \ , \tag{4.104}$$

$$A_m = \sum_{k=0}^{m} \alpha_{mk} c^k \ , \quad \alpha_{00} = 1 \ , \tag{4.105}$$

$$B_m = \sum_{k=0}^{2m} \beta_{mk} c^k \ , \quad \beta_{00} = 1 \ , \tag{4.106}$$

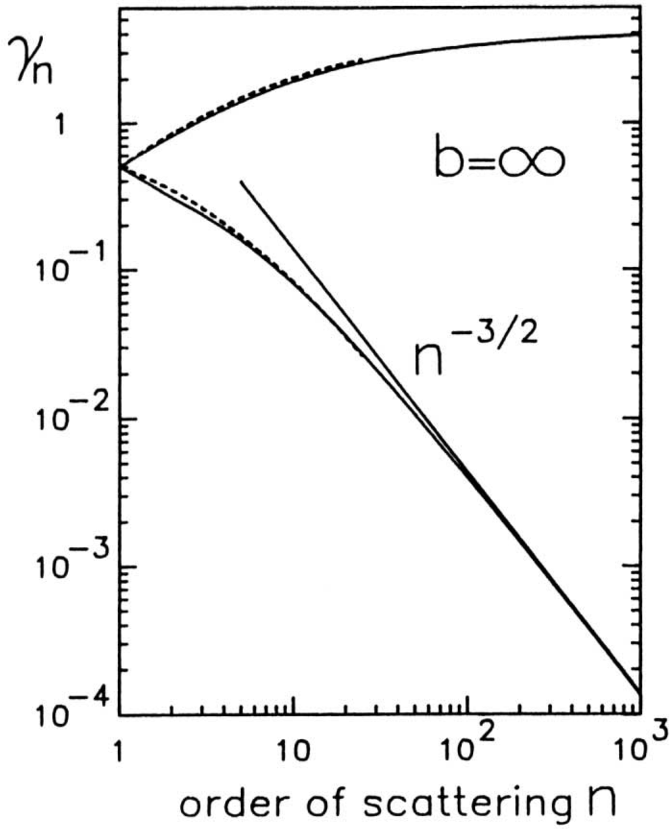

Figure 4.13:

The n^{th} order scattering contribution to the intensity γ in case $b = \infty$, $a = 1$ and $\mu_i = \mu_s = 1$ for both the exact theory (dotted lines) and the diffusion approximation (solid lines). The convergence of the high-order scattering to the $n^{-3/2}$ asymptote is clear. It is also seen, that the lower-order scattering is underestimated by the diffusion approach. The cumulative curve $\sum_n \gamma_n$ is also given. See also Table I.

Table I: *The n^{th} order scattering contribution to the total amount of scattering γ in case $b = \infty$, $a = 1$ and $\mu_i = \mu_s = 1$ for both the exact theory and the diffusion approximation. The cumulative values $\sum_n \gamma_n$ are also given. See also Fig. 4.13.*

n	$\gamma_{n,dif}$	$\gamma_{n,exa}$	$\sum_n \gamma_{n,dif}$	$\sum_n \gamma_{n,exa}$
1	0.5000	0.5000	0.5000	0.5000
2	0.3071	0.3465	0.8071	0.8465
3	0.2356	0.2611	1.0426	1.1076
4	0.1903	0.2066	1.2330	1.3142
5	0.1582	0.1692	1.3912	1.4834
6	0.1343	0.1421	1.5254	1.6254
7	0.1159	0.1214	1.6413	1.7469
8	0.1013	0.1055	1.7426	1.8524
9	0.0896	0.0928	1.8323	1.9452
10	0.0801	0.0825	1.9124	2.0277
⋮	⋮	⋮	⋮	⋮
∞	0.0000	0.0000	4.1313	4.2277

$$
\begin{aligned}
\alpha_{mk} &= (k-m)\alpha_{m-1,k} + (k-1-2m)\alpha_{m-1,k-1} \ , & (4.107)\\
\beta_{mk} &= (k-m)\beta_{m-1,k} + (k-2-2m-2\tau_0)\beta_{m-1,k-1} - 2\tau_0\beta_{m-1,k-2} \ , & (4.108)\\
\delta_{nm} &= (n-1-\frac{1}{2}m)\delta_{n-1,m} - \frac{c}{2}\delta_{n-1,m-1} \ , \quad \delta_{11} = -\frac{c}{2} \ , & (4.109)
\end{aligned}
$$

with $\alpha_{m,-1} = \beta_{m,-2} = \beta_{m,-1} = \beta_{m,2m+1} = \beta_{m,2m+2} = \delta_{n,0} = \delta_{n,n+1} = 0$ and $c = \sqrt{d}$, where d is the dimension, so here $d = 3$ (in Sect. 4.5 the results for $d = 2$ will be shown). The results of this expansion are shown in Fig. 4.13 and Table I. The value for single scattering, $\gamma_1 \equiv \gamma_s$, calculated from Eq. (4.54) is also given. It is seen that only for the very lowest orders of scattering there is some discrepancy between the values for $\gamma_{\ell,c,\infty}$ as calculated from the exact theory and the diffusion approximation. This was to be expected since a wave is only propagating diffusively after it has scattered several times. From Fig. 4.13 it is also seen that the contribution of each order of scattering is proportional to $n^{-3/2}$ for higher order scattering.

4.3.2 Analytical results for transmission

Let us now consider the transmission in the diffusion approximation. From the exact result Eq. (4.57) we can immediatly find a set of equations similar to Eqs. (4.54)-(4.56):

$$
\begin{aligned}
\tilde{\gamma}_\ell(\mu_s,\mu_i) &= \frac{1}{\mu_i}\int_0^b\int_0^b \Gamma(\tau_1,\tau_2;\alpha=0)\exp\left(\frac{\tau_1-b}{\mu_s} - \frac{\tau_2}{\mu_i}\right) d\tau_1 d\tau_2 \ , & (4.110)\\
\tilde{\gamma}_c(\mu_s,\mu_i) &= \frac{1}{\mu_i}\int_0^b\int_0^b \Gamma(\tau_1,\tau_2;\alpha)\cos\left[\frac{k_0}{\kappa}(\mu_i+\mu_s)(\tau_1-\tau_2)\right]\\
&\times \ \exp\left[-\frac{1}{2}\left(\frac{1}{\mu_i}-\frac{1}{\mu_s}\right)(\tau_1+\tau_2)\right]\exp\left(-\frac{b}{\mu_s}\right) d\tau_1 d\tau_2 \ . & (4.111)
\end{aligned}
$$

For the incoherent transmission of the slab we find for the single scattering:

$$
\tilde{\gamma}_s(\mu_s,\mu_i) = \frac{a\mu_s}{\mu_s-\mu_i}\left\{\exp\left(-\frac{b}{\mu_s}\right) - \exp\left(-\frac{b}{\mu_i}\right)\right\} \ , \tag{4.112}
$$

and for the multiple scattering

$$
\begin{aligned}
\tilde{\gamma}_\ell(\mu_s,\mu_i) &= \frac{3a^2\mu_s}{1-\mu_i^2c^2}\left[\frac{\mu_i^2}{\mu_i-\mu_s}\left\{\exp\left(-\frac{b}{\mu_s}\right) - \exp\left(-\frac{b}{\mu_i}\right)\right\}\right.\\
&+ \ \frac{P_+}{1-\mu_s c}\left\{\exp\left(-cb\right) - \exp\left(-\frac{b}{\mu_s}\right)\right\}\\
&+ \ \left.\frac{P_-}{1+\mu_s c}\exp(2c\tau_0)\left\{\exp\left(-\frac{b}{\mu_s}\right) - \exp\left(cb\right)\right\}\right] \ . & (4.113)
\end{aligned}
$$

The single scattering reduces for $\mu_i = \mu_s$ to

$$
\tilde{\gamma}_s(\mu_s = \mu_i = \mu) = \frac{ab}{\mu}\exp\left(-\frac{b}{\mu}\right) \ , \tag{4.114}
$$

and we also find the remainder of the incoming (coherent) wave

$$\tilde{\gamma}_{coh}(\mu_s = \mu_i \equiv \mu) \propto \exp\left(-\frac{b}{\mu}\right) \ . \tag{4.115}$$

We can study Eqs. (4.56) and (4.111) and find that, similarly to Eqs. (4.94) and Eqs. (4.95), we can define

$$\tilde{u} \equiv \frac{k_0}{\kappa}(\mu_i + \mu_s) \ , \tag{4.116}$$

$$\tilde{v} \equiv \frac{1}{2}\left(\frac{1}{\mu_i} - \frac{1}{\mu_s}\right) \ . \tag{4.117}$$

Now we can apply a modified version of Eq. (4.96):

$$\tilde{\gamma}_c(\mu_s, \mu_i) = \frac{1}{\mu_i}\int_0^b \int_\delta^{2b-\delta} \Gamma'(\delta, \sigma; \alpha)\cos(\tilde{u}\delta)\exp(-\tilde{v}\sigma)\exp(-b/\mu_s)d\sigma d\delta \ , \tag{4.118}$$

so that the contribution of the interference (cyclical terms) *in transmission* can with the help of Eq. (4.97) be written as

$$\tilde{\gamma}_c(\mu_s, \mu_i) = \gamma_c(-\mu_s, \mu_i; u \to \tilde{u}, v \to \tilde{v})\exp(-b/\mu_s) \ , \tag{4.119}$$

which for $\mu_s = \mu_i$ this can be shown to be

$$\tilde{\gamma}_c(\mu_s = \mu_i = \mu) = \frac{3a^2\exp(-b/\mu)}{\mu c \sinh(cB)}\left\{\frac{1 - \cosh(2c\tau_0)}{c^2 + \tilde{u}^2}\right\}\cos(\tilde{u}b) \ . \tag{4.120}$$

where $\mu_s = \mu_i = \mu \equiv \cos\theta$ implies

$$\alpha = \frac{2k_0}{\kappa}\sin\theta\cos\left(\frac{\phi_i - \phi_s}{2}\right) \ . \tag{4.121}$$

Let's examine the case where the albedo $a = 1$ and either $\phi_i = \phi_s$ (transmission in line with the incoming wave, $\alpha = (2k_0/\kappa)\sin\theta$) which gives

$$\tilde{\gamma}_c(\mu_s = \mu_i = \mu; a = 1) = \frac{3\exp(-b/\mu)}{\mu}\left\{\frac{1 - \cosh(2\alpha\tau_0)}{\alpha\sinh(\alpha B)}\right\}\left(\frac{\kappa}{k_0}\right)^2\cos(2b\frac{k_0}{\kappa}) \ , \tag{4.122}$$

or $\phi_i = \phi_s + \pi$ (the anti-specular direction, $\alpha = 0$) which gives

$$\tilde{\gamma}_c(\mu_s = \mu_i = \mu; c = 0) = -\frac{3\tau_0^2\exp(-b/\mu)}{2B\mu^3}\left(\frac{\kappa}{k_0}\right)^2\cos(2b\frac{k_0}{\kappa}) \ , \tag{4.123}$$

which is heavily damped and oscillates around zero. A negative intensity $\tilde{\gamma}_c$ should be compensated by a more positive $\tilde{\gamma}_\ell$ because the total intensity $\tilde{\gamma} = \tilde{\gamma}_\ell + \tilde{\gamma}_c$ is of course positive. The argument of the cosine, $4\pi L/\lambda$, apparently results from interference of waves

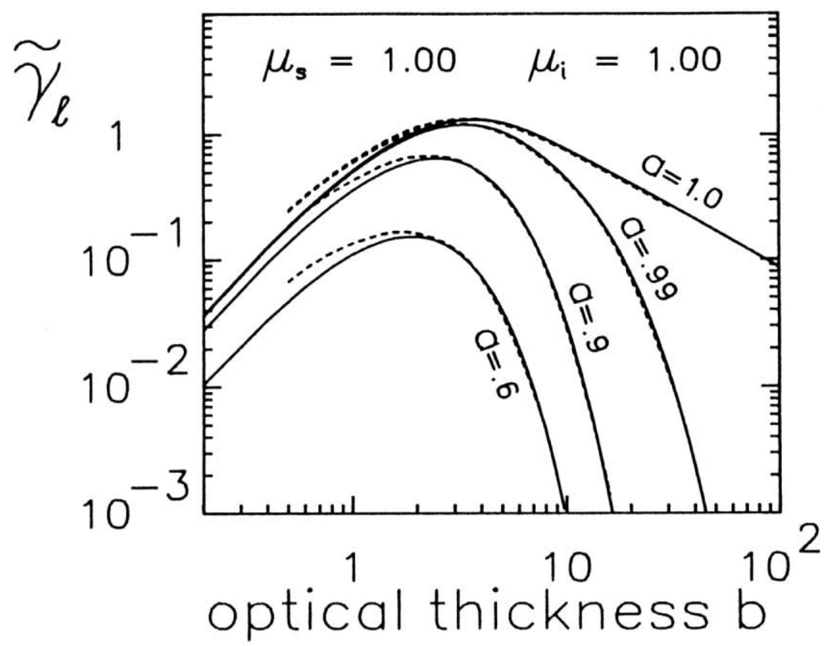

Figure 4.14: *The transmission coefficient $\tilde{\gamma}_\ell(\mu_s, \mu_i)$ with $\mu_i = \mu_s = 1$, as a function of the optical thickness b. Dashed curves represent the result from the exact theory, solid lines give the result from the diffusion approximation. Different curves correspond to different albedos.*

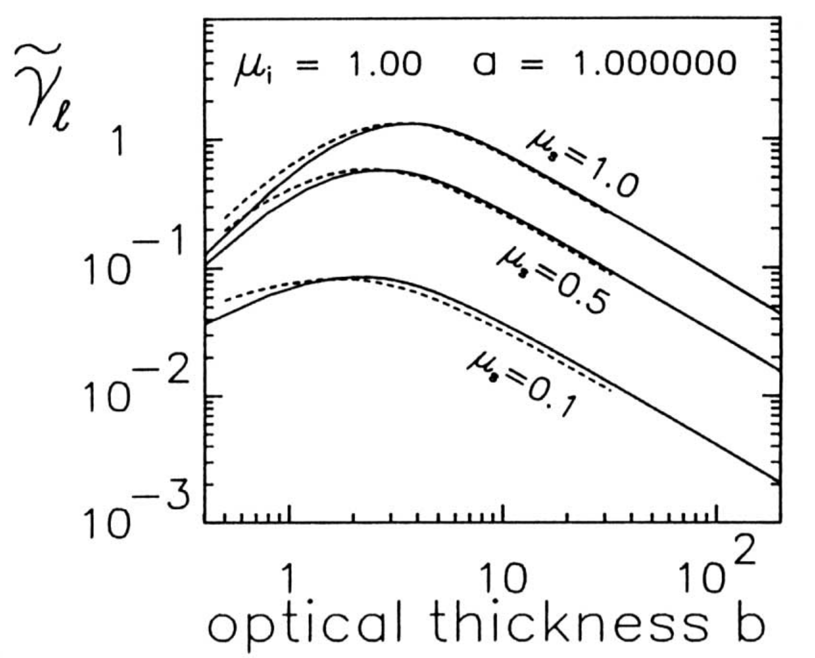

Figure 4.15: *The transmission coefficient $\tilde{\gamma}_\ell(\mu_s, \mu_i)$ with $\mu_i = 1$ and $a = 1$, as a function of the optical thickness b. Dashed curves represent the result from the exact theory, solid lines give the result from the diffusion approximation. Different curves correspond to different scattering angles.*

that have traversed the complete slab integer times, like in a Fabry-Perot interferometer. The incoherent contribution for $a = 1$ and $\mu = 1$ is

$$\begin{aligned}\tilde{\gamma}_\ell(\mu_s = \mu_i = 1; a = 1) &= \frac{3}{b + 2\tau_0}\{(\tau_0 + 1)^2 + (\tau_0 - 1)^2 \exp(-2b) \\ &- [(b + 2\tau_0)^2 + 2(1 - \tau_0^2)] \exp(-b)\} \ . \end{aligned} \tag{4.124}$$

Even for small b we find that only for $\lambda_{mf} < \lambda/4\pi$, which is far beyond the range where the diffusion approximation is expected to hold, the total intensity $\tilde{\gamma} = \tilde{\gamma}_\ell + \tilde{\gamma}_c$ can become negative.

Finally, one more limit, for $a < 1$, and $b \to \infty$:

$$\begin{aligned}\lim_{b\to\infty} \tilde{\gamma}_\ell(\mu_s, \mu_i; a < 1) &= \frac{3a^2\mu_s \exp(-cb)}{2c\,(1 - \mu_i^2 c^2)(1 - \mu_s^2 c^2)} \\ &\times \{(1 + \mu_i c) - (1 - \mu_i c)\{\exp(-2c\tau_0)\} \\ &\times \{(1 + \mu_s c) - (1 - \mu_s c)\{\exp(-2c\tau_0)\} \ , \end{aligned} \tag{4.125}$$

and for $a = 1$ we can find

$$\lim_{b\to\infty} \tilde{\gamma}_\ell(\mu_s, \mu_i; a = 1) = \frac{3\mu_s(\tau_0 + \mu_s)(\tau_0 + \mu_i)}{b + 2\tau_0} \ . \tag{4.126}$$

Remember that these equations are only valid for a close to 1. For $a \leq 2/3$, this diffusion approximation breaks down completely.

In Figs. 4.14 and 4.15 The transmission coefficient $\tilde{\gamma}_\ell(\mu_s, \mu_i)$ is shown as a function of the optical thickness b for both the diffusion theory and the exact theory. Curves are given for different albedos and scattering angles. Notice that the agreement between the rigorous theory and the diffusion theory is very good, even for thin slabs.

4.4 Time-dependent solution

It can be very useful to consider a time-dependent diffusion problem. A time-resolved light-scattering experiment with picosecond or even femtosecond resolution on strongly scattering media potentially gives the diffusion constant D ($D = c_{med}\lambda_{mf}/d$, with c_{med} the speed of light in the medium, and d the dimension). To actually determine D, a detailed theory is indispensable. As will become clear to the careful reader, a time-resolved experiment is a powerful tool in the determination of several properties of a random medium, in which one for example can characterize both λ_{tr}, and λ_{abs} in a single measurement.

Consider an infinite, lossless random medium, then it is well known, that the probability $P(\vec{r}, t)$ to diffuse over a distance r in a given time t is in arbitrary dimension d represented by

$$P(\vec{r}, t) = \frac{1}{(4\pi Dt)^{d/2}} \exp\left(\frac{-r^2}{4Dt}\right) \ , \tag{4.127}$$

with normalized probability:

$$\int_{-\infty}^{\infty} P(\vec{r},t)\, d\vec{r} = 1 \ . \tag{4.128}$$

The probability to come to any point at a distance r in arbitrary time is given by

$$\int_0^{\infty} P(\vec{r},t)\, dt \equiv P(\vec{r}\,) = \int_0^{\infty} \frac{s^{(d-4)/2}}{(4\pi D)^{d/2}} \exp\left(\frac{-r^2 s}{4D}\right)\, ds \ , \tag{4.129}$$

with the substitution $s = t^{-1}$. For $d = 3$ we can now calculate this integral and identify $P(\vec{r}\,)$ with $F_0(\vec{r}\,)$ from the diffusion theory of Sect. 4.3 (see Eq. (4.73)), for the albedo $a = 1$:

$$P(\vec{r}\,) = \frac{1}{4\pi D r} = \frac{F_0(\vec{r}\,)}{4\pi\kappa^2 c_{med}} \ , \tag{4.130}$$

but for $d = 2$ and $d = 1$ the integral (4.129) diverges. This problem can however be solved by putting some absorption term in Eq. (4.127). The absorption length is large compared to the mean free path, and therefore the propagation in the medium will still be diffusive. So we will try

$$P(\vec{r},t) = \frac{a^2}{(4\pi D t)^{d/2}} \exp\left(\frac{-r^2}{4Dt}\right) \exp\left(-Dt\kappa_a^2\right) \ , \tag{4.131}$$

which will appear to describe our problem correctly. By using (see 3.471 in Ref. 82) the identity

$$\int_0^{\infty} x^{\nu-1} e^{-\beta x - \gamma/x} dx = 2\left(\frac{\gamma}{\beta}\right)^{\nu/2} K_\nu(2\sqrt{\beta\gamma}) \ , \tag{4.132}$$

with K_ν the Bessel function of imaginary argument, we find for dimension $d = 3$, but now also for $d = 2$ and $d = 1$ respectively:

$$P_3(\vec{r}\,) = \frac{a^2}{4\pi D r} \exp\left(-\kappa_a r\right) \ , \tag{4.133}$$

$$P_2(\vec{r}\,) = \frac{a^2}{2\pi D} K_0(\kappa_a r) \ , \tag{4.134}$$

$$P_1(\vec{r}\,) = \frac{a^2}{2\kappa_a D} \exp\left(-\kappa_a r\right) \ . \tag{4.135}$$

For $d = 3$, we can see that Eq. (4.130) is in agreement with Eq. (4.73), also for $a \neq 1$. By employing Eq. (4.31), we take the Fourier transform in the translation-invariant directions and find the Green's function for the infinite space

$$\Gamma_0(\tau;\alpha;t) = c_{med} \int P(\vec{r}_\perp, z, t) \exp(-i\vec{r}_\perp \cdot \vec{q}_\perp) d\vec{r}_\perp \ . \tag{4.136}$$

For $d = 3$ this results in

$$\Gamma_0(\tau;\alpha;t) = \frac{a^2}{t_{mf}} \sqrt{\frac{3}{4\pi t}} \exp\left(-\frac{c^2 t}{3}\right) \exp\left(-\frac{3\tau^2}{4t}\right) \ , \tag{4.137}$$

where the time t is made dimensionless and with $t_{mf} \equiv \lambda_{mf}/c_{med} = (\kappa c_{med})^{-1}$ the mean free-propagation time, c_{med} the speed of light in the medium, and $c \equiv \sqrt{\alpha^2 + 3(1-a)}$.

Resuming, I have made a short cut by using $P(\vec{r},t)$ to obtain an expression for the propagator Γ which we are familiar with from the previous sections. In the previous derivation the time dependence of $\langle G\rangle\langle G^*\rangle$, which we do have to know for the incoming and scattered light from the slab, was not considered. Another problem is the possible retardation in time of the mirror images, which are needed to describe the *finite* slab (Eqs. (4.77) and (4.78)). There is also an intrinsic problem with the time in Γ because Γ allows that there is always (usually very little) probability to propagate in a time t less than r/c_{med} over a distance r. This will however appear to give no big problems.

The first problem is not so hard to solve, because we already assumed that $K' \simeq k_0$, or equivalently $c_{med} = c_{vac}/n_{empty}$, so the retardation when the light is propagating from the last scatterer towards the boundary, or from the boundary to the first scatterer is respectively $t_s = t_{mf}\tau_1/\mu_s$ and $t_i = t_{mf}\tau_2/\mu_i$.

The second problem, about the time dependence of the boundary images, is not known from the literature, and only recently came to my mind. This problem will however surely become less important for thicker slabs. Since we are, from an experimentalist's point of view, mainly interested in thick slabs and the long time behavior of the transmitted light, I will continue by assuming that the mirror images of the trapping planes are *not* time dependent. With this assumption we find

$$\begin{aligned}\Gamma(\tau_1,\tau_2;\alpha;t) &= \frac{a^2}{t_{mf}}\sqrt{\frac{3}{4\pi t}}\exp\left(-\frac{c^2t}{3}\right) \\ &\times \sum_{n=-\infty}^{\infty}\left\{\exp\left[-\frac{3}{4t}\left(\tau_1-\tau_2-2nB\right)^2\right]\right. \\ &\qquad - \left.\exp\left[-\frac{3}{4t}\left(\tau_1+\tau_2+2nB+2\tau_0\right)^2\right]\right\} . \qquad (4.138)\end{aligned}$$

Integration over the time of Eq. (4.138) indeed gives back Eq. (4.78). After some thought, or by just finding out by putting this equation in a computer, one will find that the long time behavior should give an exponential decay, except for the backscattering of a half-infinite, lossless medium where it should be proportional to $t^{-3/2}$. Analytically we can find the limit for large t by using Poisson's sum rule (see also Ref. 85):

$$\sum_{n=-\infty}^{\infty}\exp[-(nx+y)^2] = \frac{\sqrt{\pi}}{x}\sum_{n=-\infty}^{\infty}\exp\left(2\pi i\frac{ny}{x}\right)\exp\left(-\frac{\pi^2n^2}{x^2}\right) . \qquad (4.139)$$

So Eq. (4.138) can be transformed to

$$\begin{aligned}\Gamma(\tau_1,\tau_2;\alpha;t) &= \frac{a^2}{t_{mf}B}\exp\left(-\frac{c^2t}{3}\right) \\ &\times \sum_{n=1}^{\infty}\left\{\exp\left(-\frac{\pi^2n^2}{3B^2}t\right)\left[\cos\left(\frac{\tau_1-\tau_2}{B}\pi n\right)-\cos\left(\frac{\tau_1+\tau_2+2\tau_0}{B}\pi n\right)\right]\right\} , \qquad (4.140)\end{aligned}$$

which for $n=1$ indeed gives the long time behavior for a finite slab analytically.

We can use the previously derived Eqs. (4.55), (4.56), (4.110) and (4.111) to calculate the transmitted and backscattered intensities as a function of time. Define the dimensionless time $\hat{t}$ to travel from the starting boundary to the final boundary:

$$\hat{t} = t + \tau_1/\mu_s + \tau_2/\mu_i \ , \tag{4.141}$$

Since finding an analytical solution for the time-dependent transmitted or backscattered intensity is hard, or at least will result in some complicated expressions containing error functions, one more approximation should be made. I will assume that all diffusive light paths will start and stop at a depth λ_{mf} under the surface of the medium, something that in an other context was already done in Ref. 69

Take $\tau_1 = 1$ and $\tau_2 = 1$ in the Γ of Eqs. (4.55), (4.56), (4.110) and (4.111), we find for backscattering

$$\begin{aligned}
\gamma_\ell(\mu_s, \mu_i; \hat{t}\,) &\simeq \frac{1}{\mu_i}\Gamma(\tau_1 = 1, \tau_2 = 1; \alpha = 0; t) \int_0^b \int_0^b \exp\left(-\frac{\tau_1}{\mu_s} - \frac{\tau_2}{\mu_i}\right) d\tau_1 d\tau_2 \\
&= \mu_s[1 - \exp(-b/\mu_i)][1 - \exp(-b/\mu_s)]\Gamma(\tau_1 = 1, \tau_2 = 1; \alpha = 0; t) \ , \qquad (4.142) \\
\gamma_c(\mu_s, \mu_i; \hat{t}\,) &\simeq \frac{1}{\mu_i}\Gamma(\tau_1 = 1, \tau_2 = 1; \alpha; t) \int_0^b \int_0^b \cos\left[\frac{k_0}{\kappa}(\mu_i - \mu_s)(\tau_1 - \tau_2)\right] \\
&\quad \times \ \exp\left[-\frac{1}{2}\left(\frac{1}{\mu_i} + \frac{1}{\mu_s}\right)(\tau_1 + \tau_2)\right] d\tau_1 d\tau_2 \\
&= \frac{\mu_i^{-1}}{u^2 + v^2}[1 + \exp(-2vb) - 2\cos(ub)\exp(-vb)] \\
&\quad \times \ \Gamma(\tau_1 = 1, \tau_2 = 1; \alpha; t) \ , \qquad (4.143)
\end{aligned}$$

and with $\tau_1 = b - 1$ and $\tau_2 = 1$ for transmission

$$\begin{aligned}
\tilde{\gamma}_\ell(\mu_s, \mu_i; \hat{t}\,) &\simeq \frac{1}{\mu_i}\Gamma(\tau_1 = b - 1, \tau_2 = 1; \alpha = 0; t) \int_0^b \int_0^b \exp\left(\frac{\tau_1 - b}{\mu_s} - \frac{\tau_2}{\mu_i}\right) d\tau_1 d\tau_2 \\
&= \mu_s[1 - \exp(-b/\mu_i)][1 - \exp(-b/\mu_s)]\Gamma(\tau_1 = b - 1, \tau_2 = 1; \alpha = 0; t) \ , \qquad (4.144) \\
\tilde{\gamma}_c(\mu_s, \mu_i; \hat{t}\,) &\simeq \frac{1}{\mu_i}\Gamma(\tau_1 = b - 1, \tau_2 = 1; \alpha; t) \int_0^b \int_0^b \cos\left[\frac{k_0}{\kappa}(\mu_i + \mu_s)(\tau_1 - \tau_2)\right] \\
&\quad \times \ \exp\left[-\frac{1}{2}\left(\frac{1}{\mu_i} - \frac{1}{\mu_s}\right)(\tau_1 + \tau_2)\right] \exp\left(-\frac{b}{\mu_s}\right) d\tau_1 d\tau_2 \\
&= \frac{\mu_i^{-1}}{\tilde{u}^2 + \tilde{v}^2}[\exp(-b/\mu_i) + \exp(-b/\mu_s) - 2\cos(\tilde{u}b)\exp(-\tilde{v}b)] \\
&\quad \times \ \Gamma(\tau_1 = b - 1, \tau_2 = 1; \alpha; t) \ . \qquad (4.145)
\end{aligned}$$

For single scattering this approximation is certainly wrong but also not necessary to make. It is obvious that the total propagation time through the slab for a single scattering event at optical depth τ is given by

$$\begin{aligned}
\hat{t} &= \tau(\mu_s^{-1} + \mu_i^{-1}) \ , \qquad (4.146) \\
\hat{t} &= (b - \tau)\mu_s^{-1} + \tau\mu_i^{-1} \ , \qquad (4.147)
\end{aligned}$$

for reflection and transmission respectively.

As is seen from this example for single scattering, one should notice, that except for $\vec{K}_s \simeq \vec{K}_i$, some additional dispersion in the *detected* signal is found due to the difference in travel time towards and/or from the slab between different regions in the slab. For slabs with thickness comparable to the width of the illuminated area by the incident beam, this is however always negligible.

Let us now come back to Eqs. (4.138) and (4.140). With $\tau_1 = \tau_2 = 1$ for backscattering we find

$$\begin{aligned}
\Gamma(\tau_1 = 1, \tau_2 = 1; \alpha; t) = & \frac{a^2}{t_{mf}}\sqrt{\frac{3}{4\pi t}} \exp\left(-\frac{c^2 t}{3}\right) \\
& \times \sum_{n=-\infty}^{\infty} \left\{ \exp\left[-\frac{3}{4t}\left(2nB\right)^2\right] - \exp\left[-\frac{3}{4t}\left(2nB + 2(1+\tau_0)\right)^2\right] \right\} \\
= & \frac{a^2}{t_{mf} B} \exp\left(-\frac{c^2 t}{3}\right) \\
& \times \sum_{n=1}^{\infty} \left\{ \exp\left(-\frac{\pi^2 n^2}{3B^2} t\right) \left[1 - \cos\left(\frac{1+\tau_0}{B} 2\pi n\right)\right] \right\} \ ,
\end{aligned} \tag{4.148}$$

and with $\tau_1 = b - 1$ and $\tau_2 = 1$ for transmission we find

$$\begin{aligned}
\Gamma(\tau_1 = b-1, \tau_2 = 1; \alpha; t) = & \frac{a^2}{t_{mf}}\sqrt{\frac{3}{4\pi t}} \exp\left(-\frac{c^2 t}{3}\right) \\
& \times \sum_{n=-\infty}^{\infty} \left\{ \exp\left[-\frac{3}{4t}\left(2nB - 2(1+\tau_0)\right)^2\right] - \exp\left[-\frac{3}{4t}\left(2nB\right)^2\right] \right\} \\
= & \frac{a^2}{t_{mf} B} \exp\left(-\frac{c^2 t}{3}\right) \\
& \times \sum_{n=1}^{\infty} \left\{ (-1)^{n-1} \exp\left(-\frac{\pi^2 n^2}{3B^2} t\right) \left[1 - \cos\left(\frac{1+\tau_0}{B} 2\pi n\right)\right] \right\} \ ,
\end{aligned} \tag{4.149}$$

From here I will consider some special cases and limits. First of all let us take a look at backscattering from an half-infinite medium, $b = \infty$ in the limit $t \to \infty$. Using Eq. (4.142) and Eq. (4.148), from which only the term for $n = 0$ survives, and taking for convenience $\mu_s = \mu_i = 1$, we get

$$\begin{aligned}
\gamma_{\ell,\infty}(\mu_s = \mu_i = 1; \hat{t} \to \infty) &= \lim_{t\to\infty} \frac{a^2}{t_{mf}}\sqrt{\frac{3}{4\pi t}} \exp\left[(a-1)t\right] \\
& \qquad \times \left\{ 1 - \exp\left(\frac{3}{2t}(1+\tau_0)^2\right) \right\} \\
&= \frac{3a^2}{t_{mf}}(1+\tau_0)^2 \sqrt{\frac{3}{4\pi}} \exp\left[(a-1)t\right] \, t^{-3/2} \ ,
\end{aligned} \tag{4.150}$$

so indeed for $a = 1$ there is a $t^{-3/2}$ relation. The long time behavior for a *finite* slab in backscattering is the same as in transmission, and follows from Eq. (4.144) and the term

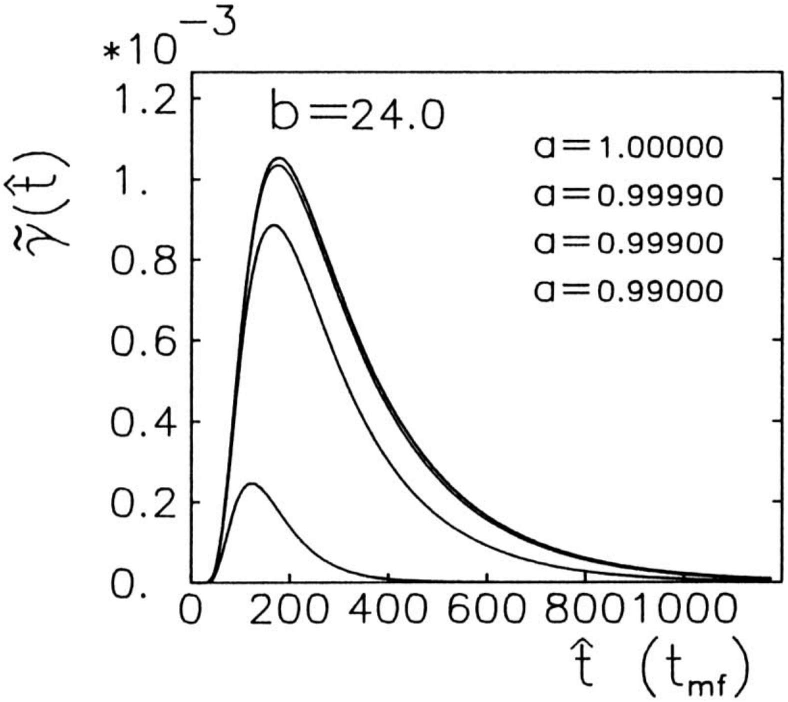

Figure 4.16: *Typical plot of $\tilde{\gamma}(\hat{t})$ on a linear scale versus time for an optical slab thickness $b = 24$ and four values of the albedo a; highest curve: $a = 1$, lowest curve $a = 0.99$*

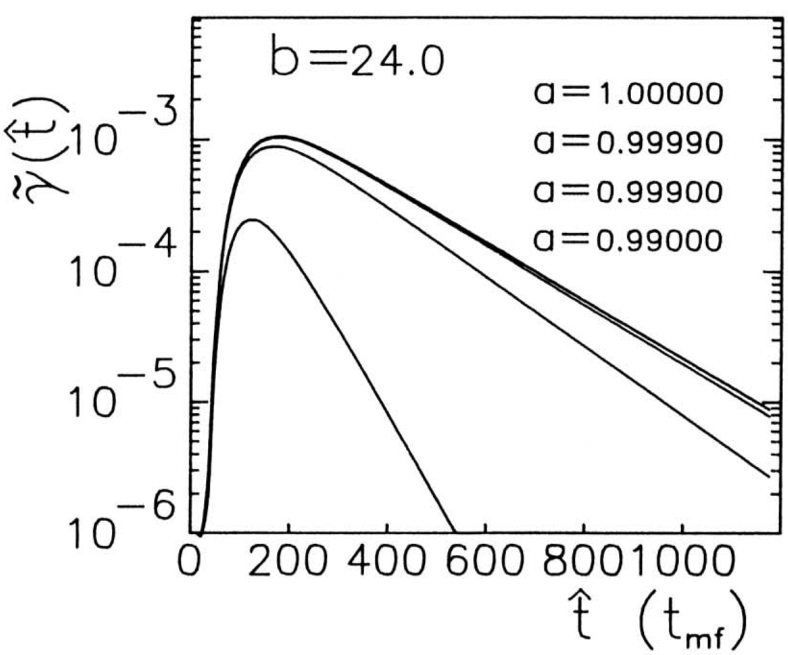

Figure 4.17: *Typical plot of $\tilde{\gamma}(\hat{t})$ on a logarithmic scale versus time for an optical slab thickness $b = 24$ and four values of the albedo a; highest curve: $a = 1$, lowest curve $a = 0.99$*

for $n = 1$ of Eq. (4.148) or Eq. (4.149):

$$\begin{aligned}\gamma_\ell(\mu_s = \mu_i = 1; \hat{t} \to \infty) &= \frac{a^2}{t_{mf} B} \exp\left[(a-1)t\right]\left[1 - \exp(-b)\right]^2 \\ &\times \left\{\left[1 - \cos\left(\frac{1+\tau_0}{B} 2\pi\right)\right] \exp\left(-\frac{\pi^2}{3B^2} t\right)\right\} . \end{aligned} \tag{4.151}$$

which gives an exponential decay with exponent

$$-\frac{1}{T} = \left(\frac{-\pi^2}{3B^2} + a - 1\right)\frac{1}{t_{mf}} = -D\left(\frac{\pi^2}{(L+2z_0)^2} + \frac{1}{\lambda_{abs}^2}\right) . \tag{4.152}$$

In Figs. 4.16 and 4.17 a typical plot for the transmitted intensity, linear and logarithmic scale respectively, versus time is given for four values of the albedo. Experimentally it is possible to extract from the exponential decay in combination with the time delay of the top of the curve, both the diffusion constant D and the albedo a. The best way to do this is by fitting a theoretical curve to the experimental one (see Sect. 5.4.2).

It sometimes is convenient to know the average time delay received by the transmitted light. The first moment of the curve for $a = 1$ is given by

$$\langle \hat{t} \rangle \simeq \frac{\int t\tilde{\gamma}(t)\, dt}{\int \tilde{\gamma}(t)\, dt} = \frac{1}{2}(b + 2\tau_0)^2 - (1+\tau_0)^2 . \tag{4.153}$$

From the previous equations we should notice that $L + 2z_0$, the distance between the trapping planes, is apparently more important than the slab thickness L.

4.5 Theory for d=2

From the previous section (see Eq. (4.131)) we know already that

$$P(\vec{r}, t) = \frac{a^2}{4\pi D t} \exp\left(\frac{-r^2}{4Dt}\right) \exp\left(-Dt\kappa_a^2\right) , \tag{4.154}$$

for which the stationary diffusion problem is described by Eq. (4.134)

$$P(\vec{r}) = \frac{a^2}{2\pi D} K_0(\kappa_a r) , \tag{4.155}$$

with $D = c_{med}\lambda_{mf}/2$ and $\kappa_a^2 = 2\kappa^2(1-a)$.

The stationary problem can also be solved from summation of all ladder and cyclical diagrams as was done in Sect. 4.2.2 and then take the diffusion approach of Sect. 4.3.

First we consider a scattering medium of infinite size and take advantage of the translational invariance in all directions. The two-dimensional Fourier transform is

$$F(\vec{r}_1, \vec{r}_2) \equiv F_0(\vec{r}_1 - \vec{r}_2) \equiv F_0(\vec{r}\,) \equiv (2\pi)^{-2} \int F_0(\vec{q}\,) \exp(i\vec{r} \cdot \vec{q}\,) d\vec{q} . \tag{4.156}$$

With the two-dimensional equivalent of Eq. (4.24) we can find

$$F_0(\vec{q}) = \frac{k_0 a\kappa}{\pi^2} A(\vec{q}) F_0(\vec{q}) + \left(\frac{2k_0 a\kappa}{\pi}\right)^2 A(\vec{q}) \ , \tag{4.157}$$

with the help of the scattering operator

$$S_\alpha(\vec{r}_1, \vec{r}_2) = -4k_0 f \delta(\vec{r}_1 - \vec{r}_\alpha)\delta(\vec{r}_2 - \vec{r}_\alpha) \ , \tag{4.158}$$

so that

$$F_0(\vec{r}) = \left(\frac{2k_0 a\kappa}{\pi}\right)^2 (2\pi)^{-2} \int \frac{A(\vec{q})}{1 - k_0 a\kappa A(\vec{q})/\pi^2} \exp(i\vec{r}\cdot\vec{q}) d\vec{q} \ . \tag{4.159}$$

With $\langle G \rangle = -(2\pi)^{-1} K_0(-iKr)$ (in accordance with Eq. (3.5)), and $K = k_0 + i\kappa/2$, $A(\vec{q})$ can be calculated as

$$\begin{aligned} A(\vec{q}) &= \int A(\vec{r}) \exp(-i\vec{r}\cdot\vec{q}) d\vec{r} \\ &= 2\pi \int_0^\infty K_0(-iKr) K_0(iK^* r) J_0(rq) r dr \\ &\simeq \frac{\pi^2}{k_0} \times \frac{1}{\sqrt{\kappa^2 + q^2}} \ , \end{aligned} \tag{4.160}$$

where I used the far-field approximation:

$$K_0(-ikr) \simeq i\sqrt{\frac{\pi}{2kr}} \exp[i(kr - \pi/4)] \ , \quad kr \to \infty \tag{4.161}$$

and also $\sqrt{k_0^2 + \kappa^2/4} \simeq k_0$, because $\kappa \ll k_0$. Substituting the result (4.160) in (4.159) performing the angular integration, and with $\kappa_a^2 = 2\kappa^2(1-a)$ gives

$$F_0(\vec{r}) = \frac{4k_0 a^2 \kappa^3}{\pi} \int_0^\infty \frac{q}{q^2 + \kappa_a^2} J_0(qr) dq = \frac{4k_0 a^2 \kappa^3}{\pi} K_0(\kappa_a r) \ , \tag{4.162}$$

with $q/\sqrt{\kappa^2 + q^2} \simeq q\kappa/(\kappa^2 + q^2/2)$ for $q < \kappa$, which provides a useful cut-off for $q > \kappa$. If we compare Eq. (4.162) and Eq. (4.155) we find

$$P(\vec{r}) = \frac{F_0(\vec{r})}{4k_0 \kappa^2 c_{med}} \ . \tag{4.163}$$

While employing this equation, we take the Fourier transform in the translation-invariant direction and find Γ_0, the Green's function for the infinite space

$$\Gamma_0(\tau; \alpha) = c_{med} \int P(r_\perp, z) \exp(-ir_\perp q_\perp) dr_\perp \ . \tag{4.164}$$

This gives with Eq. (4.155) (see also Ref. 82, formula 6.677):

$$\begin{aligned} \Gamma_0(\tau; \alpha) &= \frac{a^2 \kappa}{\pi} \int K_0\left(-\kappa_a \sqrt{r_\perp^2 + z^2}\right) \exp\left(-ir_\perp q_\perp\right) dr_\perp \\ &= \frac{a^2}{c} \exp(-c\tau) \ , \end{aligned} \tag{4.165}$$

where c_{med} is the speed of light in the medium, and $c = \sqrt{\alpha^2 + 2(1-a)}$, with for backscattering

$$\alpha = \frac{k_0}{\kappa} |\sin\theta_i - \sin\theta_s| \ , \tag{4.166}$$

and for transmission

$$\alpha = \tilde{\alpha} = \frac{k_0}{\kappa} |\sin\theta_i + \sin\theta_s| \ . \tag{4.167}$$

Introducing trapping planes in the usual way (see Eq. (4.78)), performing the summation, and with once more the defenitions (4.80)-(4.84) we get the Green's function Γ' in closed form

$$\Gamma'(\delta, \sigma; \alpha) = \frac{a^2}{c \sinh(cB)} \{\cosh[c\,(B - |\delta|)] - \cosh[c\,(b - \sigma)]\} \ , \tag{4.168}$$

with the only differences compared to the $d = 3$ result Eq. (4.85) that $\tau_0 \simeq 0.8$ (see Ref. 95), and a prefactor 2/3.

From Eq. (4.154) we can of course find the time-dependent solution as well. By employing Eq. (4.31) again, we take the Fourier transform in the translation-invariant direction and find the Green's function for the infinite space

$$\Gamma_0(\tau; \alpha; t) = c_{med} \int P(r_\perp, z, t) \exp(-i r_\perp q_\perp) dr_\perp \ , \tag{4.169}$$

this results in

$$\Gamma_0(\tau; \alpha; t) = \frac{a^2}{t_{mf}} \sqrt{\frac{1}{2\pi t}} \exp\left(-\frac{c^2 t}{2}\right) \exp\left(-\frac{\tau^2}{2t}\right) \ , \tag{4.170}$$

which is, like the stationary solution, very similar to the result for $d = 3$. The time t is made dimensionless and with $t_{mf} = \lambda_{mf}/c_{med} = (\kappa c_{med})^{-1}$, the mean free propagation time. To find the time-dependent solution of a *finite* medium, we have to perform the trapping plane trick again. The answer is certainly similar to that of $d = 3$, so I will now concentrate on the radiated intensities from the two-dimensional slab.

For the intensity we need Eq. (4.39) again. The propagation constant in the medium is again given by $K \equiv K' + iK''$, and I will again use the weakly scattering limit, $K'' \ll K' \simeq k_0$. The mean-field amplitude function from the incoming wave in the medium is

$$\langle \Psi_{inc}(\vec{r}_1) \rangle = \exp(i\vec{K}_i \cdot \vec{r}_1) \ , \tag{4.171}$$

where $\vec{K}_i$ is a vector with magnitude K and direction of the incoming wave in the medium. For $K'' \ll K' \simeq k_0$ and almost normal incidence (θ_i small), $\vec{K}_i$ can be approximated by

$$\vec{K}_i = \hat{x} k_0 \sin\theta_i + \hat{z} K_{iz} \ , \tag{4.172}$$

$$K_{iz} = \sqrt{K^2 - k_0^2 \sin^2\theta_i} \simeq k_0 \cos\theta_i + \frac{iK''}{\cos\theta_i} \ . \tag{4.173}$$

The mean Green's function using (4.161) is given by

$$\langle G(\vec{r}_1 - \vec{r}_2)\rangle = -\frac{i\exp(iK|\vec{r}_1 - \vec{r}_2| - i\pi/4)}{\sqrt{8\pi K|\vec{r}_1 - \vec{r}_2|}} \ , \tag{4.174}$$

when $\vec{r}_1$ and $\vec{r}_2$ are inside the slab, and, for backscattering

$$\langle G_B(\vec{r}_1, \vec{r}_2)\rangle \simeq -\frac{(1+i)\exp(ik_0 r_1)}{4\sqrt{\pi k_0 r_1}} \exp(-i\vec{K}_{s,B}\cdot\vec{r}_2) \ , \tag{4.175}$$

when $\vec{r}_2$ is in the slab, and when $\vec{r}_1$ is far outside the slab, and where the outgoing wave vector for backscattering $\vec{K}_{s,B}$ is given approximately by

$$\vec{K}_{s,B} = \hat{x}k_0\sin\theta_s - \hat{z}K_{sz} \ , \tag{4.176}$$

$$K_{sz} \simeq k_0\cos\theta_s + \frac{iK''}{\cos\theta_s} \ . \tag{4.177}$$

For transmission through the slab we similarly find

$$\langle G_T(\vec{r}_1, \vec{r}_2)\rangle \simeq -\frac{(1+i)\exp(ik_0 r_1)}{4\sqrt{\pi k_0 r_1}} \exp(-i\vec{K}_{s,T}\cdot\vec{r}_2)\exp(-K''L/\cos\theta_s) \ . \tag{4.178}$$

The outgoing wave vector for transmission $\vec{K}_{s,T}$ is given approximately by

$$\vec{K}_{s,T} = \hat{x}k_0\sin\theta_s + \hat{z}K_{sz} \ . \tag{4.179}$$

The scattered intensity is again described with the help of the so-called bistatic scattering coefficient γ

$$\gamma(\mu_s, \mu_i) \equiv \frac{2\pi r}{L_\perp \mu_i} I(\vec{r}) \ , \tag{4.180}$$

where $L_\perp$ is the width of the target, and $\mu_{i,s} \equiv \cos\theta_{i,s}$. We can calculate the separate contributions to $\langle R\rangle$, where we separate out the single scattering $\langle \ell\rangle$, $\langle L\rangle$ is given by Eq. (4.21), and $\langle C\rangle$ given by Eq. (4.23). By employing Eqs. (4.171) and (4.176) in Eq. (4.39) gives for the backscattering

$$\begin{aligned} I(r)_{L,C} \ &= \ \frac{1}{8\pi r k_0}\int \exp\{i[q_{\perp,i}(r_{2,\perp} - r_{4,\perp}) - q_{\perp,s}(r_{1,\perp} - r_{3,\perp})]\} \\ &\times \ \exp\{ik_0[\mu_i(z_2 - z_4) + \mu_s(z_1 - z_3)]\} \times \exp\left[-\frac{\kappa}{2}\left(\frac{z_2 + z_4}{\mu_i} + \frac{z_1 + z_3}{\mu_s}\right)\right] \\ &\times \ F(\vec{r}_1, \vec{r}_2)\delta(\vec{r}_{1,2} - \vec{r}_3)\delta(\vec{r}_{2,1} - \vec{r}_4)d\vec{r}_1 d\vec{r}_2 d\vec{r}_3 d\vec{r}_4 \ , \end{aligned} \tag{4.181}$$

We define $q_\perp = q_{\perp,i} + q_{\perp,s}$, $r_\perp = r_{1,\perp} - r_{2,\perp}$, and $R_\perp = (r_{1,\perp} + r_{2,\perp})/2$ and then, with the renormalisation from the illuminated width of the slab

$$L_\perp = \int dR_\perp \ , \tag{4.182}$$

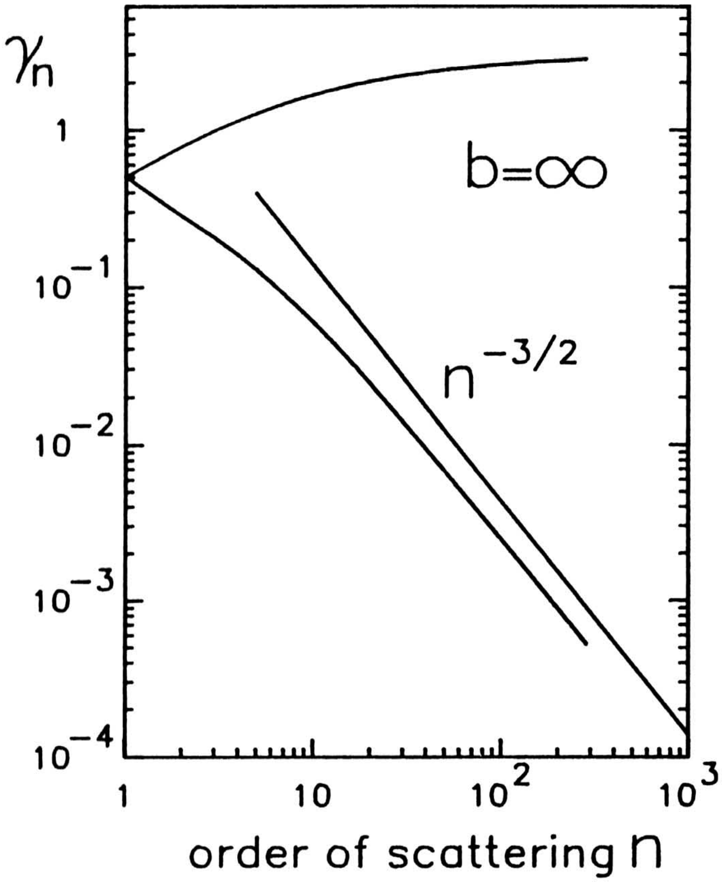

Figure 4.18:

The n^{th} order scattering contribution to the intensity γ in case $b = \infty$, $a = 1$ and $\mu_i = \mu_s = 1$ for the $d = 2$ diffusion approximation. The convergence of the high-order scattering to the $n^{-3/2}$ asymptote is clear. The cumulative curve $\sum_n \gamma_n$ is also given.

and definition (4.163)

$$\Gamma(\tau_1, \tau_2; \alpha) \equiv \frac{1}{4k_0\kappa^2} F(\vec{q}_\perp, z_1, z_2) \ , \tag{4.183}$$

we find:

$$\gamma_s(\mu_s, \mu_i) = \frac{a\mu_s}{\mu_i + \mu_s} \left\{ 1 - \exp\left[-b \left(\frac{1}{\mu_i} + \frac{1}{\mu_s} \right) \right] \right\} \ , \tag{4.184}$$

$$\gamma_\ell(\mu_s, \mu_i) = \frac{1}{\mu_i} \int_0^b \int_0^b \Gamma(\tau_1, \tau_2; \alpha = 0) \exp\left[-\left(\frac{\tau_1}{\mu_s} + \frac{\tau_2}{\mu_i} \right) \right] d\tau_1 d\tau_2 \ , \tag{4.185}$$

$$\gamma_c(\mu_s, \mu_i) = \frac{1}{\mu_i} \int_0^b \int_0^b \Gamma(\tau_1, \tau_2; \alpha) \cos\left[\frac{k_0}{\kappa} (\mu_i - \mu_s)(\tau_1 - \tau_2) \right] \times \exp\left[-\frac{1}{2} \left(\frac{1}{\mu_i} + \frac{1}{\mu_s} \right) (\tau_1 + \tau_2) \right] d\tau_1 d\tau_2 \ . \tag{4.186}$$

For the transmission of the slab we find by using (4.178) instead of (4.176):

$$\tilde{\gamma}_s(\mu_s, \mu_i) = \frac{a\mu_s}{\mu_i + \mu_s} \left\{ 1 - \exp\left[b \left(\frac{1}{\mu_s} - \frac{1}{\mu_i} \right) \right] \right\} \ , \tag{4.187}$$

$$\tilde{\gamma}_\ell(\mu_s, \mu_i) = \frac{1}{\mu_i} \int_0^b \int_0^b \Gamma(\tau_1, \tau_2; \tilde{\alpha} = 0) \exp\left(\frac{\tau_1 - b}{\mu_s} - \frac{\tau_2}{\mu_i} \right) d\tau_1 d\tau_2 \ , \tag{4.188}$$

$$\tilde{\gamma}_c(\mu_s, \mu_i) = \frac{1}{\mu_i} \int_0^b \int_0^b \Gamma(\tau_1, \tau_2; \tilde{\alpha}) \cos\left[\frac{k_0}{\kappa} (\mu_i + \mu_s)(\tau_1 - \tau_2) \right]$$

$$\times \ \exp\left[-\frac{1}{2}\left(\frac{1}{\mu_i}-\frac{1}{\mu_s}\right)(\tau_1+\tau_2)\right]\exp\left(-\frac{b}{\mu_s}\right)d\tau_1 d\tau_2 \ . \quad (4.189)$$

Comparing these equations to their three-dimensional equivalents, we see that there are only two minor differences between them, namely in the quantity c, which contains the dimension d, and, for the diffusion approximation, in the value of τ_0. The results for the width of the coherent-backscattering peak are therefore about the same for $d = 2$ and $d = 3$.

As we did for $d = 3$, we can decompose the results of the diffusion theory in a summation of terms in which each term describes the next order of scattering. In Eqs.(4.102)-(4.109) of Sect. 4.3.1, we only have to take $c = \sqrt{2}$, and $\tau_0 \simeq 0.8$. The results of this expansion are shown in Fig. 4.18. This figure shows that the contribution of each order of scattering for $d = 2$ is proportional to $n^{-3/2}$ for higher order scattering, as it was for $d = 3$.

4.6 Contribution of some special diagrams

In this section I will look somewhat closer to some contributions to the scattering which we have neglected until now. First of all, we neglected all but the simplest contributions to the self-energie Σ. In Fig. 4.2 two of these higher-order terms are depicted. These terms correspond essentially to non-self avoiding walks, in other words, the wave returns to a scatterer once, or many times. Because the wave returns, we have named these terms *boomerang* terms. Anderson localization is concerned with the enhanced backscattering to the point of origin, which is precisely what the boomerang processes are about. Therefore boomerang processes must be very important for strong localization. It will appear that their relative contribution to the total amount of scattering is dependent on the density of scatterers.

Further, we have neglected cross terms between $\langle L\rangle$ and $\langle C\rangle$ in the calculation of the reducible vertex $\langle R\rangle$ from the irreducible vertex $\langle U\rangle$, which give diagrams of the type shown in Fig. 4.19. These diagrams are generally expected to have little dependence of the intensity on the angle of scattering and thus possibly play a part in "the problem about the factor of 2", which will be discussed in Chapter 5. I will only show how to calculate the first diagram shown in Fig. 4.19, a three-particle diagram, which I will denote by $R_{mix,\mathrm{XI}}$.

Before doing so, I will first adopt a shorter notation for the scattering operator Eq. (4.20):

$$S_\alpha(\vec{r}_1,\vec{r}_2) = -4\pi f\delta_{1\alpha}\delta_{\alpha 2} \ , \qquad (4.190)$$

and for the averaged Green's function in the medium Eq. (4.6)

$$G(\vec{r}_1-\vec{r}_2) \equiv G_{12} = G_{21} \ . \qquad (4.191)$$

Using Eqs. (4.190), (4.191), and (4.16), $\langle R_{mix,\mathrm{XI}}\rangle$ looks in its mathematical form like

$$\begin{aligned}\langle R_{mix,\mathrm{XI}}\rangle &= \langle(-4\pi f)^3\delta_{2\alpha}\delta_{\alpha u}G_{uv}\delta_{v\beta}\delta_{\beta w}G_{wx}\delta_{x\gamma}\delta_{\gamma 1} \\ &\quad \times\ (-4\pi f^*)^3\delta_{4\alpha}\delta_{\alpha u}G^*_{uv}\delta_{v\gamma}\delta_{\gamma w}G^*_{wx}\delta_{x\beta}\delta_{\beta 3}\rangle \\ &= (4\pi|f|)^6V^{-3}\iiint\sum_\alpha\sum_\beta\sum_\gamma G_{\alpha\beta}G_{\beta\gamma}G^*_{\alpha\gamma}G^*_{\gamma\beta}\delta_{1\gamma}\delta_{2\alpha}\delta_{3\beta}\delta_{4\alpha}d_\alpha d_\beta d_\gamma \\ &= (4\pi)^3(4\pi|f|^2n_0)^3G_{13}G^*_{13}G_{23}G^*_{12}\delta_{24}\ . \end{aligned} \tag{4.192}$$

Now we can use Eqs. (4.52) and (4.57) for reflection and transmission respectively, to calculate the intensity coming from the slab due to these scattering processes. For reflection we in general have (see Eq. (4.52))

$$\begin{aligned}\gamma_R &= \frac{1}{\mu_i A}\int\exp\{i[\vec{q}_{\perp,i}\cdot(\vec{r}_{2,\perp}-\vec{r}_{4,\perp})-\vec{q}_{\perp,s}\cdot(\vec{r}_{1,\perp}-\vec{r}_{3,\perp})]\} \\ &\quad \times\ \exp\{ik_0[\mu_i(z_2-z_4)+\mu_s(z_1-z_3)]\}\times\exp\left[-\frac{\kappa}{2}\left(\frac{z_2+z_4}{\mu_i}+\frac{z_1+z_3}{\mu_s}\right)\right] \\ &\quad \times\ \langle R(\vec{r}_1,\vec{r}_2;\vec{r}_3,\vec{r}_4)\rangle d\vec{r}_1d\vec{r}_2d\vec{r}_3d\vec{r}_4\ , \end{aligned} \tag{4.193}$$

so we can write

$$\begin{aligned}\gamma_{mix,\mathrm{XI}} &= \frac{a^3\kappa^3}{4\pi\mu_i A}\int\exp\{-i\vec{q}_{\perp,s}\cdot(\vec{r}_{1,\perp}-\vec{r}_{3,\perp})]\}\times\exp[ik_0\mu_s(z_1-z_3)] \\ &\quad \times\ \exp\left[-\frac{\kappa}{2}\left(\frac{2z_2}{\mu_i}+\frac{z_1+z_3}{\mu_s}\right)\right]\times\exp[ik_0(|\vec{r}_2-\vec{r}_3|-|\vec{r}_1-\vec{r}_2|)] \\ &\quad \times\ \frac{\exp(-\kappa|\vec{r}_1-\vec{r}_3|)\exp[-\kappa(|\vec{r}_2-\vec{r}_3|+|\vec{r}_1-\vec{r}_2|)/2]}{|\vec{r}_1-\vec{r}_3|^2\,|\vec{r}_2-\vec{r}_3|\,|\vec{r}_1-\vec{r}_2|}d\vec{r}_1d\vec{r}_2d\vec{r}_3\ . \end{aligned} \tag{4.194}$$

Integration over the sum coordinate $\vec{r}_\perp=\vec{r}_{1,\perp}+\vec{r}_{2,\perp}+\vec{r}_{3,\perp}$ normalizes the illuminated area, and leaves an equation which essentially consists of a double convolution in the orthogonal

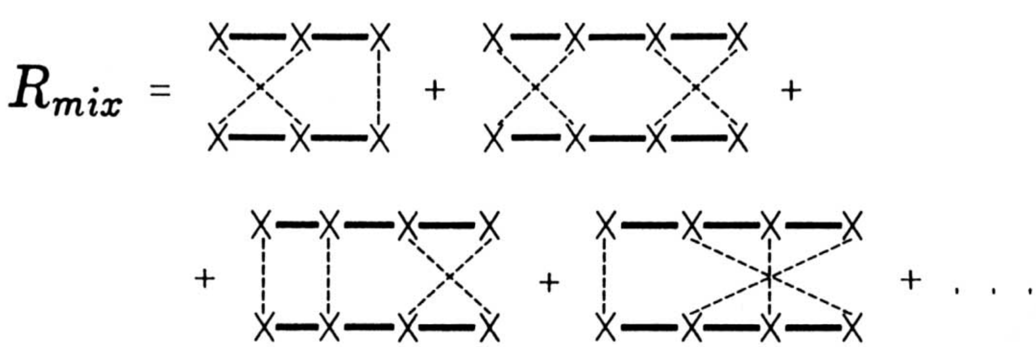

Figure 4.19: *Some possible cross terms between $\langle L\rangle$ and $\langle C\rangle$ in the reducible vertex $\langle R\rangle$.*

directions. Analytically one finds after some calculus:

$$
\begin{aligned}
\gamma_{mix,\mathrm{XI}} &= \frac{a^3}{4\mu_i}\int_0^b\int_0^b\int_0^b \exp\left[i\mu_s\frac{k_0}{\kappa}(\tau_1-\tau_3)\right]\times\exp\left[-\left(\frac{\tau_2}{\mu_i}+\frac{\tau_1+\tau_3}{2\mu_s}\right)\right] \\
&\times \int W(|\tau_1-\tau_3|;|\vec{q}_{\perp,s}-\vec{q}_\perp|/\kappa)V(q_\perp)d\vec{q}_\perp d\tau_1 d\tau_2 d\tau_3 \ , \qquad (4.195)
\end{aligned}
$$

where $W(|\tau_1-\tau_3|;|\vec{q}_{\perp,s}-\vec{q}_\perp|/\kappa)$ is defined in Eq. (4.29), and $V(q_\perp)$ is given by

$$
V(q_\perp) = \frac{\exp\left[-|\tau_1-\tau_2|\sqrt{q_\perp^2+(ik_0+\kappa/2)^2}-|\tau_2-\tau_3|\sqrt{q_\perp^2+(ik_0-\kappa/2)^2}\,\right]}{\sqrt{[q_\perp^2-k_0^2+(\kappa/2)^2+ik_0\kappa][q_\perp^2-k_0^2+(\kappa/2)^2-ik_0\kappa]}} \qquad (4.196)
$$

From here, a numerical approach seems to be necessary. A possible help in finding an answer might be that $\kappa \ll 2k_0$.

Let us discuss the two different two-particle boomerang diagrams which are shown in Fig. 4.20. The diagram on the left-hand side is a *ladder-type* boomerang, on the right-hand side a *crossed-type* boomerang diagram, which I will denote by $U_{boom,L}$ and $U_{boom,C}$ respectively. The U stands for the irreducible vertex. Again, by using Eqs. (4.190), (4.191), and (4.16), the first of these *intensity* diagrams can be written in its mathematical form:

$$
\begin{aligned}
\langle U_{boom,L}\rangle &= \langle(-4\pi f)^3\delta_{2\alpha}\delta_{\alpha u}G_{uv}\delta_{v\beta}\delta_{\beta w}G_{wx}\delta_{x\alpha}\delta_{\alpha 1} \\
&\quad\times\ (-4\pi f^*)^3\delta_{4\alpha}\delta_{\alpha u}G^*_{uv}\delta_{v\beta}\delta_{\beta w}G^*_{wx}\delta_{x\alpha}\delta_{\alpha 3}\rangle \\
&= (4\pi|f|)^6V^{-3}\int d_\gamma\iint\sum_\alpha\sum_\beta G_{\alpha\beta}G_{\beta\alpha}G^*_{\alpha\beta}G^*_{\beta\alpha}\delta_{2\alpha}\delta_{\alpha 1}\delta_{4\alpha}\delta_{\alpha 3}d_\alpha d_\beta \\
&= (4\pi|f|)^6 n_0^2\delta_{12}\delta_{13}\delta_{14}\int(G_{1\beta}G^*_{1\beta})^2 d_\beta \ . \qquad (4.197)
\end{aligned}
$$

where I shall not bother about the corrections to $\langle G\rangle$ due to the higher order terms in Σ (see Eqs. (4.7)-(4.12), which probably will essentially only give a correction to the mean free path.

What we see is that this integral *diverges* for $\vec{r}_\beta \to \vec{r}_1$. We can try to solve the problem by summing all the higher order two-particle (multiple) boomerang diagrams

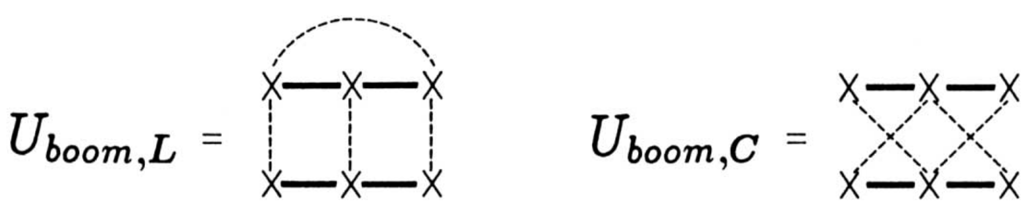

Figure 4.20: *Two of the simplest intensity boomerang diagrams.*

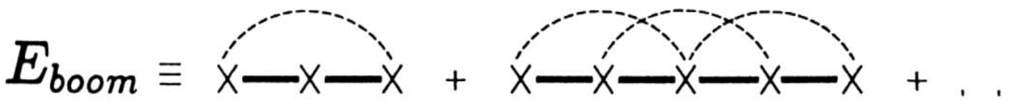

Figure 4.21: *series of two-particle amplitude boomerang diagrams.*

for the intensity. This is indeed possible but will not work either. The solution to this problem is to sum *all* boomerang diagrams of the *amplitude*, denoted by E, first and then multiply with the conjugate to obtain the intensity. Although this may seem a little odd at first sight, it is immediately clear from the physics behind it. We are treating two fixed particles, with a wave multiply scattered in between. This means that there is a *phase relation* between those diagrams, which we destroy by averaging them seperately, as we do when summing the series of intensity diagrams. So the correct answer, where I sum *all* higher order *amplitude* boomerangs, as shown in Fig. 4.21, gives

$$\begin{aligned} E_{boom} &= (4\pi f)^3 \delta_{2\alpha} G_{\alpha\beta} G_{\beta\alpha} \delta_{\alpha 1} + (4\pi f)^5 \delta_{2\alpha} G_{\alpha\beta} G_{\beta\alpha} G_{\alpha\beta} G_{\beta\alpha} \delta_{\alpha 1} + \cdots \\ &= 4\pi f \delta_{2\alpha} \delta_{\alpha 1} \frac{(4\pi f G_{\alpha\beta})^2}{1 - (4\pi f G_{\alpha\beta})^2} \,, \end{aligned} \tag{4.198}$$

In fact, E_{boom} is a dressed version of a part of Σ, see Fig. 4.2.
For the intensity diagrams $U = EE^*$ we now find

$$\begin{aligned} \langle U_{boom,L} \rangle &= \left\langle (4\pi |f|)^6 \delta_{2\alpha} \delta_{\alpha 1} \delta_{4\alpha} \delta_{\alpha 3} \frac{(G_{\alpha\beta} G^*_{\alpha\beta})^2}{[1 - (4\pi f G_{\alpha\beta})^2][1 - (4\pi f^* G^*_{\alpha\beta})^2]} \right\rangle \\ &= \frac{(4\pi a\kappa)^3}{n_0} \int \frac{(G_{1\beta} G^*_{1\beta})^2 \delta_{12} \delta_{13} \delta_{14}}{1 - (4\pi)^2 (f^2 G^2_{1\beta} + (f^* G^*_{1\beta})^2) + (4\pi a\kappa)^2 (G_{1\beta} G^*_{1\beta})^2} d_\beta \,, \end{aligned} \tag{4.199}$$

$$\begin{aligned} \langle U_{boom,C} \rangle &= \left\langle (4\pi |f|)^6 \delta_{2\alpha} \delta_{\alpha 1} \delta_{4\beta} \delta_{\beta 3} \frac{(G_{\alpha\beta} G^*_{\alpha\beta})^2}{[1 - (4\pi f G_{\alpha\beta})^2][1 - (4\pi f^* G^*_{\alpha\beta})^2]} \right\rangle \\ &= \frac{(4\pi a\kappa)^3}{n_0} \frac{(G_{13} G^*_{13})^2 \delta_{12} \delta_{34}}{1 - (4\pi)^2 (f^2 G^2_{13} + (f^* G^*_{13})^2) + (4\pi a\kappa)^2 (G_{13} G^*_{13})^2} \,. \end{aligned} \tag{4.200}$$

These integrals do not diverge, so by summing all multiple scattering between the two particles we have indeed been able to renormalize the problem.

To find the intensities coming from the slab due to these diagrams, we have to calculate the bistatic coefficient γ_{boom}. Therefore we take once again Eq. (4.39). If we take the usual Green's functions for scattering from the slab without bothering about corrections to the self-energy as mentioned above, we find for the transmission of the slab

$$\begin{aligned} \tilde{\gamma}_{boom,L,C} &= \frac{(4\pi a\kappa)^3}{\mu_i n_0 A} \int \exp\left[-\frac{\kappa}{2}(z_1 + z_3) \left(\frac{1}{\mu_i} - \frac{1}{\mu_s} \right) \right] \times \exp(-\kappa L/\mu_s) \\ &\times \exp[i(\vec{q}_{\perp,i} - \vec{q}_{\perp,s}) \cdot (\vec{r}_{1,\perp} - \vec{r}_{3,\perp})] \times \exp[ik_0(\mu_i - \mu_s)(z_1 - z_3)] \end{aligned}$$

$$\times \quad \int \frac{(G_{1\beta}G^*_{1\beta})^2 \delta(\vec{r}_{1,\beta} - \vec{r}_3)}{1-(4\pi)^2(f^2G^2_{1\beta} + (f^*G^*_{1\beta})^2) + (4\pi a\kappa)^2(G_{1\beta}G^*_{1\beta})^2} d\vec{r}_\beta d\vec{r}_1 d\vec{r}_3 \ , \quad (4.201)$$

where only the index of $\vec{r}_{1,\beta}$ in the delta function determines between L and C respectively. It is important to notice that in the latter case a formula remains that has the same shape as Eq. (4.56). This implies that there exist an *enhanced forward scattering cone* which has the same shape as the coherent backscattering cone, but is damped by a factor $(\kappa^3/n_0)\exp(-\kappa L/\mu_s)$. Observation in a light scattering experiment is therefore only possible for very thin slabs of materials with a high density of scatterers. These conditions will however make the forward scattered peak very broad, and therefore hard to separate from the background, not to mention problems with the coherent beam from the source, and complications due to anisotropic scattering of the particles and their finite size.

4.7 Appendices

4.7.1 Appendix A

To calculate the kernel $W(\tau,\alpha)$, it appears convenient to make a linear interpolation table $W(I,J)$ of $W(\tau,\alpha)$. Because $W(\tau,\alpha)$ diverges for $\tau \to 0$ as $-\ln(\tau)$, we need more interpolation points for small τ, proportional to τ^{-1}, the derivative of $-\ln(\tau)$. This is achieved by mapping τ on I^2 instead of I, starting at a value $\tau_0 = 10^{-5}$. Similar, α was mapped on J^2 in order to get a smooth picture of the backscattering cone. Integration was done with an adaptive Gaussian quadrature. In order to avoid problems for higher values of t due to the disproportion of the length of the interval Δt and its contribution to the integral, the integration interval $[1,\infty\rangle$ was mapped on $[0,1\rangle$ by use of the conform map

$$t = \frac{1+\xi}{1-\xi} \ , \quad (4.202)$$

so

$$W(\tau,\alpha) = \int_1^\infty \frac{\exp(-\tau\sqrt{t^2+\alpha^2})}{\sqrt{t^2+\alpha^2}} dt = 2\int_0^1 \frac{\exp[-\tau\eta(\xi,\alpha)/(1-\xi)]}{(1-\xi)\eta(\xi,\alpha)]} d\xi \ , \quad (4.203)$$

with

$$\eta(\xi,\alpha) = \sqrt{\alpha^2(1-\xi)^2 + (1+\xi)^2} \ . \quad (4.204)$$

4.7.2 Appendix B

To calculate the different orders of scattering with Eqs. (4.64)-(4.66) it is important to separate the integration interval in two parts chosen so that the singularity of the kernel is in the boundary. The kernel occurs twice for third order scattering, and this means we have to split the interval $[0, b]$ in three parts, namely $[0, \tau_1\rangle$, $\langle\tau_1, \tau_2\rangle$ and $\langle\tau_2, b]$ for $\tau_2 > \tau_1$, because here we have to avoid both singularities. Due to this complication Γ_3 rather than Γ_2 should be used as the starting term for iteration.

4.7.3 Appendix C

The integral equation we have to solve is a Fredholm equation with a singular kernel $W(\tau, \alpha)$.[80] In order to calculate the solution of (4.32) numerically, we have to discretize the continuous variable t. Divide the interval $[0, b]$ in N parts so $\tau_n = bn/N$ and (4.35) becomes

$$\Gamma(\tau_n, \tau_l; \alpha) = S(\tau_n, \tau_l; \alpha) + \frac{a}{2}\sum_{m=0}^{N-1}\int_{t_m}^{t_{m+1}} W(|\tau_n - \tau|; \alpha)\Gamma(\tau, \tau_l; \alpha)d\tau \ . \tag{4.205}$$

Linear interpolation of Γ between τ_m and τ_{m+1} with $\tau = \tau_m + t$ gives

$$\Gamma(\tau_m + t, \tau; \alpha) = \frac{t\Gamma(\tau_{m+1}, \tau; \alpha) + (\tau_{m+1} - \tau_m - t)\Gamma(\tau_m, \tau; \alpha)}{\tau_{m+1} - \tau_m} \ , \tag{4.206}$$

So with $x = tN/b$, and the definitions

$$\begin{aligned} \Gamma(\tau_n, \tau_l; \alpha) &\equiv \Gamma_{nl}(\alpha) \ , & (4.207) \\ S(\tau_n, \tau_l; \alpha) &\equiv S_{nl}(\alpha) \ , & (4.208) \end{aligned}$$

we find

$$\Gamma_{nl}(\alpha) = S_{nl}(\alpha) + \frac{ab}{2N}\sum_{m=0}^{N-1}\int_0^1 W(|\frac{b}{N}(n - m - x)|; \alpha)[x\Gamma_{m+1,l}(\alpha) + (1 - x)\Gamma_{ml}(\alpha)]dx \ , \tag{4.209}$$

which gives

$$\begin{aligned} \Gamma_{nl}(\alpha) = S_{nl}(\alpha) \ &+ \ \frac{ab}{2N}\Gamma_{0l}(\alpha)\int_0^1 xW(|\frac{b}{N}(n - 1 + x)|; \alpha)dx \\ &+ \ \frac{ab}{2N}\Gamma_{Nl}(\alpha)\int_0^1 xW(|\frac{b}{N}(n + 1 - N - x)|; \alpha)dx \\ &+ \ \frac{ab}{2N}\sum_{m=0}^{N-1}\Gamma_{ml}(\alpha)\int_0^1 x[W(|\frac{b}{N}(n - m - 1 + x)|; \alpha) \\ &\qquad\qquad + \ W(|\frac{b}{N}(n - m + 1 - x)|; \alpha)]dx \ . \end{aligned} \tag{4.210}$$

This can be written as

$$\Gamma_{nl}(\alpha) = S_{nl}(\alpha) + C_{nm}(\alpha)\Gamma_{ml}(\alpha) \ , \tag{4.211}$$

so that

$$\Gamma_{ml}(\alpha) = [\delta_{mn} - C_{mn}(\alpha)]^{-1}S_{nl}(\alpha) \ . \tag{4.212}$$

To find the solution Γ, we have to calculate the inverse of the $(N+1) \times (N+1)$ matrix $[\delta_{mn} - C_{mn}(\alpha)]$. A larger N results in a more accurate solution, but cpu time increases with about N^3. On a VAX 11/750 slabs up to $b = 32$ could be handled this way. Γ_3 or an higher order scattering solution should be used as a starting term to avoid the unboundness of Γ_2. Numerical routines where used from the CERN library.

Chapter 5

Experiments for d=3

In this chapter I will present results from both transmission and reflection experiments for strongly scattering media. The experiments will be compared to the theory of Chapter 4.

Detailed data have been collected on (i) the scattering and transport mean free paths λ_{sc} and λ_{tr} (the characteristic lengths associated with the attenuation of the coherent beam and of energy transport) as a function of sample composition, and (ii) the shape and width of the cones of enhanced backscattering as a function of the transport mean free path and the slab thickness L ($\equiv b\lambda_{tr}$) (see also Ref. 61).

Two types of liquid suspensions have been used as study object: polystyrene spheres in water and suspensions of TiO_2-particles in 2-methyl-pentane-2,4-diol. Further, a time-resolved experiment has been performed to determine the diffusion constant of a solid medium consisting of TiO_2 particles in air, glued together with a little PMMA (plexiglass). From these experiments scattering mean free paths and transport mean free paths have been obtained. Relative values for the transport mean free paths could also independently be inferred from the observation of the angular dependence of enhanced (interference) backscattering. The observed shapes and widths of the enhanced backscattering cones are in very good agreement with the calculated values. A less satisfying feature is that the theory predicts a backscattering intensity of twice the background intensity, while the experimental value is some 20 % lower.

Parameters which have been varied in this study are for the polystyrene suspensions concentration, particle size, and thickness of the cell, and for the TiO_2 suspensions concentration and thickness of the cell. By using a special "difference technique" we have been able to observe low-order and high-order scattering processes independently.[14,84]

The time-resolved transmission experiments show classical diffusion, but the diffusion constant appears to be very low, in fact so low that the critical mean free path λ_{cr} has to be taken into account for the interpretation of the measurements. Comparing the values of the mean free path obtained from backscattering and transmission of the same sample respectively, allows an estimation of the critical length.

5.1 Scattering and transport mean free path

In localization of waves key parameters are the scattering mean free path λ_{sc}, and transport mean free path λ_{tr}. Here I report on systematic studies of these parameters.

For suspensions of different concentrations of polystyrene spheres, with diameters of 0.215μm, 0.482μm and 1.019μm, and of 2.02μm polyvinyltoluene spheres (Dow Chemical) we calculated λ_{sc} and λ_{tr} from Mie-theory.[57] For suspensions of surface-treated TiO_2 (rutile) particles in 2-methylpentane-2,4-diol (samples were kindly supplied by Sikkens and by Sigma Coatings) we determined the scattering and transport mean free paths from transmission experiments. Fig. 5.1 shows the setup used for the determination of the transmitted intensity as a function of slab thickness: a laser beam ($\lambda_{vac} = 514.5$ nm) was passed through a weak positive lens L1 so as to obtain a long focus with its waist near the pinhole PH1. The cell consisted of another weak positive lens L2 and an optical flat F. Pinhole PH2 was chosen just big enough to make sure that no clipping occurred upon

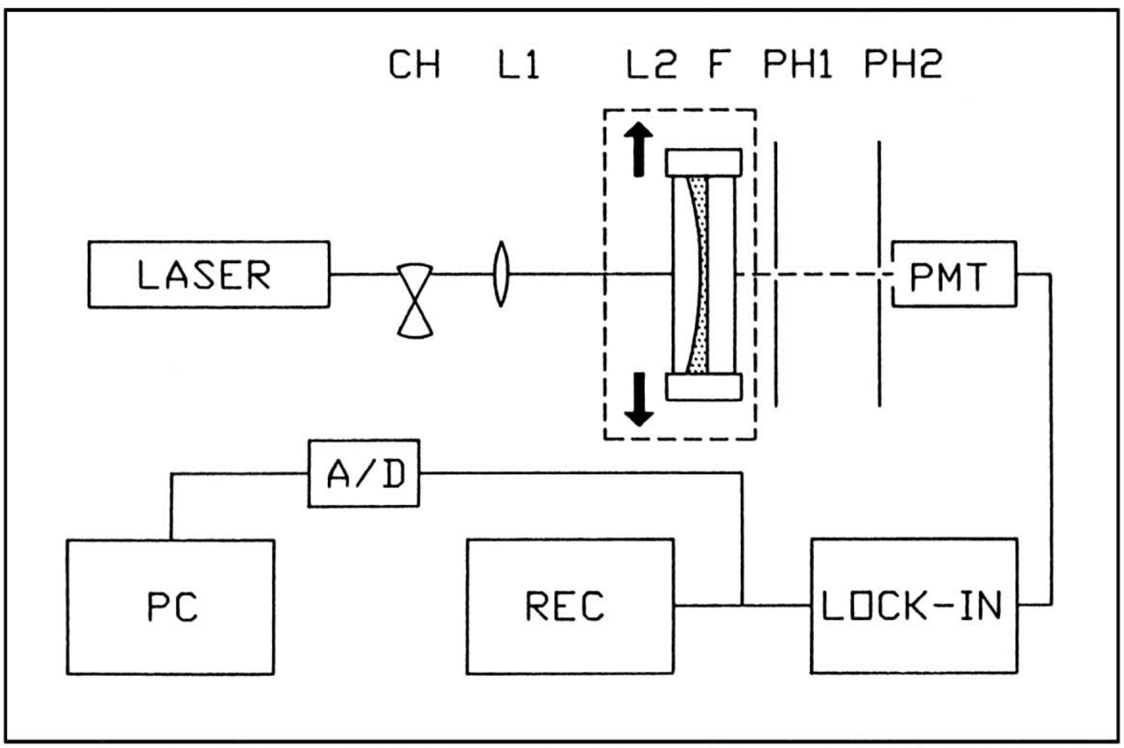

Figure 5.1: *Scheme of the experimental setup for the observation of transmitted intensity as a function of slab-thickness. CH, chopper; L1, lens; L2 & F, cell, consisting of a weak lens and an optical flat, mounted on a translation stage; PH1 and PH2, pinholes.*

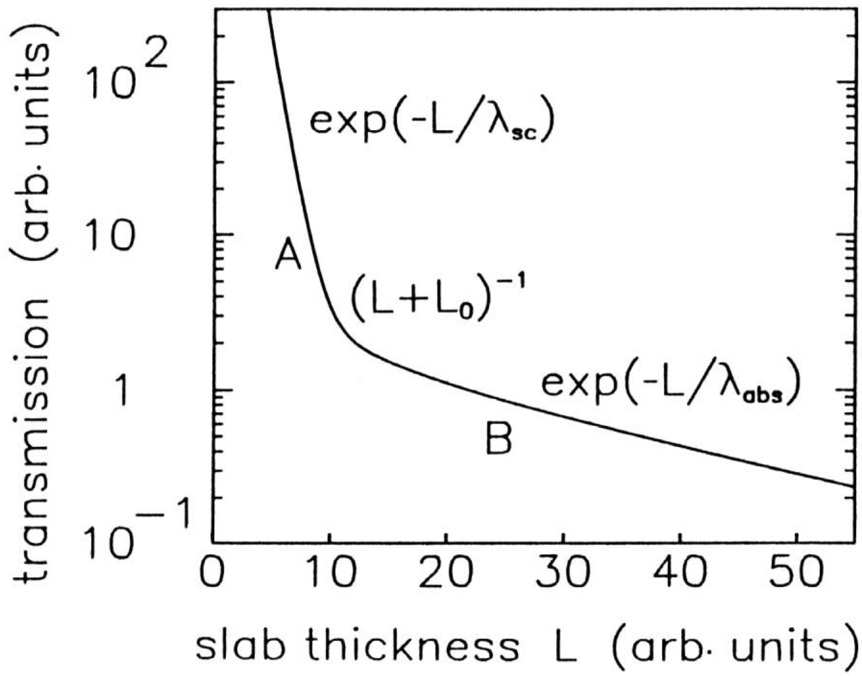

Figure 5.2: *Typical plot of the logarithm of the transmission versus slab-thickness. [1] exponential decay of coherent intensity. [2] L^{-1} decay of diffuse intensity (diffusion). [3] exponential decay of diffuse intensity (absorption).*

scanning the cell (filled with solvent only) through the beam over its full range. In Fig. 5.2 a typical curve for transmission versus slab thickness L is presented. Three different parts can be distinguished: part [1] shows the exponential decay of the transmitted coherent intensity that results from light scattering out of the beam. From its slope, the scattering mean free path λ_{sc} is found. Near point A the diffuse intensity starts to outweigh the coherent intensity, and part [2] shows the $1/L$ decay of the diffuse intensity. In this range a plot of V_{out}^{-1} (V_{out} being the amplified detector signal) versus L gives a straight line with a slope of $(C\lambda_{tr})^{-1}$, with C an as yet unknown constant of dimension Volt per length. Near point B the absorption of the sample starts to play a role, and in part [3] the decay is once more exponential. From its slope we obtain $\lambda_{abs} = \sqrt{\lambda_{tr}\lambda_{in}/3}$ where λ_{in} is the inelastic mean free path.

In Fig. 5.3 the experimental values for λ_{sc} (in μm) and $C\lambda_{tr}$ (in mV) are plotted versus the volume fraction ρ of TiO_2. For low volume fractions ($\rho < 0.1$) both λ_{sc} and λ_{tr} are inversely proportional to ρ. At higher concentrations saturation occurs (possibly earlier for λ_{tr} than for λ_{sc}), which might indicate that we are entering the dependent scattering regime. From the upper curve we found λ_{tr} as a function of ρ in the following way: in the dilute regime, λ_{tr} is known to be equal to $\lambda_{sc}/(1 - \langle\cos\theta\rangle)$, with $\langle\cos\theta\rangle$ the average cosine of the scattering angle. The average size of the TiO_2 particles is 220 nm.[86] Assuming spherical shape, Mie theory yields a value of 0.476 for $\langle\cos\theta\rangle$ and hence λ_{tr}

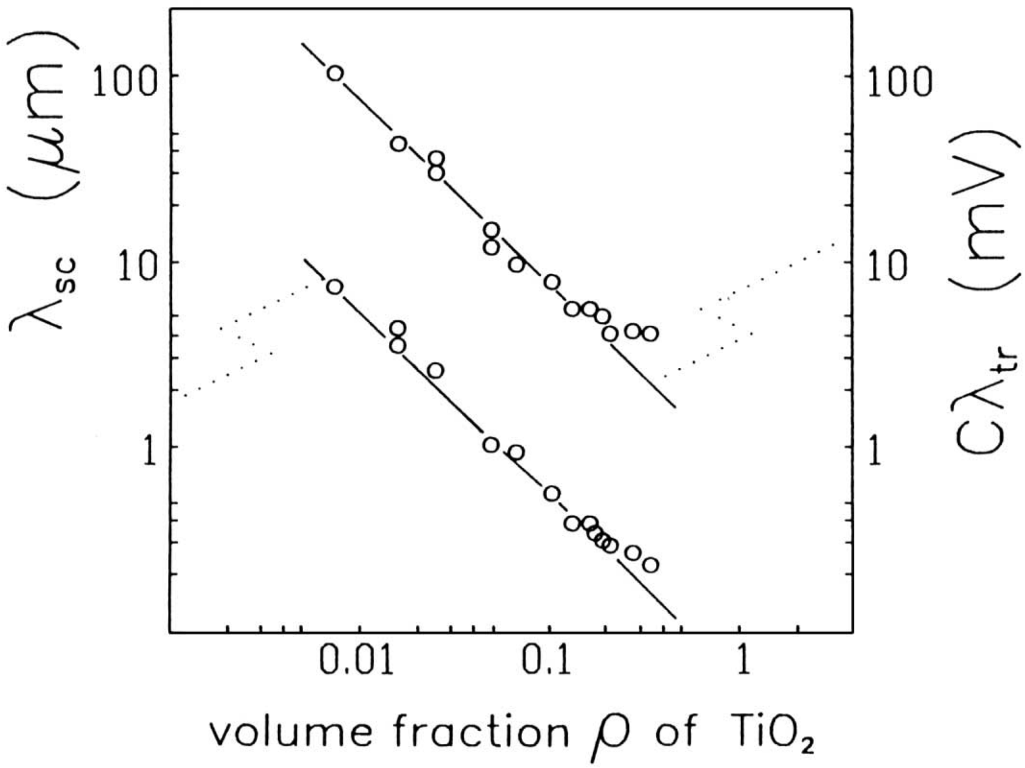

Figure 5.3: *Scattering mean free path (lower plot) and (upper plot) transport mean free path times a constant C (see text) as a function of the volume fraction of $\o \simeq 220$ nm TiO_2 particles.*

should be $\simeq 1.87\lambda_{sc}$. From this result and from the vertical distance between the two plots, the value of the constant C was calculated to be 14.3×10^3 Vm^{-1}. Using this value, we can now find λ_{tr} from the upper curve (*i.e.* from the diffusive $1/L$ decay) *also* for concentrated samples where the proportionality between λ_{sc} and λ_{tr} might no longer hold. (Taking into account that the size distribution of the crystals is wide and that their shape is not spherical, the above procedure can not be expected to give more than a reasonable estimate of λ_{tr}).

5.2 Coherent backscattering from finite slabs

Before describing our experiments, I will first just review shortly the work already done in the field. Enhanced backscattering from a random sample (consisting of polystyrene micro spheres in water)[35] was for the first time interpreted in terms of interference between time-reversed paths by Tsang and Ishimaru.[66] At first, this work was not noticed by researchers in the field of localization, probably because the authors did not make the link with localization theory. The first to make this link were Van Albada and Lagendijk[36] and Wolf and Maret.[37] Both these groups reported the observation of cones of enhanced backscattering of light from polystyrene sphere-water samples, found qualitatively the expected relationship between width of the cone and mean free path, and in addition observed a marked polarization effect: the enhanced intensity in the backscattered light is much more pronounced in the component with polarization parallel to that of the incident beam than in the perpendicularly polarized component. Enhanced backscattering from rigid random samples was later reported by Etemad c.s.,[45] who obtained the cone by adding many speckle patterns that were recorded for slightly different orientations of the sample with respect to the incident beam, and by Kaveh c.s.[87] who obtained ensemble averaging by spinning the sample. In these experiments the influence of the mean free path was not investigated, but the different enhancement factors in the parallel and perpendicular components were confirmed in Kaveh's work.

Detailed studies have been made by various groups. Coherent backscattering from polystyrene-sphere suspensions in water has been studied as a function of concentration, particle size, sample thickness, polarization of the backscattered light with respect to incident polarization, and of the spatial orientation of the scan.[84] Suspensions of TiO_2 particles in 2-methylpentane-2,4-diol have been studied as a function of concentration and sample thickness.[61] The cutoff of long light paths has also been studied by addition of absorbing dye to the samples.[88] The width of the contribution to the cone as a function of the length of the light paths has been studied in a time- resolved experiment on femtosecond scale.[41]

5.2.1 Enhanced backscattering of the co-polarized component

Enhanced backscattering was recorded using a set-up of the type drawn schematically in Fig. 5.4. A linearly polarized laser beam ($\lambda_{vac} = 514.5$ nm) was expanded and then reflected from a beam splitter onto the sample cell. The intensity backscattered through the beamsplitter was recorded as a function of the scattering angle, using a pinhole-detector assembly mounted on a stepper-motor driven translation stage and positioned with the pinhole in the focal plane of the lens L. The cell was tilted off-axis so as to keep its window reflections well away from the detector. In scans of high-viscosity samples the cell was spun around its axis to average out the strong intensity fluctuations that result from interference.[45,87]

The transmission characterisics of the beam splitter depend on the angle of observation and (depending on the extent of the scanning range) measured intensities may need to be corrected for this effect. "Response curves" were obtained illuminating the sample from the backside, *i.e.* using it as just a diffuse light source. The polystyrene-sphere samples were studied over a total scan width of $\leq$ 50mrad. Within this narrow range no corrections for response variations were needed. Dilute TiO_2 samples were studied using a scan width up to 175 mrad. For the more concentrated TiO_2 samples the setup was slightly modified:

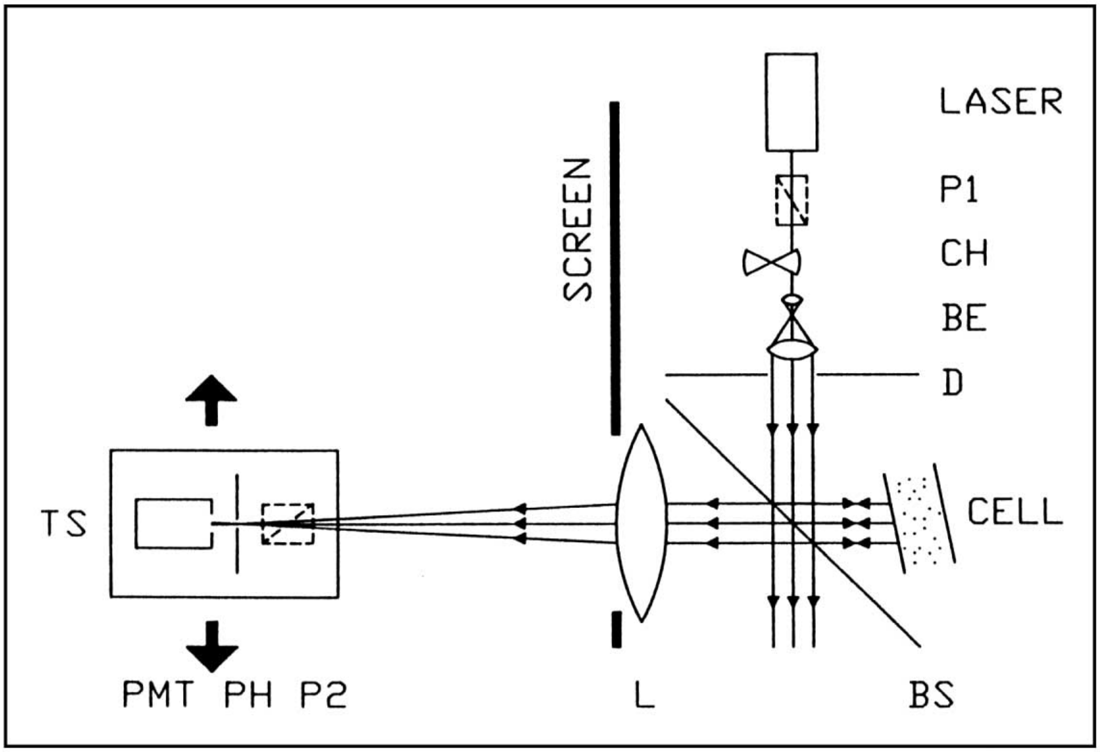

Figure 5.4: *Experimental setup for the observation of backscattering enhancement. P1 & P2, polarizers; CH, chopper; BE, beam expander; BS, beam-splitter; L, lens; PH, pinhole; TS, translation stage.*

in terms of Fig. 5.4, the detector was now moved in a plane perpendicular to the plane of the drawing (making the scan symmetrical with respect to the transmission characteristics of the beamsplitter) and along a circular path around the cell. The lens L, which in the narrow-angle scans was at a fixed position, now moved with the detector assembly. The total scan width was 600 mrad. All TiO_2 curves were corrected for the angular dependence of the response.

For a given sample, the recorded *enhancement factor* $I_{top}/I_{background}$ depends on the relative orientation of the polarizers P1 and P2. The *width* of the cone depends on λ_{tr} and for very small particle samples also on the spatial orientation of the scanning plane with respect to the direction of incident polarization: low-order scattering contributions are then abnormally broad when the cone is scanned in the plane of incident polarization.[84] The (isotropic) theory from Chapter 4 is expected to hold for the parallel light component (P1$\|$P2) and will be compared to experimental results obtained from scans perpendicular to the direction of incident polarization. In the next section I will come back in detail to polarization effects.

The theory takes into account *self-avoiding light paths* (ladder diagrams) and interfer-

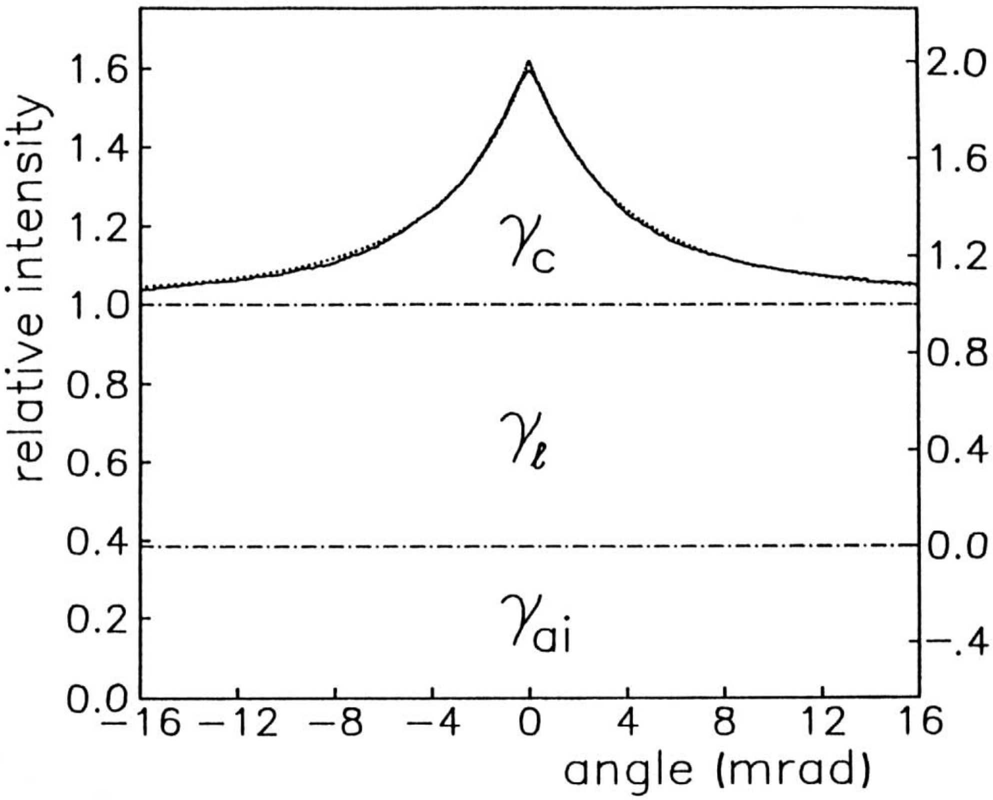

Figure 5.5: *Enhanced backscattering of the parallel light component from a 2300 μm slab of a 1.05 vol% sample of $\o \simeq 220$ nm particles of TiO_2 in 2-methylpentane-2,4-diol at $\lambda_{vac} = 514.5$ nm.*
Solid line: experimental curve; Dotted line: curve, calculated from diffusion theory, using $\lambda_{tr} = 9.68\ \mu m$.
For practical reasons, the theoretical curve convolved with the instrumental resolution of 0.5mrad, is not shown. The left-hand vertical axis corresponds to the experimental curve, while the right-hand axis corresponds to the theoretical decomposition in contributions from the ladderterms γ_ℓ, the interference terms γ_c, and the angle-independent terms γ_{ai}.

ence between such paths and their time-reversed counterparts (most-crossed diagrams). This leads to a predicted enhancement factor of 2 for the *multiple-scattered light.*[78] Single scattering however gives an almost angle independent contribution which does not double. The contribution of single scattering to the total amount of scattered light is expected to be no more than 10 %, which results in a minimum enhancement factor of approximately 1.9. In the experiment lower values are found. Reported enhancement factors are 1.6,[39] 1.65,[36] 1.70,[37] 1.75,[87] and 2.[45] (In the last case an optical isolator was used to exclude the single scattering contribution, however Fig. (2.b) in Ref. 45 shows an enhancement factor of 1.8) These values suggest that a considerable contribution to the background intensity is due to light paths that either have no time-reversed counterpart (*e.g.*, single scattering), or give rise to interference terms that are not angle dependent (I will return to this point at a later stage).

Now even if the isotropic theory would not describe the relative intensities of background and cone fully correctly, it might still correctly describe the *shape* and the *width* of the cone, provided that the latter is indeed mainly due to most-crossed-diagram type of interference. In Fig. 5.5, the backscattering pattern as recorded using a thick slab ($b \simeq 240$) of 1.05 vol % and diameter ø of 220 nm rutile particles in 2-methylpentane-2,4-diol as a sample, is plotted together with the intensity profile as calculated for this sample from diffusion theory (this slab thickness is outside the region that can be handled numerically with the exact theory), using the value for λ_{tr} that was obtained from transmission experiments. The theoretical curve was fitted to the experimental data in the following way: the calculated intensity profile was convolved with the instrumental resolution. (The advantage of convolving the calculated curve instead of deconvolving the experimental one is that no assumptions regarding the shape of the latter are needed). The tops of the resulting theoretical and experimental curves were then superimposed and the vertical scale of the calculated curve was adapted so as to make the outermost parts of its wings coincide with those of the experimental cone. The shape and width of the calculated cone is found to fit perfectly to the experimental data. At the same time we see that the observed intensity profile has an offset with respect to the calculated one that amounts to approximately 30 % of the total background. This seems to be far too much to be explained in terms of single scattering by an ideal sample, so another angle-independent scattering contribution must play a part. In Fig. 5.5, we denoted the bistatic scattering coefficient of all angle-independent (ai) terms (including single-scattering) by γ_{ai}. If the sample thickness is reduced to a few microns only, an essentially flat (no cone) backscattering pattern remains, of which the intensity is still $\simeq$ 10% of that of the background signal from a thick slab. This remaining intensity is thought to result from two contributions: (i) (near-) forward scattering in combination with reflection from the rear-window (because of the inclined position of the cell, its windows can not reflect the incident beam directly into the detector. *Scattered* light however may reach the detector after reflection from the rear-window and from the reflected incident beam light may also be scattered into the detector) and (ii) scattering from particles that adhere to the windows (if the solid component of the sample tends to adhere to the glass of the cell windows, a single scattering contribution larger than would result from an ideal sample will be found). In order to minimize the first effect, a black rear-window was used with an index of refraction close to that of the sample. If the sample is sufficiently thick, only the second effect

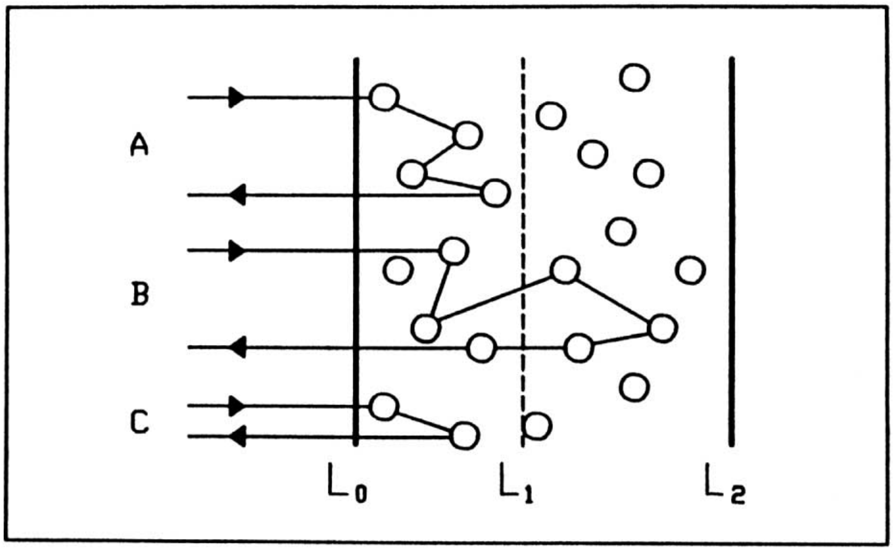

Figure 5.6: *The intensity pattern of the "full slab" ($L_0 - L_2$) contains contributions of A, B, and C; that of the "front slab" ($L_0 - L_1$) contains contributions of A and C. Subtraction of these patterns yields the pattern of the "deep slab" ($L_1 - L_2$) containing only the "long path" contribution B.*

remains.

As explained in Sect. 4.3.1, we used a difference technique to probe the width and the enhancement factor of the contribution to the backscatter cone as a function of the depth in the sample: subtracting the backscattering patterns of slabs of thickness L_1 and L_2 ($L_2 > L_1$), the scattering contributions coming from the front layer of the sample ($z < L_1$) cancel out, and what remains is the contribution of light that has "seen" the deeper part of the slab ($L_1 < z < L_2$), see Fig. 5.6. In this way the single-scattering contribution (which has no angle-dependent interference term) can be eliminated. It is also possible to exclude the contribution of the very long light paths that give rise to the narrow top of the cone by choosing L_2 relatively small.

Fig. 5.7a shows difference cones that were obtained with this technique, using the sample that gave the full cone of Fig. 5.5. In order to present several curves in the same figure without loosing clarity, a normalization procedure was performed that is more conveniently outlined if we first discuss the corresponding calculated cones. The latter are plotted in Fig. 5.7b and were obtained in the following way: the intensity profiles were calculated from diffusion theory using experimentally obtained λ_{tr} values, and convolved with the instrumental resolution. The resulting (convolved) curves were normalized, each with respect to its own background level. We return now to the experimental curves: the vertical scales of the cones in Fig. 5.7a were adapted so as to match their heights

Table II: *Experimental values for width, relative intensity and enhancement factor, and values calculated for width and relative intensities from diffusion theory for difference slabs as a function of λ_{tr} and optical depth. Relative intensities were normalized with respect to the total intensities of the difference slabs given for each sample.*

Concentration ρ (vol%)	Optical depth τ_d	Width $\Delta(\tau_d)$ (mrad)		Relative intensity		Enhancement factor
		exper.	calc.	exper.	calc.	exper.
0.36	0.35 - 0.9	7.8	7.5	0.09	0.13	2.0
$\lambda_{tr} = 28.2\mu$m	0.9 - 1.6	4.6	5.0	0.26	0.19	1.83
	1.6 - 4.6	2.4	2.6	0.45	0.46	1.69
	4.6 - 8.9	1.1	1.2	0.21	0.22	1.60
1.05	0. - 1.3	21.	20.	0.24	0.22	1.38
$\lambda_{tr} = 9.68\mu$m	1.3 - 2.6	10.3	10.4	0.21	0.21	1.87
	2.6 - 5.2	5.4	5.9	0.21	0.23	1.71
	5.2 - 10.3	3.1	3.1	0.17	0.17	1.69
	10.3 - 103.	1.2	1.1	0.16	0.17	1.65
2.50	2.0 - 6.1	17.	15.	0.54	0.57	1.71
$\lambda_{tr} = 4.06\mu$m	6.1 - 9.8	8.0	7.0	0.17	0.17	1.63
	9.8 - 49.1	3.9	3.0	0.28	0.27	1.61
9.81	5.8 - 12.5	29.	25.	0.53	0.56	1.67
$\lambda_{tr} = 1.04\mu$m	12.5 - 24.	15.	13.	0.21	0.27	1.54
	24. - 48.	7.9	6.8	0.26	0.16	1.65

(intensities) to those of their calculated counterparts. The experimental and calculated widths and relative intensities and the experimental enhancement factors for series of difference cones that were recorded using samples with different volume fractions of TiO_2, are listed in Table II. (The values listed for the 1.05 vol % sample correspond to the cones of Figs. 5.7.

Comparing the shapes, widths and relative intensities of the calculated and experimental cones, we find a good general agreement. Comparing the enhancement factors (Table II), we see that in general the experimental values are lower than the predicted value of two. The cones of the 1.05 vol % sample may serve as an example: (for illustrative purposes the -less reliable- front slabs are also given) in the very front layer the enhancement factor is lowest, and this is thought to be a result of the single scattering contribution. In the next layer, which is the first *difference* slab, a relatively high value is

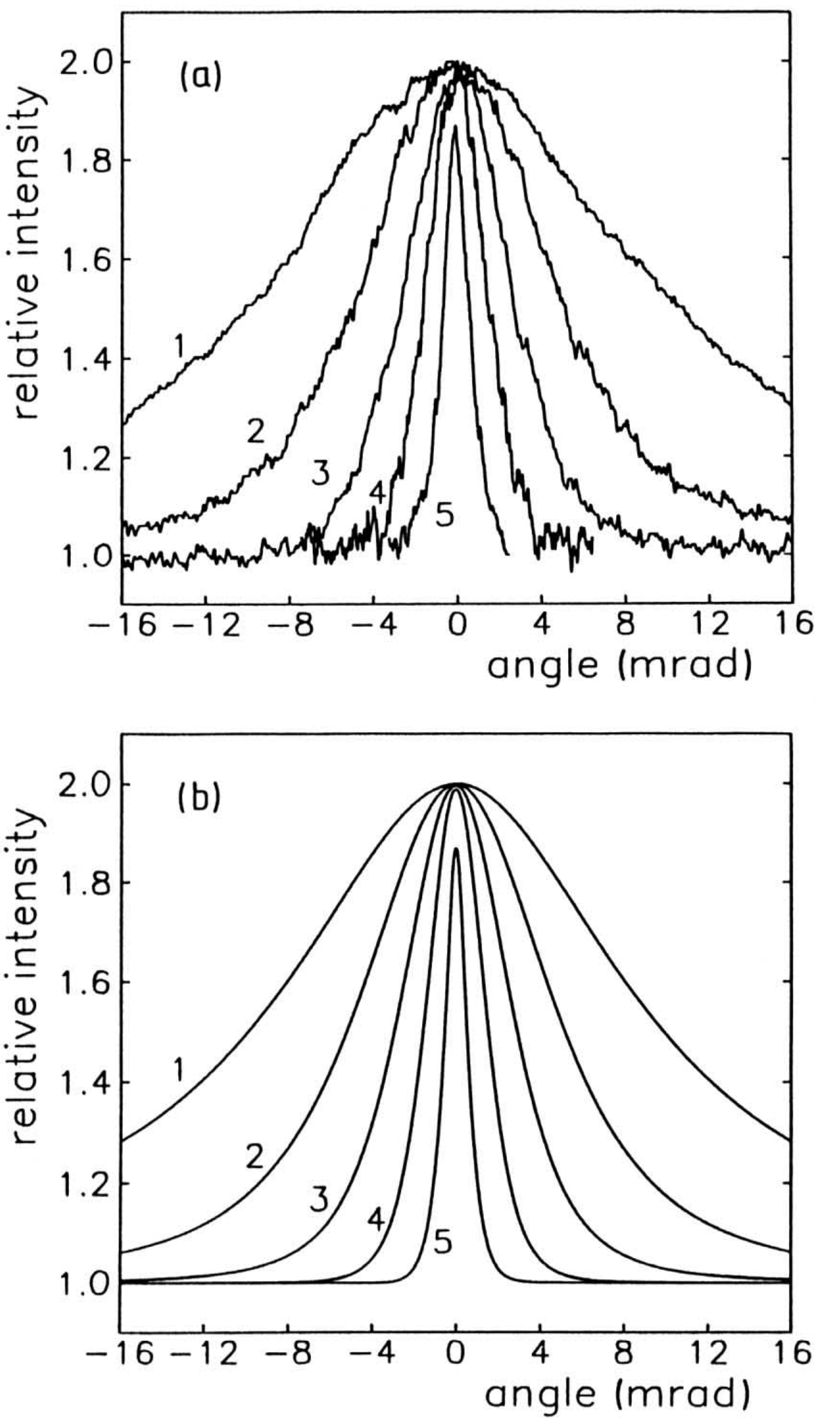

Figure 5.7: *(a) Normalized (see text) difference cones recorded for the parallel light component using the sample of Fig. 5.5.*
Difference slabs: curve 1: 0 - 13 μm;
curve 2: 13 - 25 μm; curve 3: 25 - 50 μm;
curve 4: 50 - 100 μm; curve 5: 100 - 1000 μm.
(b) Normalized backscattering curves, calculated from diffusion theory for the difference slabs of (a), using $\lambda_{tr} = 9.68\,\mu m$

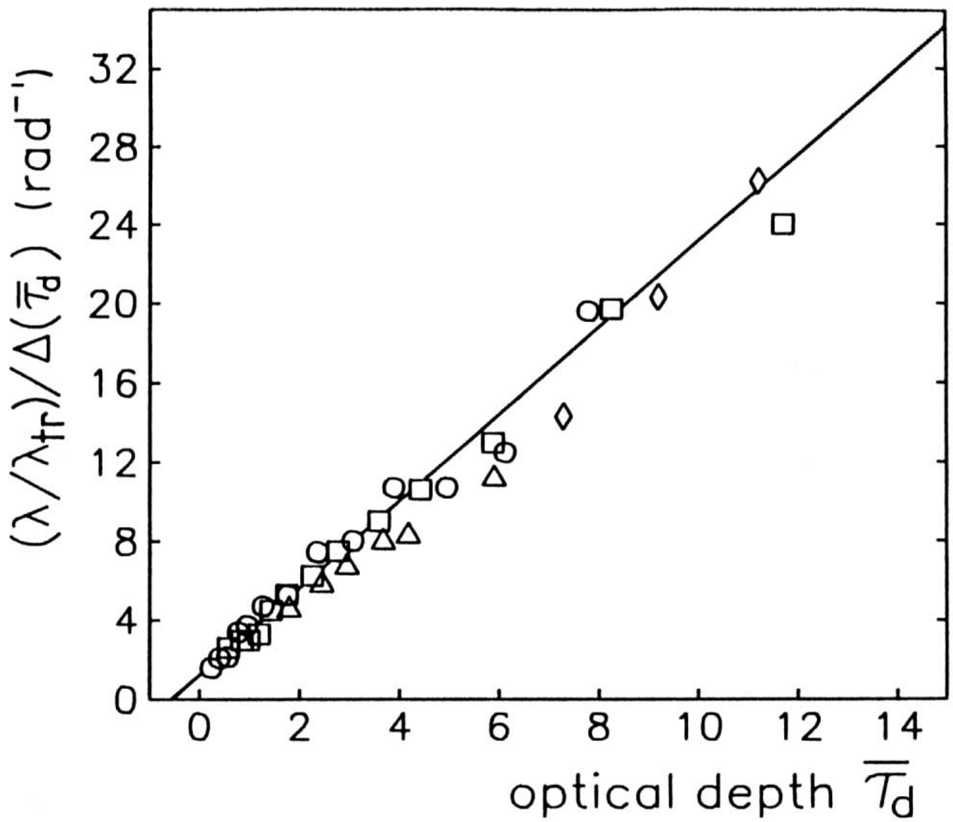

Figure 5.8: $(\lambda/\lambda_{tr})/\Delta(\overline{\tau_d})$ *versus* $\overline{\tau_d}$ *for difference slabs in samples of different volume fractions of* TiO_2 *particles in 2-methylpentane-2,4-diol.* $\bigcirc = 0.36$ *vol %;* $\square = 1.05$ *vol %;* $\triangle = 2.50$ *vol %;* $\diamondsuit = 9.81$ *vol %. line:* $(\lambda/\lambda_{tr})/\Delta(\overline{\tau_d}) = 2.2(\overline{\tau_d} + 0.5)$. *See also Fig. 4.12.*

found. To obtain the difference cone associated with this slab, a pattern containing a relatively big contribution *via* the rear-window (see before) is subtracted from one in which this contribution is attenuated by passing through a thicker slab. As a consequence the background of the resulting difference cone is too low, and the corresponding enhancement factor is too high. For deeper difference slabs, the enhancement factor seems to become constant. We have reported earlier on difference cones that were recorded using polystyrene spheres in water.[84] In that study we found an enhancement factor near 2 for a difference slab of two slabs with optical thicknesses $b_1 = 0.6$ and $b_2 = 1.8$. On the basis of our present results we believe that the effect of the rear-window may have played a part there and that the real factor is probably lower.

It remains to be explained why the experimental enhancement factors found are smaller than two. Single-scattering contributions can not be expected to be of importance in the backscattering patterns from deep slabs. Light paths that return to their starting point (loops) would contribute angle-independent interference terms and therefore also apparently reduce the enhancement factor. However, we expect the relative contribution of loops to decrease with increasing order of scattering, and decreasing concentration ($\rho \propto n_0$) (see Sect 4.6). Another possibility would be the contribution of the mixed type of diagrams which I also discussed in section 4.6, because there the density of scatterers is not explicitly involved, and therefore might also explain the results of the experiments with dilute samples.

From Figs. 5.7 and Table II it is obvious that the deeper a difference slab is situated in the sample, the narrower its contribution to the cone. The width of such a contribution is inversely proportional to the average distance between both ends of the light paths associated with the difference slab. Those light paths have in common that their deepest point is situated in that difference slab. Since the light performs a random walk, the average distance between the ends of a light path will be proportional to the greatest depth of that light path, which explains why the deeper a difference slab is situated in the sample, the narrower its contribution to the cone indeed.

Classes of light paths that traveled to the same *optical* depth τ_d in media with different λ_{mf} are expected to yield contributions to their respective cones of which the width relate as λ_{mf}^{-1}. In Fig. 5.8 we have plotted values of $(\lambda/\lambda_{mf})/\Delta(\overline{\tau_d})$ as found for series of difference cones from four different concentrations of TiO_2 suspensions versus $\overline{\tau_d}$ (where $\overline{\tau_d}$ is the average value of the optical thicknesses b_2 and b_1 of the subtracted slabs). The relationship between the two quantities was also evaluated from diffusion theory (*c.f.* Fig. 4.12) and for albedo $a = 1$ the result may be fitted as $(\lambda/\lambda_{mf})/\Delta(\overline{\tau_d}) \simeq 2.2(\overline{\tau_d} + 0.5)$. This relationship is shown in Fig. 5.8 as a continuous line. Good agreement with experiment is once more found. From Fig. 5.8 we conclude that the width $\Delta(\overline{\tau_d})$ of the contribution to the cone by a difference slab at depth L is proportional to $(L + \lambda_{mf}/2)^{-1}$ or, essentially independent of λ_{mf} once $L \gg \lambda_{mf}$.

In Fig. 5.9 experimental width W for complete cones of enhanced backscattering as measured for the light component polarized parallel to the incident beam are plotted versus $\lambda_{tr}/\lambda_{med}$, with λ_{med} the wavelength in the medium. The measurements for the TiO_2 samples where done at a wavelength $\lambda_{vac} = 514.5$ nm, all others at $\lambda_{vac} = 633$ nm. The experimentally found width was, using Snell's law, corrected for refraction at the interface of the sample, so the widths given in the figure correspond to a value as would have been found by a measurement in a medium with the same refractive index as that of the random medium. In fact, for high concentration ρ of scatterers, the *average* index of refraction rather than the refractive index of the solvent should be taken, and so λ_{med} is defined as:

$$\lambda_{med} \equiv \lambda_{vac}/[\rho n_{scat} + (1-\rho) n_{solv}] \ . \tag{5.1}$$

Notice that for localization $\lambda_{tr}/\lambda_{med}$ rather than $\lambda_{tr}/\lambda_{vac}$ is the important parameter. The refractive indeces of TiO_2 and 2-methylpentane-2,4-diol are 2.80 and 1.425 at $\lambda_{vac} =$

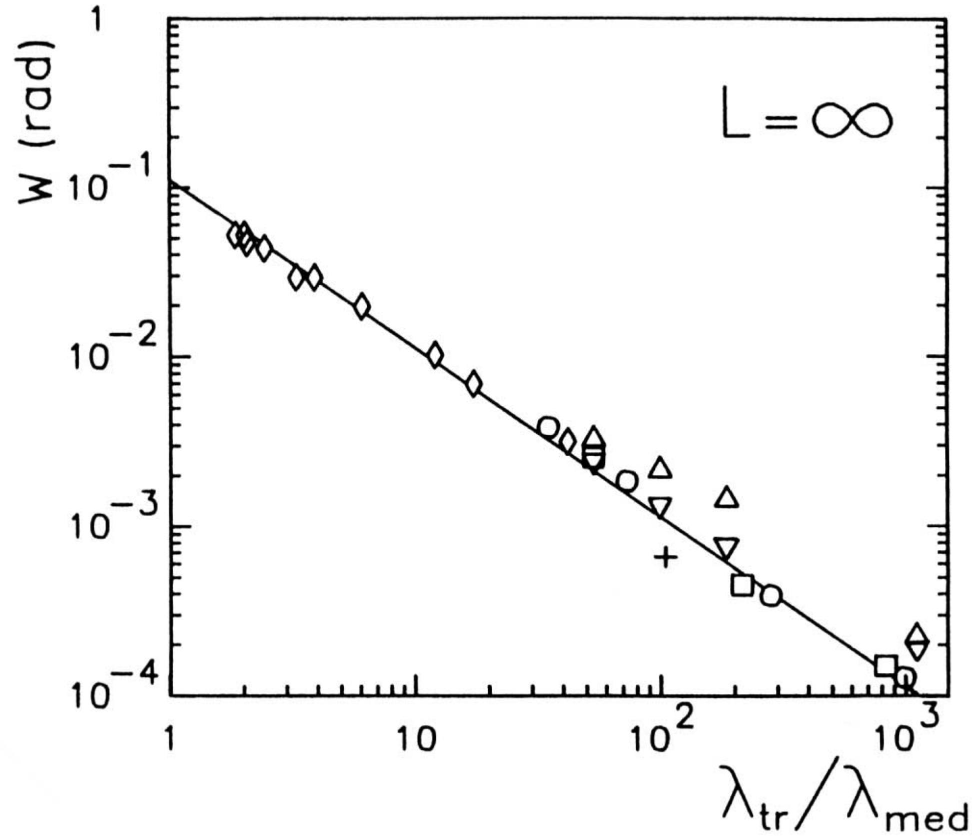

Figure 5.9: *Full width W of the cone of enhanced backscattering versus λ_{tr}/λ for very thick slabs. $\diamondsuit$ = 220 nm TiO_2 in 2-methylpentane-2,4-diol; $\bigcirc$ = 1.091 μm polystyrene speres in water; $\square$ = 0.482 μm polystyrene spheres in water; $\triangle$ = 0.214 μm polystyrene spheres in water ($\|$ scan); $\bigtriangledown$ = 0.214 μm polystyrene spheres in water ($\perp$ scan); + = 2.02 μm polyvinyltoluene spheres in water.*
line: $W \simeq (0.7/2\pi)(\lambda/\lambda_{tr})$, the extrapolated result from the exact theory for $b = \infty$.

514.5 nm respectively, and for water and polystyrene 1.33 and 1.59 at $\lambda_{vac} = 633$ nm. Our exact isotropic theory predicts that the two quantities should relate as

$$W \simeq \frac{0.7}{2\pi}(\lambda_{med}/\lambda_{tr}) \ . \tag{5.2}$$

This relationship is represented in Fig. 5.9 by a solid line, which is (except for the $\triangle$ data points that I will explain in the next section) in agreement with the experimentally found inverse proportionality of the data points. This demonstrates that the backscattering enhancement is indeed a result of interference, and not a geometrical effect. Historically seen, this is in fact one of the most important results in the field of localization because it is the direct *proof* of the actual persistence of *interference in disordered systems.*

5.2.2 Polarization effects in weak localization of light

So far I only discussed the scattering of *scalar* waves. Light is a transverse wave, it is what we call a *vector* wave. In the description of the propagation of light, this vector refers to the state of polarization. One of the reasons why localization of light is of particular interest, is because the vector character of electromagnetic waves introduces new aspects. This section deals with manifestations of the vector-wave character in the weak localization of light.

In light-scattering experiments on random media, one can distinguish three different effects of the vector character on the state of the scattered light. If a linearly polarized plane wave is used as a source, it is possible to observe the following polarization effects in the backscattered light from a slab:

(1) the polarized cone is spatially anisotropic,
(2) the depolarized light component also shows a slight enhancement,
(3) there is partial retention of polarization in the multiple-scattered light in the background.

It appears that the manifestation of these effects is strongly dependent on the particle size. We can distinguish essentially two types of scatterers, the small point-dipole scatterer (Rayleigh scatterer) and the bigger "spotlight" scatterer, which scatters in the forward direction mainly.

In three papers[84,89,90] we proved experimentally that the three effects are due to lower-order scattering contributions, and explained them. A computer simulation of enhanced backscattering from a medium containing randomly distributed Rayleigh scatterers confirmed our interpretation. Other workers also published on this subject.[67,68,91,92]

The importance of polarization as a parameter is illustrated in Fig. 5.10. The incident wave propagates in the direction perpendicular to the plane of the drawing, and is vertically polarized. The polarization vectors of the waves that are backscattered via the "light paths" s_1, s_2, s_3 and s_3, s_2, s_1 are $\vec{P}^{+}$ and $\vec{P}^{-}$ respectively. It is seen that the polarized components $\vec{P}_{\parallel}^{+}$ and $\vec{P}_{\parallel}^{-}$ are equal, whereas the depolarized components $\vec{P}_{\perp}^{+}$ and $\vec{P}_{\perp}^{-}$ are not. Thus, in the 180° direction there will be constructive interference (doubled intensity) in the polarized component, whereas in the depolarized component the interference depends on the geometry of the light path, and may be anything from totally constructive to totally destructive. From this, one would expect enhancement factors slightly lower than two for the polarized component (the single scattering contribution to backscattering has no interference term) and near one for the depolarized component.

The relative importance of the different orders of scattering depends on the scattering function $S(\theta)$ of the scatterers, and therefore the shape of the cone may depend on e.g. particle size. Very small particles show deviating behavior in Fig. 5.9. Intensity profiles as recorded for the polarized and depolarized components of the light backscattered from

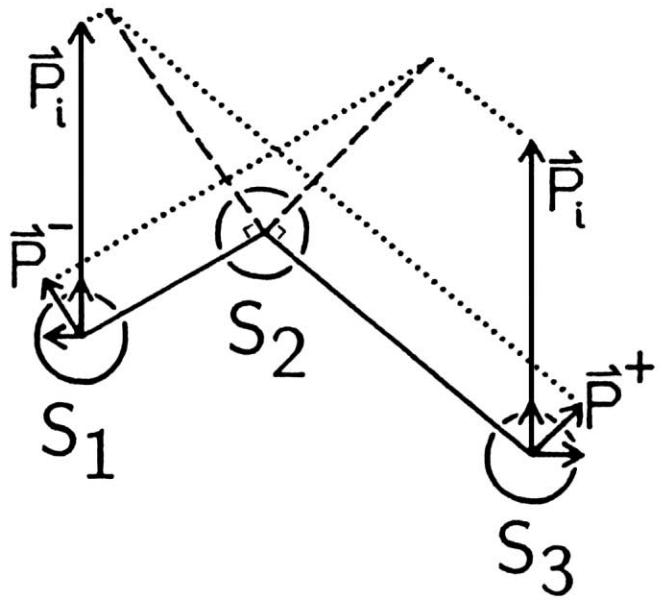

Figure 5.10: *Three-paricle scattering via s_1, s_2, s_3 and s_3, s_2, s_1 of light with polarization vector $\vec{P}_i$, incident in the direction perpendicular to the plane of the drawing. The components of the backscattered light of $\vec{P}^+$ and $\vec{P}^-$ parallel to $\vec{P}_i$ are equal, whereas the perpendicular components are not.*

a thick 9.6 vol% sample of 0.215 μm polystyrene spheres in water are shown in Fig. 5.11a. The lower curve corresponds to the depolarized component, the upper and middle curves to the polarized component scanned parallel and perpendicular to the direction of incident polarization respectively. It is seen that the background backscattered light is partially polarized, the enhancement factor $I_{top}/I_{background}$ is somewhat less than two for the polarized component and slightly larger than one for the depolarized component, and the intensity profile for the polarized component is spatially anisotropic. The curves in Fig. 5.11b were obtained by subtracting intensity profiles recorded for a thin sample from those of the thick sample. Thus, the contributions from short light paths that never enter the "deep" part of the thick sample cancel out, and what remains is the contribution of light paths long enough to have passed through this deep part. Comparing the curves associated with long light paths, we see that background polarization is now almost completely scrambled, the intensity profile of the polarized component is isotropic, and no enhancement is left in the depolarized component. It follows that the three polarization effects are due to lower-order scattering.

Figure 5.12 shows data corresponding to those of Fig. 5.11a but recorded using a 1500 μm sample of 9.6 vol% 1.091 μm spheres. The background polarization is nearly completely scrambled, and no spatial anisotropy is seen in the polarized cone. On the

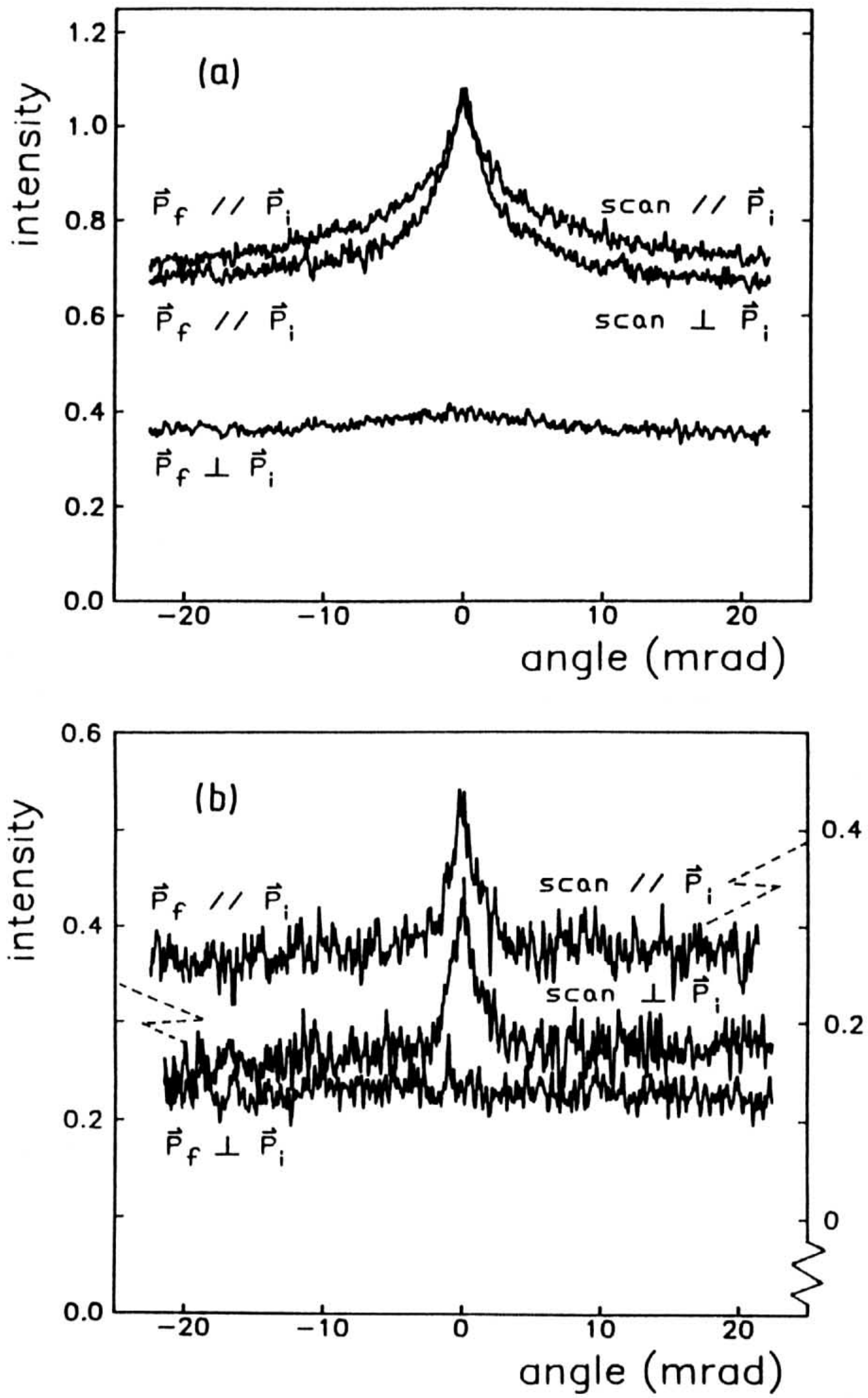

Figure 5.11: *(a) Coherent backscattering from a thick slab (2400 μm) of 9.6 vol % 0.215 μm polystyrene spheres in water ($\lambda_{vac} = 633$ nm). upper curve: polarized component, scan $\parallel \vec{P}_i$. middle curve: polarized component, scan $\perp \vec{P}_i$. lower curve: depolarized component ($\parallel$ and $\perp$ scans coincide). (b) as for (a), but from the "deep" slab between 60 and 2400 μm behind the interface of the sample.*

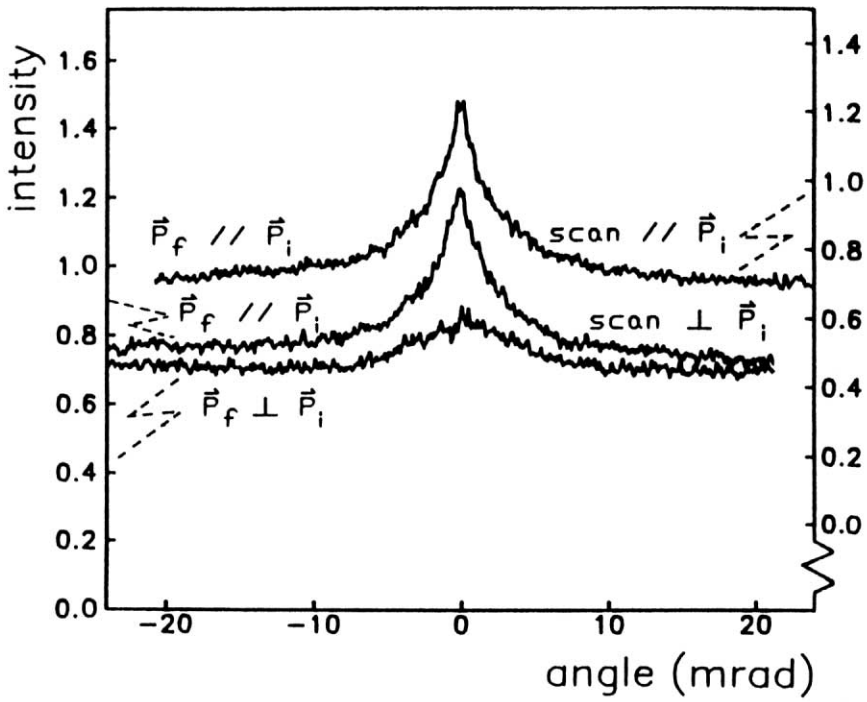

Figure 5.12: *Backscatter cones from a 1500 μm slab of 9.6 vol % 1.091 μm polystyrene spheres in water ($\lambda_{vac} = 633\,nm$).*
upper curve: polarized component, scan $\parallel \vec{P}_i$.
middle curve: polarized component, scan $\perp \vec{P}_i$.
lower curve: depolarized component.

other hand the enhancement in the depolarized component is more pronounced here.

So if we compare Figs. 5.11 and 5.12, we find the following differences:

- For the smaller scatterers, polarization is partly retained in the backscattered light (as may be seen from the relative levels of the incoherent background for both polarizations) indicating that (very) low- order processes play an important part in the total backscattering. For the larger scatterers, the scambling of polarization is very nearly complete.

- For the smaller scatterers the parallel cone is spatially anisotropic, being broader in the scan parallel to the polarization of the incident beam than in the perpendicular direction. The triangular tops are equally wide in both scans, indicating that the broadening of the cone in the parallel scan is a lower-order multiple scattering effect.

- The perpendicular cones have rounded-off tops, indicating that only short paths (lower-order scattering processes) contribute.

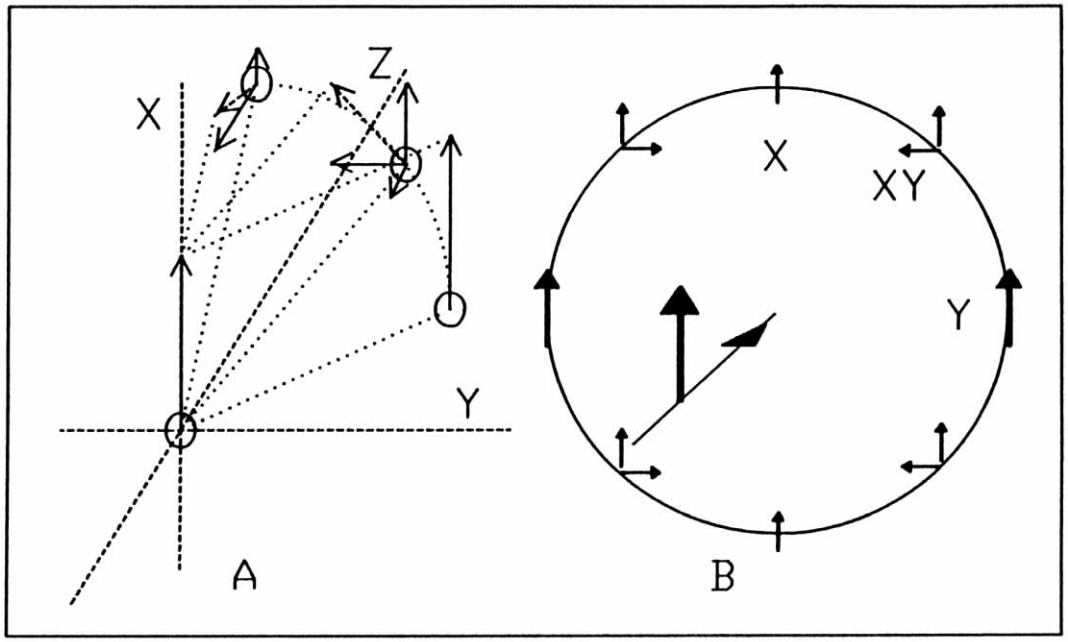

Figure 5.13: *(a) Three second-order light paths for Rayleigh scattering.*
(b) Direction and amplitude of the backscattered wave in second-order Rayleigh scattering as a function of the relative orientations of the scattering particles.
(c) Stereoscopic pair of (a).

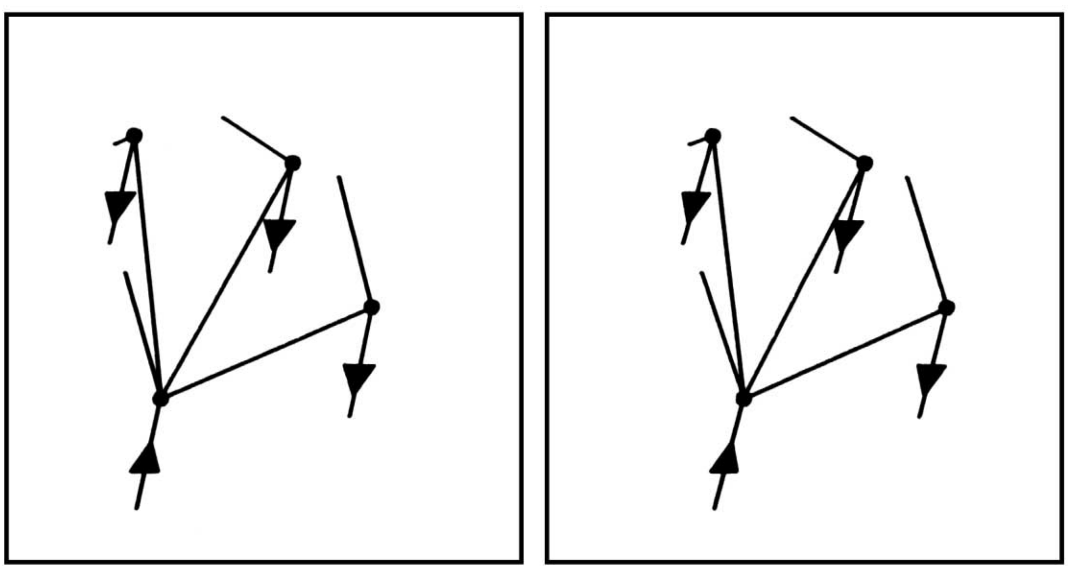

In the previous chapter we have seen that a lot of theoretical work has already been done to explain the shape and width of the backscatter cone of the isotropic scattering of scalar waves: A rigorous theory[61,66] and diffusion approximations[61,78,93] have been developed. The shape and width of the backscatter cone predicted by these scalar theories agree quite accurately with those found experimentally in the polarized light component for all but the smallest scatterers, but scalar theory can not be used to describe the depolarized component.

In other work the vector character is considered: The enhancement factor for the depolarized component for multiple Rayleigh scattering was calculated,[89] and diffusion theory for point-dipole scattering was developed,[67,91] which correctly predicts the partial retention of polarization and the weak enhancement in the depolarized component, but not the spatial anisotropy in the polarized cone.

From here we will present qualitative explanations in terms of the symmetry of the scattering function $S(\theta)$ of the particles for the observed vector character effects. Since these effects originate from low-order multiple-scattering processes, we will discuss them on the basis of properties of the very lowest-order processes that contribute significantly to the backscattering.

For the small-particle case we will assume Rayleigh scattering. In Fig. 3.5 the radiation pattern of a typical small particle is given. For those particles the second-order scattering contribution to the coherent backscattering is larger than that of any other individual order. In a second-order process there is only one plane of scattering through the scattering particles and the polarization direction, and therefore the interference between time-reversed waves is always constructive in both the polarized and depolarized components (see Fig. 5.13a). Figure 5.13b represents a part of the air-sample interface; $x-$polarized light is incident in the z direction. The directions of polarization and the relative amplitudes of waves scattered via a first particle somewhere at the negative z axis and a second particle somewhere behind the interface areas marked x, y and xy are represented by vectors.

In the Mie case (see Fig. 3.6 for the scattering function of a typical Mie particle), the power scattered by a particle is almost completely confined to a cone in the forward direction, the apex angle θ of which decreases with increasing size of that particle. As a consequence, light paths including scattering angles $> \theta$ will contribute very little. The very lowest-order light paths that do contribute significantly to the backscattering are therefore essentially coplanar configurations of π/θ scatterers (see Fig. 5.14a). Figure 5.14b shows the large-scatterer limit for the direction of polarization and the relative amplitude of a scattered wave as a funtion of the relative orientation of the two ends of a lowest-order light path. Since within the narrow cone of forward scattering associated with larger particles the amplitude of the scattered wave is practically independent of the angle ϕ between the incident polarization and the normal to the plane of scattering ($S_{\parallel}(\theta) \simeq S_{\perp}(\theta)$), the x, y, and xy processes are equally efficient in this limit.
From Figs. 5.13b and 5.14b the vector character effects are easily understood:

(1) The spatial anisotropy found in the polarized cone of small-particle samples results

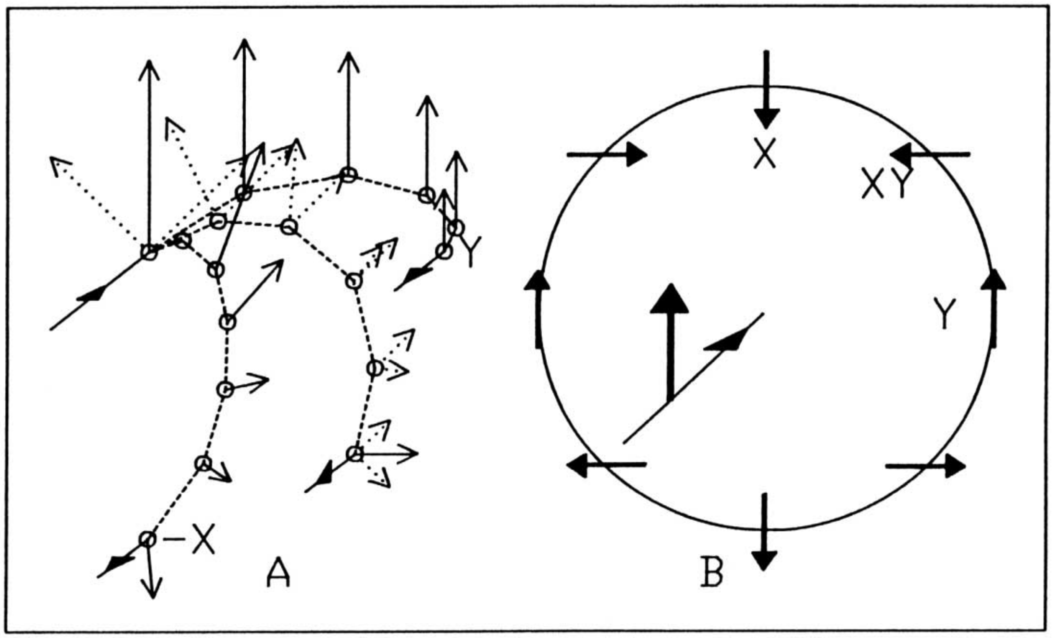

Figure 5.14: *(a) Three "lowest"-order light paths in (large particle) Mie scattering.*
(b) Direction and amplitude of the backscattered wave as a function of orientation of the "shortest" light path in Mie scattering.
(c) Stereoscopic pair of (a).

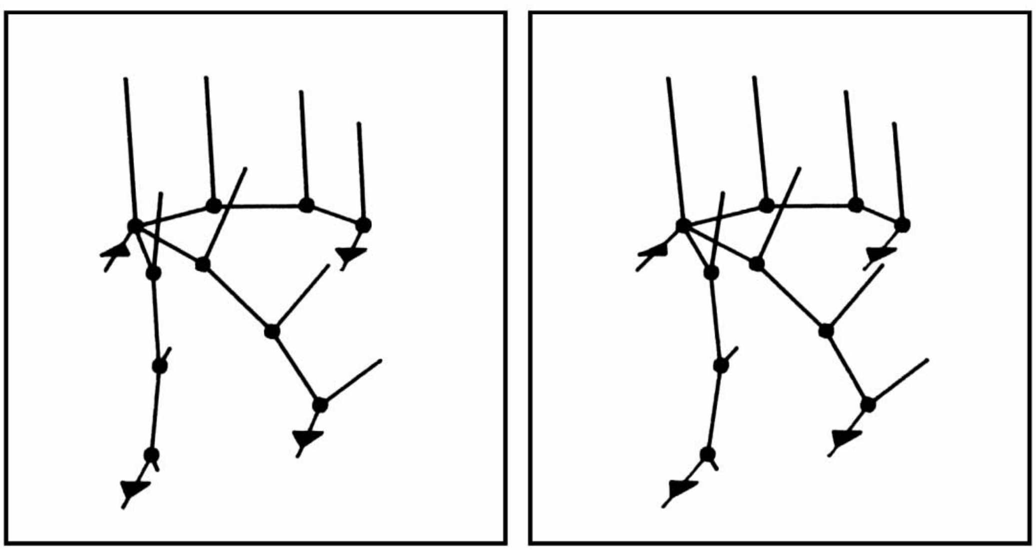

from the circumstance that the separation between both ends of the average polarization-preserving light path is larger in the y direction than in the x direction. On average, the two-point-source interference patterns that constitude the cone are therefore broader in the x than in the y direction. In the large-particle limit this anisotropy does not occur

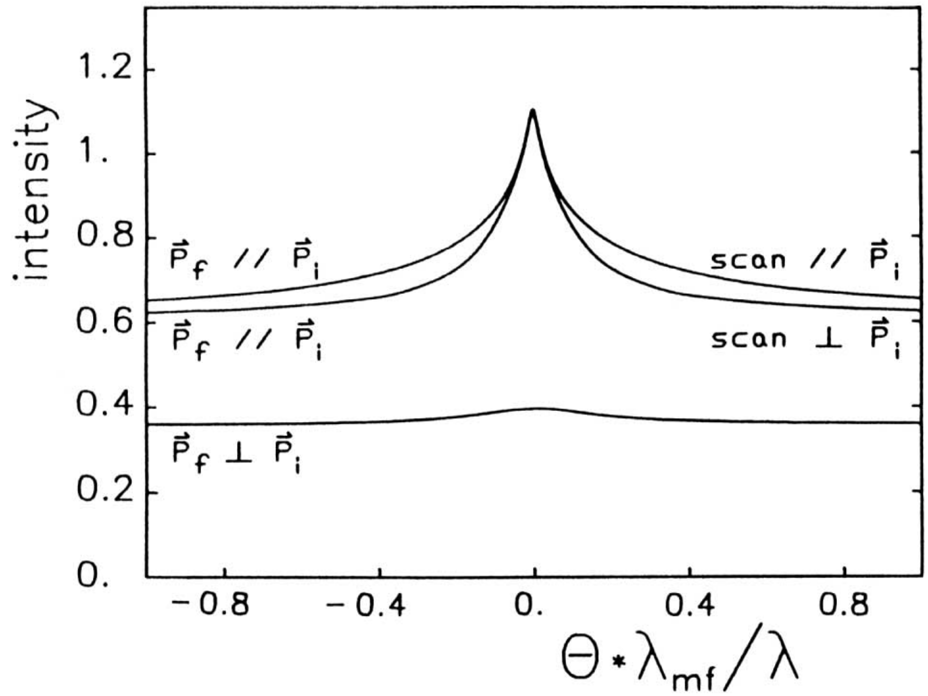

Figure 5.15: *Simulated backscatter cones for multiple Rayleigh scattering; attribution of curves as in Fig. 5.11 (from Ref. 89).*

(see Fig. 5.14b).

(2) Enhancement in the depolarized component will occur if constructive interference between the depolarized components of time-reversed pairs of waves outweighs destructive interference. In both the small- and large-particle limits we find that in the lowest-order light paths the scattering centers are in a coplanar configuration and therefore the polarization vectors of the time-reversed waves are parallel. With increasing order the light paths may assume more arbitrary shapes, and in the depolarized component destructive interference will become increasingly important, until in the high-order limit it balances constructive interference. Because of the low-order contributions, a net excess of constructive interference (and hence enhancement) in the depolarized component will occur in both the small- and large-particle limits, in contrast to the partial retention of polarization and anisotropy, which only occur in the small particle case.

(3) The partial retention of polarization found for small-particle samples occurs because in this case much of the original polarization survives low- order scattering processes. In large-particle samples even the lowest-order light paths that contribute to an important extent completely scramble the polarization.

We verified our explanation for the spatial anisotropy in the polarized cone for Rayleigh scatterers by simulation.[89] Simulated values for the full width at half maximum W^n for

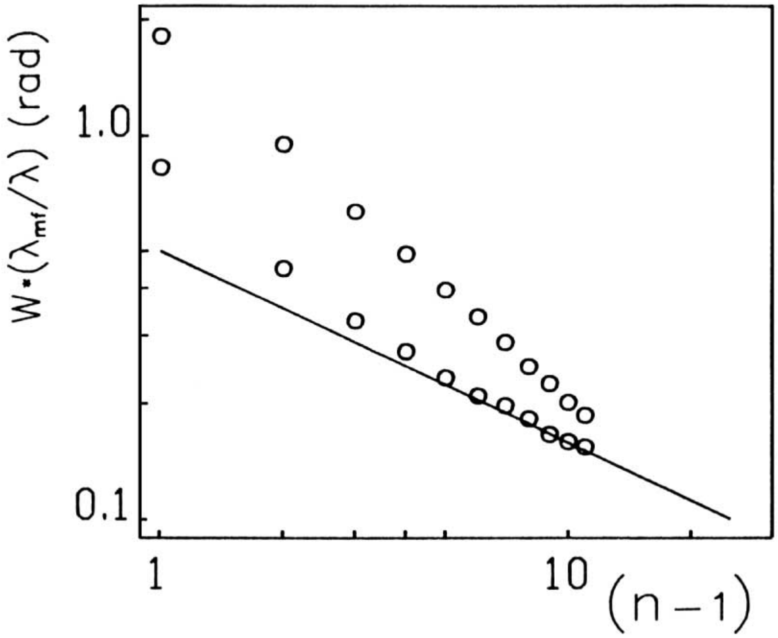

Figure 5.16: *The width W^n of simulated backscatter cones for the polarized component as a function of the order of scattering in case of Rayleigh scattering (from Ref. 89).*
upper series: scan $\parallel \vec{P}_i$, lower series: scan $\perp \vec{P}_i$,
solid line: $W^n = \lambda/(\lambda_{mf} 2\sqrt{n-1})$.

$x-$ and $y-$scans of the n^{th} order polarized cone for a slab of thickness $20\,\lambda_{mf}$ are given in the Fig. 5.15. For low n the values are larger for the (parallel) $x-$scan than for the (perpendicular) $y-$scan. For high n, the value W_x^n/W_y^n converges towards unity, so the high order asymptotic behavior is the same for both scanning directions. By extrapolation of the W_y^n-values, the empirical relationship $W^n = \lambda/(\lambda_{mf} 2\sqrt{n-1})$ obtains, shown as a solid line in Fig. 5.15. Fig. 5.16 shows the $x-$ and $y-$polarized intensity profiles as calculated for the orders $1-1000$, using simulated contributions for the orders $2-12$, and assuming high-order asymptotic behavior for the orders from 13 upward. It is seen that indeed the anisotropy of the Rayleigh phase function leads to anisotropy in the polarized cone.

An analogous simulation for large-particle scattering is possible, but requires much more computing time. This difficult job was however performed in our group by Roos Eisma. The results indeed confirm our interpretation of the measured polarization effects.

A more quantitative explanation of the three vector-character effects for the Rayleigh scatterers is possible,[89,94] which I will present here. Suppose light with polarization vector $\vec{P}_i$ is incident in the z direction, and consider the pair of light paths s_1, s_2, …, s_n.

The polarization vectors $\vec{P}^+$ and $\vec{P}^-$ of the waves emerging from s_n and s_1. In the $-z$ direction are parallel to the $z = 0$ plane (as is $\vec{P}_i$), and therefore relate to $\vec{P}_i$ according to $\vec{P}^+ = M^+\vec{P}_i$ and $\vec{P}^- = M^-\vec{P}_i$, M^+ and M^- being (2x2) matrices, related by $M^- = (M^+)^T$. Let s_1 be located in the origin and let (x_n, y_n, z_n) be the position of s_n. If the direction of observation is changed over a small angle θ, this will hardly affect the matrix elements M_{ij}. On the other hand, phase shifts of $\simeq x_n \sin\theta/\lambda$ and $\simeq y_n \sin\theta/\lambda$ respectively will develop for displacements of the detector in the (x, z) and (y, z) planes. If θ is sufficiently large, the phase shift for individual light paths will be random and the detected depolarized and polarized intensities will be $\langle M_{12}^2\rangle + \langle M_{21}^2\rangle = 2\langle M_{12}^2\rangle$ and $2\langle M_{11}^2\rangle$ respectively (the triangular brackets represent averaging over all light paths). The intensities observed in the $-z$ direction will be $\langle(2M_{11})^2\rangle$ and $\langle(M_{12} + M_{21})^2\rangle$. For the enhancement factors in the polarized and depolarized components $E_\parallel$ and $E_\perp$ and for the polarized and depolarized fractions of the total backscattering $F_\parallel$ and $F_\perp$ it follows

$$E_\parallel = \frac{\langle(2M_{11})^2\rangle}{2\langle M_{11}^2\rangle} = 2 , \tag{5.3}$$

$$E_\perp = 1 + \frac{\langle M_{12}M_{21}\rangle}{\langle M_{12}^2\rangle} , \tag{5.4}$$

$$F_\parallel = \frac{\langle M_{11}^2\rangle}{\langle M_{11}^2\rangle + \langle M_{12}^2\rangle} , \tag{5.5}$$

$$F_\perp = \frac{\langle M_{12}^2\rangle}{\langle M_{11}^2\rangle + \langle M_{12}^2\rangle} . \tag{5.6}$$

It is easily seen that for 2$^{\mathrm{nd}}$ order backscattering $M_{12} = M_{21}$, and this already suffices to explain that $E_\perp > 1$. Likewise, if the angle between the incident polarization vector $(\hat{x})$ and the normal to the scattering plane is ϕ, the backscattered polarized amplitude will have maxima for $\phi = 0,\ \pi$, and minima for $\phi = \pi/2,\ 3\pi/2$, so that for the polarized component the average light path has $y_n > x_n$. Thus, a displacement of the detector over an angle θ in the (y, z) plane will affect the average phase shift to a larger extent than would an equal displacement in the (x, z) plane or, the 2$^{\mathrm{nd}}$ order contribution to the polarized "cone" is broader in the $x-$ than in the $y-$direction. Moreover, for 2$^{\mathrm{nd}}$ order scattering $\langle M_{11}^2\rangle > \langle M_{12}^2\rangle$ so that polarization is partially retained.

So, the 2$^{\mathrm{nd}}$ order contribution to the backscattering exhibits the three polarization effects. Let us now evaluate the sum of the contributions of all orders: if C_n is the fraction of the total backscattered intensity that is due to n^{th} order scattering processes, the total depolarized enhancement factor will be

$$E_{\perp,tot} = \frac{\sum_{n=1}^{\infty} C_n F_{\perp,n} E_{\perp,n}}{\sum_{n=1}^{\infty} C_n F_{\perp,n}} \tag{5.7}$$

Assuming Rayleigh scattering it can be calculated[89] that

$$E_{\perp,n} = 1 + \frac{3}{2}\left(\frac{0.7^{n-1} - 0.5^{n-1}}{1 - 0.7^{n-1}}\right) , \tag{5.8}$$

$$F_{\perp,n} = \frac{\langle (M_{12}^{(n)})^2 \rangle}{\langle (M_{11}^{(n)})^2 \rangle + \langle (M_{12}^{(n)})^2 \rangle} = \frac{1 - 0.7^{n-1}}{2 + 0.7^{n-1}} , \tag{5.9}$$

A simulation[89] yielded values for C_n that fit well to $C_n \simeq 2[(n+3)^{-1/2} - (n+4)^{-1/2}]$. By substitution in (5.7) we find $E_\perp \simeq 1.11$. (Vector) diffusion theory yields $E_\perp \simeq 1.12$,[67] and for the samples described in the previous subsection it was found that $E_\perp = 1.12 \pm 0.02$.

5.3 On the factor of two

Basically the theory of weak localization is well understood. The shape and width of the backscattered intensity profile in a variety of experimental situations are reasonably well described. A disturbing feature however is the enhancement factor, defined as the ratio of the total backscatter intensity and the incoherent background intensity. An accurate experimental determination of the factor is difficult for technical reasons and because the factor depends on the nature of the scatterers involved. Some experimentalists maintain that they found evidence for an enhancement factor differing from two, whereas others claim that an exact factor of two is being measured.

So far, all theories add up to a description of backscattering in terms of exclusively self-avoiding light paths (ladder diagrams) and interference exclusively between time-reversed pairs of such paths (most-crossed diagrams). This description leads to a doubling of the intensity of all multiple-scattering contributions in the 180° direction both for scalar waves and for the parallel polarized component in the case of vector waves, since each multiple-scattering ladder diagram has a most-crossed counterpart. The first-order ladder diagram however, is identical to its most-crossed counterpart (time-reversal symmetry) and does not yield an interference term. The single-scattering contribution therefore is not doubled in the 180° direction. In the case of isotropic scattering of scalar waves by pointscatterers, the single-scattering contribution is about 12 % of the incoherent background intensity.

Some time ago it was stated that the phenomenon of weak localization for scalar waves is principally different from that of electromagnetic waves in the sense that electromagnetic theory in contrast to scalar theory would allow for an enhancement factor differing from two.[96] This statement is based upon a misinterpretation of theoretical results of Stephen and Cwillich,[67] who calculated the enhancement factors in the backscattering of scalar- and vector waves, neglecting single scattering in the scalar case but not in the vector case.

If in addition to the self-avoiding light paths also non-self-avoiding paths are considered, classes of diagrams may be identified that will further decrease the predicted enhancement factor.[60] I already discussed two of those classes of light paths in Sect. 4.6, which are expected to scatter almost isotropically (angle-independent) and therefore apparently contribute to the incoherent background. The so-called boomerang diagrams in fact renormalize the first-order scattering efficiency, and their contribution may be up to a few percent of the total first-order scattering, depending on the density of scatterers, and their complex scattering amplitude f. In addition one can easily indicate time-reversal invariant more-particle scattering events ("loop"-type boomerang diagrams). I do not have an indication about the contribution of the mixed ladder-crossed diagrams yet, but it can of course be calculated from the results in Sect. 4.6.

So far, neither the multiple-scattering time-reversal invariant diagrams nor isotropic interference contributions had been included in the theoretical work. I showed that in addition to the well-known incoherent background (ladder diagrams) and interference contribution between time-reversed events (cyclical diagrams) other contributions to the backscattering from a random medium exist. The experimental observation of these events would make this area of research unique in the field of physics of scattering as to the experimental possibility of discrimination between various types of multiple-scattering events. We tried to measure the contribution of the simple boomerang diagrams from Sect. 4.6 in a transmission experiment, but did not succeed because apparently the experimental error was too large, mainly due to many unknown subtleties in the properties of the sample.

In the Rayleigh limit "the problem with the factor of 2" can be solved by assuming the existence of a correlation between the incident and scattered wave[97] in single scattering: If a wave is only *singly* scattered, apparently both the way to and from the scatterer are clear, so there is *no* attenuation of the scattered wave when it comes out of the medium (this statement is not generally accepted). So in case of correlation we should drop the attenuation for singly scattered light which leaves the slab in the reversed way it came in. Thus Eq. (4.54) is apparently wrong, and should for retroreflection ($\mu_i = \mu_s = \mu$) read

$$\gamma_s(\mu_i = \mu_s = \mu) = a[1 - \exp(-b/\mu)] \tag{5.10}$$

which for thick slabs gives twice the amount of single scattering compared to Eq. (4.54). Moreover, this means that the source function $S(\tau)$ for the diffusive multiple-scattering intensity $J(\tau)$ is reduced, which amplifies the effect even more.

In our group, Roos Eisma did a simulation on a slab in which she took care of the mentioned correlation. For Rayleigh scatterers with a size parameter $x = 0.013$ this leads to a single-scattering fraction in the background of about 40%, and hence an enhancement factor near 1.6. A typical example, comparable to Fig. 5.13a is given in Fig. 5.17. For larger scatterers however, where the backward radiated intensity is not a substancial part of the scattering by the particle (see Fig. 3.6), the enhancement factor found by simulation remains essentially 2.

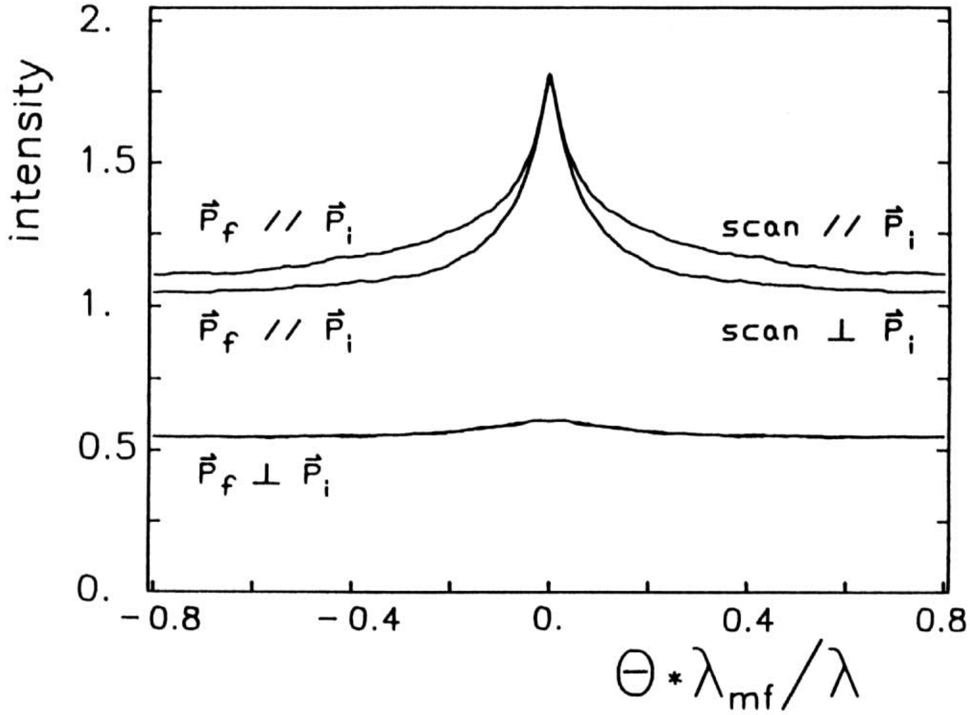

Figure 5.17: *Simulated coherent backscattering for polystyrene microspheres (n = 1.59) with a diameter of 200 nm in water (n = 1.33) at $\lambda_{vac} = 633$ nm. The enhancement factor is significantly lower than 2. (Simulation by Roos Eisma)*

It is clear that the question of the enhancement factor still deserves much more study, both experimentally and theoretically.

5.4 Time-resolved experiments

5.4.1 Measurement of the backscattering

The relationship between path length and width of the contribution to the coherent backscattering cone was studied in a time-resolved experiment by Vreeker and coworkers,[41,42] which I will describe here shortly. A Colliding-Pulse-Modelocked (CPM) laser was used to generate 70 fs pulses at a center wavelength of 620 nm. Fig. 5.18 shows cones recorded at 30 fs and 330 fs after the CPM-laser pulse respectively, using a 6.8 vol% TiO_2 in 2-methylpentane-2,4-diol sample ($\lambda_{tr} \simeq 2\,\mu$m). The theoretical curves were calculated from the approximate diffusion theory from Sect. 4.4 in which the shape of the backscattering cone is found by integration over all contributing path lengths, with a fixed depth of the first and last scatterer at one optical depth under the surface of the slab ($\tau_1 = \tau_2 = 1$):

$$\gamma_c(\mu_s,\mu_i;\hat{t}\,) \simeq \frac{\mu_i^{-1}}{u^2+v^2}[1+\exp(-2vb)-2\cos(ub)\exp(-vb)] \times\ \Gamma(\tau_1=1,\tau_2=1;\alpha;t)\ , \quad (5.11)$$

with $\hat{t}=t+\mu_s^{-1}+\mu_i^{-1}$, and where $\Gamma(\tau_1=1,\tau_2=1;\alpha;t)$ is given by Eq. (4.148). So for $a=1$ and $b=\infty$ we find

$$\gamma_c(\mu_s,\mu_i;\hat{t}\,) \simeq \frac{(\mu_i t_{mf})^{-1}}{u^2+v^2}\sqrt{\frac{3}{4\pi t}}\left\{1-\exp[-\frac{3}{2t}(1+\tau_0)^2]\right\}\exp(-\frac{\alpha^2 t}{3})\ , \quad (5.12)$$

which for α small and t large gives

$$\gamma_c(\theta,t) \simeq \frac{3}{4t_{mf}}\sqrt{\frac{3}{\pi}}(1+\tau_0)^2 t^{-3/2}\exp\left(-\frac{tk_0^2\theta^2}{3\kappa^2}\right)\ . \quad (5.13)$$

The equation describes a Gaussian-shaped backscattering cone with a width of the order $\lambda/(\lambda_{mf}\sqrt{t})$. In principle the equation is only valid for times t long enough for the scattering

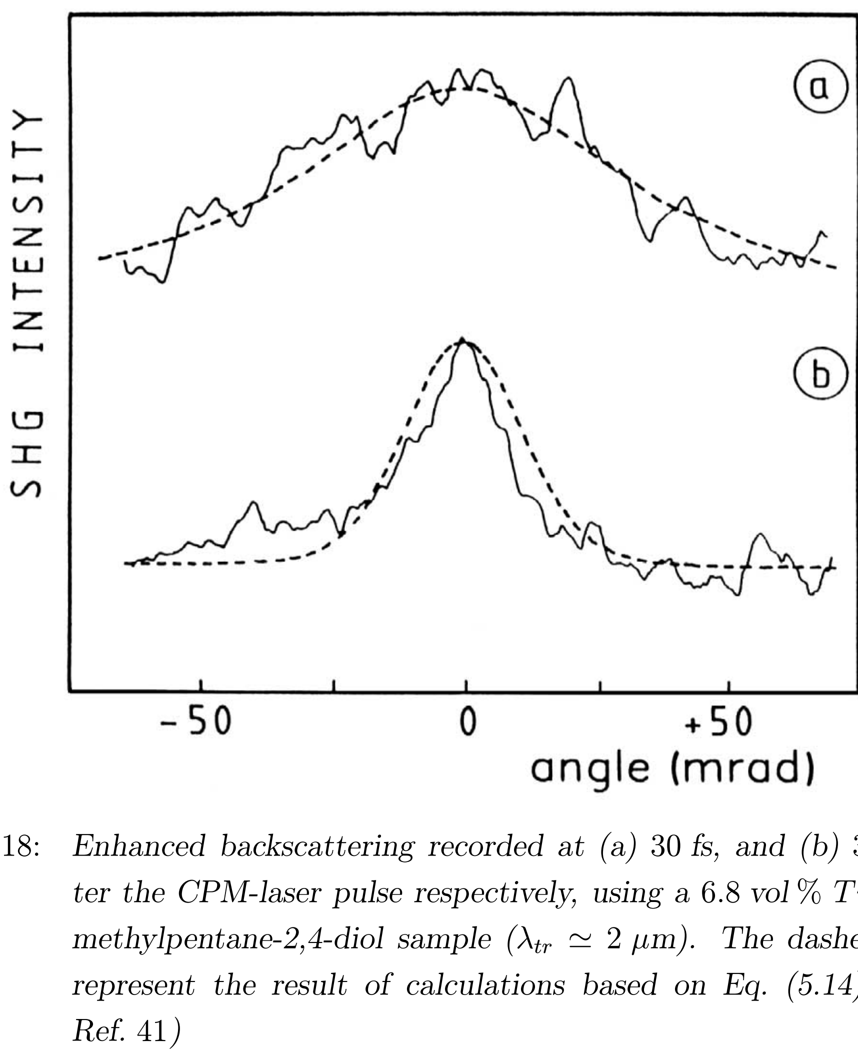

Figure 5.18: *Enhanced backscattering recorded at (a) 30 fs, and (b) 330 fs after the CPM-laser pulse respectively, using a 6.8 vol% TiO_2 in 2-methylpentane-2,4-diol sample ($\lambda_{tr} \simeq 2\ \mu m$). The dashed curves represent the result of calculations based on Eq. (5.14). (from Ref. 41)*

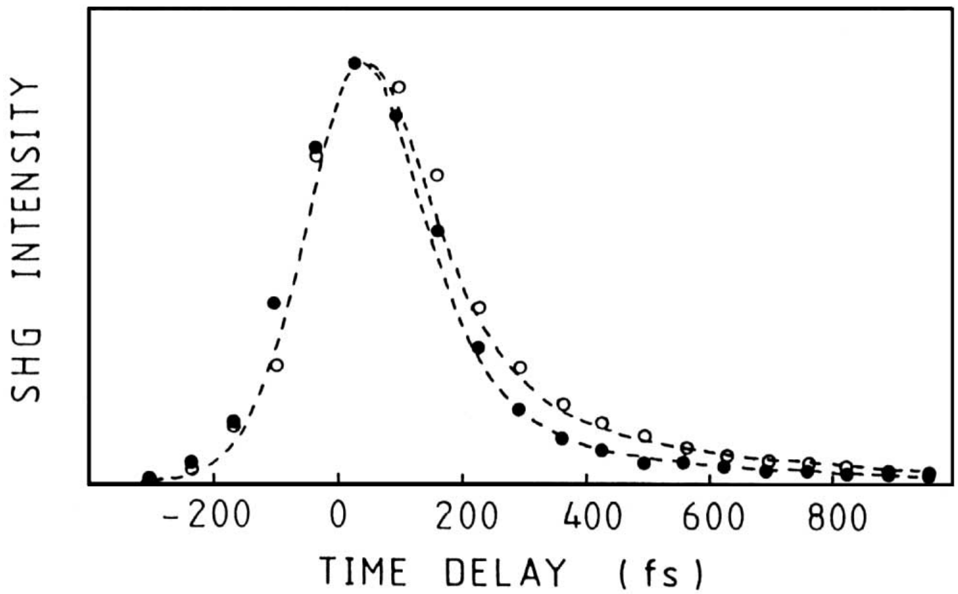

Figure 5.19: *Backscattered intensity as a function of time from the sample of Fig. 5.18 measured for $\theta = 0$ mrad (open circles) and $\theta = 27$ mrad (full circles). The dashed curves represent the result of calculations based on Eq. (5.14) (from Ref. 42).*

to have reached the diffusive limit, but this condition was apparently met within the error of the experiment, since the data are well described by the theory. Since the duration of the pulses from the laser is, although very short, still comparable to the delay between the excitation and probe, the observed intensity at a particular angle θ still has to be convolved with the pulse shape. We then get

$$\gamma_c'(\theta, t) = \int\!\!\int \gamma_c(\theta, t - t' - t'') I_p(t') I_p(t'') dt' dt'' \ , \tag{5.14}$$

in which the first integral gives the backscattered signal as a convolution of the impulse response function of the scattered $\gamma(\theta, t)$ with the incident pulse shape $I_p(t)$. The second integral gives the measured signal as a convolution of the backscattered signal with a light-gating pulse, which is used in case of ultra fast detection. In this particular case, a second-harmonic generation (SHG) technique was used.

In Fig. 5.18 theory and experiment are compared. The structure in the experimental curves is due to speckle, which in a time-resolved experiment on femtosecond scale can not be averaged out by e.g. spinning the sample for practical reasons. The agreement between theory and experiment is excellent.

Fig. 5.19 shows the time decay of pulses scattered from the sample, as measured at fixed angles with the direction of pure backscattering. At exact backscattering interference between time-reversed pairs is constructive at all times. At small angles with the backscattering direction, the time-reversed pairs dephase with $t^{1/2}$, and hence their coherent contribution decays during a short period following the laser flash. At longer times, only the incoherent contribution persists, which corresponds to half the intensity at pure backscattering.

5.4.2 Time-resolved measurement of the diffusion constant

As I have pointed out before, the most important parameter in the study of localization is the diffusion constant. The most direct, and therefore potentially the most accurate way to determine this constant, is to measure the transmission of a short laser pulse through the slab as a function of time. In a transmission experiment, one really probes the transport in the *bulk* of the medium. However, measurement of the transmission in a time-resolved experiment has some difficulties. On the one hand, one wants to obtain a large spread in time of the output pulse compared to the input pulse in order to have sufficient time resolution, where on the other hand enough transmitted intensity is required to detect the signal.

It appears that both conditions are not easily met at the same time for the kind of samples that are interesting in the study for Anderson localization. This is because the diffusion constant D is still to high to have enough time resolution to do the experiment with electronic devices (response time $\tau_{resp} \simeq 40$ ps) unless the samples are made so thick, that the absorption of the scatterers causes the transmitted intensity to drop exponentially (see Eq. (4.152), so that an extremely sensitive detector would be required. Time resolution can of course be increased by optical detection of the transmission in a pump-probe pulsed experiment, as was done for the backscattering by Vreeker et al.[41,42] To obtain enough cross-correlate signal from the diffusive transmission with a probe pulse in an experiment of this type, high peak power is required in combination with high repetition rate. A CPM laser may do the job, but a disadvantage is that it works only at a single wavelength.

Only recently, triggered by the work of Drake and Genack[98] who found very low diffusion constants in samples made of TiO_2 (anatase) spheres in air, I realized that for solid samples of small TiO_2 (rutile) particles in air the diffusion constant might appear to be low enough to allow *electronic* time-resolved detection of the transmission, which of course has many advantages. Indeed the diffusion constant of light in such a sample appears to be measurable this way, and, what is very interestingly, its value seems to be in contradiction with the diffusion constant as derived from earlier measurements on the coherent backscattering of these kind of samples. As I will explain at the end of this section, two explanations of this effect are possible.

Here I will present some very recent experimental results. We used a synchronously-

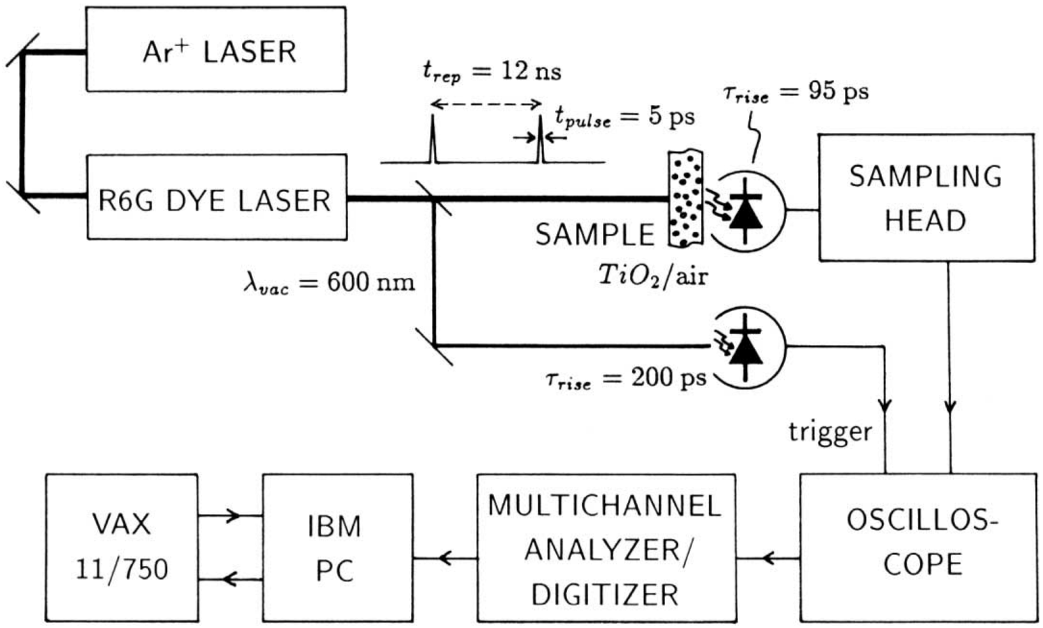

Figure 5.20: *Experimental set-up for determination of the diffusion constant D of very strongly scattering media. The value of D can be found from measuring the time-resolved transmission of a slab.*

pumped dye laser to measure the evolution of the transmitted intensity from a very opaque slab as a function of time. The slab consisted of rutile TiO_2 particles (average diameter of 220 nm in air, glued together with 1 mass % PMMA, prepared from a chloroform solution. In Fig. 5.20 the experimental set-up is shown. The through the sample transmitted pulse was registrated with an avalanche photodiode having a rise time of 95 ps, which was connected to a sampling unit. The triggering of this sampling unit was done by a second photodiode (rise time 200 ps) which was illuminated by a low-power beam, split off from the main dye laser beam. The duration of the pulses from the (R6G) dye laser was approximately 5 ps, and the repetition rate was 82 MHz. Many scans could be recorded and averaged automatically by the multi-channal analyser/digitizer, which was connected to an IBM-PC for data analysis. Also a data link to our VAX 11/750 was available.

In Fig. 5.21 a time-resolved measurement on a slab of rutile particles in air is shown. Also the response of the diode on the 5 ps pulses from the dye laser ($\lambda_{vac} = 600$ nm) is shown. This curve was obtained by replacing the sample by a thin absorbtion filter, and so calibration of time is obtained. The theoretical curve was obtained from the convolution (see Eq. (5.17)) of the theory of Sect. 4.4 with the instrumental (diode) response by fitting both D and λ_{abs}. The thickness $L = 165 \pm 7\,\mu$m of the sample was found from focussing with a microscope on the sample and its substrate respectively, and registration of the

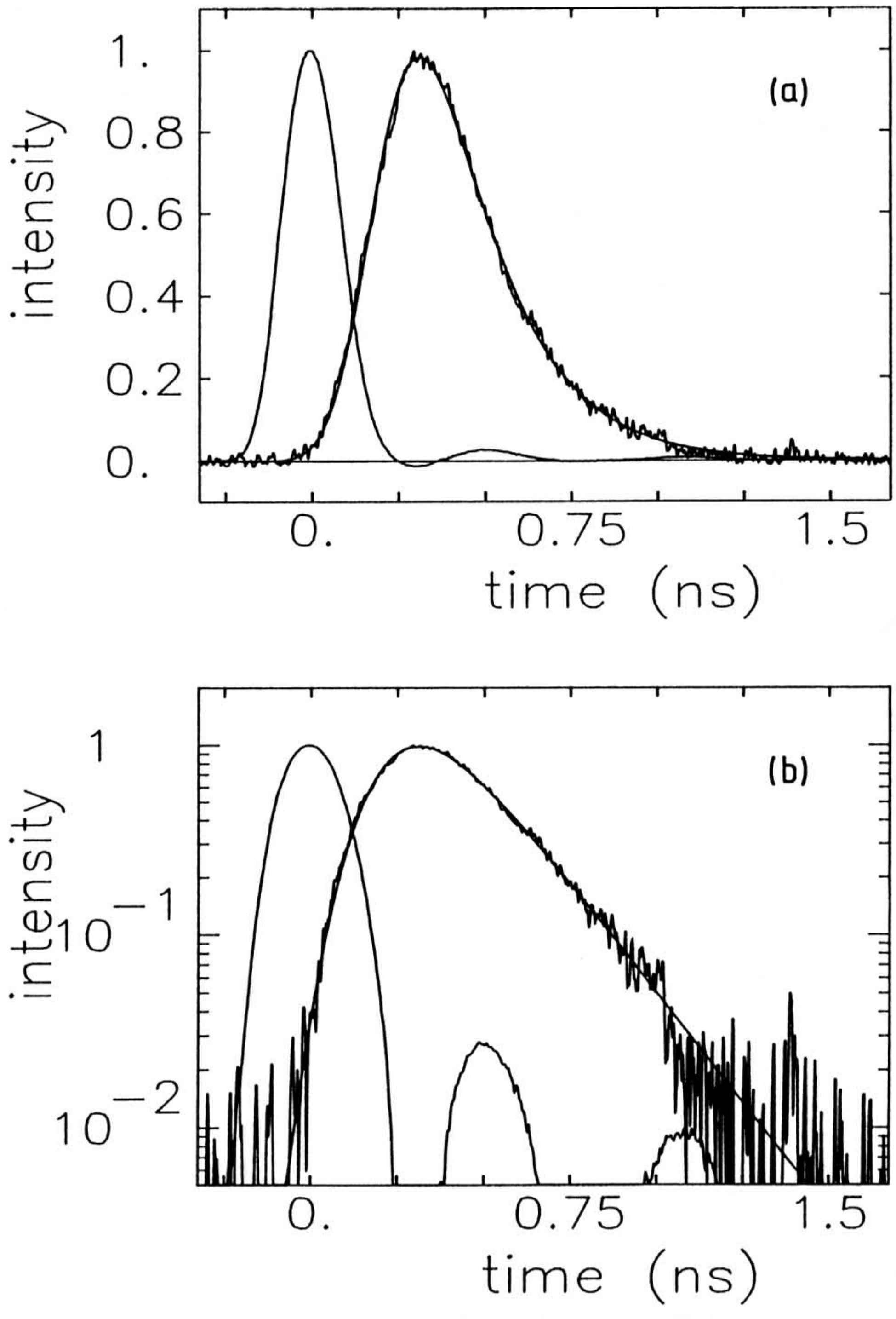

Figure 5.21: *(a) Time-resolved measurement of the transmission at a wavelength $\lambda_{vac} = 600$ nm of a $L = 165 \pm 7$ μm slab of rutile TiO_2 particles in air, glued together with 1 mass % PMMA. The curve to the left is the measured response of the diode to the 5 ps pulses from the dye laser. The curves on the right are the measured transmission curve and the fitted theoretical curve (see text).*
(b) logarithmic plot of (a)

necessary displacement of the tubus with a micrometer.

The shape of the transmitted pulse (in Figs. 4.16 and 4.17 some typical theoretical curves were shown) is given by substituting Eq. (4.149) in Eq. (4.144) which for large t gives rise to an exponential decay with

$$\frac{1}{T} = D\left(\frac{\pi^2}{(L+2z_0)^2} + \frac{1}{\lambda_{abs}^2}\right) . \tag{5.15}$$

where the diffusion constant $D = c_{med}\lambda_{tr}/3$. Sometimes it is convenient to use the absorption time, which is given by $t_{abs} \equiv \lambda_{abs}^2/D$, as a parameter instead of λ_{abs}. The speed of light in the medium c_{med} is approximately given by

$$c_{med} = c_{vac}/[\rho n_{scat} + (1-\rho)n_{solv}] . \tag{5.16}$$

The time-dependent transmitted intensity convolved with the instrumental resolution $\mathcal{R}_i(t)$ is given by

$$\tilde{\gamma}(t) = \int \tilde{\gamma}_\ell(\mu_s = \mu_i = 1; t-t')\mathcal{R}_i(t')dt' , \tag{5.17}$$

where we approximated the experimentally obtained $\mathcal{R}_i(t)$ by a Gaussian-shaped pulse with the same width.

From a (convolved) fit on the measured time-resolved transmission, we find $T = 191 \pm 5$ ps, a diffusion constant $D = 7.4 \pm 1.3$ m^2/s and a reciprocal absorption time $t_{abs}^{-1} = 2.6 \pm 0.6$ ns^{-1}, which gives an absorption length $\lambda_{abs} = 54 \pm 9$ μm, from which we in principle can find the albedo with the help of Eqs. (4.1) and (4.2). To calculate the mean free path λ_{tr}, from this result, we first have to know the speed of light c_{med} in the medium, and hence the density ρ and refractive index n of its components. Careful measurement of the area, thickness and weight of some pieces of the sample gives a density for the sample of 1.4 ± 0.07 g/cc, combined with the specific gravity of TiO_2 (4.26 g/cc) and PMMA (1.18 g/cc) results in $\rho_{TiO_2} = 31.9$ vol % and $\rho_{\mathrm{PMMA}} = 1.2$ vol %.

Combination of this result with the refractive indices $n_{TiO_2} = 2.70$ and $n_{\mathrm{PMMA}} = 1.49$, and Eq. (5.16) gives $c_{med} = 1.94 \times 10^8$ m/s, or for the average refractive index of the medium $n_{med} = 1.55$. This results in a value for the mean free path of $\lambda_{tr} = 115$ nm with a wavelength in the medium of $\lambda_{med} = 387$ nm.

Let us now speculate about the proximity of Anderson localization. The Ioffe-Regel criterion (see Chapter 1) can give an indication. We find that $2\pi\lambda_{tr}/\lambda_{med} \simeq 1.86$, which is remarkably close to 1. In fact, being so close to the Ioffe-Regel condition, the expression for the Boltzmann diffusion constant $D_B = \lambda_{tr}c_{med}/3$, which is only appropriate in the limit $\lambda_{tr} \gg \lambda_{cr}$, is no longer valid. Instead we have $D = \lambda_{tr}^* c_{med}/3$, with $\lambda_{tr}^* = \lambda_{tr} - \lambda_{cr}$ which includes critical mean free path λ_{cr} (see also Chapter 7). The value of the critical mean free path is unknown, but from the Ioffe-Regel condition it follows that

$$\lambda_{cr} \equiv \frac{\zeta}{2\pi}\lambda_{med} , \tag{5.18}$$

with ζ a constant which is expected to be close to 1. So in fact, we have $\lambda^*_{tr} = 115$ nm rather than $\lambda_{tr} = 115$ nm. We can calculate the transport mean free path from $\lambda_{tr} = \lambda^*_{tr} + \lambda_{cr} = 115\,\text{nm} + \zeta \times 61.6\,\text{nm}$, with ζ yet unknown.

Backscattering experiments on the same sample at a wavelength $\lambda_{vac} = 633$ nm show a cone of enhanced backscattering with a width not much larger than 104 mrad, which gives, using Eq. (5.2) also a value for the transport mean free path, namely $\lambda_{tr} = 670$ nm. This value indeed disagrees with the interpretation that $\lambda_{tr} = 115$ nm obtained from the time-resolved transmission experiment. From the values $\lambda_{tr} = 670$ nm and $\lambda^*_{tr} = 115$ nm we find $\lambda_{cr} = 555$ nm, and hence a $\zeta = 9$. This explanation is, though seductive, not very likely because we do not observe any departure from classical behavior, while the ratio $\lambda_{tr}/\lambda_{cr}$ is about 1.2. Further, the value $\zeta = 9$ is rather large compared to 1. Here I assumed that the value of λ_{tr} as calculated from the backscattering is indeed the correct one.

An other explanation may come from a paper by Lagendijk c.s.,[99] where the impedance mismatch of the light at the boundaries of the medium is treated. It is believed that due to internal reflection the average light path will be longer in a medium which has a considerably different refractive index than the outside world. This will result in a narrower coherent backscattering cone for the same mean free path. I will qualitatively explain this effect in the appendix of this chapter, and continue here with a calculation based on Ref. 99. In Fig. 5.22 the essential results of their calculations are given. The figure gives the ratio of the width W of the coherent-backscattering cone for unmatched and matched media ($W_{matched}$) versus the refractive-index ratio $n_{med}/n_{outside}$ of the medium and the outside world.

For a refractive index $n_{med} = 1.55$, we find a reflection coefficient from the sample to air (averaged over all angles) of $R = 0.61$. Using this value, the ratio of the widths of the cone from the matched medium and the unmatched medium has a value of 1.75. This is less than the ratio we would expect, namely $670/115 = 5.83$. So assuming that this is all true, we still have a deviation of a factor of $5.83/1.75 = 3.33$ between the measured mean free paths in transmission (λ^*_{tr}) and backscattering (λ_{tr}), and we can again calculate a value for ζ. We now find $\lambda_{tr} = 115\,\text{nm} + \lambda_{cr} = 383\,\text{nm}$, and so $\lambda_{cr} = 268\,\text{nm}$ and $\zeta = 4.35$, which is indeed closer to 1 and therefore probably more realistic.

Of course the assumption made in Ref. 99 which I used here, that the average index of refraction of the random medium may be considered to be homogeneous and therefore has something like a critical angle resulting in a very high value of the internal reflection, is plausible but not proved, and thus may be wrong. Another possibility is that the calculated reflection coefficient may have a considerably different value, resulting in an other relation between width of the coherent backscattering and the refractive index of the random medium. We performed a first, preliminary experiment to verify the theory, which

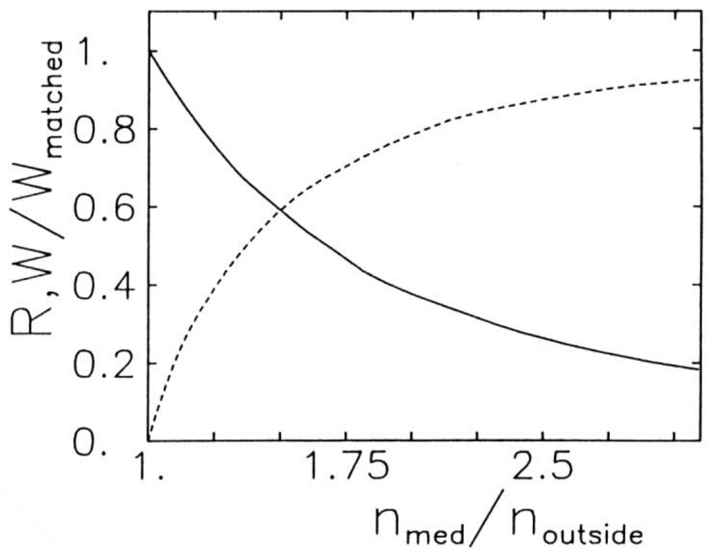

Figure 5.22: *Ratio of the width W of the coherent-backscattering cone for unmatched (W) and matched media ($W_{matched}$) (full line), and the reflection coefficient R (dashed line) versus the refractive-index ratio $n_{med}/n_{outside}$, composed from the results in Ref.* 99.

shows for example that the coherent backscattering of the described sample through a glass interface is wider (138 mrad) than for air 104 mrad, as expected, but that the amount of backscattered light was about a factor 1.4 *lower* instead of higher.

In conclusion we can say, maybe in a little optimistic interpretation, that these time-resolved experiments give evidence that we indeed have arrived in the critical regime.

It is clear that more detailed experiments on the coherent backscattering in relation with mismatch at the boundaries are urgent, and should be compared to data obtained from time resolved transmission experiments. Determination of the diffusion constant from fluctuation experiments[49,13] in *both* transmission and reflection on the same samples may be the key to understanding this problem, and hence might give a clue to finding Anderson localization.

5.5 Appendix

5.5.1 Impedance mismatch at the boundaries

In all the models up to now the following restrictive assumption on the boundary condition of the random medium was adopted: when the light diffuses to the boundary it will escape with probability one. This allows one to use the simplifying reflection principle in the calculation of Green's functions.[100] The experimental optimization of the multiple scattering in a random medium requires the maximization of the contrast in index of refraction. This results usually in a situation in which the average index of refraction in the medium differs considerably from the index of refraction of the outside world and as such causing internal (and external) reflection. The estimate is that in strongly scattering media the internal reflection coefficient, averaged over all angles, could be as high as 0.85. This urges the question to what extent this finite reflectivity influences the dynamics of the propagation. Lagendijk c.s. have developed a theory which incorporates the effect of internal reflection.[99] For experiments requiring backscattering geometries, like coherent backscattering and time-resolved incoherent backscattering it was demonstrated that internal reflection seriously modifies the outcome. It turns out the backscattering cone becomes narrower when one introduces a finite internal reflection. The fact that the cone becomes narrower on increasing the reflectivity can easily be understood. The influence of finite reflectivity is to force the light paths in the sample to be longer. But longer light paths get out of phase easier and consequently the backscattering cone becomes narrower.

In transmission experiments the significance of the corrections depends on the thickness of the slab (in units of mean free path) and the influence disappears for very thick slabs. To a large extent this effect can be accounted for by renormalizing the diffusion coefficient with a length-scale dependent reduction factor. Of course the overall absolute intensities are always seriously affected by finite reflection coefficients.

The occurrence of internal reflection can partially be circumvented by matching of index of refraction. A true match however is intrinsically only possible in the Rayleigh limit. For a medium with macroscopic spheres ($r \gg \lambda$), it is immediately clear that only either the solvent or the scatterer can be matched. An optimum match may be obtained with an outside material having a refractive index somewhere close to the average index of refraction of the system. Experiments performed in the past, where the coherent backscattering has been measured for concentrated titania samples, could have been seriously affected by the effect of internal reflection. So, in Sect. 5.1, the interpretation that the saturation of the mean free path in Fig. 5.3 is due to dependent scattering might be incomplete, and indeed the behavior of λ_{tr} can be explained within the experimental error in terms of internal reflection. No corrections in λ_{sc} are expected, because it is derived from the exponential decay of the coherent beam. Only the absolute value of the coherently transmitted intensity should reduce by a few percent due to reflection at the boundaries.

The interpretation of experiments with pulses, but also fluctuation experiments, in backscattering and transmission through thin slabs will seriously be influenced by the presence of internal reflection.

Chapter 6

Experiments for d=2

Up to now it has not been possible to find strong localization in a 3-dimensional sample, although the diffusion constant as obtained from a time resolved experiment on TiO_2-air samples suggests one can get rather close. The prediction is, that in a 2-dimensional random medium of infinite size any degree of disorder will lead to localization, while for d=3 a certain critical degree of disorder, approximately given by the Ioffe-Regel condition, is needed. Therefore in a 2-dimensional system, even if it has a finite size or suffers from some loss, it might be somewhat easier to obtain Anderson localization. Many workers have developed theory or have done experiments on two-dimensional random systems for electrons, sound[102] or electromagnetic waves.[95,103] For electrons corrections to the conductance due to interference were observed indeed.[12,104] A different type of two-dimensional localization, the so-called "transverse localization", has been studied numerically by De Raedt et al.[105]

6.1 How to construct a 2-dimensional medium

Since we are living in a three-dimensional world, we have to neutralize one of these dimensions in order to prevent coupling of wave energy into this dimension, and vice versa, to obtain a two-dimensional system. Basically, there are two ways to solve this problem, these are (i) confine the wave in the third dimension by creating a (single-mode) cavity made of two parallel mirrors, or (ii) make the system translation invariant in the third dimension so that no scattering will occur into this dimension.

Although in a 2-d medium Anderson localization is possible for any amount of disorder it only occurs in a medium for which both the absorption length λ_{abs} and sample size L are larger than the localization length λ_{loc}. It appears that this still gives a tight bound on the systems parameters. In the following two subsections we will see that the amount of *absorption* by realistic 2-d systems is not very small, and under all practical circumstances effectively larger than in similar 3-d systems. This implicates that the amount of disorder in a medium should still be rather large in order to make it a candidate for observing Anderson localization.

6.1.1 The single-mode cavity

Construction of a parallel-plane single-mode waveguide seems to be a very good way to achieve a system which is effectively two-dimensional, because the third dimension can be eliminated completely. A cavity supports only one mode if the two planes are separated by a distance in the order of a wavelength.

There are two types of cavities that one could think of, namely the conducting-plate cavity and the dielectric cavity. Based on the guiding priciple of optical fibers as being used in telecommunication, a dielectric cavity should consist of a high refractive index dielectricum sandwiched between two lower refractive index materials. Such a system may work very well and can have a very long absorbtion length λ_{abs}. It is by the way important to notice that for a system without scatterers $\lambda_{abs} = \lambda_{in}$, as follows from the defenitions of $\lambda_{abs}$and λ_{in}, see Sect. 4.1). If scattering takes place due to refractive index fluctuations in either the high- or low refractive index dielectrics, then at every scattering event some light will be lost in the third dimension, thereby decreasing the effective inelastic length enormously. The multiple scattering inside the cavity now makes the difference between λ_{in} and λ_{abs}, which results in the relation $\lambda_{abs} = \sqrt{\lambda_{in}\lambda_{tr}/2}$, see Sect. 4.1.

A waveguide made of two conducting parallel plates will certainly not allow an electromagnetic wave to escape from the cavity, even if there is a strongly scattering medium between the plates. Therfore in a *perfectly* conducting cavity no additional cavity losses are introduced by scatterers of arbitrary shape. On the other hand, the scattering efficiency of impurities in a cavity may be changed significantly compared to scattering in free space. Cavity losses are however dependent on the conductivity of the plates, so absorption in the waveguide itself may be an important factor. Moreover, scattering from some particle in an imperfectly conducting single-mode cavity will excite more modes than the fundamental single mode (Only in a perfectly conducting cavity these higher modes are truely forbidden). Since these modes are cut-off by the guide they are completely absorbed, and so an extra loss mechanism is introduced by the scattering itself. It is therefore important to use scatterers, for example rods, having a shape which does not disturb the mode profile very much, but only changes the direction of mode propagation.

In Fig. 6.1 an example of the described cavity with scatterers is shown. A study of propagation of electromagnetic waves[106] through wave guides makes clear that conduction losses in the plates of the cavity can be minimized by using modes of the TE_{0n} type, for which the polarization of the electromagnetic wave, the direction of the electric field vector

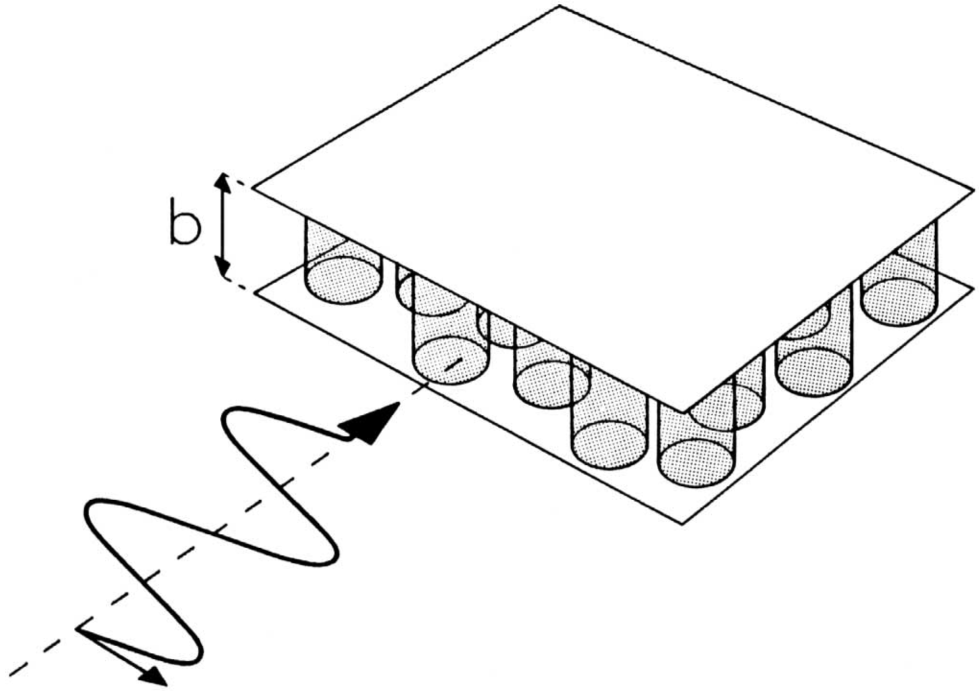

Figure 6.1: *Example of a parallel-plane waveguide containing scatterers. If the distance b between the two (perfectly) conducting plates is made in the order of the wavelength, only a single mode (perpendicular to the plates) is supported, and so propagation in the system is only possible in two dimensions.*

$\vec{E}$, is parallel to the plates. The advantage of using the fundamental TE_{01} mode over for instance the TE_{10} mode is about a factor of 10 in loss, which can be explained from the mode profiles.

The loss in a parallel-plate wave quide of the TE_{0n} modes originates from the non-zero value of the electric field close to the imperfectly conducting plates. This is because the field can penetrate a non ideal conductor over a distance δ_{skin}, the skin depth, which is given by

$$\delta_{skin} = \frac{\lambda_{vac}}{2\pi n_i} \ . \tag{6.1}$$

A measure for the loss in the cavity is the ratio of the total intensity in the plates and between the plates. For a TE_{10} mode, the field along an axis perpendicular to the plates is constant, but for a TE_{01} mode the field is (in the ideal case) a half sinus (see Fig. 6.15 in the appendix), and thus has much more field energy between the plates than in the plates, explains where the difference in attenuation between these modes. Having understood this loss mechanism, it becomes clear what material the scatterers should be made of. If we should use conducting scatterers, then we would introduce loss due to the same mechanism as found in the empty cavity for the unfavorable TE_{10} mode. In case we should use dielectric scatterers, the advantage of using the TE_{01} mode is maintained. So dielectric scatterers are probably the best to use.

We can conclude that a single-mode guide (supporting the TE_{01} mode), made of two perfectly conducting (≡broad-band) mirrors containing lossless (dielectric) scatterers would be ideal. The question is how close we can get to this ideal. The exact solution for the propagation of a wave between two conducting plates (with loss but without scatterers) can be derived rigorously from Maxwell's equations, as I will show in the appendix of this chapter. Here I will only discuss the results of these calculations.

Before we can use the calculations from the appendix, we have to know what material is the most suitable conductor in a certain part of the electromagnetic spectrum. In other words we have to know the (complex) refractive index $n \equiv n_r - in_i$ of some conductors over a large frequency range. Here we have to keep in mind that wavelengths longer than a few centimeter are not very interesting, since a typical size of the cavity will be hundreds of wavelengths, resulting in a system larger than a few square meters, which may be unpractical and expensive. Wavelengths shorter than the near ultraviolet (UV) will certainly give problems in finding a good conductor, not to mention the necessary small scale of the cavity.

After some study one finds that only the following few conductors appear to be interesting: copper, silver, aluminium, gold, sodium, and some superconductors. Starting with the superconductors, it is clear that, even for high-T_c types, one should cool the system to helium temperature and a frequency sufficiently lower than that corresponding to the band gap should be used. Only wavelengths close to a centimeter are practical here, demanding quite a large cavity and thus a large low-temperature set-up. For practical reasons this idea was abandoned.

Let us take a closer look at the properties of some metals. In Fig. 6.2 the complex refractive index of silver (Ag) is given as a function of wavelength, and may serve as a typical example for the properties of the metals mentioned above over a wide wavelength range. The data between $\lambda_{vac} = 300\,\mathrm{nm}$ and $\lambda_{vac} = 12\,\mu\mathrm{m}$ result from reflection measurements on vacuum deposited films as reported in Ref. 107, where the long wavelength data ($\lambda_{vac} < 1\,\mathrm{mm}$) were calculated from the DC conductivity σ of bulk silver at room temperature using:

$$\sigma = 4\pi\varepsilon_0 \frac{c}{\lambda_{vac}} n_r n_i \ , \tag{6.2}$$

and $n_i \simeq n_r$, which only hold for long wavelengths. Long wavelengths are those far to the right from the bending over as can be seen in Fig. 6.2 for silver around $\lambda_{vac} = 70\,\mu\mathrm{m}$. This wavelength corresponds to the collision frequency Γ ($\Gamma = c/\lambda$) of the conduction electrons in the metal with the lattice. This is described by the well known Drude model,[108] which gives the frequency dependence of the complex dielectric constant of a metal as a result

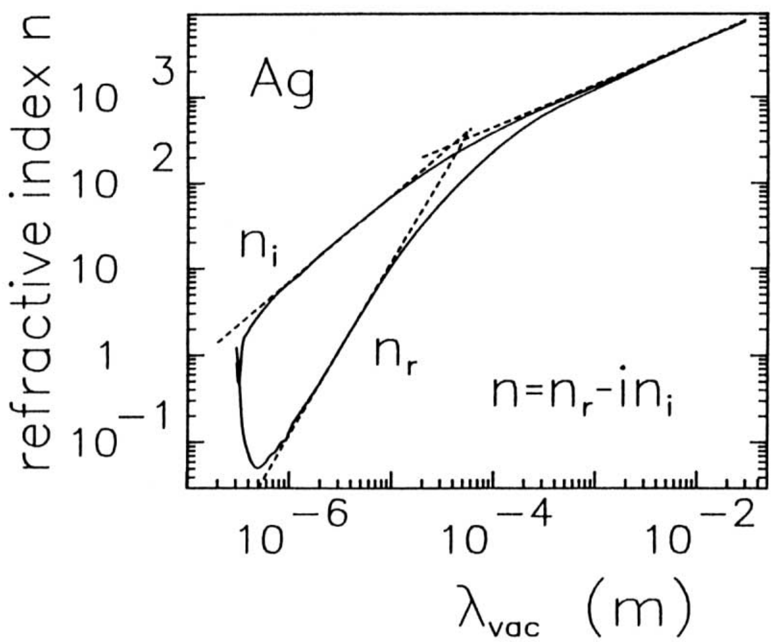

Figure 6.2: *The (complex) refractive index $n \equiv n_r - in_i$ of silver as a function of wavelength (solid lines), spanning a range from the UV to cm-waves. The dashed lines give the wavelength dependence of n_i and n_r as follows from the Drude model (see text). The curved part of the solid lines between $\lambda_{vac} = 15\ \mu m$ and 1 mm is the result of interpolation.*

of the motion of the free electrons:

$$\varepsilon_{free} = 1 - \frac{\omega_p^2}{\omega^2 + \Gamma^2}\left(1 + i\frac{\Gamma}{\omega}\right) \ , \tag{6.3}$$

with $\omega_p = \sqrt{\sigma\Gamma/\varepsilon_0}$ the plasma frequency, which in case of silver corresponds to a wavelength close to 135 nm. In the far UV, for $\omega > \omega_p$, ε becomes positive and hence the metal will become transparent.

To describe the dielectric constant completely we also have to take the rest of the metal atoms, the core, into acount. If the free electrons are well separated from the core, which means that (virtual) transitions between the core and the conduction band are negligible, we can omit this term. So we have:

$$\varepsilon_{free} \simeq \varepsilon \equiv \varepsilon_r - i\varepsilon_i \ , \tag{6.4}$$

The relation between the dielectric constant and the refractive index is given by

$$\varepsilon_r = n_r^2 - n_i^2 \ , \tag{6.5}$$

$$\varepsilon_i = 2n_r n_i \ , \tag{6.6}$$

From Eqs. (6.3)-(6.6) we can easily find that for $\omega < \Gamma$ $n_i \simeq n_r$ and that n_r and n_i are both proportional to $\sqrt{\lambda_{vac}}$. In the same way we find for $\omega > \Gamma$ that n_r and n_i are proportional to λ_{vac}^2 and λ_{vac} respectively. The dashed lines in Fig. 6.2 are fits to the experimental data of these proportionalities. The values for n_r and n_i were interpolated between $\lambda_{vac} = 15\,\mu$m and 1 mm (full curves in the figure) because no experimental data seem to be available for this region.

In Table III the DC conductivity at room temperature and nitrogen temperature as well as the complex refractive index for a typical optical wavelength are listed for the earlier mentioned metals.[107,108] From Fig. 6.2 and Table III we find that, except for the very reactive and therefore unpractical sodium, silver is the best material in the optical region of the electromagnetic spectrum, and even in the millimeterwave region it is only surpassed at lower temperatures (77 K) by copper. Altough aluminium is often used for its high reflectivity, its refractive index appears not well suited for making a cavity. The only advantage of gold is that its surface does not degenerate for a very long period of time.

Using these data and the theory from the appendix, we can calculate the complex wave vector $\vec{k}$ in the cavity for each of the metals. The imaginary part of $\vec{k}$ gives the attenuation of the *amplitude* of the wave between the plates, so the inelastic length is given by $\lambda_{in} = (2\,\mathrm{Im}\{k\})^{-1}$.

In Fig. 6.3 the calculated inelastic length λ_{in} is shown versus λ_{vac} for the TE_{01} mode of an (empty) parallel-plane waveguide made of silver. In the theory it implicitly is assumed that the size of the plates L is much larger than their mutual distance b. Here $b = \lambda_{vac}$ was taken. The calculation was done with the theory from the appendix, using the data for the refractive index as shown in Fig. 6.2. In Table IV calculated values of $\lambda_{in}/\lambda_{vac}$ of some more metals are given for two wavelengths and temperatures. The value of the dielectric constant for long wavelengths, $\omega \ll \Gamma$, can be calculated from

$$\varepsilon_r \simeq -\frac{\sigma}{\varepsilon_0 \Gamma} , \tag{6.7}$$

$$\varepsilon_i \simeq \frac{\sigma}{\varepsilon_0 \omega} , \tag{6.8}$$

In this paragraph I will discuss the the propagation in the cavity as a function of the plate distance b. Up to now I have assumed that $b = \lambda_{vac}$ is a reasonable value for the mutual distance of the plates in order to make a single mode cavity. Apart from determining the number of propagating modes in the cavity, b determines also the attenuation of each mode. The mode structure and attenuation in the waveguide is of course also changed if a dielectric is put between the plates. In Fig. 6.4 the inelastic length versus plate distance for a guide made of silvered plates at a wavelength of $\lambda_{vac} = 633\,\mathrm{nm}$ is shown. The full lines represent the TE_{01} to TE_{04} modes in case of a vacuum between the plates. The dashed lines represent the TE_{01} to TE_{06} modes in case the cavity is filled

Table III: *The DC conductivity σ at two temperatures and the complex refractive index $n \equiv n_r - in_i$ at a wavelength of $\lambda_{vac} = 633$ nm for some metals.*

metal	σ ($10^6\ \Omega^{-1}\mathrm{m}^{-1}$)		Γ (10^{12} rad s^{-1})		n ($T \approx 293$ K)	
	$T = 77$ K	$T = 293$ K	$T = 77$ K	$T = 293$ K	n_r	n_i
Ag	333	61.2	5.00	26.6	0.066	4.05
Al	333	37.5	15.4	133.	1.210	6.89
Au	200	45.5	8.33	35.5	0.162	3.21
Cu	500	59.0	4.76	39.4	0.157	3.37
Na	125	21.8	5.88	33.8	0.024	3.06

Table IV: *Calculated values of $\lambda_{in}/\lambda_{vac}$ for some metals of the TE_{01} mode of a (vacuum) parallel-plane waveguide with a plate distance $b = \lambda_{vac}$. The calculation was done with the theory from the appendix, using the data from Table III.*

metal	$\lambda_{vac} = 1$ cm		$\lambda_{vac} = 633$ nm	
	$T = 77$ K	$T = 293$ K	$T = 77$ K	$T \approx 293$ K
Ag	17500	7330	-	300
Al	17200	5720	-	40
Au	13500	6360	-	85
Cu	21600	7300	-	95
Na	10600	4390	-	540

with a material having a refractive index of $n_{med} = 1.59$, such as polystyrene. From the same figure we can see that the cavity is only truely single mode between $b \approx 0.4\lambda_{vac}$ and $b \approx 0.9\lambda_{vac}$ if there is a vacuum in the cavity. Nevertheless, in a cavity with a plate distance of many wavelengths just the single TE_{01} mode may propagate. At the introduction of scatterers in the cavity, coupling to all propagating higher TE_{0n} modes will take place (Notice that if these scatterers are all symmetric around an imaginary plane centered between the two plates, only the *odd* modes can be excited due to symmetry).

In the next paragraphs, first an idea will be given of what a possible realization of a cavity may look like in the optical region, and the absorption in relation to the possibility of observing Anderson localization in such a system will be discussed. Second, the same problem will be briefly discussed for the microwave region.

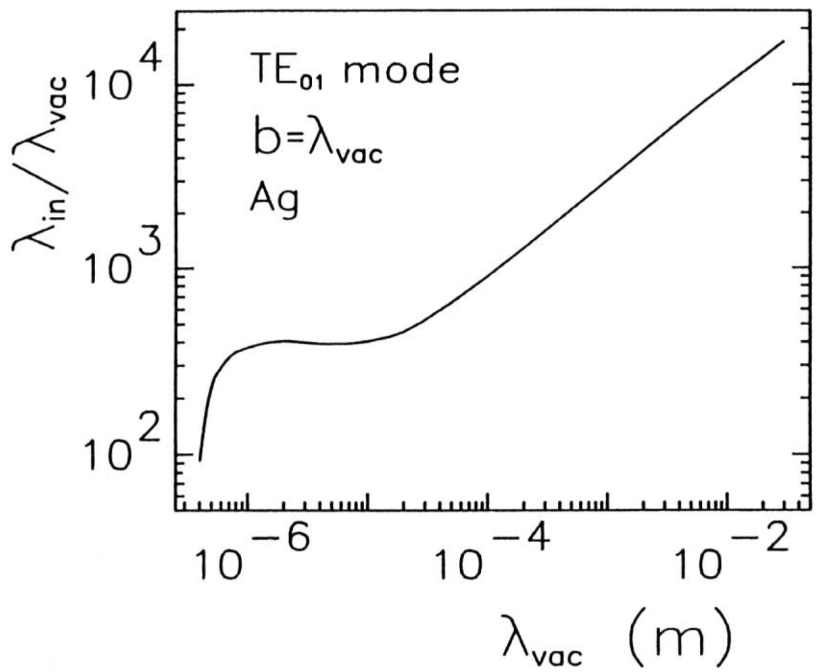

Figure 6.3: *$\lambda_{in}/\lambda_{vac}$ as a function of λ_{vac} for the TE_{01} mode of an empty parallel-plane waveguide made of silver. The mutual distance of the plates is $b = \lambda_{vac}$. The inelastic length λ_{in} was calculated with the theory from the appendix, using the data for the refractive index as shown in Fig. 6.2.*

Imagine a cavity as referred to in Fig. 6.4, at some areas completely filled with vacuum, and at others completely filled with polystyrene. We make the distance between the plates $b = 0.85\lambda_{vac}$, so that in the vacuum only a single mode, the TE_{01} mode, can propagate (see figure), and in the polystyrene two modes, the TE_{01} mode, and the *even* TE_{02} mode. If we make the the interfaces between the vacuum and the polystyrene symmetric to both plates, there will be no way to excite the TE_{02} mode if we started with a TE_{01}, and the system will remain single mode. The inelastic lengths will be $150\lambda_{vac}$ and $300\lambda_{vac}$ in the vacuum and the polystyrene respectively. As I have pointed out earlier, a small mismatch in the mode profile between the TE_{01} mode in the vacuum and the TE_{01} mode in the polystyrene due to the dissipation in the plates will result in excitation of odd non-propagating modes, which will introduce some extra losses.

In a study on Anderson localization, experiments on samples which have different sizes will very likely be involved. If we assume that we can make samples with sizes up to a few hundred mean free paths, classical diffusion can be studied over only two orders of magnitude of the thickness L, because diffusive behavior starts no earlier than at a thickness of approximately $L = 4\lambda_{mf}$ (see Chapter 4). For Anderson localization we have

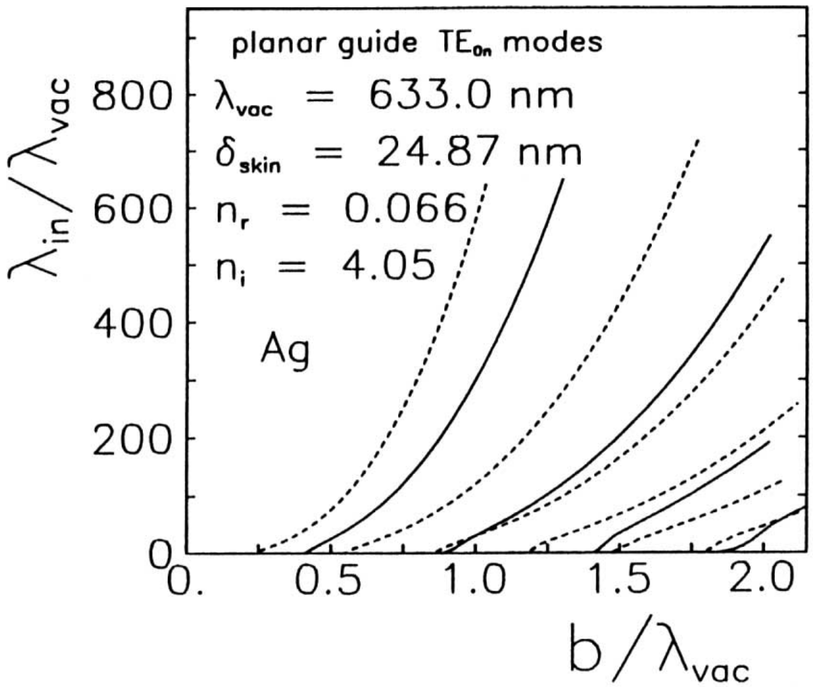

Figure 6.4: *Inelastic length versus plate distance for a guide made of silvered plates at a wavelength $\lambda_{vac} = 633$ nm. The full lines represent the TE_{01} to TE_{04} modes in case of a vacuum between the plates. The dashed lines represent the TE_{01} to TE_{06} modes in case the cavity is filled with a material having a refractive index of $n_{med} = 1.59$, such as polystyrene.*

to find a deviation from this behavior, and therefore the absorption length λ_{abs} in the medium should be longer than about a few hunderd mean free paths, which results in an inelastic length of tenthousands of mean free paths (see Sect. 4.1). If we assume that we can obtain a mean free path equal to a vacuum wavelength, which is already quite short, this means that we should try to make a system for which at least $\lambda_{in} = 10000\lambda_{vac}$. From Table IV, we can see that the inelastic lengths we do find in the optical region are not very promising for observing Anderson localization, although cooling down of the system may give some relief.

Fig. 6.3 shows that in the millimeter region the prospects are much better. Because we want to make the scatterers of a dielectric, we also have to find materials with a low absorption at these frequencies. From Table V, which shows the inelastic length of some bulk dielectrics for some wavelengths,[109–111] we observe that the absorption in the long-wavelength regime is much larger than in the optical region. In the centimeter regime the best material seems to be high density (HD) polyethylene (the values given are for the 960 type). Probably cooling will improve the quality of the materials.

Table V: $\lambda_{in}/\lambda_{vac}$ *of some bulk dielectrics for some wavelengths.*

λ_{vac}	TiO_2 rutile	Al_2O_3 sapphire	SiO_2 quarts	PTFE teflon	poly-styrene	TPX	HD poly-ethylene
3.0 cm	>9	490	820	275	200	-	1100
1.0 cm	-	-	-	-	-	-	1050
0.5 cm	-	100	100	200	75	>400	>400
633 nm	>31000	-	6.9×10^8	-	$\approx 10^6$	-	-

In conclusion we may say that it is very hard to realize 2-d localization experiments in a cavity, because quite some absorption is always present. Observation of Anderson localization may be possible in a cavity at low-temperature.

6.1.2 The translation-invariant medium

In this subsection I will discuss the second option for constructing a 2-d medium, the translation invariant medium. In Fig. 6.5 an example of such a medium is shown. Many parallel dielectric rods, placed at random positions form a disordered medium which is illuminated by a plane wave coming in at a right angle with respect to the long axes of the rods. In this situation, the wave can only be scattered in a plane perpendicular to the rods, and so there will be no coupling to the (translation-invariant) third dimension.

Whenever a linearly polarized light source is used, the polarization of the incoming wave can be chosen either parallel ($E_{\|}$) or perpendicular ($E_{\perp}$) to the axes of the rods. This will result in two distinct scattering problems since the scattering properties of the rods depend on polarization. Here it is important to notice that the direction of polarization for scattering in a plane is conserved in case the wave is linearly polarized either perpendicularly or parallel to that plane. This will allow us to do two distinct scattering experiments on the same medium at the same wavelength, which may prove to be a powerful tool, especially when the system is close to localization for just one direction of polarization.

Let us consider the loss in this type of quasi 2-d medium. In the first place absorption in both the scatterers and the space between the scatterers plays a part, like in a 3-d medium. A second loss mechanism comes from diffraction or scattering into the third dimension. This mechanism is only important if the system is too small in the third dimension, either because the rods are to short, which will result in 3-d scattering at the ends of the rods, or because the illuminated area is to small, which means we are not using a plane wave, so diffraction into the third dimension will take place. A third loss

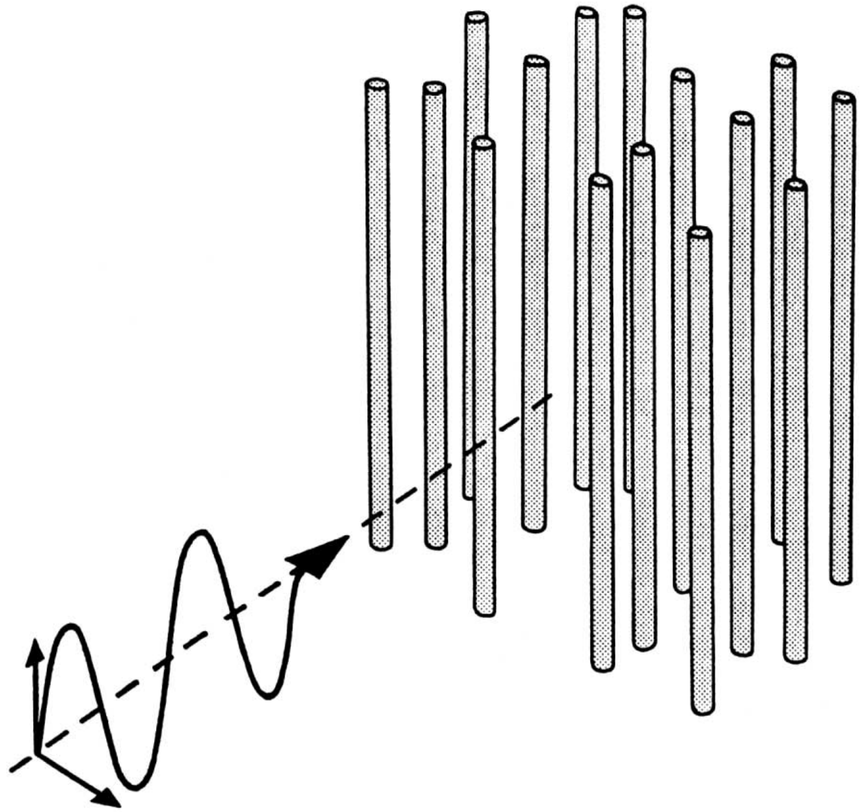

Figure 6.5: *Example of a translation invariant medium made of many parallel, very long and homogeneous rods. The incoming plane wave is incident at right angle to the orientation of the rods.*

mechanism, which may be the most important, is loss of energy into the third dimension due to imperfect parallelism of the rods. Only a very small deviation in the orientation of the rods will already result in a fast decay of the multiple-scattered wave, since the divergence of the propagation from the 2-d plane *multiplies* at each scattering event. This is different from the case of absorption, where the loss at each scattering event only adds (leading to an exponential decay of the intensity).

From the previous subsection it is already clear that the absorption of dielectrics can be very low at wavelengths in the range of the visible and near-infrared part of the electromagnetic spectrum. In this wavelength range lasers are available to serve as suitable light sources, detectors are available in the form of photodiodes, and very thin glass fibers can serve as low-loss scatterers.

In the following paragraphs I will specify the properties which a 2-d medium should have in more detail.

From Fig. 3.4 we can find that for a refractive index of the fibers $n = 1.55$, the strongest scattering occurs for a size parameter $x = 3$. At a wavelength of $\lambda_{vac} = 633\,\mathrm{nm}$,

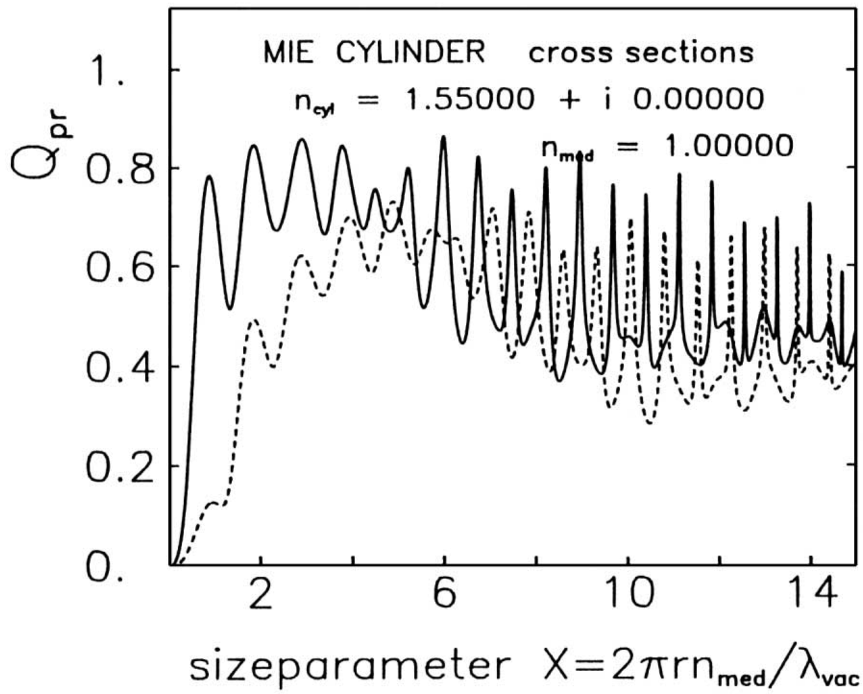

Figure 6.6: *The efficiency factors for radiation pressure Q_{pr} for both $E_{\|}$ (solid line) and $E_{\perp}$ (dashed line) are shown for fibers with a refractive index of $n = 1.55$ (compare Fig. 3.4).*

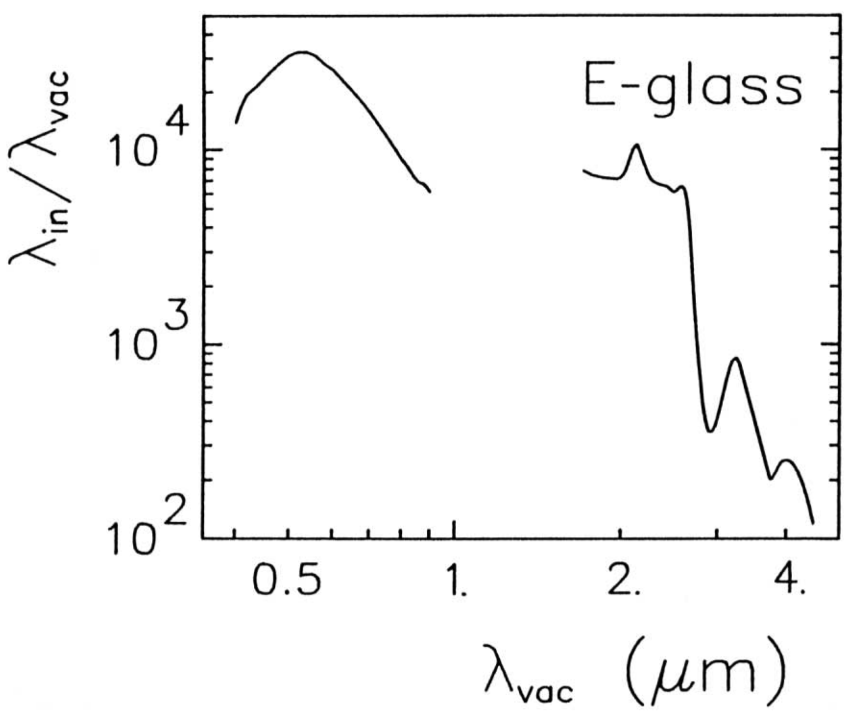

Figure 6.7: *Absorbtion of "E" textile glass in terms of $\lambda_{in}/\lambda_{vac}$ shown as a function of wavelength.*

this size parameter implies that the diameter of the fibers should at least be approximately 300 nm, which is rather thin. It is in fact even worse, because it is the transport mean free path rather than the scattering mean free path that is important. In Fig. 6.6 the cross sections for radiation pressure, which are related to λ_{tr}, for both $E_{\parallel}$ and $E_{\perp}$ are shown for fibers with a refractive index of $n = 1.55$. In this figure it can be seen that at a value of the size parameter $x = 1$ the highest scattering density in a multiple-scattering medium may be obtained. Very thin glass fibers, made of so-called "E" glass having a refractive index around 1.55, are commercially available. The thinnest fibers have a diameter of 3 μm (manufactured by Owens-Corning) and 5 μm (manufactured by Vetrotex), which for obtaining a size parameter of 1 demand a wavelength of $\lambda_{vac} = 9\,\mu$m and $\lambda_{vac} = 15\,\mu$m respectively. These fibers are textile fibers a.o. used as reinforcement in composite materials such as the epoxy carrier for printed circuits, and are therefore not optimized for transmission of light. In any case, glass consisting for a large amount of SiO_2, like "E" glass, will never be very transparent for wavelengths longer than 2.2 μm. In Fig. 6.7, where the absorption of "E" glass is shown as a function of wavelength, we see that the transmission is highest in the green part of the visible light, and may have considerable absorption in the near infrared between $\lambda_{vac} = 0.9\ \mu$m and $\lambda_{vac} = 1.7\ \mu$m. The glass becomes practically opaque at $\lambda_{vac} = 2.5\ \mu$m. Nevertheless, glasses which are very transparent in the $2 - 15\ \mu$m range do exist, and are still being improved for future use in telecommunications.[112]

From Fig. 6.6 we can read that the efficiency factor for radiation pressure for a cylinder with a refractive index $n = 1.55$ is $Q_{pr} \simeq 0.8$ at size parameter $x \simeq 0.9$, which for a packing fraction of fibers of $\rho = 0.1$ gives $\lambda_{tr}/\lambda = x/(4\rho Q_{pr}) = 2.8$. For even higher scattering efficiency, which may appear to be crucial in the study of strong localization, a fiber having a higher index of refraction than $n = 1.55$ is needed. Fibers made of TiO_2 with a diameter in the order of 200 nm may be the very best. In Fig. 6.8 the efficiency factors for radiation pressure are shown for both $E_{\parallel}$ and $E_{\perp}$ for fibers with a refractive index of $n = 2.5$. Note the enormous difference in cross section between $E_{\parallel}$ and $E_{\perp}$ for $x < 1$, which may serve as a convenient probe for the transport properties of a random system made of these fibers. Possibly Anderson localization will occur only for the component $E_{\parallel}$ of the incident light, while the same sample shows classical diffusion at the same wavelength, but for the $E_{\perp}$ component.

We can conclude from this, that the properties of commercially available fibers are quite far from the optimum for our task.

There is another serious problem yet to solve. How can we put many thousands of fibers all at random positions, and still keep them very parallel, or, the other way around, how can we put the fibers all parallel without ordering them into a lattice? An answer to this question is, that if we introduce very little disorder in the third dimension by

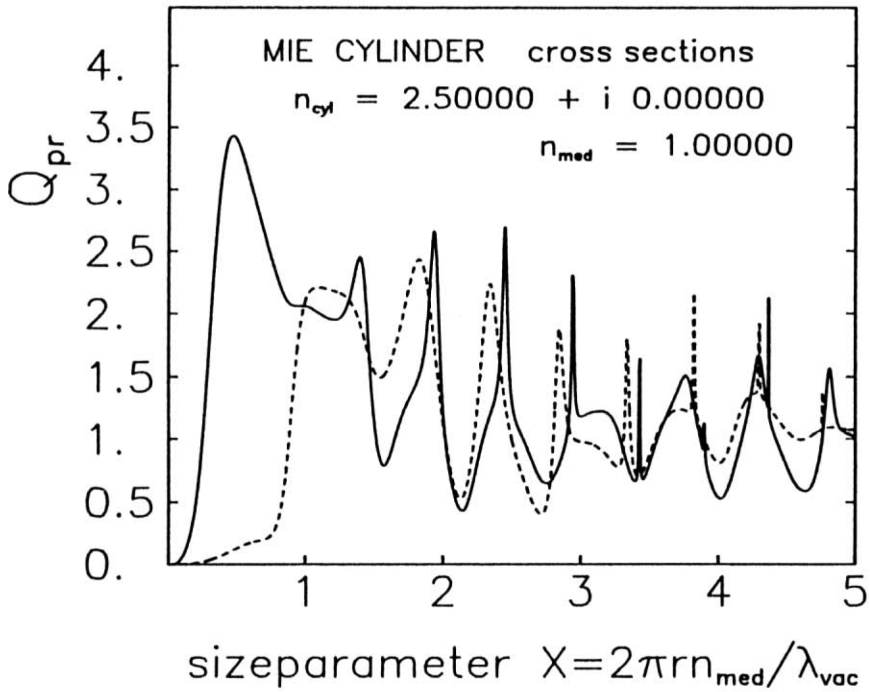

Figure 6.8: *The efficiency factors for radiation pressure Q_{pr} for both $E_{\parallel}$ (solid line) and $E_{\perp}$ (dashed line) are shown for fibers with a refractive index of $n = 2.5$ (compare Fig. 6.6). Note the enormous difference in cross section between $E_{\parallel}$ and $E_{\perp}$ for $x < 1$.*

making the fibers randomly cross each other over a very large distance, say in the order of centimeters, we prevent the fibers from forming a lattice. This means that there will be no long range correlation in the position of the fibers. Only at a very short range (nearest neighbor) some correlations may occur (this follows from scattering experiments on these samples, as I will come to later, which did not show Bragg reflection peaks in the scattered light, as is expected for an ordered system). Further, there is some spread in the diameter of the fibers, which typically can be more than 15%, inducing randomness as well.

I will now give a detailed description of the method we used to construct some translation-invariant two-dimensional media. The fiber we mainly used was a the type $EC5$ $Z40$ 11 $T3$ from Vetrotex, which is a bundle of 200 fibers with a diameter of 5μm each, twisted around each other 40 times per meter. The "E" in the code denotes the type of glass, the "11" gives the weigth of 1000 m of a strand in grams (which implies that there are 200 filaments), and the "$T3$" indicates the type of "finish", a protective layer, has been put on the bundle. This "finish" consists of some grease and starch to make the fibers stick together and is necessary to prevent breaking of the single filaments in the bundle due to (mutual)

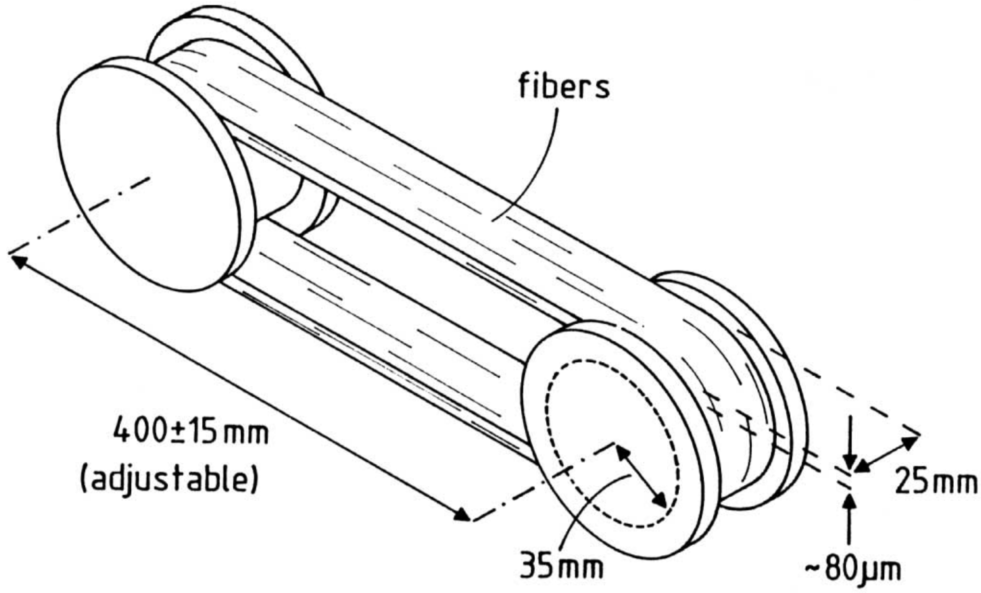

Figure 6.9: *Schematic drawing of the racetrack-shaped frame.*

friction when it is worked up.

In order to realize a 2-d medium, we constructed a 25 mm wide and 400 mm long racetrack-shaped frame, with the bends having a radius of curvature of 35mm (see Fig.6.9). The fiber bundle could be wound over the rounded-off edges. One of these edges could be moved in order to increase the tension on the fibers, and thereby possibly influence their parallelism. The maximum obtainable parallelism of the fibers is determined by the length of the frame and the winding accuracy, and was estimated to be approximately 0.2 mrad. (The winding accuracy is mainly determined by displacement of single filaments within the bundle, which is typically less than 80 μm)

Before winding the bundle on this frame, we first carefully untwisted the bundle so that potentially all of the 200 fibers where parallel. An untwisted bundel is much more fragile with respect to microscopically rough contact surfaces in the winding set-up, like on pulleys and conductors. One has to take extreme care in handling the fibers because every broken filament is a potential 3-d scatterer. Winding one layer of the untwisted bundle of fibers on the frame while incrementing the position of the bundle with respect to the frame with 75 μm per revolution gives a slab with an estimated thickness of 14 to 16 fibers, and a width of 25 mm. Repeating this procedure, it is in principle possible to make a slab of any thickness. The winding itself, where 200 fibers are laid down simultaneously, introduces enough disorder in the position of the fibers to garantee a large amount of randomness in the system.

An other problem remains to be solved. Since the grease and starch are not homogeneously spread over the fibers they cause a lot of scattering into the third dimension.

Therefore the grease and starch has to be removed. This can be done by washing the complete frame with fibers in an ultrasonic bath. Using a biological active washing powder in de-mineralized water at a temperture of 60°C in a big ultrasonic (80 kHz) bath during one hour and rinsing it with de-mineralized water, it is possible to obtain very high quality slabs, as will be shown in the next section. A very striking phenomenon is that these slabs possess a metallic lustre, though they consist of a dielectric only. This phenomenon can be explained from the fact that (quasi-) specular reflection of light occurs in the translation-invariant direction. A major disadvantage of this cleaning method is that diffusion of the active parts of the washing powder into the sample as well as the diffusion out of the sample of the dirt, takes quite a long time. Although the ultrasonic vibrations speed up the process enormously, slabs thicker than two layers of bundles can not be rinsed completely. Moreover, single fibers start to break or come loose out of the sample after some time due to the ultrasonic vibrations, so that a longer washing time seems no solution.

An alternative of washing the sample has to be found in order to make thicker samples of the same high quality. Eventually, a thick slab made of the right type of fiber (which we probably do not have) should show localization. For the time being, the study of coherent backscattering from slabs of different optical thickness and showing the feasibility of making high-quality thick slabs is the reason to find such an alternative.

A possible alternative is to burn off both the starch and the grease from the fibers. For thin slabs this can be done by heating the complete frame in an oven to 600°C. For thick slabs this gives problems because the oxygen cannot penetrate to well beyond the fibers. More promising was (and maybe still is) the technique were the fiber bundle is drawn through a tube oven at a temperature of approximately 620°C just before it is wound on the frame. A flow of oxygen is conducted in opposite direction through the oven. In this way, we are usually able to clean the fibers completely. As I have mentioned, the part of the bundle that has passed the oven becomes extremely fragile. By using smooth pulleys made of teflon, and greasing the bundle with iso-propanol, which is volatile and leaves no residue, the problem of friction on external surfaces can be reasonably solved.

The mutual friction of the filaments still remains a big problem. When the fiber bundle is wound on the a racetrack-shaped frame, some of the fibers in the outer bend break, although they have to follow a radius of curvature of approximately only 70 μm longer compared to the inner fibers. The outer fibers break only at the end of the bend, independently of the radius of curvature of the bends of the racetrack, which indicates that internal friction is the cause. Some other clean and volatile fluid than iso-propanol may help to grease the fibers better. Nevertheless, the whole procedure of untwisting, winding and cleaning certainly does not leave the fibers unharmed, even if the most of care is spent to it.

In conclusion I can say that it is apparently hard to clean these fibers and make a good sample out of them. All these problems can be solved at once by drawing a fiber oneself and winding it on a racetrack at the same time. This may nevertheless be extremely difficult as well.

6.2 Experimental results

In order to realize a 2-d medium, we constructed a 25 mm wide sample of 40 cm long glass fibers with a mean diameter of 5 μm using the technique described in the previous section. The thickness of the sample was approximately 80 ± 5 μm (just one layer of the 200 filament bundle was used), and the packing fraction was close to 65 vol %.

The sample was illuminated (at right angle) with a spatially filtered and very parallel laser beam with a vacuum wavelength λ_{vac} of 1092.6 nm, 633.0 nm or 441.7 nm respectively. The divergence ϑ of the beam ($\tan\vartheta = 2\lambda/\pi W$) was less than 0.05 mrad, and its width was $W = 20$ mm. The incident beam was linearly polarized either parallel ($E_{\|}$) or perpendicularly ($E_{\perp}$) to the fibers. The wavelength could be changed by opening and closing some shutters, without moving the sample or anything in the experimental set-up. The divergence of the laser beam into the third dimension was, due to its width, negligible compared to the parallelism of the fibers in our sample. Further, the amount of speckle recorded by the detector is inversely proportional to the illuminated area of the sample. This is quite important, because these 2-d samples are essentially solid and cannot, like for 3-d samples, be spun to average out the speckle, since the fibers have to remain orientated with respect to the incident polarization of the laser beam. Shaking of the sample can solve this problem, but may frustrate the sample because it demands substancial acceleration to obtain a sufficient averaging. Nevertheless, it is possible to make the fibers vibrate a little, like strings, by flowing some clean air over the sample, thus obtaining averaging of the speckle as well.

The backscattered light from the sample was imaged onto an optical multichannal analyzer (OMA), where the intensity was recorded as a function of angle. Depending on the orientation of the detector with respect to the sample, either an angular scan parallel (denoted by $\text{scan}_{\|}$) or perpendicular to the axes of the fibers ($\text{scan}_{\perp}$) could be performed. A sheet polarizer was used to filter out only the polarization component parallel ($E_{\odot}$) or perpendicular ($E_{\otimes}$) with respect to the polarization of the incident light. I have tried to visualize this in Fig. 6.10.

We can do some interesting experiments in which we can find how well the sample behaves as if it were a truly two-dimensional random system. The dimensionality d of the system is determined by the parallelism of the fibers. In a perfectly two-dimensional system, $d = 2$, where all (infinitely long) fibers are perfectly parallel, all radiation from

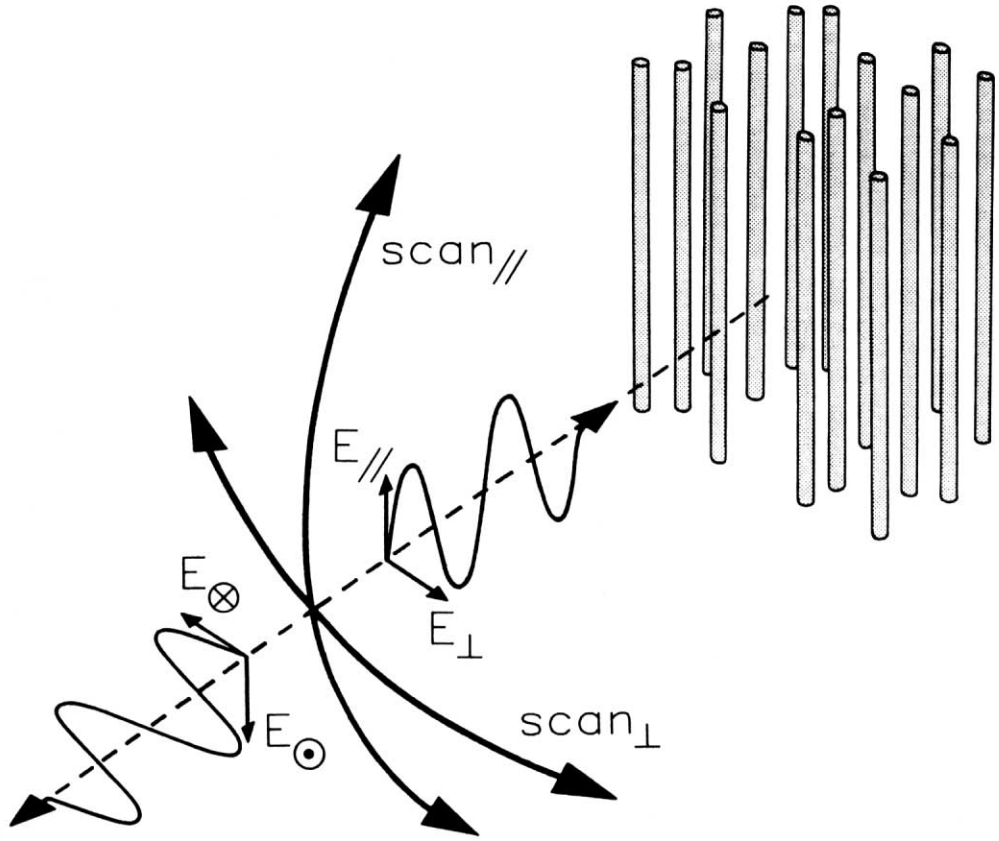

Figure 6.10: *Visualization of the definitions of the direction of polarization of the incident light, which can be either parallel ($E_{\|}$) or perpendicular ($E_{\perp}$) to the fibers, the angular scan, which can be either* in *the plane of 2-d scattering (perpendicular to the fibers) denoted by scan$_{\perp}$, or parallel to the fibers (scan$_{\|}$). The direction of polarization of the recorded intensity is given with respect to the* incident *polarization, either co-polarized ($E_{\odot}$) or cross-polarized ($E_{\otimes}$).*

the sample would be constricted to a plane, and hence an angular scan of the detector perpendicularly through this plane would give no signal except for a spike when the plane is crossed. For a laser beam coming in at arbitrary angle with the axes of the fibers, this spike occurs at the *specular angle*. If the fibers are not perfectly parallel, this spike will alter into a peak with some finite width Δ, which means that some light is scattered into the third dimension. We can attribute an artificial dimension $d = 2 + \epsilon$ to such a system, were ϵ is a measure for the deviation from 2-d, which we may define as the square root of the ratio of the mean free path λ_{mf} in the 2-d plane and $\lambda_{mf,\perp}$, the mean free path

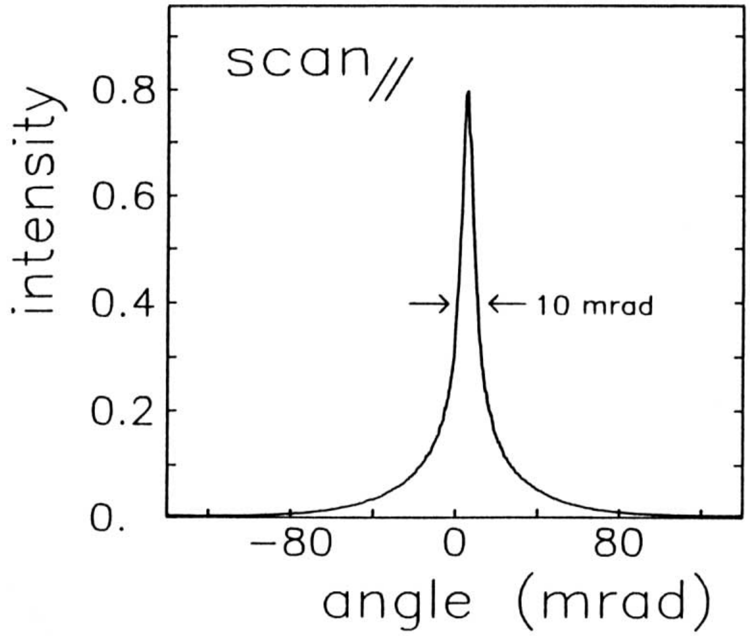

Figure 6.11: *The (specularly) backscattered intensity of our sample as a function of angle perpendicular to the 2-d plane (scan$_{\parallel}$). The width of the peak is a measure for the deviation from 2-d behavior of the sample as characterized by ϵ. This measurement appeared insensitive to which wavelength or polarization was used.*

perpendicular to this plane:

$$\epsilon = \sqrt{\frac{\lambda_{mf}}{\lambda_{mf,\perp}}}\ , \tag{6.9}$$

which results from the study of an anisotropic diffusion problem.[95] It seems to be a resonable definition because it gives the correct result for both $d = 2$ ($\lambda_{mf,\perp} = \infty$) and $d = 3$ ($\lambda_{mf} = \lambda_{mf,\perp}$).

In Fig. 6.11 the backscattered intensity of our sample is shown as a function of angle perpendicular to the 2-d plane. The full width at half maximum Δ of the peak is 10 mrad, and appeared to be only marginally dependent on the wavelength and polarization of the incident laser beam. The width Δ is proportional to the mean deviation angle $\overline{\varphi}$ of the fibers, with $\overline{\varphi} = \sqrt{\langle\varphi^2\rangle}$, and is a measure for the value of ϵ. It is clear that for $\overline{\varphi} = \pi/4$ the system will have the same mean free path in all directions and hence $\epsilon = 1$ and $d = 3$. Further, for $\overline{\varphi} = 0$ we should find $\epsilon = 0$. In Ref. 95 the connection between ϵ and $\overline{\varphi}$ is presented, which can be described by the ad hoc formula $\epsilon \simeq \sqrt{2\langle\sin^2\varphi\rangle}$, where Eq. (6.9) seems to suggest that $\epsilon \simeq \overline{\tan\varphi} \simeq \lambda_{mf}/\lambda_{mf,\perp}$, which deviates a factor $\sqrt{2}$ for small angles from the previous result.

If we assume that the width Δ_n from a n^{th}-order scattering contribution increases with

$2\overline{\varphi}$ at every next order of scattering, or if we assume that Δ_n doubles for every next order n, we find for both assumptions that the width Δ of the specular peak that $\Delta \approx 4\overline{\varphi}$. In the experiment we find $\Delta \simeq 10\,\text{mrad}$ and so $\overline{\varphi} \approx 2.5\,\text{mrad}$, which is an order of magnitude larger than the theoretical limit of 0.2mrad for the racetrack frame. The contribution of every order of scattering γ_n in a 2-d experiment can be estimated from Fig. 4.18. Doing this calculation, one has to notice that the value of γ_n is the *integral* ($\gamma_n \approx \Delta_n p_n$) rather than the peak p_n value of the n^{th}-order contribution. This explains why Δ is insensitive to the assumptions about the coupling to the third dimension, while Δ_n for large n is indeed very sensitive to these assumptions.

Another measure for the dimensionality is the retention of polarization in the multiple-scattered light. Coming in with arbitrary polarization, the degree of polarization, $E_{\odot}/E_{\otimes}$, of the backscattered intensity was measured to be better than 600 : 1, limited by the quality of the polarizer we used. This ratio is a measure for $\overline{\varphi}$ and hence also for ϵ^{-1}. Possibly $E_{\odot}/E_{\otimes} = \overline{\tan\varphi}$, so $\overline{\varphi} \lesssim 1/600\,\text{rad}$.

From the previously described experiments we can conclude, using the value of the mean tilt angle $\overline{\varphi} \simeq 2.5\,\text{mrad}$, that $\epsilon \simeq \sqrt{2\langle\sin^2\varphi\rangle} \approx 0.004$. Equivalent to the absorption length $\lambda_{abs} = \lambda_{tr}/\sqrt{2(1-a)}$, we can define a length over which the light is lost into the third dimension $\lambda_{3d} \simeq \lambda_{tr}/\sqrt{\epsilon}$, which with $\epsilon \approx 0.004$ implies that $\lambda_{3d} \approx 15\lambda_{tr}$. Of course we should keep in mind that these figures are obtained by hand-waving arguments. Some theory of multiple scattering on fibers can however be found in the literature.[113–115]

A very important experiment is the measurement of the coherent backscattering. In Fig. 6.12, the backscattered intensity for both parallel ($E_{\parallel}$) and perpendicular ($E_{\perp}$) polarization of the incident light with respect to the fiber direction as a function of scattering angle in the 2-d plane (scan$_{\perp}$) is shown. The direction of detetected polarization was chosen parallel to the incident polarization ($E_{\odot}$).

At precisely backscattering (0 mrad) we find a sharp peak of which the width is dependent on wavelength, polarization and density of scatterers (not shown in the figure), and thus is the result of weak localization. The transport mean free path λ_{tr} can be estimated from the width of the peak or be calculated with Mie-theory. The density of scatterers could be changed by varying the tension on the fibers, which makes them to relax a little, mainly in the middle of the 400 mm long sample. Besides a decrease in density of fibers at lower tensions which makes the coherent backscattering narrower, the parallelism becomes worse, and so the specular peak becomes wider.

The broad structures in Fig. 6.12 may be the consequence of both the single-fiber scattering and/or Bragg reflection due to nearest-neighbor correlation in the position of the fibers. To examine this in more detail, we recorded the backscattering pattern of a *single* fiber for all of the three wavelengths, and both polarizations. The results of these measurements are shown in Figs. 6.13. Fits to the measurements are shown at the right of

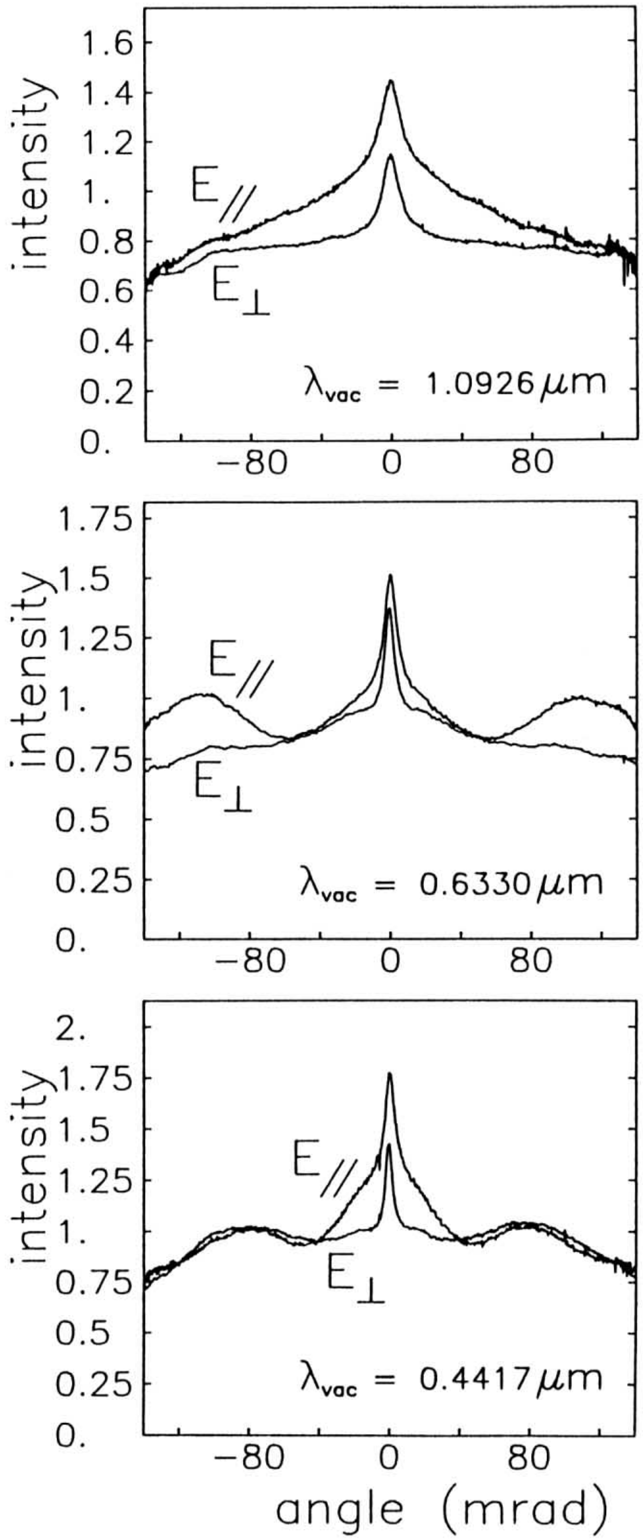

Figure 6.12: *Backscattered intensity of our sample as a function of scattering angle for three different wavelengths. The co-polarized ($E_\odot$) detected signal for both incident states of polarization, $E_\parallel$ and $E_\perp$, are given.*

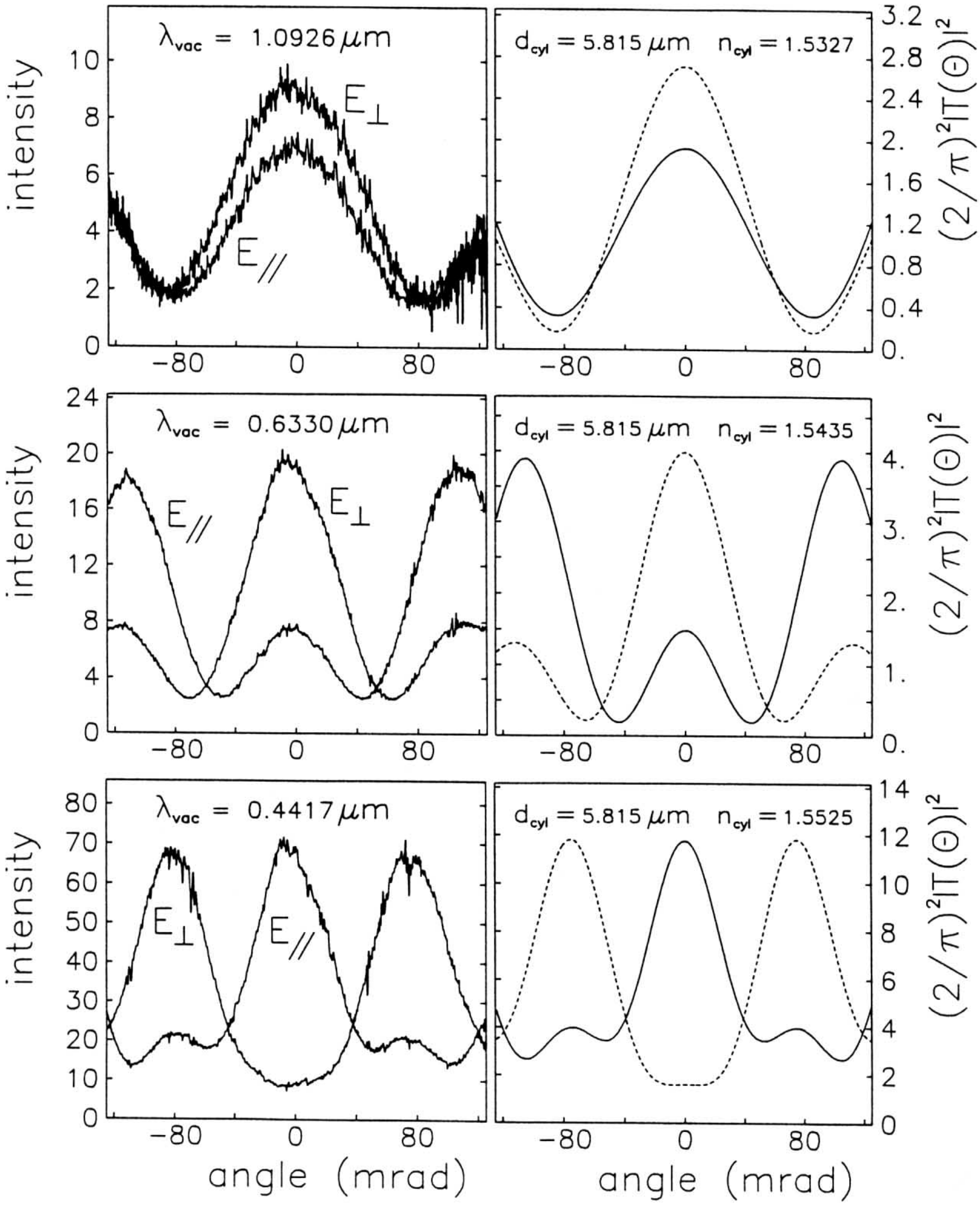

Figure 6.13: *Backscattered intensity from a single fiber as a function of scattering angle (scan$_\perp$) for three wavelengths. Experimental data are in the left figures, fitted curves in the right figures. They show the co-polarized ($E_\odot$) detected signal for both incident states of polarization, $E_\parallel$ and $E_\perp$.*

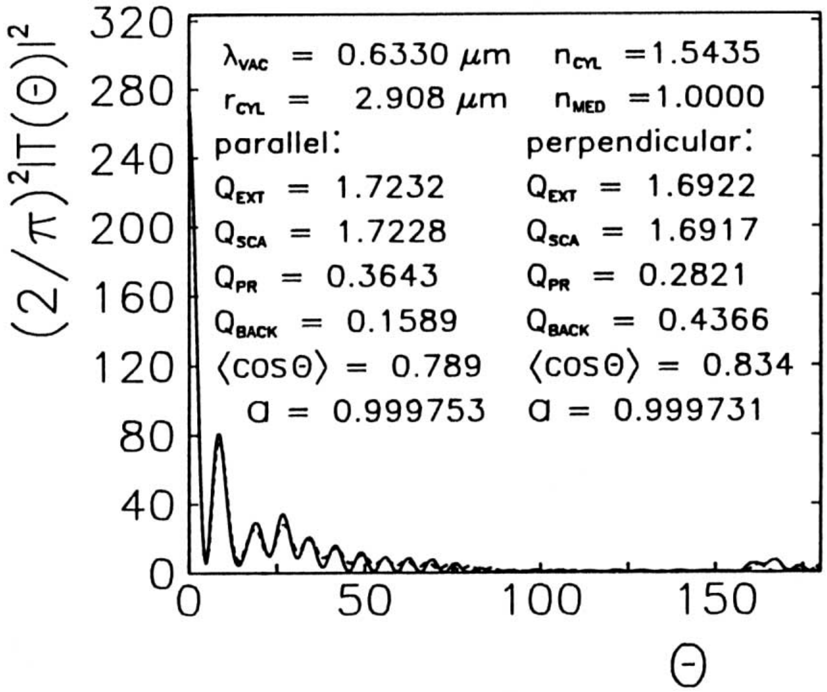

Figure 6.14: *The scattered intensity as calculated for the* 5.815 : μm *fiber for the two polarization states over the complete angular interval of* 180° *at a wavelength of* $\lambda_{vac} = 633.0$ *nm.*

these figures, from which we obtain both the refractive index and the diameter (5.815 μm) of the fiber. Although the fits are quite good, they are not as perfect as for the 125 μm fiber shown in Sect. 3.2.1. Possibly this is due to small fluctuations in the diameter of the fiber as a result of slightly varying drawing tension in the fabrication process. The measurements shown in Figs. 6.13 were done with a 2 cm wide laser beam, and hence shows the average of the scattering properties of the fiber over this length. Measurement on different locations of the same fiber showed a typical change of 15 nm in the average diameter of the fiber over a length of 15 mm. These figures show approximately the same structure as the diffuse background in Figs. 6.12. Transmission experiments identical to those shown in Figs. 6.12 for backscattering on the random medium show no structure at all, giving an angle-independent intensity. Together with the fact that the structure in Figs. 6.12 is quite dependent of the wavelength and state of polarization, we can conclude that single scattering probably plays a more important role than fiber-fiber correlations in the explanation of this feature. If we subtract the measured data for single scattering from those of the slab, some structure still remains, which probably results from double and triple scattering.

Some more information can be extracted from the mesurements of Figs. 6.13. From

Table VI: *A summary of some properties of the 80 μm thick sample with a packing fraction $\rho = 0.65$ of glass fibers having an average diameter of 5 μm.*

measured				calculated			
λ_{vac} (μm)	n n_r	n_i	incident polarization	λ_{sc} (μm)	λ_{tr} (μm)	albedo	λ_{abs} (μm)
1.0926	1.5327		$E_{\parallel}$	2.61	14.1		
			$E_{\perp}$	2.61	16.4		
0.6330	1.5435	3.60×10^{-6}	$E_{\parallel}$	3.87	14.6	0.9998	331
			$E_{\perp}$	3.87	17.6	0.9998	363
0.4417	1.5525	3.62×10^{-6}	$E_{\parallel}$	3.16	15.4	0.9997	285
			$E_{\perp}$	3.16	18.8	0.9997	315

Fig. 6.7, we can find at a wavelength of 633 nm that $\lambda_{in}/\lambda_{vac} \simeq 22100$. Using the relation

$$\lambda_{in} = \frac{\lambda_{vac}}{4\pi n_i} , \tag{6.10}$$

and taking n_r from Figs. 6.13 we find the complex refractive index of the fiber glass $n \equiv n_r + in_i = 1.5435 + i\,0.0000036$. Using this, we can calculate a number of scattering quantities of the fibers. In Fig. 6.14 a table of these quantities and the scattered intensity as calculated for the 5.815 μm fiber for the two polarization states over the complete angular interval of 180° is shown. Important is to notice the value of the albedo a and of Q_{sca} and Q_{pr}, from which we can calculate the λ_{abs}, λ_{sc} and λ_{tr}. We can do this similarly for the two other wavelengths. If we assume a packing fraction $\rho = 0.65$ as follows from the diameter of the fibers and the sample thickness of 80 μm we find the results shown in Table VI (the cross sections were averaged for many different diameters over an interval of $4.2 - 5.8$ μm).

From the width of the coherent backscattering, we can in principle also find the transport mean free path. This is not very easy, because the level of the diffuse background is due to the structure in the wings of the coherent backscattering not well defined. Also we are dealing with a slab of finite thickness of approximately $5\lambda_{tr}$, and therefore have to use Fig. 4.11 in order to find the proper relation between the width W of the coherent backscattering and λ_{tr}. We find $\lambda_{tr} \simeq 0.18\lambda_{vac}/W$, and some resulting values are given in Table VII. Despite these complications we find fairly good agreement, within the experimental error, with the values given by Table VI. In Table VII the measured and calculated values for λ_{tr} are compared. If we compare the values obtained for $E_{\parallel}$ and $E_{\perp}$, we see that the deviation is apparently the same for both incident states of polarization, which

Table VII: *The measured value (see Fig. 6.12) of λ_{tr} compared to the calculated value from Table VI and the average wavelength in the random medium λ_{med}.*

measured			calculated		
λ_{vac} (μm)	incident polarization	λ_{tr} (μm)	$\lambda_{tr}/\lambda_{tr,calc}$	n_{med} ($\rho = 0.65$)	$2\pi\lambda_{tr}/\lambda_{med}$
1.0926	$E_{\parallel}$	17.4	1.23	1.346	136
	$E_{\perp}$	19.7	1.20	1.346	154
0.6330	$E_{\parallel}$	15.2	1.04	1.353	205
	$E_{\perp}$	18.1	1.03	1.353	245
0.4417	$E_{\parallel}$	14.4	0.94	1.359	279
	$E_{\perp}$	16.8	0.90	1.359	325

suggests that the differences per wavelength are the result of a systematic rather than an accidental error.

As mentioned, it is likely that a systematic error comes from the improperly defined diffusive background. It is however intriguing that a part of the systematic error may be due to total internal reflection in the sample as refered to in the appendix of Chapter 5. For a packing fraction of 0.65, we find a mean refractive index in the medium of $n_{med} \simeq 1.355$, which with Fig. 5.22 results in a reduction factor of 1.45 of the width of the coherent backscattering. However, total internal reflection plays a less important role for $d = 2$ than for $d = 3$, thus the factor 1.45 should be regarded as an upper limit. If internal reflection plays a part, it will have the same effect on all of the three measurements, thereby improving the agreement between the calculated and measured value of the transport mean free path for the $\lambda_{vac} = 1.0926\,\mu$m experiment, but for the $\lambda_{vac} = 441.7\,$nm experiment it gets worse.

Finally, let us pay some attention to strong localization. Because we are considering a finite and lossy 2-d system, there is a mobility edge to cross before we obtain strong localization. Using the criterion given in a somewhat different context by John[116]:

$$\left(\frac{2\pi\lambda_{mf}}{\lambda}\right)^{1+\epsilon} \lesssim \frac{1}{\epsilon}\,, \tag{6.11}$$

which for $\epsilon = 1$ gives the Ioffe-Regel condition. With the last column of Table VII and since we have $\epsilon^{-1/1+\epsilon} \simeq 250$, we find that we may have entered the localization regime for $\lambda_{vac} = 1092.6$nm and $\lambda_{vac} = 633.0$nm. However, localization occurs only if the localization length λ_{loc} is shorter than the size of the sample, and also smaller than λ_{abs} and λ_{3d}. If the localization length exceeds the size of the sample, still the so-called logarithmic correction[21,104] to the amount of transmitted light (which results from scaling theory[20,23]) might be observed by varying the size of the sample. For the amount of transmitted light $\tilde{\gamma}$ we should find:

$$\tilde{\gamma} \propto \frac{\lambda_{mf}}{L}\left[\frac{\pi^2\lambda_{mf}}{\lambda} - \ln\frac{L}{\lambda_{mf}}\right] , \tag{6.12}$$

where the first term comes from the classical diffusion and the second, logarithmic, term is the result of interference loops in the sample. Whenever the difference of these terms becomes of the order unity strong localization occurs with a localization length $\lambda_{loc} \approx L$.

In our case, the sample has too much absorption to obtain the large dynamic range in sample size that would be required for an experiment to see a phenomenon that is so weakly dependent on the sample size as the logarithmic term. On the other hand we do have a large dynamic range in wavelength (441.7 nm-1092.6 nm) and in our set-up the behavior of the light in the sample can *in situ* be compared to behavior at other wavelengths which gives a powerful handle on the variable λ in Eq. (6.12). This may be important for seeing any departure from classical behavior at a certain wavelength.

From Eq. (6.12) we can see that it is really important to have the mean free path comparable to the wavelength when one wants to observe Anderson localization because otherwise the necessary size of the system explodes otherwise. This means that to do a successful experiment one should make high-refractive-index fibers which should not be thicker than a wavelength and have an outstanding transparency. And then, having done so, a sample with an very high parallelism between the fibers should be made.

6.3 Appendix

6.3.1 The guiding by a planar cavity

In this appendix, I will give the exact solution for the guiding of the so-called TE_{0n}-modes in a cavity consisting of some lossless dielectric sandwiched between two imperfectly conducting plates. These modes have their electric field vector $\vec{E}$ *parallel* to the conducting plates, and perpendicular to the direction of propagation. The mode profile of the lowest two modes is shown in Fig. 6.15, where the propagation of the wave is in the z-direction.

The two curl equations of the fields are

$$\nabla \times \vec{E} = -i\omega\vec{B} , \tag{6.13}$$

$$\nabla \times \vec{H} = -i\omega\varepsilon\vec{E} , \tag{6.14}$$

where the current term in Eq. (6.14) has been hidden in ε. Further we have $\nabla \cdot \vec{B} = 0$, and because we shall be dealing with field in the regions where the density of free charge is negligible, we can also take $\nabla \cdot \vec{E} = 0$. Doing some vector calculus we find the wave equation

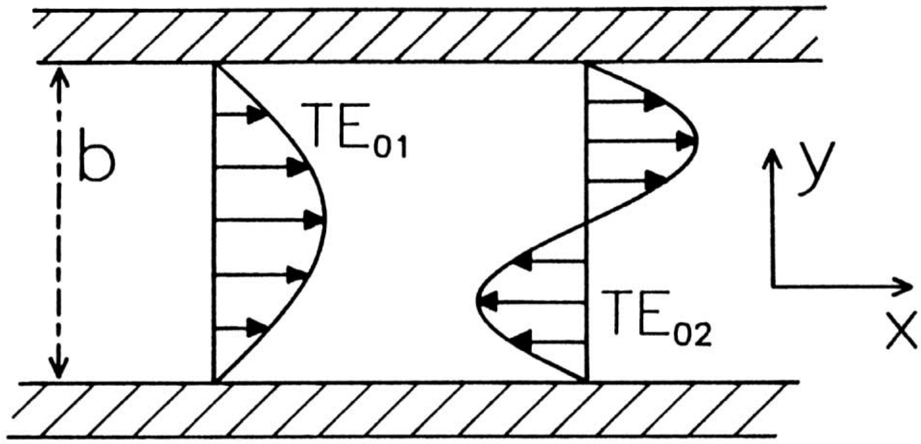

Figure 6.15: *The mode profiles of the TE_{01} and TE_{02} modes in a parallel-plate waveguide. The solid arrows represent the electric field $\vec{E}$.*

$$\nabla^2 \vec{E}(x,y,z) = -\mu\varepsilon\omega^2 \vec{E}(x,y,z) \ , \tag{6.15}$$

which holds not only for each of the components E_x, E_y and E_z, but also for each of the components of the magnetic field H_x, H_y and H_z. We will now concentrate on the solution of the problem for one of these components, E_x, from which we finally can find all fields. The component E_x will in general be a function of all three space coordinates (the time dependence $\exp(i\omega t)$ has already been accounted for by insertion of $i\omega$ for the operator $\partial/\partial t$.) If we write out Eq. (6.15) in full for E_x, we see that we may assume a product solution of the form

$$E_x(x,y,z) = X(x)Y(y)Z(z) \ , \tag{6.16}$$

which gives

$$\frac{X''}{X} + \frac{Y''}{Y} + \frac{Z''}{Z} = -\mu\varepsilon\omega^2 \ . \tag{6.17}$$

After identification of $\mu\varepsilon\omega^2 = k^2 = k_x^2 + k_y^2 + k_z^2$, with k complex, we obtain

$$\frac{X''}{X} = -k_x^2 \ , \qquad \frac{Y''}{Y} = -k_y^2 \ , \qquad \frac{Z''}{Z} = -k_z^2 \ , \tag{6.18}$$

The solution of the z-dependent factor of E_x is just a traveling wave with propagation constant $\pm ik_z$. Since we are interested in modes with the electric field parallel to the *infinite* conductors, $E_y = 0$ and the x-dependent factor of E_x is a constant. The y-dependent factor in the dielectric has the form of a standing wave between the conductors, and an exponential decay in the conductors. We find

$$E_x(x,y,z)\exp(-i\omega t) = Y(y)\exp[-i(\omega t \pm k_z z)] \ , \tag{6.19}$$

with

$$Y(y) = E_{x,+}\exp(ik_y y) + E_{x,-}\exp(-ik_y y)\ , \tag{6.20}$$

In the dielectric we have

$$\mu_0\varepsilon_0\varepsilon_d\omega^2 \equiv k_d^2 = n_{med}^2 k_{vac}^2\ , \tag{6.21}$$

with n_{med} the refractive index of the dielectric and $k_{vac} = 2\pi/\lambda_{vac}$. In the conductor we have

$$\mu_0\varepsilon_0(\varepsilon_r + i\varepsilon_i)\omega^2 \equiv k_c^2\ , \tag{6.22}$$

with

$$\varepsilon_c = \varepsilon_r + i\varepsilon_i\ . \tag{6.23}$$

The propagation constants in the conductor and the dielectric should be matched, so $k_z \equiv k_{z,c} = k_{z,d}$, and because we use a plane wave propagating in the z-direction, $k_{x,c} = k_{x,d} = 0$. We find that $k_{y,c}^2 - k_c^2 = -k_z^2 = k_{y,d}^2 - k_d^2$, so with the definitions $k_{y,c} \equiv k_m$ and $k_{y,d} \equiv k_g$ we obtain

$$k_m^2 - k_g^2 = k_c^2 - k_d^2 = \mu_0\varepsilon_0\omega^2(\varepsilon_r - \varepsilon_d + i\varepsilon_i)\ . \tag{6.24}$$

The curl equations 6.13 and 6.14 can be written into components, and, because we want to study the TE-modes, substitute $E_z = 0$. It indeed follows that $E_y = 0$, and also $H_x = 0$, because E_x and thus $\partial_y E_x$ is independent of x. Further we have

$$H_y = \frac{\pm k_z}{\omega\mu_0}E_x\ , \tag{6.25}$$

$$H_z = \frac{-i}{\omega\mu_0}\partial_y E_x\ , \tag{6.26}$$

so with Eqs. (6.19) and (6.20) we find

$$H_z(x,y,z)\exp(-i\omega t) = \frac{k_y}{\omega\mu_0}\left[E_{x,+}\exp(ik_y y) - E_{x,-}\exp(-ik_y y)\right]\exp[-i(\omega t \pm k_z z)]\ . \tag{6.27}$$

The boundary conditions on the interface of the conductors and dielectric at $y = \pm b/2$ give

$$E_{x,c} = E_{x,d}\ , \tag{6.28}$$

$$\mu H_{y,c} = \mu_0 H_{y,d}\ , \tag{6.29}$$

$$H_{z,c} = H_{z,d}\ , \tag{6.30}$$

where we take the permeability of the metal $\mu = \mu_0$. Let us concentrate on the boundary at $y = -b/2$. We find that in order to make the field go to zero for $y \to -\infty$ in the metal, the constant $E_{x,-}$ should be taken zero. Because the field in the dielectric has the form of a standing wave in the y-direction (it has to be either symmetric or anti-symmetric due to the symmetry of the problem), we have $E_{x,-} = \pm E_{x,+} \equiv E_d$. If we further define in the metal that $E_{x,+} = E_c$, we find using the boundary conditions 6.28 and 6.30, and the equations for E_x and H_z:

$$
\begin{aligned}
E_c \exp(-ik_m b/2) &= E_d \left[\pm \exp(ik_g b/2) + \exp(-ik_g b/2)\right] \ , \qquad (6.31)\\
E_c \exp(-ik_m b/2) &= \frac{k_g}{k_m} E_d \left[\mp \exp(ik_g b/2) + \exp(-ik_g b/2)\right] \ , \qquad (6.32)
\end{aligned}
$$

from which follows with Eq. (6.23) that

$$
\frac{\mp 4k_g^2 \exp(-ik_g b)}{[1 \pm \exp(-ik_g b)]^2} = \mu_0 \varepsilon_0 \omega^2 (\varepsilon_r - \varepsilon_d + i\varepsilon_i) \ . \qquad (6.33)
$$

The $\pm$ sign selects between the even and odd TE$_{0n}$-modes. If we divide the real and imaginary part of this equation, we find with $k_g b \equiv p + iq$:

$$
\frac{\varepsilon_r - \varepsilon_d}{\varepsilon_i} = \frac{(p^2 - q^2)(1 \pm \cos p \cosh q) \mp 2pq \sin p \sinh q}{2pq(1 \pm \cos p \cosh q) \pm (p^2 - q^2) \sin p \sinh q} \ . \qquad (6.34)
$$

In a cavity without loss we find $p = n\pi$, which means that the mode is precisely sinusoidal. This can only be so if the field does not penetrate into the conductors, which means that $n_i = \infty$ and hence $\varepsilon_i = \infty$. From Eqs. (6.33) and (6.34) we can find p and q numerically. If we now use that $k_{x,d}^2 + k_{y,d}^2 + k_{z,d}^2 \equiv k_d^2$, with $k_{x,d} = 0$, $k_{y,d} \equiv k_g$, $k_{z,d} \equiv k_z \equiv k' + ik''$ and $k_d^2 = \varepsilon_d k_{vac}^2$, we find

$$
(k' + ik'')^2 = \frac{4\pi^2 \varepsilon_d}{\lambda_{vac}^2} - \frac{(p + iq)^2}{b^2} \ . \qquad (6.35)
$$

This results in

$$
k' = \frac{1}{\sqrt{2}} \left[\frac{4\pi^2 \varepsilon_d}{\lambda_{vac}^2} + \frac{q^2 - p^2}{b^2} \pm \sqrt{\left(\frac{4\pi^2 \varepsilon_d}{\lambda_{vac}^2} + \frac{q^2 - p^2}{b^2} \right)^2 + \frac{4p^2 q^2}{b^4}} \right]^{1/2} \ , \qquad (6.36)
$$

and

$$
k'' = \frac{-pq}{k' b^2} \ . \qquad (6.37)
$$

The inelastic length of the guide can now be found from

$$
\frac{\lambda_{in}}{\lambda_{vac}} = \frac{k_{vac}}{4\pi k''} \ . \qquad (6.38)
$$

Finally, it is interesting to notice that the wavelength in the guide is longer in the guide than in vacuum, and diverges close to cut-off.

Chapter 7

Very strongly-scattering media and Anderson localization

After some years of research, the occurrence of weak localization of electromagnetic waves is well established. Recently, some strong experimental evidence for the existence of a mobility edge was given by Drake and Genack,[98] and independent evidence was given in this thesis (see Sect. 5.4.2). So the question as to whether it will be possible to observe strong localization of light in a 3-d medium should be considered. The crucial parameter is the transport mean free path λ_{tr}, which should be as short as possible. It seems that a suspension of TiO_2 in air or in some low refractive-index substance is the system in which the shortest λ_{tr}-values for visible light may be realized in practice, which is confirmed by theoretical work.[117] Altough we tried very hard, it seems (almost?) impossible to make λ_{tr} short enough to obtain Anderson localization. The question arises then whether or not there is a *fundamental barrier* to enter the localization regime. Such a barrier may exist in the form of dependent scattering, correlation between scatterers, or the impossibility of obtaining high contrast in refractive index in combination with a low absorption coefficient of the high refractive index material. It even may be possible that a fundamental barrier exists for example only for electromagnetic waves, possibly as a consequence of their vector nature, as I have mentioned in Sect. 1.3 and Sect. 2.1.1 (notice that the vector character is unimportant in 2-d media).

The first point, dependent scattering, may be the hardest to fathom. Dependent scattering is the phenomenon that the effective cross sections of particles which are in each others near field can be altered due to the proximity of the other scatterers. For resonant scatterers, as used in localization experiments for their high scattering efficiency, this means that they are brought off resonance by the vicinity of other particles, thereby decreasing the cross section per particle. It is believed that the occurence of dependent scattering is coupled to the overlap of the cross sections of the particles. For resonant point scatterers, the cross section σ may be as large as λ^2, and, to prevent overlap, the density should not be larger than $n_0 < \lambda^{-3}$, so we find $\lambda_{mf} = (n_0\sigma)^{-1} > \lambda$. Although some unknown prefactors are missing here, this answer is quite discouraging because the Ioffe-Regel criterion demands a *maximum* value for λ_{mf} that is even a factor of 2π less. Experiments already have shown that the mean free path can actually be less than the wavelength, but still this barrier may separate us from Anderson localization.

The second point, correlation between scatterers, probably can be circumvented by using scatterers having a much higher effective cross section than geometrical cross section, which means that Q_{pr} should be as high as possible. At the same time the scatterers should preferably be much smaller than the wavelength. Under such conditions it is possible to have a high optical density without bringing the particles very close to each other.

This brings us to the last point. A very high value of Q_{pr} can only be obtained for a large contrast in refractive index, which intrinsically is connected to absorbtion by the Kramers-Kronig relation. The question is whether there exist materials from which scatterers can be made which combine a high scattering efficiency with a long absorption length, at least longer than the localization length. To be more precise, it is the ratio $\lambda_{tr}/\lambda_{in} = (1-a)\lambda_{tr}/\lambda_{sc}$ that should be as small as possible. It is indeed the inelastic length λ_{in} that is more fundamental than the absorption length λ_{abs} (see Sect. 4.1), because the relation $\lambda_{abs} = \sqrt{\lambda_{tr}\lambda_{in}/d}$ is based on the assumption of a d-dimensional random walk, which breaks down at localization. In diffusive transport, close to the critical regime, we expect to find $\lambda_{abs} = \sqrt{\lambda_{tr}^{*}\lambda_{in}/d}$. Since returning to a point is largely enhanced, it seems obvious that at localization the absorption length will be much smaller than would be expected from diffusive transport. A general formula for the absorption length in any regime seems to be $\lambda_{abs} = \sqrt{D\lambda_{in}/c_{med}}$. This formula implies that in the critical regime the absorption length will become scale dependent as a consequence of the scale dependence of the diffusion constant D. The dependence of absorption on the diffusion constant near the mobility edge is however still subject of discussion among scientists.

Two more phenomena complicate the behavior of very strongly-scattering media made of very high refractive index materials.

The first is the occurence of a significant mismatch at the interfaces of the random medium with the outside world, resulting in a large amount of reflection of the light back into the medium. This problem was already dealt with theoretically in the appendix of Chapter 5. Experimentally, there is still very little known about the scattering from these boundaries. Measurement of the reflection of a coherent beam as a function of angle from the outside surface of a flat medium may reveal the complex refractive index $n \equiv n_r - in_i$ of the surface. Here, the imaginary part of n is expected to relate to the scattering mean free path by $4\pi n_i = \lambda_{vac}/\lambda_{sc}$. Some preliminary experimental results on a polished TiO_2

sample with $\rho \simeq 0.47$ show however no evidence for the existence of an imaginary part of the refractive index and a puzzling low value for the real part $n_r \simeq 1.28$. Measurement of the width of the coherent backscattering peak from a sample, but with different index-matching materials on the surface, may also give important information on this effect.

The second phenomenon is the trapping of light inside the scatterers. In a medium consisting of resonant scatterers having a very narrow width of the resonance, such as of the spikes in Fig. 3.3, a significant time delay compared to the mean propagation time between scatterers may occur at each scattering event. In a time resolved experiment as it has been described in Sect. 5.4.2, it is impossible to discriminate this effect from diffusion, and hence the value of the diffusion constant following from such an experiment may be largely underestimated. Very narrow and well-separated resonances are however only to be expected in very regularly shaped scatterers like spheres.[118–120] Therefore it is not very likely that this effect plays a part in the experiment of Sect. 5.4.2, where irregularly-shaped rutile particles where used. However, it possibly may have played a role in the important experiments done by Drake and Genack,[98] who used anatase *spheres*. A rough estimate of the possible effect by resonant particles on the time of residence in the sample can be destilled from Fig. 3.3, where the dashed line represents Q_{pr} for the (size-distributed) particles ($2.5 < x < 4.5$) as have been used in the experiments of Ref. 98. The area under the resonances is a measure for the fraction (approximately 10 %) of particles which are on resonance. The relative width $\Delta x/x$ of the resonances is a measure for the delay of the light at such a resonant particle. If we estimate that $\Delta x/x \approx 10$, we find that the light is on the average delayed by a factor of ten at every tenth particle. This results in an average delay of no more than approximately a factor 2 in the diffusion constant.

7.1 Dependent scattering and correlated scatterers

Many theories of elastic multiple scattering in random media are based on two assumptions that become highly questionable at high densities of scatterers. These assumptions are (i) that particle-particle correlations are absent, and (ii) that scattering paths which go through the same scatterer more than once may be neglected: Independent-Scattering Approximation (IPA).

Inclusion of particle-particle correlations is desirable at high densities, but interaction between scatterers complicates matters enormously. Even with the simplest possible forms such as hard-sphere interaction, the static behavior of a collection of scatterers, expressed in terms of density-density correlation functions, becomes an insolvable many-body system. Approximative methods exist to obtain reliable values for density-density correlation functions. The problem with multiple scattering is that one needs higher-order density correlation functions, that are difficult to obtain. Usually one relies on decoupling procedures to express high-order density correlation functions in terms of products of lower-order correlation functions. Anyhow, the introduction of even approximate particle-particle correlations makes the multiple-scattering problem much more difficult. Now without knowing the precise magnitude of the corrections induced by particle-particle correlations, it is to be expected that in general the trend will be to reduce the scattering efficiency or, starting from a weakly-scattering medium, increasing the density of scatterers will result in a reduction of the mean free path until the effect of particle-particle correlations balances that of the increasing density and saturation occurs.

For very high densities, mean-field approximate theories exist to calculate amplitude Green's functions. These methods are known under names as average-t-matrix approximation (ATA), and coherent-potential approximation (CPA).[121] They find useful application in the theory of electronic structure of disordered composites, for instance: In an AB disordered crystalline system, both limits (100 % A and 100 % B) should be described correctly and the mean-field theories are tailored to do so. The theories also include some dependent-scattering corrections. The mean-field theories are usually optimized to calculate the real part of the self energy of the amplitude Green's function, which is expressed as an effective dielectric constant. We are more interested in the mean free path, which is associated with the *imaginary* part of the self energy of the amplitude Green's function.

The independent-scattering approximation (IPA) is expected to break down when the scatterers get very close. For instance for two particles the IPA implies that there are contributions to the t-matrix of the type t_1, t_2, t_1t_2, and t_2t_1, excluding all higher-order multiple scattering between the two particles. However, when the particles are close compared to the wavelength, multiple scattering between the two particles may become very important. One sees that in this situation the particle correlations may also become important. To get more insight in the effect of dependent scattering without the simultaneous influence of particle correlations, Reiter and Lagendijk studied *point* scatterers in an isotropic scalar theory.[122] This theory yields the total t-matrix as the inversion of a matrix with a dimension equal to the number of particles. Their t-matrix is not averaged yet over the realizations of the sample and is therefore a configuration-dependent t-matrix. The inversion allows for an exact numerical diagonalization for a finite but large (in the order of 1000) number of particles. This numerical result can then be compared with the approximate theories to check their quality. In addition the theory of Reiter and Lagendijk can be used to average over the particle realizations and obtain dependent-scattering corrections to the amplitude Green's function.

Before discussing the implications of the effects of particle correlations and dependent scattering on localization we want to point out that in principle localization is connected with unaveraged amplitude Green's functions or configurationally averaged intensity Green's functions. In the preceding paragraph we discussed mainly the results for

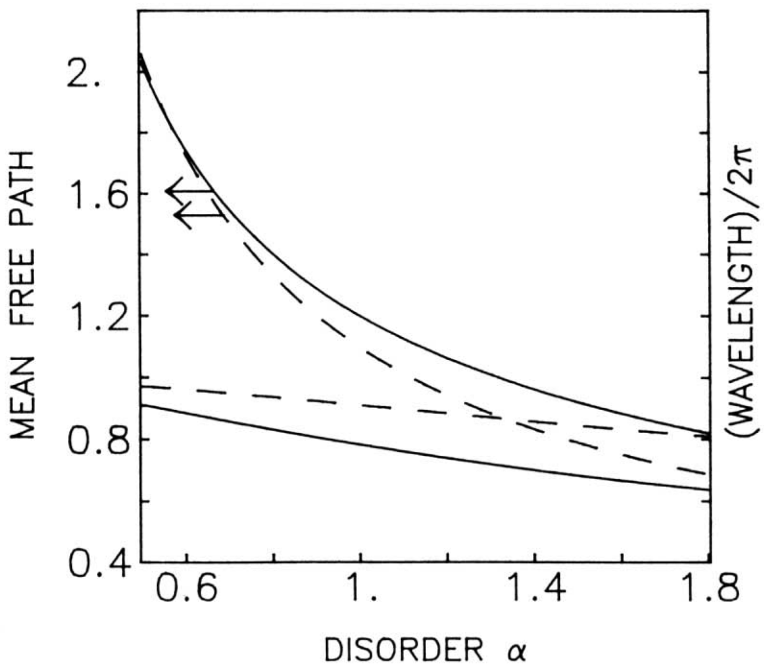

Figure 7.1: *Mean free path and wavelength as a function of the disorder parameter α for resonating particles. Dashed lines refer to the independent scattering result and solid lines are the result of a self-consistent theory which incorporates dependent-scattering corrections (from Ref.* 122*).*

the averaged amplitude Green's function. In principle, no information on localization is contained in these results, as is for instance illustrated very well by the Lloyds model.[123] Of course, the results for the intensity Green's function depend on those for the amplitude Green's function. In practice it is very likely that if corrections of the type just discussed make the scattering (described by the scattering mean free path λ_{sc}) less efficient, the scattering in the intensity Green's function, as described by the transport mean free path λ_{tr}, will also be less efficient. In Fig. 7.1 the results of a renormalized theory including all types of two-particle dependent scattering on the mean free path and the effective wave vector are displayed as a function of the disorder parameter α, defined as

$$\alpha = \frac{4\pi n_0}{k_0}\mathrm{Im}\{f\} , \tag{7.1}$$

in which $n_0 = N/V$ is the density of scatterers, f is the scattering amplitude of the scatterers, and k_0 is the bare wave vector of the medium.

We see that indeed the dependent-scattering corrections make the scattering mean free path longer. We expect that this will also make the transport mean free path longer and as such make the possible observation of localization of waves more difficult.

7.2 About Anderson localization

The main question, how we can measure strong localization if it exists, remains. To give an answer to this question, one has in the first place to know more precisely what behavior of the system to expect when it approaches the mobility edge.

As emphasized before, the important parameter is the transport mean free path λ_{tr}. The transition from diffusive transport to localized states occurs around $\lambda_{tr} = \lambda_{cr}$, where the critical mean free path λ_{cr} is in $d = 3$ approximately given by the Ioffe-Regel condition:

$$\lambda_{cr} \approx \frac{\lambda_{med}}{2\pi} , \tag{7.2}$$

For a slab of finite thickness L, localization will however only occur for $L > \lambda_{loc}$. In Fig. 7.2 an impression of the phase diagram is given. The curve at the left in the figure is given by the relation $L = -{\lambda_{tr}}^2/\lambda^*_{tr} \propto \lambda_{loc}$, the curve at the right by $L = {\lambda_{tr}}^2/\lambda^*_{tr}$, with $\lambda^*_{tr} = \lambda_{tr} - \lambda_{cr}$. These curves separate the following regions in the figure. Classical diffusion and weak localization exists in the right-most region. The middle part of the figure represents the so-called critical regime, where the diffusion constant D becomes scale dependent, and hence the L^{-1} law (similar to Ohm's law for electrons) of the diffusion breaks down. In the left part of the figure, strong localization occurs, and the diffusion constant is virtually zero ($D \approx 0$).

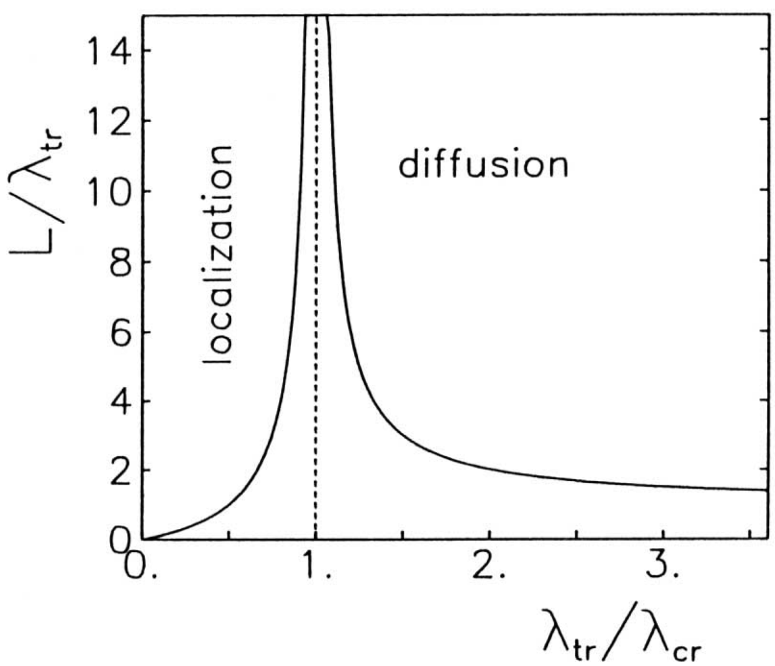

Figure 7.2: *Impression of the Anderson phase diagram (see Ref. 6). The transition from diffusive transport to localized states occurs around $\lambda_{tr} = \lambda_{cr}$.*

To detect strong localization one should study light which traveled through the medium over at least the localization length, λ_{loc}, which near the localization transition may be larger than λ_{tr} by orders of magnitude. Since in backscattering lower-order scattering contributions are dominant, transmission experiments seem to be indicated for the detection of strong localization. Whereas in the regime of classical diffusion the transmission $\tilde{\gamma}$ decays with increasing length L of the sample according to L^{-1}, in the localized regime this decay is expected to be faster: possibly starting as L^{-2} for $L < \lambda_{loc}$ and exponential for $L > \lambda_{loc}$. Absorption by the sample is a complicating factor, as it in the diffusive regime already leads to an exponential decay. See Fig. 7.2.

In the diffusive regime, a measurement of fluctuations, a time-resolved experiment or a measurement of the coherent backscattering give in principle all exactly the same information about λ_{tr}, because there is a simple relation between the mean time to propagate over a certain distance, and the mean dephasing over that distance. In the critical regime, diffusion theory starts to break down due to enhancement of loop-type scattering events. It is clear that there is now another relationship between the mean propagation time and the separation of begin and end of a path. For example, a measurement of the coherent backscattering probes this *separation* and is therefore a measure for λ_{tr}, where a time resolved experiment measures the *delay*, and is thus sensitive to the presence of loops in the path the light has traveled. Hence such an experiment probes the value of λ_{tr}^* rather than λ_{tr}.

Finally, I want to emphasize that it is the *combination* of the described experimental techniques which form a powerful tool in measuring Anderson localization of light.

References

[1]P.W. Anderson, “Absence of diffusion in certain random lattices”, Phys. Rev. **109**, 1492 (1958).

[2]For a recent collection of papers on Anderson localization, see: “Anderson Localization”, edited by T. Ando and H. Fukuyama (Springer, Berlin, 1988).

[3]W. Götze, “A theory for the conductivity of a fermion gas moving in a strong three-dimensional random potential”, J. Phys. C **12**, 1279 (1979); W. Götze, “The mobility of a quantum particle in a three-dimensional random potential”, Phil. Mag. B **43**, 219 (1981).

[4]D. Vollhardt and P. Wölfle, “Diagrammatic, self-consistent treatment of the Anderson localization problem in $d \leq 2$ dimensions”, Phys. Rev. B **22**, 4666 (1980).

[5]N.F. Mott, “Electrons in disordered structures”, Adv. Phys. **16**, 49 (1967); see also: Norman Gee and Gordon R. Freeman, “Electron transport in dense gases: limitations on the Ioffe-Regel and Mott criteria”, Can. J. Chem. **64**, 1810 (1986).

[6]P.W. Anderson, “The question of classical localisation. A theory of white paint?”, Philos. Mag. B **52**, 505 (1985).

[7]S. John and M.J. Stephen, “Wave propagation and localization in a long-range correlated random potential”, Phys. Rev. B **28**, 6358 (1983).

[8]S. John, “Electromagnetic Absorption in a Disordered Medium near a Photon Mobility Edge”, Phys. Rev. Lett. **53**, 2169 (1984).

[9]T.R. Kirkpatrick, “Localization of Acoustic Waves”, Phys. Rev. B **31**, 5746 (1985).

[10]M.P. van Albada, M.B. van der Mark and A. Lagendijk, “Towards observation of Anderson localization of light”, in ”Analogies in Optics and Micro Electronics”, edited by W. van Haeringen and D. Lenstra, (Kluwer, 1990).

[11]B.L. Al’tshuler and P.A. Lee, “Disordered Electronic Systems”, Physics Today, p. 36, december (1988).

[12]L. Van den Dries, C. Van Haesendonck, Y. Bruynseraede, and G. Deutscher, “Two-Dimensional Localization in Thin Copper Films”, Phys. Rev. Lett. **46**, 565 (1981).

[13]M.P. van Albada, M.B. van der Mark and A. Lagendijk, “Experiments on Weak Localization of Light and their Interpretation”, in “Scattering and localization of classical waves in random media”, edited by Ping Sheng (World Scientific, Singapore, 1990).

[14]A. Lagendijk, M.P. van Albada and M.B. van der Mark, "Localization of Light: The Quest for the White Hole", in Statphys 16, edited by H.E. Stanley, Physica **140**, 183 (1986).

[15]M.Ya. Azbel, "Localization and Dimensionality", Sol. St. Commun. **47**, 699 (1983).

[16]C. Flesia, R. Johnston and H. Kunz, "Strong Localization of Classical Waves: A Numerical Study", Europhys. Lett. **3**, 497 (1987).

[17]R. Orbach, "Dynamics of Fractal Networks", Science **231**, 814 (1986).

[18]P. de Vries, H. De Raedt, and A. Lagendijk, "Localization of Waves in Fractals: Spatial Behavior", Phys. Rev. Lett. **62**, 2515 (1989).

[19]M.N. Barber and B.W. Ninham, "Random and Restricted Walks", (Gordon and Breach, New York, 1970).

[20]E. Abrahams, P.W. Anderson, D.C. Licciardello, and T.V. Ramakrishnan, "Scaling Theory of Localization: Absence of Quantum Diffusion in Two Dimensions", Phys. Rev. Lett. **42**, 673 (1979).

[21]N.F. Mott and M. Kaveh, "The conductivity of disordered systems and the scaling theory", J. Phys C **14**, L659 (1981); M. Kaveh and N.F. Mott, "Diffusion and logarithmic corrections to the conductivity of a disordered non-interacting 2D electron gas: powerlaw localisation", J. Phys C **14**, L177 (1981).

[22]M.Ya. Azbel, "Anderson-localization dimensionality dependence: Further comments", Phys. Rev. B **26**, 4735 (1982).

[23]D. Chowdhury, "One Parameter Scaling Theory of Localization", Commun. Sol. St. Phys. **12**, 69 (1986).

[24]B. Souillard, "Electrons in Random and Almost-Periodic Potentials", Phys. Rep. **103**, 41 (1984).

[25]S. Das Sarma, A. Kobayashi, and R.E. Prange, "Proposed Experimental Realization of Anderson Localization in Random and Incommensurate Artificially Layered Systems", Phys. Rev. Lett. **56**, 1280 (1986).

[26]P. Sheng, B. White, Z.Q. Zhang, and G. Papanicolaou, "Minimum wave-localization length in a one-dimensional random medium", Phys. Rev. B **34**, 4757 (1986).

[27]E. Bouchard and M. Daoud, "Reflection of light by a random layered system", J. Physique **47**, 1467 (1986).

[28]D.J. Thouless, “Localization in One Dimension”, in ”Physics in One Dimension”, edited by J. Bernasconi and T. Schneider, p. 306 (Springer-Verlag, Berlin, 1984).

[29]S. He and J.D. Maynard, “Detailed Measurement of Inelastic Scattering in Anderson Localization”, Phys. Rev. Lett. **57**, 3171 (1986).

[30]T.T. Wu, “Fermi pseudopotentials and resonances in arrays”, in ”Resonances- Models and phenomena”, lecture notes in physics 211, p. 293 (Springer, 1984) (proceedings of Bielefeld conference 1984).

[31]A. Grossmann and T.T. Wu, “Fermi pseudopotentials in higher dimensions”, J. Math. Phys. **25**, 1742 (1984).

[32]M.J. Stephen, “Temporal fluctuations in wave propagation in random media”, Phys. Rev. B **37**, 1 (1988).

[33]G. Maret and P.E. Wolf, “Multiple Light Scattering from Disordered Media. The Effect of Brownian Motion of Scatterers”, Z. Phys. B **65**, 409 (1987).

[34]Yu.N. Barbaranenkov, “Wave corrections to the transferequation for backscattering”, Izv. Vysch. Uch. Zav.-Radiofiz., **16**, 88 (1973).

[35]Y. Kuga and A.Ishimaru, “Retroreflection from a dense distribution of spherical particles”, J. Opt. Soc. Am. A **1**, 831 (1984).

[36]M.P. van Albada and A. Lagendijk, “Observation of Weak Localization of Light in a Random Medium”, Phys. Rev. Lett. **55**, 2692 (1985).

[37]P.E. Wolf and G. Maret, “Weak Localization and Coherent Backscattering of Photons in Disordered Media”, Phys. Rev. Lett. **55**, 2696 (1985).

[38]B. Cellini Autobiography, through M. Minnaert, Natuurkunde van het vrije veld, fifth edition, Vol. I, p. 267 (Thieme, Zutphen, 1974).

[39]W.W. Montgomery and R.H. Kohl, “Opposition effect experimentation”, Opt. Lett. **5**, 546 (1980).

[40]T.S. Trowbridge, “Retroreflection from rough surfaces”, J. Opt. Soc. Am. **68**, 1225 (1978).

[41]R. Vreeker, M.P. van Albada, R. Sprik, and A. Lagendijk, “Femtosecond Time-Resolved Measurements of Weak Localization of Light”, Phys. Lett. A **132**, 51 (1988).

[42]R. Vreeker, M.P. van Albada, R. Sprik, and A. Lagendijk, “Depolarization of femtosecond laser pulses in disordered media”, Opt. Commun. **70**, 365 (1989).

[43]G.H. Watson, Jr., P.A. Fleury, and S.L. McCall, "Search for Photon Localization in the Time Domain", Phys. Rev. Lett. **58**, 945 (1987).

[44]A.Z. Genack, L.A. Ferrari, J. Zhu, N. Garcia, J.M. Drake, "Optical and Microwave propagation in random dielectric and metallic media", proceedings of the 1987 ILS conference (1987).

[45]S. Etemad, R. Thompson and M.J. Andrejco, "Weak Localization of Photons: Universal Fluctuations and Ensemble Averaging", Phys. Rev. Lett. **57**, 575 (1986).

[46]P.A. Lee and A.D. Stone, "Universal Conductance Fluctuations in Metals", Phys. Rev. Lett. **55**, 1622 (1985).

[47]B.Z. Spivak and A.Yu. Zyazin, "Fluctuations of coherent light transmission through disordered media", Sol. St. Commun. **65**, 311 (1988).

[48]A.Z. Genack, "Optical Transmission in Disordered Media", Phys. Rev. Lett. **58**, 2043 (1987).

[49]N. Garcia and A.Z. Genack, "Crossover to Strong Intensity Correlation for Microwave Radiation in Random Media", Phys. Rev. Lett. **63**, 1678 (1989).

[50]M.P. van Albada, J.F. de Boer and A. Lagendijk, "Observation of Long-Range Intensity Correlation in the Transport of Coherent Light through a Random Medium", to be published.

[51]S. Feng, C. Kane, P.A. Lee, and A.D. Stone, "Correlations and Fluctuations of Coherent Wave Transmission through Disordered Media", Phys. Rev. Lett. **61**, 834 (1988).

[52]L. Wang, and S. Feng, "Correlations and fluctuations in reflection coefficients for coherent wave propagation in disordered scattering media", Phys. Rev. B **40**, 8284 (1989).

[53]B. Shapiro, "Large Intensity Fluctuations for Wave Propagation in Random Media", Phys. Rev. Lett. **57**, 2168 (1986).

[54]M.J. Stephen and G. Cwillich, "Intensity Correlation Functions and Fluctuations in Light Scattered from a Random Medium", Phys. Rev. Lett. **59**, 285 (1987).

[55]I. Freund, M. Rosenbluh, and S. Feng, "Memory Effect in Propagation of Optical Waves through Disordered Media", Phys. Rev. Lett. **61**, 2328 (1988).

[56]R. Berkovits and M. Kaveh, "Angular correlations of waves in disordered systems: New numerical results", preprint.

[57]H.C. van de Hulst, "Light scattering by small particles" (Dover, New York, 1981).

[58]C.F. Bohren and D.R. Huffman, "Absorption and scattering of light by small particles" (Wiley, New York, 1983).

[59]Light Scattering by Irregularly Shaped Particles, edited by D.W. Schuerman (Plenum, New York, 1979).

[60]U. Frisch, "Wave Propagation in Random Media" in "Probabilistic Methods in Applied Mathematics", edited by A.T. Barucha-Reid, Vol. I, p. 76 (Academic Press, New York, 1968).

[61]M.B. van der Mark, M.P. van Albada, and A. Lagendijk, "Light Scattering in Strongly Scattering Media: Multiple Scattering and Weak Localization", Phys. Rev. B **37**, 3575 (1988).

[62]S. Chandrasekhar, "Radiative Transfer" (Dover, New York, 1960).

[63]A. Ishimaru, "Wave Propagation and Scattering in Random Media", Vols. I and II (Academic, New York, 1978).

[64]H.C. van de Hulst, "Multiple Light Scattering", Vols. I and II (Academic, New York, 1980).

[65]Multiple Scattering and Waves in Random Media, edited by P.L. Chow, W.E. Kohler and G.C. Papanicolaou (North-Holland, Amsterdam, 1981).

[66]L. Tsang and A. Ishimaru, "Backscattering enhancement of random discrete scatterers", J. Opt. Soc. Am. A **1**, 836 (1984); "Theory of backscattering enhancement of random discrete isotropic scatterers based on the summation of all ladder and cyclical terms", ibid. **2**, 1331 (1985); "Radiative wave and cyclical transfer equations for dense nontenuous media", ibid. **2**, 2187 (1985).

[67]M.J. Stephen and G. Cwillich, "Rayleigh scattering and weak localization: Effects of polarization", Phys. Rev. B **34**, 7564 (1986).

[68]G. Cwillich and M.J. Stephen, "Rayleigh scattering and weak localization: Geometric effects and fluctuations", Phys. Rev. B **35**, 6517 (1987).

[69]E. Akkermans, P.E. Wolf, and R. Maynard, "Coherent Backscattering of Light by Disordered Media: Analysis of the Peak Line Shape", Phys. Rev. Lett. **56**, 1471 (1986).

[70]V. Twersky, "Transparences of pair-correlated, random distributions of small scatterers, with applications to the cornea", J. Opt. Soc. Am. **65**, 524 (1975).

[71]L. Tsang, J.A. Kong and T. Habashy, "Multiple scattering of acoustic waves by random distribution of discrete spherical scatterers with the quasicrystalline and Percus-Yevick approximation", J. Acoust. Soc. Am. **71**, 552 (1982).

[72]A. Ishimaru and Y. Kuga, "Attenuation constant of a coherent field in a dense distribution of particles", J. Opt. Soc. Am. **72**, 1317 (1982).

[73]G. Bergmann, "Weak localization in thin films; a time of flight experiment with conduction electrons", Phys. Rep. **107**, 1 (1984). G. Bergmann, "Localization in thin films. A time-of-flight-experiment with conduction electrons", Physica **126B**, 229 (1984).

[74]Kmel'nitskii, "Localization and coherent scattering of electrons", Physica **126B**, 235 (1984).

[75]C.A. Condat and T.R. Kirkpatrick, "Observability of Acoustical and Optical Localization", Phys. Rev. Lett. **58**, 226 (1987).

[76]P. Sheng and Z.Q. Zhang, "Scalar-Wave Localization in a Two-Component Composite", Phys. Rev. Lett. **57**, 1879 (1986).

[77]K. Arya, Z.B. Su and J.L. Birman, "Anderson Localization of electromagnetic Waves in a Dielectric Medium of Randomly Distributed Metal Particles", Phys. Rev. Lett. **57**, 2725 (1986).

[78]E. Akkermans and R. Maynard, "Weak localization of waves", J. Physique Lett. **46**, L1045 (1985).

[79]M. Abramowitz and I.A. Stegun, "Handbook of Mathematical Functions" (Dover, New York, 1972).

[80]K.E. Atkinson, "A Survey of Numerical Methods for the Solution of Fredholm Integral Equations of the Second Kind" (Society for Industrial and Applied Mathematics, Philadelphia, 1976).

[81]H.H. Kagiwada, R.Kalaba, and S. Ueno, "Multiple Scattering Processes" (Addison-Wesley, Reading, 1975).

[82]I.S. Gradshteyn and I.M. Ryzhik, "Table of Integrals, Series, and Products" (Academic, New York, 1980).

[83]A.A. Golubentsev, "Suppression of interference effects in multiple scattering of light", Sov. Phys. JETP **59**, 26 (1984) [Zh. Eksp. Teor. Fiz. **86**, 47 (1984)].

[84]M.P. van Albada, M.B. van der Mark and A. Lagendijk, "Observation of Weak Localization of Light in a Finite Slab; Anisotropy Effects and Light-Path Classification", Phys. Rev. Lett. **58**, 361 (1987).

[85]E.R. Hansen, "a table of series and products" (Prentice-Hall, 1975).

[86]W.A. Kampfer, Pigment Handbook (Patton) Vol. I (Wiley, New York, 1973).

[87]M. Kaveh, M. Rosenbluh, I. Edrei and I. Freund, "Weak Localization and Light Scattering from Disordered Solids", Phys. Rev. Lett. **57**, 2049 (1986).

[88]S. Etemad, R. Thompson, M.J. Andrejco, S. John, and F.C. MacKintosh, "Weak Localization of Photons: Termination of Coherent Random Walks by Absorption and Confined Geometry", Phys. Rev. Lett. **59**, 1420 (1987).

[89]M.P. van Albada and A. Lagendijk, "Vector Character of Light in Weak Localization: Spatial Anisotropy in Coherent Backscattering from a Random Medium", Phys. Rev. B **36**, 2353 (1987) (Rapid communication).

[90]M.P. van Albada, M.B. van der Mark and A. Lagendijk, "Polarisation effects in weak localisation of light", J. Phys. D **21**, S28 (1988) (ECOOSA '88).

[91]F.C. MacKintosh and S. John, "Coherent backscattering of light in the presence of time-reversal-noninvariant and parity-nonconserving media", Phys. Rev. B **37**, 1884 (1988).

[92]F.C. MacKintosh, J.X. Zu, D.J. Pine, and D.A. Weitz, "Polarization memory of multiply scattered light", Phys. Rev. B, **40**, 9342 (1989) (Rapid communications).

[93]P.E. Wolf, G. Maret, E. Akkermans and R. Maynard, "Optical coherent backscattering by random media: an experimental study", J. Phys. France **49**, 63 (1988); E. Akkermans, P.E. Wolf, R. Maynard and G. Maret, "Theoretical study of the coherent backscattering of light by disordered media", J. Phys. France **49**, 77 (1988).

[94]E. Akkermans, "Propagation d'ondes dans les milieux desordonnés", University of Grenoble thesis (1986).

[95]I. Freund, M. Rosenbluh, R. Berkovits, and M. Kaveh, "Coherent Backscattering of Light in a Quasi-Two-Dimensional System", Phys. Rev. Lett. **61**, 1214 (1988).

[96]M. Rosenbluh, I. Edrei, M. Kaveh, and I. Freund, "Precision determination of the line shape for coherently backscattered light from disordered solids: Comparison of Vector and Scalar theories", Phys. Rev. A **35**, 4458 (1987).

[97] Yu.A. Kravtsov and A.I. Saichev, "Effects of double passage of waves in randomly inhomogeneous media", Sov. Phys. Usp **25**, 494 (1982).

[98] J.M. Drake and A.Z. Genack, "Observation of Nonclassical Optical Diffusion", Phys. Rev. Lett. **63**, 259 (1989).

[99] A. Lagendijk, R. Vreeker and P. de Vries, "Influence of internal reflection on diffusive transport in strongly scattering media", Phys. Lett. A **136**, 81 (1989).

[100] P.M. Morse and H. Feshbach, "Methods of theoretical physics" (McGraw-Hill, New York, 1953).

[101] A.D. Stone, "Magnetoresistance Fluctuations in Mesoscopic Wires and Rings", Phys. Rev. Lett. **54**, 2692 (1985).

[102] S.M. Cohen and J. Machta, "Localization of Third Sound by a Disordered Substrate", Phys. Rev. Lett. **54**, 2242 (1985).

[103] M.B. van der Mark and A. Lagendijk, "Experiments on 2-Dimensional Weak Localisation of Light", EQEC '88 (1988); M.B. van der Mark and A. Lagendijk, "Light scattering experiments on a 2-dimensional random medium", QELS '89 (1989).

[104] R.A. Davies and M. Pepper, "Logarithmic and power law corrections in two-dimensional electronic transport" J. Phys C **15**, L371 (1982).

[105] H. De Raedt, A. Lagendijk, and P. de Vries, "Transverse Localization of Light", Phys. Rev. Lett. **62**, 47 (1989).

[106] H.A. Atwater, "Introduction to Microwave Theory" (McGraw-Hill, 1962).

[107] G. Hass and L. Hadley, "Optical Properties of Metals", page 6-103, American Institute of Physics Handbook, 2$^{\text{nd}}$ edition (McGraw-Hill, 1963).

[108] N.W. Ascroft and N.D. Mermin, "Solid State Physics" (CBS Publishing ASIA, 1976).

[109] A.J. Bur, "Dielectric properties of polymers at microwave frequencies: a review", Polymer, **26**, 963 (1985).

[110] M.N. Afsar, "Precision Dielectric Measurements of Nonpolar Polymers in the Millimeter Wavelength range", IEEE Trans. Microwave Theory Tech., **MTT-33**, 1410 (1985); M.N. Afsar, "Precision millimeter wave measurements of complex refractive index, complex dielectric permittivity and loss tangent of common polymers", IEEE, **CH2267**, 94 (1986).

[111]M.N. Afsar, J.R. Birch and R.N. Clarke, “The Measurement of the Properties of Materials”, proc. of the IEEE, **74**, 183 (1986).

[112]P. Klocek, “Infrared Fiberoptics, how good they are now, how good they will be and what they are good for”, Lasers & Applications, p. 43, october (1982).

[113]D.E. Freund, R.L. McCally, and R.A. Farrell, “Effects of fibril orientations on light scattering in the cornea”, J. Opt. Soc. Am. A **3**, 1970 (1986).

[114]B. Schlicht, K.F. Wall and R.K. Chang, “Light scattering by two parallel glass fibers”, J. Opt. Soc. A **4**, 800 (1987).

[115]H.A.Yousif, S. Köhler, “Scattering by two penetrable cylinders at oblique incidence. I The analytical solution”, J. Opt. Soc. A **5**, 1085 (1988); ibid., “II Numerical examples”, J. Opt. Soc. A **5**, 1097 (1988).

[116]S. John, “Localization and absorption of waves in a weakly dissipative disordered medium”, Phys. Rev. B **31**, 304 (1985).

[117]C.M. Soukoulis, E.N. Economou, G.S. Grest and M.H. Cohen, “Existence of Anderson Localization of Classical Waves in a Random Two-Component Medium”, Phys. Rev. Lett. **62**, 575 (1989).

[118]D. Sornette and B. Souillard, “Strong Localization of Waves by Internal Resonances”, Europhys. Lett. **7**, 269 (1988).

[119]J.R. Propert-Jones, “Surface waves in backscattering and the localization principle”, J. Opt. Soc. Am. **73**, 503 (1983); ”Resonance component of backscattering by large dielectric spheres”, J. Opt. Soc. Am. A **1**, 822 (1984).

[120]C.A. Condat, “Acoustic localization and resonant scattering”, J. Acoust Soc. Am. **83**, 441 (1983).

[121]V.A. Davies and L. Schwartz, “Electromagnetic propagation in close-packed disordered suspensions”, Phys. Rev. B **31**, 5155 (1985).

[122]G.F. Reiter and A. Lagendijk, “Dependent-scattering effects in the determination of the criterion for the localization of waves”, unpublished.

[123]P. Lloyd, “Exactly solvable model of electronic states in a three-dimensional disordered Hamiltonian: non-existance of localized states”, J. Phys. C **2**, 1717 (1969).

Summary for scientists

In this thesis I investigate the propagation of light in disordered media. The final goal of this investigation is the observation of the phenomenon of Anderson localization. Localization as introduced by P.W. Anderson refers to a dramatic change in the propagation of an electron when it is subject to a spatially random potential. Normally the electron is scattered diffusively, resulting in a finite conductivity. In this multiple scattering process, interference can be neglected. At localization, where the diffusion constant vanishes, the interference of (multiple) scattered waves cannot be neglected any more, but indeed its influence becomes essential. Because it is just the interference of *waves* that is important, diffusive behavior of multiple scattered light may as well show a transition to localized states. This phase transition is expected to occur when the mean free path λ_{tr} becomes smaller than the wavelength in the medium λ_{med}, and is known as the Ioffe-Regel criterion. In Chapter 1 this is explained in detail.

In Chapter 2 a global strategy for observation of Anderson localization is discussed. The scattering efficiency of the single particles in the random medium should be as high as possible in order to obtain the smallest possible mean free path. As usual for phase transitions, the occurence of Anderson localization is strongly dependent on the dimensionality of the random medium. It is believed that in an infinite lossless two-dimensional random medium there is always localization. Therefore observation of localization in a (quasi) two-dimensional medium may be possible.

In Chapter 3 and 4 theory for scattering of waves from a single particle, and a multiple scattering theory for isotropic point scatterers are given respectively. Some attention is paid to the mapping of scalar and vector waves in Sect. 4.1. Both a rigorous theory and a diffusion theory of multiple scattering by a slab are given, and their results are compared. Further, a time-resolved diffusion theory and a diffusion theory for a two-dimensional system are presented.

Chapter 5 reports of various experiments which have been performed. These experiments are compared to the theory as presented in Chapter 4. Experiments in which the backscattered intensity of light from a random slab is recorded, show an enhancement of almost a factor of two at precisely backscattering. This phenomenon is known as "coherent backscattering" and is the result of interference in multiple scattering. Coherent backscattering is seen as a precursor to Anderson localization, and is therefore often refered to as weak localization. A very interesting experiment is described in Sect. 5.4.2. In this time-resolved experiment the transmission of a slab of TiO_2 particles in air for 5 ps input pulses at $\lambda_{vac} = 600\,\mathrm{nm}$ is recorded. From this experiment the diffusion constant is determined to be $7.4\,\mathrm{m}^2/\mathrm{s}$. Comparison to the Ioffe-Regel criterion, with the average re-

fractive index of the medium $n_{med} = 1.55$, leads to $2\pi\lambda_{tr}/\lambda_{med} = 0.775 n_{med}^2 \simeq 1.86$ which is remarkably close to the critical value of 1. Moreover, the mean free path as determined from the coherent backscattering of the same sample is significantly larger than the value as obtained from the time-resolved transmission experiment. These results give strong evidence that we indeed are very close to Anderson localization.

In Chapter 6 some possibilities of constructing a two-dimensional random medium are discussed. In Sect. 6.2 experimental results are given of some measurements on a translation-invariant type of two-dimensional medium, consisting of many parallel glass fibers with a diameter of 5 μm. These results show that it is indeed possible to construct high-quality quasi-two-dimensional random systems. Observation of Anderson localization in such a medium will however only be possible if the mean free path is shortened. This may be done by either drawing much thinner fibers or by using fibers of the same size but which are transparent in the infrared. In order to make the mean free path as short as possible, media having a high density of scatterers are usually studied. This may result in complications in the form of particle-particle correlations or dependent scattering. Some considerations about these phenomena are given in Chapter 7.

A very important conclusion is that the determination of the diffusion constant or mean free path should be done with different techniques on the same sample. In the diffusive regime those techniques will all lead to the same answer for the diffusion constant, where in the critical or localization regime significantly different answers are expected if the measurements are interpreted in terms of a theory which assumes diffusive behavior of the scattered light.

Samenvatting voor iedereen

Dit proefschrift gaat over voortplanting van licht in sterk verstrooiende wanordelijke systemen. Voorbeelden van deze wanordelijke systemen zijn bijvoorbeeld het papier waarop deze tekst is gedrukt, een glas melk, de wolken aan de hemel, kortom alles wat wit is. In zekere zin gaat dit proefschrift dus over wat er gebeurt als licht op een wit voorwerp valt. Waarom witte voorwerpen nu eigenlijk wit zijn is al sinds jaar en dag bekend. Ze zijn opgebouwd uit een mengsel van (minstens) twee volledig transparante materialen. Zo bestaan wolken (mist) uit vele miljarden piepkleine waterdruppeltjes met daar tussen gewoon lucht. Lucht en water zijn elk afzonderlijk transparant. Blijkbaar gaat bij een zeer fijne verdeling van water in lucht deze doorzichtigheid verloren. Dit komt doordat het licht bij ieder waterdruppeltje wordt weerkaatst of afgebogen in een willekeurige richting. Daardoor verdwaalt het licht in de wolk; het weet niet meer waar het oorspronkelijk vandaan kwam, noch waar het heen ging. Na op deze manier een heleboel keer van het kastje naar de muur gestuurd te zijn, zal het licht uiteindelijk toch de rand van de wolk bereiken en daar in een willekeurige richting (diffuus) naar buiten komen. De wolk straalt het oorspronkelijk ingekomen licht weer uit in de vorm van diffuus licht, anders gezegd, de wolk is wit. In het onderzoek zoals beschreven in dit proefschrift gaat het er om, om het licht dat in een wanordelijk systeem zoals een wolk zit, zo snel mogelijk te doen verdwalen. Hiervoor is behalve de afmeting van de waterdruppeltjes ook hun onderlinge afstand van belang.

Al aan het eind van de jaren '50 heeft de natuurkundige P.W. Anderson voorspeld dat golven (zoals licht) die in een of ander medium zeer sterk worden verstrooid (verdwalen), ten gevolge daarvan opgesloten kunnen worden in dat medium. Dit verschijnsel staat nu bekend als Anderson-lokalisatie. Essentieel hierbij is het optreden van interferentie. Interferentie is het effect dat twee golven die elkaar tegenkomen, elkaar zowel kunnen versterken als uitdoven. Versterking treedt op als de golfbewegingen van beide samenkomende golven gelijktijdig maximaal zijn. Uitdoving ontstaat als een maximum en een minimum samen komen; de tegengestelde bewegingen van beide golven heffen elkaar op. Het opmerkelijke is nu dat er in het verstrooiings proces van een golf in een wanordelijk medium altijd versterking optreedt op de plaats waar de golf oorspronkelijk vandaan kwam. Het gevolg hiervan is dat de golf steeds een iets grotere kans heeft om terug te komen op een eerder bezochte plek. Hierdoor kan de golf in de buurt van zo'n plek blijven ronddolen, de nachtmerrie voor een ieder die verdwaald is. Ik moet u dan ook terstond gerust stellen: hoewel mensen op andere wijze wel degelijk kunnen interfereren, treedt dit effect alleen maar op voor golven en domme detectives in de woestijn.[*)] Het voorgaande wordt in o.a. hoofdstuk 1 besproken.

In hoofdstuk 2 wordt ingegaan op het doel van het onderzoek en op de te gebruiken experimentele methoden. Zo kan men bijvoorbeeld een bundel laser licht op een wanordelijk medium doen schijnen en vervolgens meten hoeveel licht er in verschillende richtingen door dat medium weer wordt uitgestraald. Hierbij kan men dan ook nog de grootte van het medium of de concentratie van het aantal verstrooiende deeltjes (bijvoorbeeld waterdruppeltjes) veranderen. Het gebruik van laser licht is van belang, omdat het gemakkelijk gebundeld kan worden, maar één golflengte bevat en bovendien een hoge intensiteit bezit. Om inderdaad het uiteindelijke doel, het waarnemen van Anderson-lokalisatie van lichtgolven, te kunnen bereiken is het op de eerste plaats noodzakelijk een medium te construeren dat het licht nog veel sterker verstrooit dan de hierboven beschreven waterwolk. Het blijkt dat titaandioxide deeltjes met een diameter van $0,0002\,\mathrm{mm}$ gemengd met lucht het licht veel sterker kunnen verstrooien dan een waterwolk.

Om een nauwkeurig inzicht te verkrijgen in de verstrooiings-eigenschappen van een wanordelijk systeem waarin nog geen Anderson-lokalisatie optreedt en het licht zich derhalve nog gewoon diffuus voortplant, wordt in de hoofdstukken 3 en 4 een hoeveelheid theorie gepresenteerd.

Hoofdstuk 5 bevat een verslag van een aantal uitgevoerde experimenten, waarvan de resultaten worden vergeleken met de theorie van hoofdstuk 4. Deze experimenten laten bijvoorbeeld zien dat interferentie-effecten inderdaad van belang zijn bij voortplanting van licht in wanordelijke media. Een bewijs hiervoor is het optreden van de zogenaamde ,,coherente terugverstrooiing", die vanwege de verwantschap met Anderson-lokalisatie ook wel wordt aangeduid met ,,zwakke lokalisatie". Coherente terugverstrooiing is het effect dat, ten gevolge van interferentie, de intensiteit van het diffuus verstrooid licht in de richting precies terugwaarts naar de bron altijd bijna tweemaal zo hoog is als in alle andere bijna terugwaartse richtingen.

Een belangrijk experiment wordt beschreven in paragraaf 5.4.2. In dit experiment worden met behulp van een laser lichtpulsen met een tijdsduur van $0,000.000.000.005$ seconde geschoten op een wanordelijk medium bestaande uit titaandioxide deeltjes en lucht. Aan de andere kant van het medium word gemeten hoe lang het licht er over doet om door het medium heen te komen. Vergeleken met andere experimenten en de theorie van hoofdstuk 4 blijkt het licht aanzienlijk langer binnen het medium te blijven dan op grond van normaal diffuus gedrag zou worden verwacht. Dit is een sterke aanwijzing dat we in dit geval dichtbij het optreden van Anderson-lokalisatie zijn gekomen. Het optreden van Anderson-lokalisatie zelf hebben we echter (nog) niet kunnen waarnemen.

In de wereld waarin we leven kunnen we ruimtelijke gezien drie onafhankelijke richtingen onderscheiden, te weten hoogte, breedte en diepte. Zo'n wereld noemen we driedimensionaal. In deze wereld blijken mogelijkheden voor het experimenteel waarnemen van Anderson-lokalisatie uitermate onzeker. Op theoretische gronden weten we echter dat in een *tweedimensionale* wereld, een platte wereld waarin alleen maar lengte en breedte bestaat, Anderson-lokalisatie veel gemakkelijker zal kunnen optreden. In hoofdstuk 6 worden verschillende technieken besproken om een wanordelijk medium te construeren dat zich effectief als een tweedimensionaal medium gedraagt. Hierbij wordt op verschillende wijze de verstrooiing van licht naar de derde dimensie belet. Het prepareren van een tweedimensionaal medium blijkt zo gecompliceerd, dat het alleen met zeer geavanceerde technieken mogelijk moet zijn om een medium te maken waarin Anderson-lokalisatie ook inderdaad experimenteel kan worden waargenomen. Niettemin wordt verslag gegeven van een aantal uitgevoerde experimenten aan een zogenaamd translatie-invariant tweedimensionaal medium, bestaande uit vele duizenden parallelle glasvezels, waarbij aannemelijk wordt gemaakt dat het medium tot op zekere hoogte voldoet aan de criteria voor lokalisatie. Het zijn hier met name de afmetingen van het medium en de absorptie in de glasvezels die een succesvolle observatie van Anderson-lokalisatie in de weg staan.

Tot slot wil ik benadrukken dat het belang van deze studie naar de voortplanting van licht in wanordelijke systemen veel verder strekt dan men op het eerste gezicht zou vermoeden. Resultaten uit dit onderzoek met lichtgolven hebben in principe ook consequenties voor het gedrag van andere soorten van golven in de natuur zoals geluidsgolven of quantummechanische golven. Omdat het juist deze quantummechanische golven zijn die de materie in het universum beschrijven, en we derhalve kunnen zeggen dat in feite de hele wereld om ons heen uit golven is opgebouwd, wordt het wetenschappelijk belang van de mogelijke ontdekking van een nieuw effect zoals Anderson-lokalisatie van licht duidelijk.

[*)] Hergé, ,,Kuifje en het zwarte goud" (Casterman, 1950).

Nawoord

Gedurende de tijd die ik, eerst als student, later als promovendus heb doorgebracht op het Natuurkundig laboratorium der Universiteit van Amsterdam, heb ik vele mensen binnen het lab leren kennen als vrienden die altijd met hun diensten voor mij klaar stonden. Alvorens een poging te doen al deze mensen te noemen wil ik eerst mijn zeer gewaardeerde promotor Ad Lagendijk bedanken voor zijn intensieve betrokkenheid bij mijn experimentele-, maar vooral bij mijn theoretische werk. Het is zeker dat ik zonder hem aan hoofdstuk 4 nooit was toegekomen.

Voor de technische ondersteuning van mijn experimenten zijn in de loop der tijd verschillende instrumentmakers in touw geweest. Ron Manuputy, Ad Wijkstra, Willem Martijn, Theo Huymans, René Rik, Rinse Bethlehem, Ruud Scheltema, Jan Hoffman, Hans Ellermeijer en enige stagiaires. Zonder uitzondering hebben zij klasse werk afgeleverd en vaak nog heel snel ook.

Over klasse werk gesproken moet ik onmiddellijk Ton Riemersma en Hugo Schlatter noemen. Deze jongens weten altijd een nòg betere oplossing aan te dragen. Paul Langemeijer is nog zo'n zeldzaam nuttig persoon.

Vele anderen hebben een belangrijke steen bijgedragen, te weten Mariet Bos, Kho, Eddy Inoeng, Ben Harrison, Charlie Alderhout, Ad Veen, Bert Zwart, Klaas van Paasschen, Ben Leonards, Michiel Groeneveld, Joost Overtoom en Jan Dekker.

Voor het prepareren van tweedimensionale media was het ter beschikking stellen van een ultrasoonbad door de heer Postma van biochemie een uitkomst. Dick Bebelaar van fysische chemie was steeds weer zo vriendelijk om snelle electronica of infrarood optiek aan mij uit te lenen. Ook Dr. A. Michels van het Van der Waals laboratorium hielp me bijzonder door het uitlenen van o.a. een HeCd-laser. Ab Kuntze van Technische Natuurkunde der TUD was in staat, geheel op maat, een zeer breedbandige deelspiegel te maken. Van groot belang was ook de levering van glasvezel textiel door dhr. Vanneuville en dhr. Van Wilderode van Vetrotex Brussel en door Owens-Corning. Dr. Ronald Hond van Sigma Coatings en de heer J.H. Franssen firma Sikkens B.V. zorgden voor onze titaandioxide deeltjes. I wish to thank Mr. J. Smith of Mullard Mitcham for kindly supplying some microchannel plates. Door de Stichting FOM ben ik in staat gesteld een cursus management te volgen op Nijenrode. Het ter beschikking stellen van een computer door de firma Homer B.V. was een uitkomst. Pa Mulder en Peter den Outer worden van harte bedankt voor het doorlezen van het manuscript.

Meint van Albada komt veel dank toe voor de aanzienlijke bijdrage aan dit proefschrift door al het werk dat we samen hebben gedaan en de vele waardevolle discussies die we hebben gevoerd. Mede door jouw zeer eigen manier van het benaderen van een probleem

ben ik je steeds meer gaan waarderen. Zonder de inzet, het geduld en vakmanschap als instrumentmaker van mijn paranimf Wim Koops was de preparatie van tweedimensionale media onmogelijk geweest. Mijn andere paranimf, Rudy Hertroys, is immer tot mijn vreugde al in menig activiteit mijn metgezel geweest.

Als ik weer eens vast zat met mijn berekeningen, was Pedro de Vries altijd klaar om uitkomst te bieden; ook Adriaan Tip is me zo eens belangrijk van dienst geweest. Veel dank gaat ook uit naar Peter Molenaar, die een belangrijke bijdrage heeft geleverd door het uitvoeren van de tijdopgeloste experimenten. Johan de Boer, Rob Vreeker, Roos Eisma en Rudolf Sprik worden allen zeer bedankt voor hun directe of indirecte bijdrage aan dit proefschrift. Met plezier denk ik ook terug aan de in verschillend opzicht kleurrijke aanwezigheid van Jaap Berkhout, Mick Baggen en Raymond van Roijen gedurende de meeste jaren die ik op het lab heb door gebracht. Alle (oud)leden van de onderzoeksgroep ,,Spectroscopie van de verdichte materie” wil ik bijzonder bedanken voor de goede en leerzame sfeer waarin ik al de afgelopen jaren heb mogen werken. De vrijdagmiddagbijeenkomsten waren daarbij inderdaad in menig opzicht vaak een hoogtepunt.*) Ik verheug me op voortzetting van onze door de jaren heen buiten werktijd (?) ondernomen activiteiten.

Ouders en ,,schoon” ouders, bedankt voor de goede zorgen die u voor mij en Inge over hebt gehad. Inge, mijn liefste, als ik wist dat er geen betere lectuur voor je bestond had ik dit boekje zeker aan je opgedragen. Zonder jouw steun en vergiffenis voor vele eenzame nachten zou de totstandkoming hiervan wel heel dicht bij het onmogelijke gelegen hebben.

*)R. Sprik, ,,Experiments on spin-polarized atomic hydrogen at high density” (proefschrift, 1986); M.P. van Exter, ,,Ultra-fast spectroscopy of vibrational excitations and surface plasmons” (proefschrift, 1988); R. van Roijen, ,,Atomic hydrogen in a magnetic trap” (proefschrift, 1989).